SCHOOL OF ENGINEERING
The Department of Civil Engineering and Industrial Design

Impact Response of Recycled Aggregate Concrete Filled Steel Tube Columns Strengthened with CFRP

Thesis submitted in accordance with the requirement of the University of Liverpool for the degree of Doctor of Philosophy in Civil and Structural Engineering

By

Alaa Salam Shakir Al-Husainy

B.Sc. (Hons) Structural Engineering

M.Sc. Structural Engineering

April 2017

DEDICATION

To the spirit of my father who has given me all the support I need to be what I wanted to be and who has been the source of inspiration to me throughout my life;

To my mother for her love and her prayers for me during my life;

To my brother and sisters for their encouragement and their support;

To my wife Sura Salim for her personal support, encouragement and great patience during the research period;

Finally, to my beloved children, Fatema, Sakina and Muhammad who are the glow of my life;

I dedicate this work.

Declaration

This thesis is the result of my own work and any quotation from, or description of the work of others is acknowledged herein by reference to the sources.

This thesis is not the same as any that I have submitted for any degree, diploma or other qualification at any other university. No part of this thesis has been or is being concurrently submitted for any such degree or other qualification.

Alaa Salam Shakir Al-Husainy

Liverpool, April 2017

ACKNOWLEDGEMENTS

First and foremost, I would like to express my utmost appreciation and gratitude to my primary supervisor, Dr. Zhongwei Guan for his valuable guidance, supervision, continuous support, patience and encouragement throughout my PhD research. His technical and personal support is deeply acknowledged. I also would like to express my gratitude to my second supervisor, Dr. Steve Jones for his constructive advice and helpful suggestion and assistance. I am grateful to Dr. Robert Birch, who helped me to learn using the Laser Doppler equipment and the processing of the data.

I would like to acknowledge the financial support given by the Iraqi government via the Higher Committee for Education Development in Iraq (HCED). The efforts given by the staff in Placement UK, Monitoring UK, Monitoring 8 and the Finance section to assist with the administration and financial issues of my scholarship are really appreciated.

I would like to thank Sloyan Doyle demolition company (Liverpool, England), for providing the recycled aggregate.

I am grateful to Dr. William Atherton, Liverpool John Moores University, for providing me the opportunity to carry out the compression test at the lab of Department of civil engineering. I would like to thank the lab's technicians in particular Mr. John Sinclair for helping me during the test.

I would like to thank the staff of the School of Engineering at the University of Liverpool, especially Mr. Adam Mannis, Mr. Stephen Pennington, Mr. David Hunter, Mr. Marc Bratley, Mr. Derek Neary, Mr. John Curran, Mrs. Lesia Swain and Mr. Steven Bode. I am indebted to them for their assistance during my work.

Many thanks also go to the postgraduate admission of the School of Engineering and to the postgraduate admission staff of the University of Liverpool and the international support team (IST) for giving me all the help I needed during my PhD research.

Finally, I offer my regards and blessings to my friends and colleagues in the research group who supported me in all respects during my PhD research.

LIST OF PUBLICATIONS

Journal Papers:

A.S. Shakir, Z.W. Guan, S.W. Jones (2016). The lateral impact response of concrete filled steel tube columns strengthened with CFRP. Engineering Structures, 116, 148-162

A.S. Al-Husainy, Z.W. Guan, S.W. Jones, Q.Y. Wang (2016). The Compression Behaviour of Concrete Filled Steel Tube columns: Experimental and Numerical Investigation (Submitted).

A.S. Al-Husainy, Z.W. Guan, S.W. Jones, C. Su (2017). Modelling the impact response of the recycled and normal aggregate concrete filled steel tube columns (Submitted).

Conference Papers:

A.S. Shakir, Z.W. Guan, S.W. Jones (2014). Nonlinear finite element analysis of concrete filled steel tube (CFST) columns under projectile impact loading. The 5th International Conference on Computational Methods (ICCM), Cambridge, UK / {Best Paper Award}.

A.S. Shakir, Z.W. Guan, S.W. Jones (2015). The compression behaviour of concrete Filled steel tube columns: experimental and numerical investigation. The 3rd International Conference on Advances in Civil, Structural and Mechanical Engineering (CSM), Birmingham, UK.

ABSTRACT

The aim of this research work is to gain a deep insight and understanding into the impact response of the recycled aggregate and normal aggregate concrete filled steel tube (RACFST and NACFST) columns strengthened with carbon fibre reinforced plastic (CFRP). It also includes an investigation on the compressive behaviour of RACFST and NACFST columns under concentric or eccentric loadings. The environmental protection is an important factor which requires engineers to recycle as many materials as possible to conserve natural resources. Therefore, using the recycled aggregates fits with this trend.

In this project, material tests were initially carried out to obtain the mechanical properties of the concrete, steel and the CFRP. Structural tests on RACFST and NACFST columns were then undertaken to gain the corresponding lateral impact and axial compressive behaviour. The main parameters studied for the dynamic tests were the L/D ratio, impactor configuration (i.e. flat and spherical and size), concrete type (i.e. normal and recycled aggregate), the D/t ratio and the strengthening with CFRP. The CFST specimens were also tested under concentric or eccentric loadings to investigate the influence of the D/t ratio, the type of the concrete and the CFRP wrapping on the structural behaviour of those specimens. The results indicate that under impact loading both the RACFST and NACFST specimens show a similar deformation mode, which also applies to compressive loading case. However, the load carrying capacity of the RACFST specimens is slightly lower than that of the NACFST columns. The results also show that the additional confinement of the CFRP reduces the global displacement for both the RACFST and NACFST specimens. It is found that the concrete filling increases the maximum force by 217, 182 and 157 % respectively for the short, medium and long tubes. The impactor configurations have great effects on the impact force and the displacement for the tubes filled with normal and recycled aggregate concrete. The D/t ratio also has a considerable influence on the compression behaviour of the CFST column irrespective the type of the concrete.

3-D finite element models were developed using the commercial code ABAQUS/Standard and ABAQUS/Explicit to simulate the compressive behaviour and impact response of the NACFST and RACFST columns, respectively. All the numerical models were validated against the corresponding experimental data, with a very good agreement. The finite element models for both the dynamic and quasi-static tests produced accurate predictions of the force-displacement traces and deformation modes. Using the validated models, parametric studies were carried out to investigate the influence of several parameters such as the impact energy, material properties, the CFRP coverage and D/t ratio.

Based on the research output, it is recommended that the RACFST column can be used as a structural composite member for construction due to the comparable load carrying capacity to the NACFST tube. This will further contribute to the conservation of the natural resources as using the recycled aggregates with appropriate mechanical properties.

NOTATIONS

L	length of the tube
D	outer diameter of the tube
t	thickness of the tube
M_p	plastic bending moment of concrete filled steel tube
$f_{c'}$	cube compressive strength of the concrete
r_i	inner radius of the tube
γ_0	angular location of the plastic neural axis
f_y	yield strength of the steel tube
r_m	mean radius
F	maximum impact force
N_o	fully plastic axial force
δ_{max}	maximum total displacement
IE	impact energy
Θ'	rotation angle at the tube end
f_{cc}	cylinder compressive strength for the confined concrete
f_{ck}	cylinder compressive strength of the concrete
$\mathcal{E}_{cc}$	confined concrete strain
$\mathcal{E}_{ck}$	corresponding strain with the *fcc*
r	radius of the tube
f_u	ultimate force for the confined concrete
$\mathcal{E}_u$	corresponding strain with *fu*
f_{yd}	dynamic yield strength of the steel
f_{ys}	static yield strength of the steel
$\dot{\varepsilon}$	Strain rate
D_{cs}	(Cowper-Symonds) model parameter
f_{td}	dynamic tensile strength of the concrete

f_{tc} static tensile strength of the concrete

f_{cd} dynamic compressive strength of the concrete

f_{cs} static compressive strength of the concrete

$\dot{\varepsilon}_s$ static strain rate of the steel

V velocity

σ_{co} compression failure stress

σ_{to} tensile failure stress

σ_{cu} ultimate stress

d_t damage variable in tension

d_c damage variable in compression

ε_t^{pl} equivalent plastic strain in compression

ε_c^{pl} equivalent plastic strain in tension

Θ temperature

fi field variable

E_0 elastic stiffeners

E_{cc} elastic modulus of confined concrete

w_c crack width

w_{cc} critical crack width

List of Content

Table of Content

List of Figures

List of Tables

CHAPTER 1

INTRODUCTION

1.1 Overview

Concrete filled steel tubes (CFSTs) are used increasingly in many structural applications, such as seismic-resistant construction, high rise buildings, bridge piers and offshore structures (Shanmugam and Lakshmi, 2001; He et al., 2011; Sundarraja and Prabhu, 2011). Fig. 1.1 shows some concrete filled steel tube applications. CFSTs have more advantages than the conventional reinforced concrete and structural steel members, namely the high speed of construction work resulting from the omission of formwork and reinforcing bars, low structural costs and conservation of the environment (Morino et al., 2001; Morino and Tsuda, 2002; Lam and Wong, 2005; Starossek et al., 2008). CFSTs also offer good damping properties and excellent seismic resistance (Kang et al., 2007). Moreover, CFSTs have a good fire resistance compared with ordinary reinforced concrete, which leads to a reduction in the use of fireproof materials (Morino et al., 2001, Jiang et al., 2010).

Shenxigon Bridge in China Mode-Gakuen Spiral Towers in Japan

Figure 1.1. Concrete filled steel tube applications
(Source: www.funonthenet.in; www.highestbridges.com)

CFST provides a high load carrying capacity due to the interaction between the concrete core and the steel tube, which provides concrete confinement and delays the buckling of the tube. This enhancement results from the composite action of the concrete core, which has a high compressive strength and the steel tube with high ductility and tensile strength (Shams and Saadeghvaziri, 1997, Kovac, 2010). In addition, the local buckling in CFST columns can be delayed due to the contact between concrete core and steel tube (Perea, 2010).

During the service life, structures may experience impact loading. For examples, bridge columns could be impacted by a vehicle or boat, high buildings could be attacked by aircraft, or falling loads due to an accidental explosion (Chakradhara et al., 2011). The columns of bridge piers and a multi-story building are very important structural members and their failure caused by an impact loading may lead to progressive collapse further to disproportionate collapse. Therefore, attention should be given to study and understand the overall behaviour of a column under lateral impact loading, in particular for CFST columns which provide a high bearing capacity as mentioned earlier. This is a wide research area and the work presented in this study only forms one part of it.

With increasing the construction and demolition wastes resulted from the rapid development of the construction industry, recycling the waste of concrete becomes necessary to preserve the environment and to conserve the natural resources of gravel and sand. The hollow structural steel sections filled with recycled aggregate concrete (RAC) are called recycled aggregate concrete filled steel tubes (RACFST). The harmful environmental factors, such as wind, temperature and water, have less impact on RAC used in CFST columns because of the protection provided by the steel tube. Many studies investigated the response of the RACFST columns under quasi-static and cyclic loading but studying their behaviour under lateral impact loading is still limited.

The use of the carbon fibre reinforced plastic (CFRP) jackets has become increasingly popular to repair or strengthen concrete columns. It was found that the additional confinement provided by the CFRP strips increases the bearing capacity of the column and delayed its local buckling (Sundarraja and Prabhu, 2012). In general, the enhancement of the bearing capacity of concrete filled steel tubes by using CFRP jacketing only in the critical areas can lead to more economic structures. Although these findings related to static and cyclic loadings are available but there is a lack of information on the behaviour of the CFST strengthened with CFRP under lateral impact loading. Thus, it will be valuable to investigate the impact response of the CFST columns strengthened with CFRP, especially the ones filled with RAC. In addition, it is very useful to produce a NACFST and RACST columns with a high load carrying capacity and limited quantity of CFRP reinforcement.

Despite many past researches on the structural behaviour of the CFST columns under qausi-static loading, the impact behaviour of the NACFST and RACFST is not well studied and understood. To date, there has been limited research on the behaviour of the NACFST columns especially of the RACFST columns under lateral impact loadings. In addition, the impact behaviour of the strengthened circular RACFST columns with CFRP local reinforcement has not been investigated under lateral drop-weight loading.

The finite element code ABAQUS (ABAQUS 6.14) was used to simulate and understand the lateral impact and axial compression responses of NACFST and RACFST columns. ABAQUS is very popular finite element analysis software due to the robust theoretical framework and the high ability to model different materials. The comparison between the ABAQUS numerical results and the corresponding experimental ones for large studies show its potential. In addition to its availability, ABAQUS is adopted in present study for the following reasons.

- Two main solvers are used in ABAQUS, i.e. the implicit solver ABAQUS/Standard and explicit solver ABAQUS/Explicit. The former is

able to analyse the linear and nonlinear static and dynamic response of structure (low speed). The latter provides capability for analysing the lateral impact problems such as drop weight tests and crash analysis of structural members,

- The interaction between the contacted surfaces used to predict the impact force is relatively easily formulated in ABAQUS/ Explicit. Also, with the robust contact algorithm in ABAQUS/Explicit, no additional degrees of freedom needed to be added to the model.
- The convergence checking and iteration are not required in ABAQUS/Explicit.
- The material's failure and element deletion for elastic and plastic materials are included in ABAQUS/Explicit which lead to its explicit analysis procedure with more accurate modelling for the mode of failures (local and global) with mitigation of the convergence problems,
- The large number of the element types in ABAQUS is able to model many different types of problems, and
- ABAQUS/ Explicit is capable of efficiently solving the big problems with small disk spaces.

1.2 Research Objectives

The first goal of this study is to experimentally understand the impact response of the NACFST and RACFST with and without CFRP strengthening and to numerically simulate the corresponding dynamic behaviour of the NACFST and RACFST columns, including the prediction of the force-displacement traces and modes of failure, using the finite element analysis. The purpose of this part of the work is to gain a thorough understanding on how the CFST column components, i.e. steel tube and concrete core, respond to a low velocity lateral impact loading. The influence of different geometrical

and material parameters on the CFST columns behaviour under low velocity lateral impact loading will be investigated in parametric studies.

The second goal of this work is to gain understanding of the axial compression behaviour of the NACFST and RACFST columns with and without CFRP strengthening by conducting experimental and numerical investigations.

Even though extensive experimental and numerical work has been carried out on concrete filled steel tube columns under axial load, very limited research work has been undertaken to investigate the effect of recycled aggregate concrete on the structural response of CFST columns under lateral impact loading. The research work proposed in this project will provide a better understanding of the structural behaviour of recycled aggregate concrete filled steel tube columns strengthened with CFRP under axial compression and lateral impact loadings.

The main objectives of this study are:

1) To obtain an improved understanding of the eccentric and concentric axial compression behaviour of RACFST columns strengthened with CFRP by carrying out experimental tests and finite element modelling;
2) To have an insight into understanding of the behaviour of RACFST and NACFST columns strengthened with CFRP under lateral impact loading through both experimental and numerical investigations;
3) To perform a numerical analysis in order to efficiently study the effect of the important parameters on the impact behaviour of RACFST and NACFST columns, such as the diameter to thickness ratio (D/t), the impact energy (IE), the length of CFRP bond, and the ultimate strength of concrete and steel tube.

1.3 Layout of the thesis

This thesis presents an extensive literature review of the existing research related to this study. The experimental results of the quasi-static and dynamic tests are presented and discussed. The validation of numerical simulations, parametric studies and the simplified

theoretical models are also explained and examined. The thesis consists of seven chapters and is organized as follows:

Chapter 1: Presents an introduction of the CFST, RAC, FRP and the finite element analysis. In addition, the main objectivises of the research as well as the thesis outline are included.

Chapter 2: Reviews the previous research work relevant to the present investigation. The experimental investigations and theoretical analysis on RACFST and NACFST columns under quasi-static and dynamic are presented and discussed. The finite element analysis investigations on the CFST columns are also included.

Chapter 3: Describes the experimental work which includes the materials, mix design, casting and post casting curing, recycled aggregate treatment and the preparation of specimens. The CFRP strengthening process is also presented. This chapter also includes the test setup and the description of devices used for both the lateral impact and axial compression tests conducted in this study. The processing of the data obtained from the high speed camera and Laser Doppler Velocimeter is also presented.

Chapter 4: The experimental results obtained from the impact and compression tests are presented and discussed. This chapter consists of two parts, i.e. the impact test results and the results of the columns subjected to eccentric and concentric axial loading. The results in relation to various parameters such as the CFRP reinforcement, type of concrete, tube length and impactor configuration covered in this study are compared and analysed.

Chapter 5: Presents the development of the finite element analysis to simulate the structural behaviour of the CFST column under lateral impact and axial compression using the commercial code ABAQUS/Explicit and Implicit. The chapter describes materials properties, constitutive models, loading conditions, failure criteria, mesh sensitivity study, the interaction between the steel tube and the concrete core, as well as the boundary conditions. All numerical models were validated against the experimental findings.

Parametric studies using the validated numerical models developed in this chapter were carried out to investigate the effects of several parameters on the impact and compression response of the CFST columns. Here, the results obtained from these studies are compared and discussed.

Chapter 6: Draws the main conclusions of the research findings and gives suggestions for the future research work.

CHAPTER 2

LITERATURE REVIEW

2.1 Introduction

An overview on concrete filled steel column behaviour obtained from the existing literature is presented here. The previous work relevant to the current research is reviewed in this chapter. The existing knowledge related to the studies on concrete filled steel tubes under compression and impact loadings covers the experimental work and analytical research. It also includes reviewing the previous studies on the structural behaviour of recycled aggregate concrete filled steel tubes (RACFST). Furthermore, the research carried out on the structural behaviour of the concrete filled FRP tube and the FRP strengthened CFST are presented, together with a review of the numerical analyses of CFST columns. Finally, the strain rate effect on the CFST columns is discussed and the related researches are reviewed.

2.2 Overview

The Fig. 2.1 (a) shows the cross section shapes used in CFST column systems, which are circular, square and rectangular (Kovac, 2010). However, some researchers have conducted studies on the behaviour of elliptical sections (Lam and Testo, 2008, Dai and Lam, 2010), whilst others have investigated an innovative X section (Chen and Jin, 2010). The round ended rectangular and polygon cross section shapes are used for architectural reasons (Han et al., 2014), as shown in Fig. 2.1 (b).

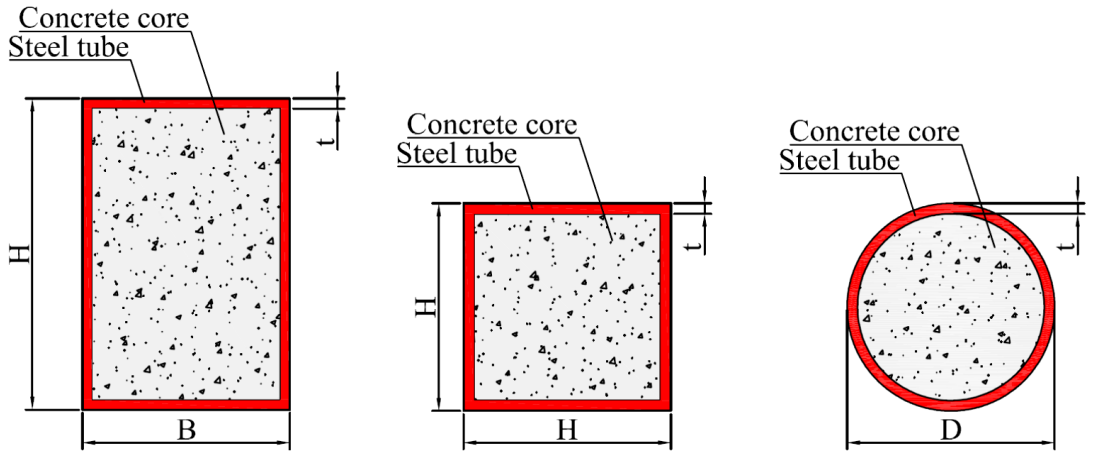

(a) The most widely used cross section shapes

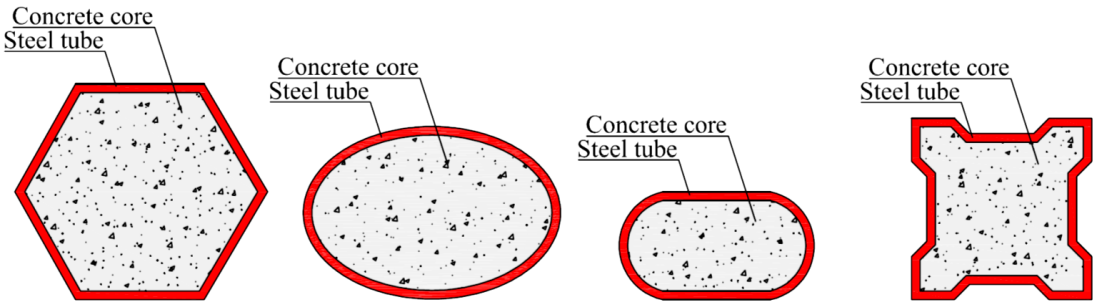

(b) Rarely used cross section shapes

Figure 2.1. Typical cross section shapes for the CFST columns (Han et al., 2014)

It is believed that the confinement offered by the steel tube has a significant effect on the behaviour of CFST, especially for a CFST column under axial loading. As the Poisson's ratio of steel (0.3) is higher than that of concrete (0.15-0.22), the confinement effect can be negligible at the initial stage of loading and the concrete core will not be confined, since the steel tube will expand more in the lateral direction than the concrete core (Shanmugam and Lakshmi, 2001; Susantha et al., 2001). The change of Poisson's ratio of concrete resulting from the increase in the axial loading causes a lateral dilation of concrete greater than that of steel, which in turn causes a radial pressure at the contact area between concrete and steel. At this point, the steel tube will restrain the concrete core, which generates a hoop tension in the steel (Knowles and Park, 1969; Shanmugam and Lakshmi, 2001; Susantha et al., 2001;

Kovac, 2010), as shown in Fig. 2.2. The ultimate load of CFST is greater than the sum of loads which can be obtained from the independent loading of concrete and steel (Susantha et al., 2001).

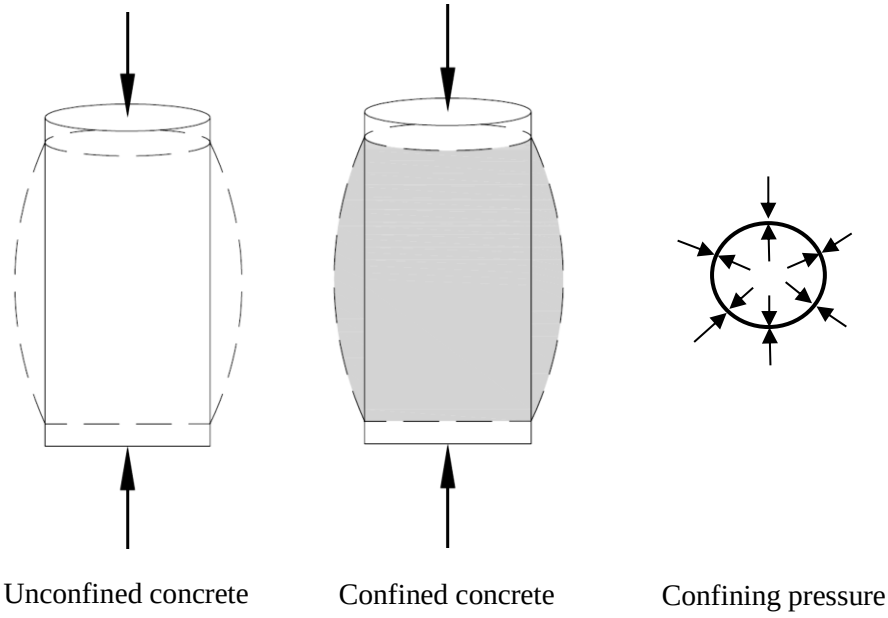

Figure 2.2. Confining pressure engaged by dilation of concrete (Harries and Kharel, 2003)

In general, the post yield strength and stiffness for the circular tubes are higher than those with square and rectangular cross sections, due to the high confinement offered by the circular section. In the rectangular and square sections, the confinement is limited and it is located around the corners and in the centre, as there is weakness of the straight parts of these sections to resist the internal pressure, due to the dilation of the concrete core (Shams and Saadeghvaziri, 1997; Schneider, 1998; Huang et al., 2002; Hu et al., 2003; Kovac, 2010). Fig. 2.3 shows the difference of the confinement effects between circular and square sections. Due to the strong confining effect in the circular section, local buckling is less likely to occur (Hu et al., 2005).

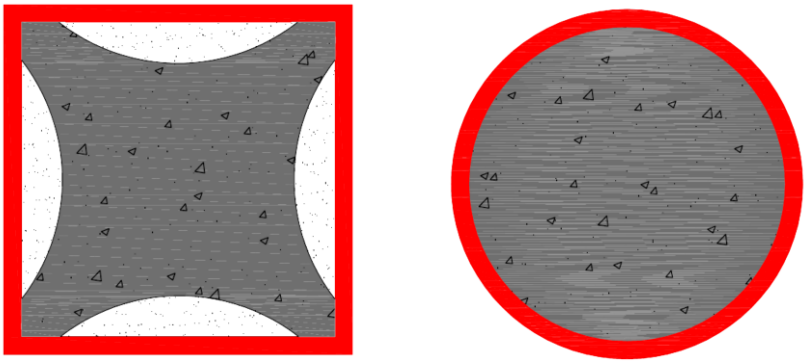

(a) Partial confinement (b) Full confinement

Figure 2.3. The confinement effect in circular and square sections (de Oliveira et al., 2009)

Under axial compression, the unfilled steel tube exhibits inward and outward local buckling, while the combination of shear and splitting failures result in the failure in the unconfined concrete. The shear failure causes the failure of the confined concrete and however, the splitting failure is avoided even for low levels of confinement level. The shear damage occurs in the restricted region of the concrete filled tube and initiates near the maximum stress (de Oliveira et al., 2009). The comparison between the failure mode of CFST with the steel tube and concrete is shown in Fig. 1.6 (a).

When the unconfined reinforced concrete is subjected to bending loading, the top surface crushes and the bottom surface cracks, whilst the unfilled steel tube exhibits inward buckling and deflection. The combination between the steel and concrete can change the deformed shape (Han et al., 2014). Thus, the cracks and the crack width of the concrete core will be reduced and the steel tube buckling and deflection will be less. Moreover, the overall deflection for the concrete and steel tube decreases due to the composite action between the steel and concrete. Fig 1.6 (b) shows the effect of the combination between steel tube and concrete on the failure mode. The concrete filled tube specimen could hold its shape without crushing, in comparison to the plain concrete specimen which was crushed under the same loading (Xiao et al., 2009).

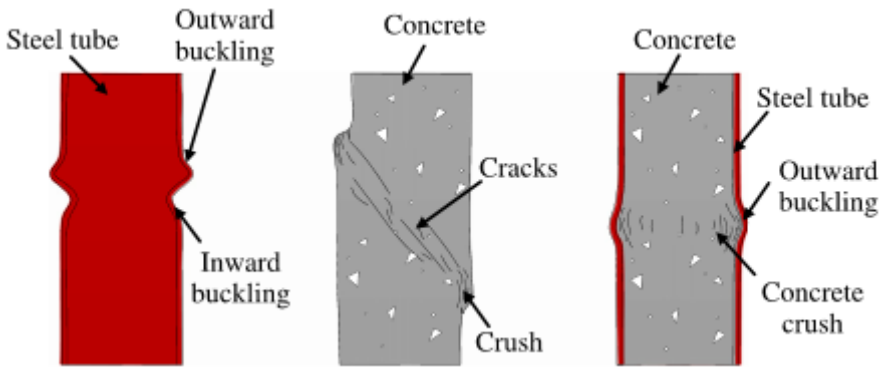

(a) Compression loading

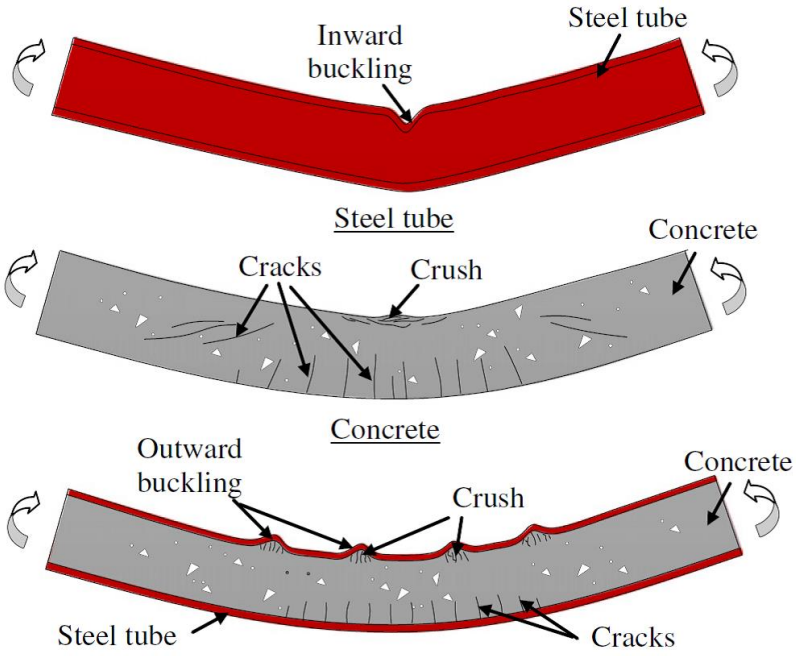

(b) Flexural loading

Figure 2.4. The modes of failure under compression and flexural loadings (Han et al., 2014)

2.3 The compression behaviour of concrete filled steel tubes

At the early twentieth century a number of structures were built using composite sections of composite structures, namely CFST. Many buildings in Europe included CFST members, such as the M4/M5 Almonds-bury Motorway Interchange in the UK, the International Labour Organization in Geneva, a Gymnasium at Martigny-Boury in Switzerland, and Charleroi Railway Station in Belgium (Shams, 1997). Many research projects were carried out to investigate the behaviour of CFST columns under various load conditions with different parameters, such as the tube cross sectional shape (i.e. circular, square and

rectangular), the ratio of the tube length to the outer diameter (L/D), the diameter to wall thickness ratio (D/t), strength of steel tube, strength of concrete and the load eccentricity. It was found that the load carrying capacity of concrete was increased due to the confining stress of the steel tube, which was resulted from increasing the concrete volume at a certain value of longitudinal compression (Knowles and Park, 1969; Xiao et al., 2005; Dundu, 2012). The post yield strength and stiffness of the circular tube was higher than those with square and rectangular cross sections (Schneider, 1998; Huang et al., 2002). However, the load carrying capacity of the columns decreased with increasing the (L/D) ratio (Zeghiche and Chaoui, 2005; Dundu, 2012).

The CFST columns with circular or square sections were studied by Knowles and Park (1969) under eccentric and concentric axial loading. The variables studied were the slenderness ratio, the concrete core strength and the strength of the steel tube. They found that the columns with a circular section exhibited a higher strength than those with a square section. An experimental study and the related analysis were presented by Schneider (1998) to investigate the compression response of the concrete filled short steel tube columns subjected to concentric axial load. The experimental work included testing of 14 specimens with different cross sections (circular, square and rectangular). Two main parameters were studied i.e., the L/D ratio and the D/t ratio. It was found that the stiffness and the bearing capacity for the tubes with square or rectangular section was less than those with circular section. A comparison between the experimental data and the results obtained from the AISC and LRFD codes (AISC 306-05, 2005; LRFD, 1995) showed that these codes were sufficient to predict the axial peak load of CFST. Abed et al. (2013) studied the compression behaviour of the concrete filled steel tube column. Six specimens were tested with two main parameters; the diameter to wall thickness ratio and the compression strength of the concrete. They concluded that the stiffness and the axial load carrying capacity of the CFST columns were decreased with increasing the D/t ratio.

The effect of the compaction methods on the bearing capacity of concrete filled steel tubes was studied by Han (2000). Sixteen short columns and five long columns were tested in the study. The main parameters investigated were the load eccentricity and slenderness ratio. The results showed that the ultimate strength of the short and long columns which filled with compacted concrete using a poker vibrator was higher than those filled with concrete compacted by hand.

Giakoumelis and Lam (2004) concluded that the axial displacement decreased when the concrete strength increased. Also, they found that for the specimens with a high concrete strength, the difference in the bearing capacity between greased and non-greased tubes was 17 %, as shown in Fig. 2.5. Bruneau and Marson (2004) proposed a design equation for concrete filled steel tubes under axial and flexural loadings based on the comparison between the experimental results and those obtained from the standard specifications. The theoretical predictions showed a good agreement with the experimental data. Young and Ellobody (2006) presented an experimental investigation to study the behaviour of concrete filled high strength steel tube columns under uniform compressive load. Different parameters were examined, such as the strength of steel tube, the compression strength of concrete, the cross section shape (square and rectangular), the width to thickness ratio, and height to width ratio. The results showed that the high strength steel specimens with a relative high slenderness ratio failed in local buckling, while the specimens with compact section failed with crushing of the concrete and local buckling. Based on the comparison between the experimental results and those predicted from the American, Australian and New Zealand specifications, they recommended to employ the standards of these codes to design the concrete filled high strength stainless steel tube columns.

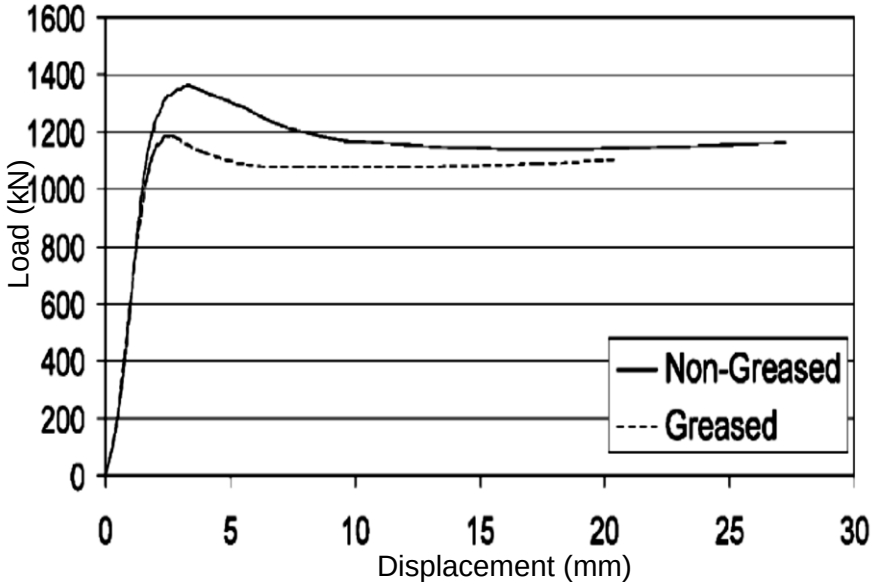

Figure 2.5. The comparison between the greased and non-greased steel tubes filled with high strength concrete (Giakoumelis and Lam 2004)

Yu et al. (2007) investigated the behaviour of the circular steel tubes filled with self-compacting concrete under compressive loading. They examined the effect of several parameters such as the loading conditions and the concrete strength. It was demonstrated that the load carrying capacity increased when the concrete strength increased. The results also showed that the steel confinement was affected by the loading condition. The confinement effect decreased when the steel tube was loaded initially, while loading the concrete first or alone caused an enhancement in the confinement effect. Han et al. (2008) conducted an experimental research to study the response of the concrete filled steel tube stub columns under local compression loading. They examined the effect of the cross section shape, the end plate thickness and the loading area. It was found that the CFST column under a local compressive loading showed a ductile failure with less bearing capacity. Also the thin endplate reduced the numbers of bulges of the steel tube due to the local failure of the top endplate. The local compression effects on the behaviour of the CFST columns were studied by Ding et al. (2015). Twenty columns included twelve circular and eight square tubes were tested. They found that the maximum capacity increased when the local loading area increased due to increasing the confinement effect. The ductility and the load carrying capacity for the square section

was less than those with a circular section. Also the bearing capacity increased when the concrete compressive strength increased.

Zeghiche and Chaoui (2005) tested 27 circular concrete filled steel columns with lengths between 2 m and 4 m. Fifteen columns were loaded concentrically, whilst 8 specimens were subjected to eccentric axial loading. It was concluded that the load carrying capacity of the columns decreased when the tube length and loading eccentricity increased. The behaviour of CFST stub columns loaded eccentrically was investigated by Yang and Han (2011). The study consisted of two parts, i.e. experimental and numerical investigations. The experimental part included the testing of 28 specimens with different parameters, such as the distance between the loading centre and the centre of the column (eccentricity ratio, 0-0.4) and the tube cross sectional shape (circular, square and rectangular). They demonstrated that the CFST columns exhibited ductile behaviour under eccentric loading and the capacity of the rectangular and square columns was again less than the circular column. Portoles et al. (2011) conducted an experimental investigation to study the behaviour of circular CFST columns under eccentric loading. The research included several parameters such as the concrete strength, the D/t ratio and the L/D ratio. The eccentricity ratio was varied from 0.16 to 0.5. The results indicated that increasing the tube length and the eccentricity ratio led to a reduction in the maximum capacity of the columns. In addition, the load carrying capacity of the tube was enhanced by reducing the D/t ratio and increasing the concrete compressive strength.

2.4 The impact response of concrete filled steel tube member

CFST members used in bridges and high buildings may be impacted by a vehicle or boat or it could be attacked by an aircraft during their service life. Falling loads on CFST members in any structure due to an accidental explosion or a terrorist attack can cause an impact failure. These incidents increase the need to study and to understand the behaviour of the CFST members under impact loading via both experimental and numerical research.

Some research work was initially conducted to study the flexural behaviour of NACFST under bending (Gho and Liu, 2004; Kang et al., 2007 and Deng et al., 2012). Elchalakani et al. (2001) conducted experiments on 12 specimens of NACFST under pure bending. The results showed that the energy absorption and ductility were enhanced. Also the flexural strength for the thin circular hollow section was improved more by the concrete filling than that for the thick one. They presented a theoretical model to predict the ultimate bending strength for the circular NACFSTs, which was in good agreement with the experimental data. The plastic bending moment in Fig 2.6 can be expressed as

$$M_p = \frac{2}{3} f_c' r_i^3 cos^3\gamma_0 + 4 f_y r_m^2 t cos\gamma_0 \tag{2.1}$$

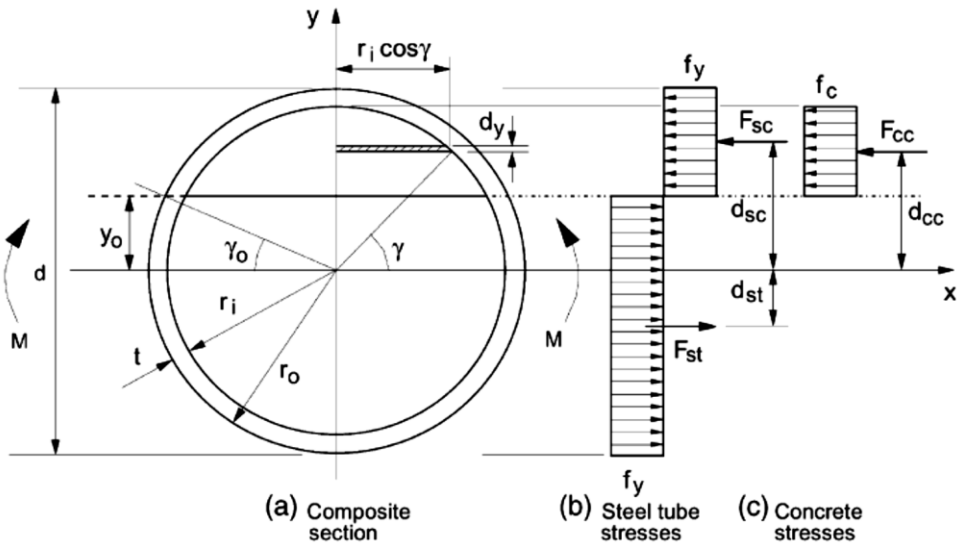

Figure 2.6. The ultimate bending moment capacity of the circular CFSTs (Elchalakani et al. 2001)

where $f_c^{'}$ is the cylinder compressive strength of the concrete, f_y is the yield strength of the steel tube, t is the tube thickness, r_i is the inner radius of the tube, and $r_m = (r_i+R)/2$ is the mean radius. γ_0 is the angular location of the plastic neutral axis that can be calculated by the following equation.

$$\gamma_0 = \frac{\frac{\pi}{4}\left(\frac{f_c^{'} r_i^2}{f_y r_m t}\right)}{2 + \frac{1}{2}\left(\frac{f_c^{'} r_i^2}{f_y r_m t}\right)} \tag{2.2}$$

The performance of the recycled aggregate concrete filled steel tubular columns under constant axial loading and cyclic flexural load was investigated by Yang et al. (2009). Thirteen circular columns were tested; ten of them were filled with RAC while the others were filled with NAC. The experimental test parameters were the type of the concrete and the loading ratio (the applied axial force to the maximum axial capacity ratio). They demonstrated that the behaviour of CFST columns with RAC was similar to those with NAC. The bearing capacity of the CFST with RAC was lower than the corresponding ones with NAC. The CFST made from RAC with 50 % recycled aggregate content can be used in a seismic zone. Fig. 2.7 shows the typical failure mode for the concrete filled steel tube columns.

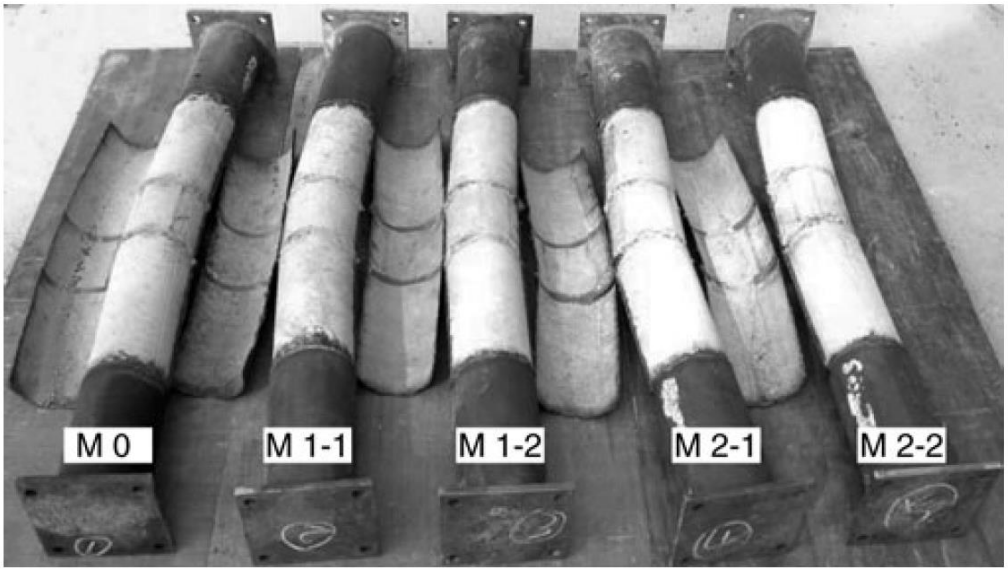

Figure 2.7. Typical failure modes of the CFST columns (Yang et al., 2009)

Experimental studies were conducted to investigate the effects of the lateral impact loading on the unfilled and filled tubes with different filling materials and tube materials (Prichard and Perry, 2000; Shan et al., 2007; Huo et al., 2009). Xiaoqing and Stronge (1985) studied the impact damage on hollow, water and sand filled steel tubes hit by spherical missiles. The results showed that the water and sand filling reduced the deflection and increased the

stiffness of the tube. Nishida and Tanaka (2006) investigated the perforation and cracking of water filled aluminum tubes impacted by six steel spherical indenters with different diameters. It was concluded that under the conditions adopted in their study, the strength of the tube wall was reduced due to filling with water which reduced the impact velocity. The behaviour of hollow and polyurethane foam filled steel tubes under axial impact load was investigated by Reid et al. (1986). It was found that the foam filled tubes had a better bearing capacity than the empty tubes. The concrete filled tube specimen could hold its shape without crushing, in comparison to the plain concrete specimen which was crushed under the same load (Xiao et al., 2009). Remennikov et al. (2011) conducted an experimental and numerical investigation to study the effect of the low speed impact load on the structural hollow tube filled with rigid polyurethane foam (RPF) and concrete. The adopted tube sections in this study were mild steel and stainless steel square sections. The experimental results showed that the bearing capacity of the square tubes filled with concrete was higher than those filled with RPF. The RPF increased the energy absorption and it could enhance the hollow tubes' resistance against the impact and blast loadings. The numerical results obtained from the LS-DYNA model were in a good agreement with experimental data, as can be seen from Fig. 2.8, which shows the comparison between the numerical and experimental results for the mild steel hollow tube filled with RPF (MDF1).

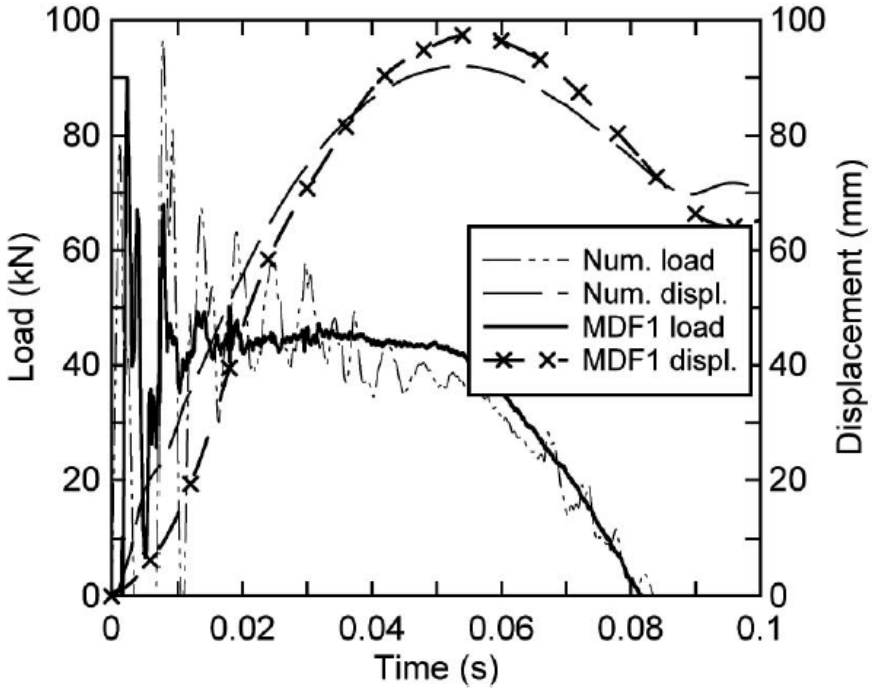

Figure 2.8. The comparison between the numerical and experimental results for MDF1 specimen (Remennikov et al. 2011)

In recent years, a number of studies on the impact behaviour of the normal aggregate concrete filled steel tube (NACFST) members have been conducted through experimental work, theoretical work and finite element analysis (Bambach, 2011; Qu et al. 2011and Deng and Tuan, 2013). The behaviour of the concrete filled square steel tube subjected to heavy mass and low velocity impact was studied by Bambach et al. (2008). The experimental work included testing a fully clamped beam with three different sizes under transverse impact load. However, the analytical part of this study included developing an elastic-plastic theoretical model to predict the maximum force for the CFST member with fixed ends under static and impact loadings based on a rigid-plastic analysis, which may be expressed as

$$F = \frac{6M_p}{L}\left(\frac{N_0\delta_{max}}{4M_p}\right)^2 + \frac{8M_p}{L} \tag{2.3}$$

where N_0 is the fully plastic axial force of the steel tube that can be calculated from:

$$N_0 = 4Dtf_y \tag{2.4}$$

It was concluded that the moment capacity of the concrete filled section was higher than the hollow section. A good agreement was obtained between the experimental results and those predicted from the proposed relationships, as can be seen in Table 2.1.

Table 2.1. Comparison between the theoretical and experimental results (Bambach et al. 2008)

	F (kN) static-test	F (kN) impact-test	F (kN) theo.	F static theo./test	F impact theo./test
50 x 50 x 1.6 hollow	32.8	40.2	38.8	1.18	0.97
50 x 50 x 1.6 concrete filled	39.5	42.6	41.3	1.05	0.97
35 x 35 x 1.6 hollow	22.9	22.6	27.3	1.19	1.21
35 x 35 x 1.6 concrete filled	19.3	20.6	23.8	1.23	1.15
20 x 20 x 1.6 hollow	12.7	11.8	13	1.02	1.1
20 x 20 x 1.6 concrete filled	10.6	12.7	12.5	1.18	0.98

A numerical model to study the behaviour of a circular concrete filled steel tube undergoing lateral impact load was presented by Qu et al. (2011). The software LS-DYNA was adopted in this study to undertake the numerical analysis. A good agreement was obtained between the experimental and finite element analysis results, as shown in Fig. 2.9. They derived a simplified analytical model to predict the maximum total displacement "δmax*"* at the mid-span of the fixed-pin ended circular CFST column under impact loading. The model assumes that the impact energy (IE) is dissipated by two plastic hinges formed at the maximum deflection of the mid-span of the column. The local deformation of the column is ignored in this model and the maximum total displacement can be predicted as follows:

$$\delta_{max} = \frac{L}{2} \times \Theta' \tag{2.5}$$

where L is the column length and Θ' refers to the rotation angle at the tube end, which can be obtained from

$$\theta' = \frac{IE}{3M_p} \tag{2.6}$$

Here, M_p refers to the dynamic plastic moment of the column section which is calculated from the experimental sustained impact force based on the bending moment diagram with consideration of the strain rate effect for both steel tube and concrete core by using a dynamic enhancement factor. The results in Table 2.2 showed that the proposed model can be used to predict the maximum deflection.

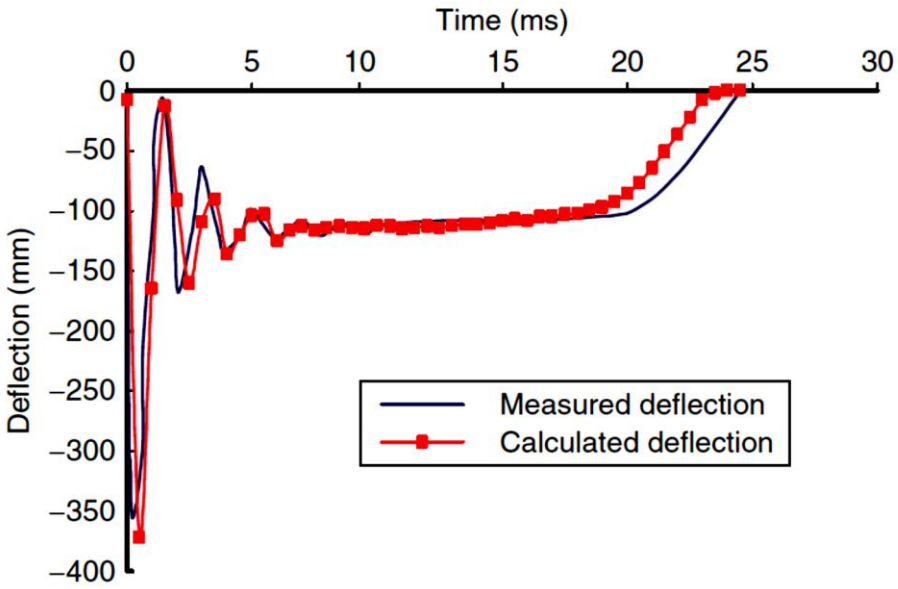

Figure 2.9. The mid-span cross section moment history from LS-DYNA_3D analysis (Qu et al., 2011)

Deng et al. (2012) carried out an experimental investigation to study the behaviour of twelve simply supported CFST members under lateral impact loading. The test included nine CFSTs, two post-tensioned CFSTs and one steel fibre concrete filled steel tube. The results showed that the specimens failed with tensile fracture or circumferential rupture. Also, the results indicated that the concrete reinforcement with steel fibre and prestressing strands enhanced the impact resistance.

Table 2.2. Comparison of the maximum deflection (Qu et al., 2011)

	Drop height (m)	Maximum deflection at mid span (mm) Pred.	Maximum deflection at mid span (mm) Theo.	Pred./theo.
CFT1	6	88.1	93.9	93.7
CFT2	8	118	124.4	94.8
CFT3	8.37	125	130	96.1

Wang et al. (2013) investigated the impact performance of the concrete filled steel tube members. Twenty two specimens were tested. The main test parameters were the impact energy, the axial load level and the constraining factor. A finite element model was built using the commercial code, ABAQUS. The concrete was modelled with 8-node brick elements and concrete damage plasticity model, while the steel tube was modelled using 4-node shell elements and an elasto-plasticity model. They demonstrated that the axial load did not affect the lateral displacement and the impact force. The finite element analysis results were in a good agreement with those obtained from the experimental tests. A study of three test series was conducted by Yousuf et al. (2012, 2013, and 2014). They investigated the transverse impact resistance of the hollow and concrete filled mild and stainless steel square tube columns. The structural behaviour of those columns was also studied through finite element analysis using ABAQUS. The comparison between the numerical results and the experimental data showed a good agreement. They found that the impact strength was improved by using stainless steel columns and the axial compression load did influence the static and impact strength, especially for the stainless steel tubes. Han et al. (2014) studied the impact behaviour of unfilled and concrete filled steel tubes. The main test parameters were the boundary conditions, the tube length, the impact velocity and the dropped weight. The experimental results showed that the concrete filling increased the tube ductility and enhanced the deformation resistance by reducing the local buckling and the tube deflection. They also developed finite element models using ABAQUS to simulate the impact response, which were validated against the experimental findings.

Aghamy et al. (2015) presented a numerical study on the impact behaviour of the CFST columns. The LS-DYNA code was used to model the columns. The interaction between the concrete and steel tube was set to the surface to surface contact with coefficient of friction of 0.6. Fig. 2.10 shows that the numerical results were in a good agreement with those obtained from the experimental tests. Parametric studies were also conducted and the results showed that the maximum force and the maximum deflection were highly affected by the t/D, slenderness ratio, impact location and the impactor mass.

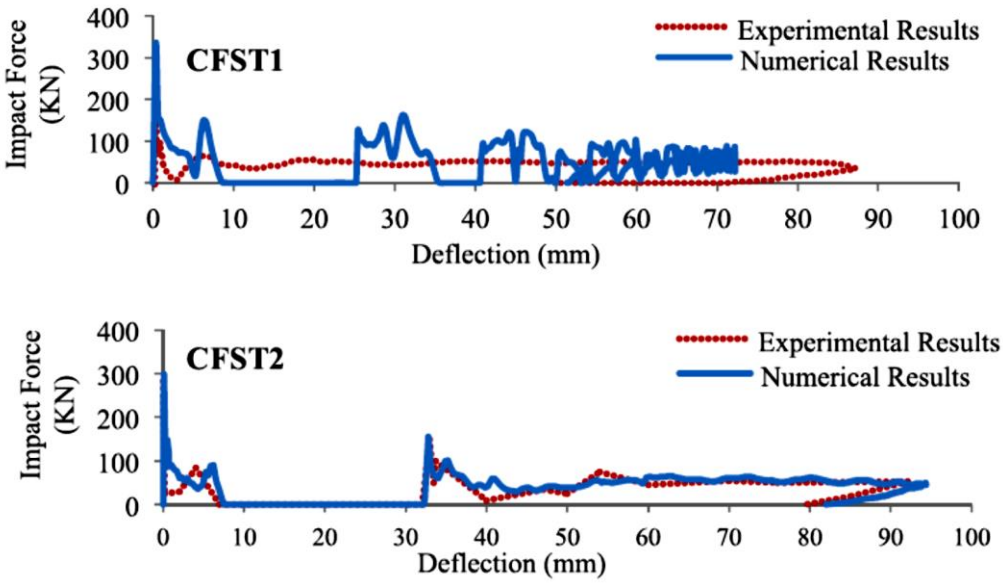

Figure 2.10. Comparison of experimental and numerical force versus time history (Aghamy et al. 2015)

Chen et al. (2014) tested eleven simply supported specimens to study the impact response of circular concrete filled steel tubes wrapped with FRP. Two types of FRP were used, i.e. CFRP and GFRP with one or two layers. Nine tubes were wrapped longitudinally, whilst one was wrapped transversely. Only one tube was tested without FRP to examine the effect of the FRP wrapping. The maximum drop weight mass was 80 kg dropped from a height of 1.5 m with a hemispherical head impactor. They concluded that the additional confinement enhanced the impact resistance by increasing the impact energy absorption and reducing the overall deflection particularly for the specimens

wrapped with GFRP. The results showed that when the number of the FRP layers increased the overall deflection decreased.

Alam et al. (2015) presented a numerical analysis of concrete filled steel tube columns strengthened with FRP under lateral impact loading. The finite element code ABAQUS was adopted in this study and the numerical models were validated with the experimental work by Chen et al. (2014). The confined concrete properties were obtained from theoretical confined concrete model shown in Fig. 2.11, proposed by Mander et al. (1988) and implemented in the concrete damage plasticity to simulate the behaviour of the confined concrete core. Elastic-plastic response was adopted to simulate the steel behaviour. To model the CFRP failure, Hashin failure criteria (Hashin, 1973) were adopted. Based on the validated models, they conducted parametric studies to examine the effect of several parameters, such as the impact velocity, the number of the CFRP layers, impact location, impact mass and the axial force. The numerical models correlated well with the experimental results. They demonstrated that the lateral deformation resistance was enhanced by increasing the number of CFRP layer from one to two. The axial force could reduce the lateral deformation and the increase of the impact velocity led to an increase of the lateral deflection, especially when the impactor hit the mid-span of the tube.

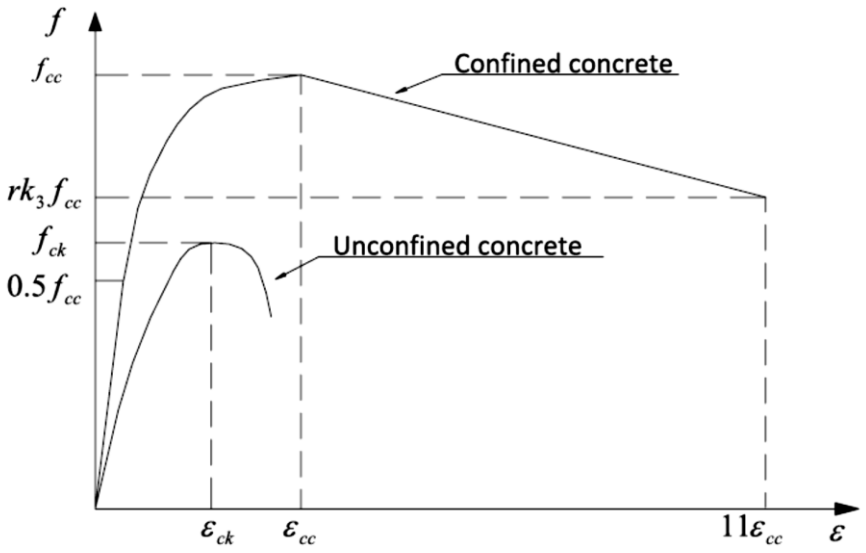

Figure 2.11. Comparison between the confined and unconfined concrete for circular tube (Dai and Lam, 2010)

Yang et al. (2015) studied the effect of the recycled aggregate replacement ratio on the impact behaviour of the concrete filled square steel tubes. The average concrete strength was 40.2, 35.9 and 33.7 MPa for the concrete with the recycled aggregate replacement ratio of 0, 50 and 100 %, respectively. The yield strength of the steel tube was 379.8 MPa and the span length was 1200 mm. The main test parameters were the impact height and the axial force ratio n (the applied compressive load/ the stability bearing capacity of RACFST member). They found that the RACFST specimens failed in the same manner as the corresponding specimens with normal aggregate. The results indicated that with increasing the replacement ratio of the recycled aggregate, the impact force decreased and the lateral displacement slightly increased. When the axial force ratio decreased and the impact height increased, the impact force increased. The experimental results were used to validate the numerical model. The concrete core was modeled using 8-node brick elements with reduced integration, while the steel tube was simulated using 4-node three dimensional shell elements with reduced integration. Good agreement was observed from the comparison between the numerical and experimental results, as can be seen from Fig. 2.12.

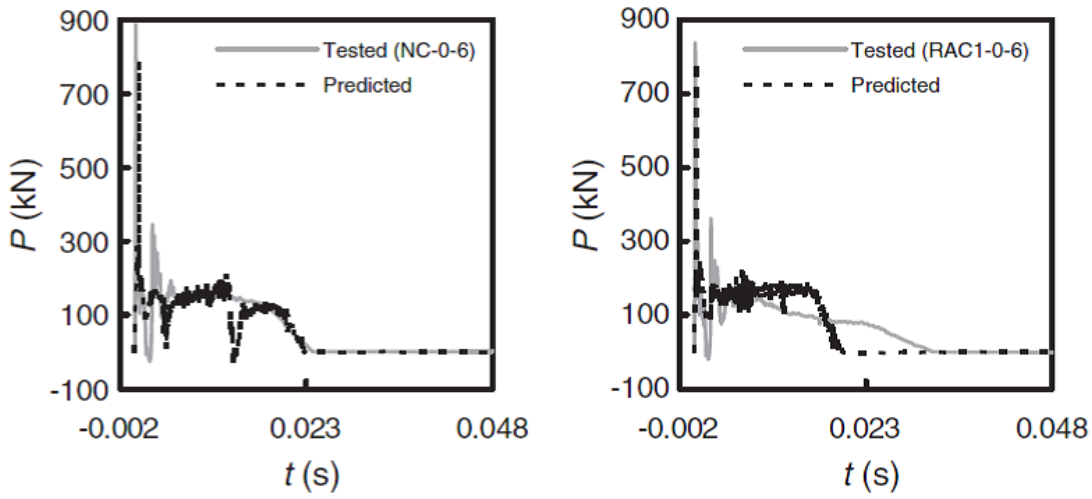

Figure 2.12. Comparison between the finite element analysis results with the test data (Yang et al. 2015)

It can be observed that the previous research on the impact behaviour of the CFST columns are still limited. In addition, very limited studies were carried out to investigate the impact response of RACFST columns, which only cover the square sections. The impact response of the circular RACFST column with and without CFRP strengthening has not been studied yet according to the knowledge of the author. Also, even very limited research was undertaken to investigate the strengthened NACFST columns under lateral impact loading.

The current research proposes to study and compare the results of the lateral impact tests of both the tubular NACFST and RACFST columns with and without CFRP strengthening.

2.4.1 The effect of the axial force on the response and mode of failure of the columns under lateral impact loading.

The behaviour of the axially compressed CFST column under lateral impact loading was studied by a small number of researchers (Yousuf et al., 2012, Yousuf et al., 2013, Wang et al., 2013; Yousuf et al., 2014 and Alam et al., 2015). However, a number of studies were conducted to study the axially compressed columns (Zeinoddini et al., 1999;

Zeinoddini et al., 2002; Adachi et al., 2004; Zeinoddini et al., 2008a; Zeinoddini et al., 2008b).

Zeinoddini et al. (2002) found that under transverse impact with high axial compression loading, the mode of failure was plastic global buckling. Under low axial loading, the deformation mode was mainly a local deformation at the impacted area with an indentation.

Adachi el al. (2004) studied the impact response of small scale axially compressed aluminum columns under lateral impact loading. They found that regardless of the impact location, the column buckles in the lower buckling mode when it is subjected to lateral impact loading with axial loading.

Al-Thairy and Wang, (2011); Al-Thairy and Wang, (2013) and Makarem and Abed, (2013) found that the axial force increases the lateral displacement within a short time, caused a large plastic deformation.

Wang et al. (2015) found that the axial force ratio which is the ratio of the applied axial force to the axial capacity of the column has no obvious effect on the impact force and the lateral displacement. Yousuf et al. (2014) found that the strength of the impacted stainless steel column with pre-compression was 3% lower than those with no pre-compression loading.

Alam et al. (2016) numerically studied the effect of the axial load on the impact response of the fully scale CFRP strengthened CFST column. They demonstrated that the lateral displacement increased with increasing the axial force for the CFST column without CFRP strengthening. However, increasing the axial force from 25 % to 100 % of the axial capacity of the strengthened CFST column did not affect the impact response of the column.

It can be demonstrated that the axial force has an effect on the columns subjected to lateral impact loading. This influence changes with the column conditions and the level of the applied axial force and it leads to increase the deformation and reduce the load carrying capacity of the column.

2.5 The structural behaviour of concrete filled steel tube strengthened with FRP and concrete filled FRP tube columns

Fibre reinforced plastic (FRP) has been used in many civil engineering applications. It is used to enhance the strength of the structural members in the form of a jacket, as a reinforcement material, or in the form of bars instead of steel reinforcement rods, or in concrete filled tube columns. FRP can be used to repair damaged concrete members to restore their strength, to restrict the crack growth due to increasing the designed or sustained loads and to increase the bearing capacity of the concrete members (Rao et al., 2006). In the long term, FRP can offer a high creep resistance. Also, it resists the weathering and temperature changes, UV radiation, humidity and atmospheric pollution. Advanced fibrous composite materials have important material characteristics such as "non-corrosiveness, high strength, high stiffness-to-weight ratios, light weight, weather resistance, dimensional stability, radar transparency, high impact strength, low maintenance, good specific mechanical properties, good durability in most environments, readily formed into complex shapes and low thermal conductivity" (Halliwell, 2002).

The use of the carbon fibre reinforced plastic (CFRP) jackets has become increasingly popular to repair or strengthen concrete columns (Teng and Lam, 2004). It was found that the additional confinement provided by the carbon fibre reinforced plastic (CFRP) strips increases the bearing capacity of the column and delayed its local buckling (Sundarraja and Prabhu, 2011). It was also found that the CFRP jackets have a significant effect on the ultimate capacity of the circular section, whilst its effect on the rectangular section is not effective (Tao et al., 2007). In general, the enhancement of the ductility and bearing capacity

of concrete filled and hollow steel tubes by using FRP jacketing in the critical areas can lead to more ductile and economic structures (Xiao, 2004).

Mirmiran et al. (1998) studied the effect of several parameters such as the slenderness ratio, the cross section shape, and the bond properties on the compression behaviour of the confined concrete by FRP tube. They demonstrated that the confinement effect for the circular tubes was higher than those with square cross sections. They also found that there is no effect for the chemical adhesive bond properties on the bearing capacity of the concrete columns confined by FRP.

Shan et al. (2007) investigated the performance of concrete filled steel tubes (CFT) and confined concrete filled steel tubes (CCFT) under high velocity impact. The CFST was wrapped by one layer of unidirectional carbon fibre reinforced polymer CFRP. They tested CFT and CCFT tubes under axial impact load by using a high speed gas gun and projectile with a mass of 815 g. They demonstrated that the dynamic strength increased by the additional confinement of the CFRP.

An investigation was carried out by Tao et al. (2007) to study the behaviour of the strengthened concrete filled steel tubular stub columns strengthened with carbon fibre reinforced plastic (CFRP) composite under axial compression loading. Nine circular and rectangular specimens were tested, which included 6 tubes being fully strengthened by unidirectional CFRP, while the others were reference tubes. The main test parameters were the cross sectional shape and the number of the CFRP layers. The results showed that the load bearing capacity of circular columns was enhanced by using CFRP jackets, as shown in Fig. 2.13. Also, they found that for the circular tube, the load carrying capacity increased and the ductility decreased with increasing the number of the CFRP layers.

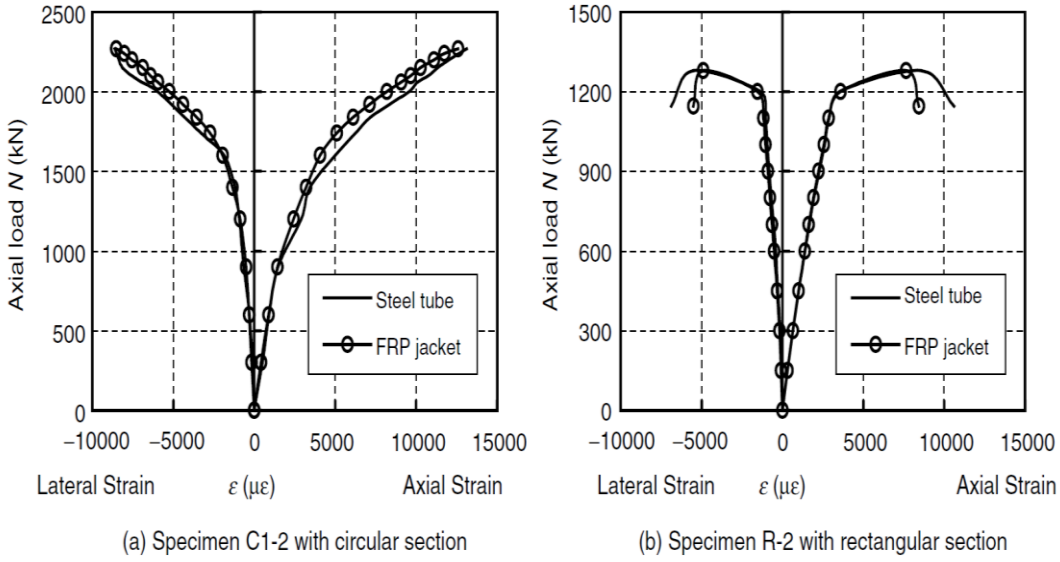

Figure 2.13. Comparison between measured strains of the steel tubes and FRP jackets (Tao et al., 2007)

Fitzwilliam and Bisby (2010) carried out an investigation to study the effects of the slenderness ratio on the circular reinforced concrete columns confined with CFRP under eccentric axial compression. Eighteen small scale circular reinforced concrete specimens were tested. The specimens tested were strengthened with longitudinal and circumferential wrap. The results showed that the strength and deformation capacity were increased with using CFRP hoop warps for both short and slender columns. Also, the longitudinal warps did improve the performance of the slender circular concrete columns.

Mohamed et al. (2010) presented a series of experimental tests on 22 concrete filled fibre reinforced polymer tube (CFFT) specimens to understand the effect of the slenderness ratio on the critical buckling load of axially loaded CFFT columns. They examined three parameters i.e. thickness of FRP tube, the compressive strength of concrete and slenderness ratio. Two types of FRP tube were used, i.e. type I and type II with wall thickness of 2.65 and 6.4 mm, respectively. They concluded that due to the confining effect of the FRP tubes, the axial strength and stiffness of the slender columns were increased. The results also

showed that the ultimate load carrying capacity increased as a result of increasing the FRP tube thickness.

Sundarraja and Prabhu (2012) conducted an experimental study to investigate the structural behaviour of CFST strengthened with carbon fibre reinforced plastic (CFRP) under axial compression load. The number of layers, the width and the spacing between the CFRP strips were the main parameters studied. Fig. 2.14 shows the adapted wrapping scheme. They demonstrated that the additional confinement provided by the CFRP strips increased the bearing capacity of the column, as can be seen from Fig. 2.15 and delayed its local buckling.

The performance of the circular CFST strengthened with CFRP under combined tension and bending was examined by Wang et al. (2015). Nineteen specimens, including thirteen strengthened tubes with CFRP and six unwrapped tubes, were tested. The main parameters studied were the eccentricity ratio, the number of the CFRP layers and the CFRP orientation. It was found that the strengthening with CFRP increased the load carrying capacity of the tube especially with the longitudinal strengthening. They also presented a numerical model using the finite element code ABAQUS. The brick element with reduced integration points (C3D8R) was used to simulate the steel tube and the concrete core, while the CFRP was simulated using the three dimensions membrane element. The contact between the steel tube and concrete was assumed to be a hard one. Fig. 2.16 shows that the numerical results correlated well with the corresponding experimental findings.

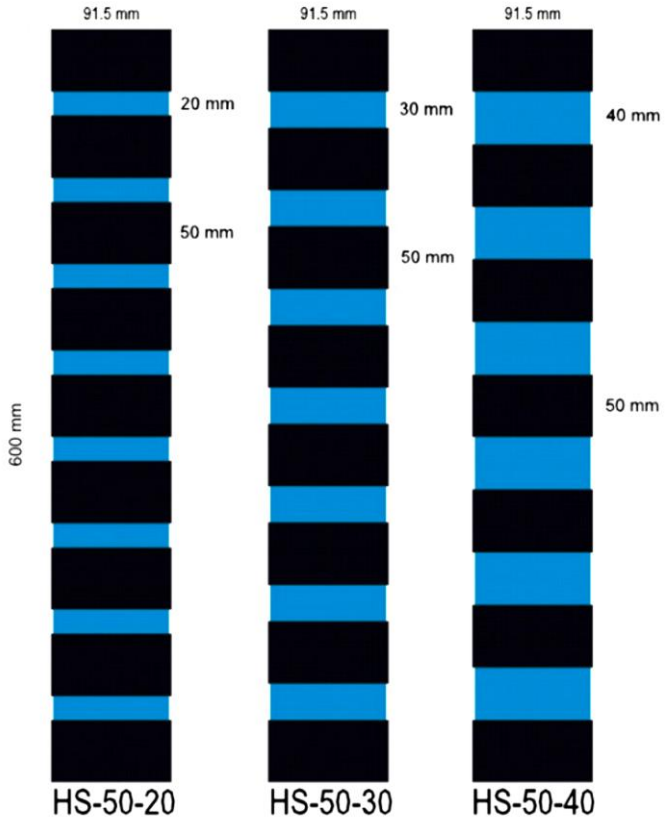

Figure 2.14. The CFRP strengthening scheme (Sundarraja and Prabhu, 2012)

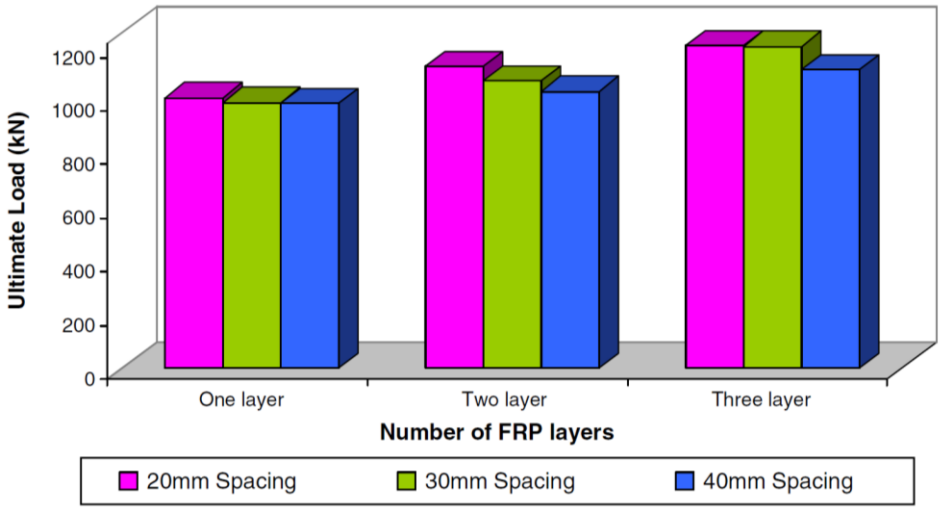

Figure 2.15. Ultimate load for all columns with different FRP layers (Sundarraja and Prabhu, 2012)

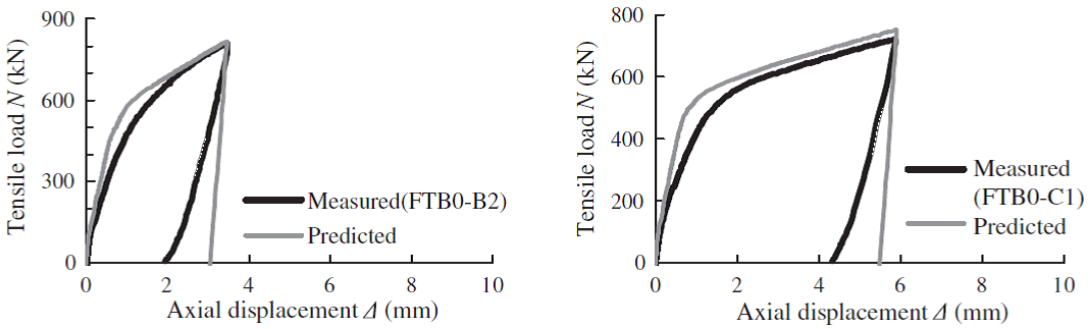

Figure 2.16. The comparison between the numerical and experimental load-displacement curves (Wang et al. 2015)

The compression behaviour of the CFRP strengthened CFST columns still needs more research, in particular the RACFST columns under eccentric loading. The current study will investigate the behaviour of the NACFST and RACFST columns under concentric and eccentric compression loading with and without CFRP strengthening. The results will be presented and compared, which will be then used to validate the numerical models developed using the finite element analysis.

2.6 The response of the recycled aggregate concrete filled steel member under quasi-static loading

With increasing the construction and demolition wastes resulted from the rapid development of the construction industry, recycling the waste of concrete becomes necessary to preserve the environment and to conserve the natural resources of gravel and sand (Yang et al., 2008). The use of the recycled aggregate in construction projects is becoming an essential need to conserve the natural resources. In spite of the mechanical properties of the recycled aggregates which affect the bearing capacity of the recycled aggregate concrete (RAC) members, a lot of research output indicated that the response of the RAC is similar to normal aggregate concrete (NAC) and the bearing capacity of the RAC is slightly lower than that of the NAC.

Many studies have been carried out to investigate the behaviour and the properties of the recycled aggregate concrete (RAC). The main findings are: (i) recycled aggregate (RA)

is considerably affected by the crushing method of the parent concrete, (ii) RA has infrequent particle shape with a rougher surface than that of normal aggregate, (iii) the required water quantity for RAC is more than that required for the normal concrete for the same workability, (iv) the compressive strength, modulus of elasticity and the density for normal concrete are higher than that of RAC, and (v) due to the high water content of RAC, the carbonation rate, permeability and the risk of the corrosion of steel reinforcement are higher than that in normal aggregate (Padmini et al., 2009).

The hollow structural steel sections filled with RAC are called recycled aggregate concrete filled steel tubes (RACFST). The harmful environmental factors, such as wind, temperature and water, have less impact on RAC, which is used in CFST columns because of the confinement effect and the protection provided by the steel tube (Yang and Han, 2006). It was found that the bearing capacity of RACFST decreases with increasing the replacement ratio of recycled aggregate (Konno et al., 1998; Konno et al., 1999; Yang and Han, 2006; Yang et al., 2008). The bearing capacity of normal aggregate concrete filled steel tube (NACFST) columns is slightly higher than those of RACFST (Yang and Han, 2006). The research shows that under axial and cyclic flexural loading the behaviour of the tubular columns filled with recycled aggregate concrete is similar to those of columns filled with normal aggregate concrete (Yang et al., 2009).

The properties of the RACFST columns under axial compression were studied by Konno et al. (1998). They concluded that the ultimate capacity and stiffness of normal confined concrete columns was higher than those of recycled confined concrete and the load carrying capacity of recycled aggregate concrete columns is sufficient to be used.

Yang and Han (2006) investigated the behaviour of the recycled aggregate concrete filled steel tubular columns under axial loading (RACFST). The Thirty specimens were tested including 24 specimens with recycled aggregate concrete and 6 specimens with normal aggregate concrete. The main parameters in their study were the cross sectional shape

(circular and square), the concrete type (recycled and normal concrete) and the load eccentricity ratio (0 – 0.53). The test results were compared with the computed results from the codes available (ACI 318-1999, AIJ-1997, AISC-LRFD-1999, BS5400-1979, DBJ13-51-2003 and EC4-1994). The results showed that the failure modes of normal aggregate concrete filled steel tube columns (NCFST) were similar to those filled with recycled aggregate concrete. The bearing capacity of NCFST columns was slightly higher than those of RACFST. The predicted strengths from the codes for both circular and square RACFST columns were conservative.

Yang et al., (2008) studied the effect of shrinkage and creep on recycled aggregate concrete filled steel tubes. They tested eight CFSTs with RAC and four CFSTs with NAC. The major parameters of the study were the cross sectional shape of the tube, type of concrete and long-term sustained load levels. It was concluded that in terms of the long-term deformation, the CFSTs filled with RAC have a similar deformation to those of CFSTs filled with NAC and the creep and shrinkage of CFSTs filled with RAC are higher than the CFSTs filled with NAC.

Xiao et al. (2012) evaluated the mechanical properties of confined recycled aggregate concrete under axial loading. The experimental study included confined RAC by steel and glass fibre reinforced plastic (GFRP) tubes. The tube material properties and the recycled aggregate content were the main parameters studied. It was found that the confinement has an explicit effect on the RAC mechanical properties and these properties were better in RAC confined by steel tube compared with those confined by GFRP tube under the same test condition. Also, they found that the bearing capacity of RAC confined by steel and GFRP tubes decreased when the recycled aggregate replacement ratio increased. A numerical simulation using the finite element code ANSYS was undertaken to study the effect of the tube thickness on the confined RAC. The results showed that the bearing capacity increased with increasing the tube thickness.

Fig. 2.17 shows the load versus strain curves for both the recycled aggregate concrete filled steel tubes and GFRP tubes.

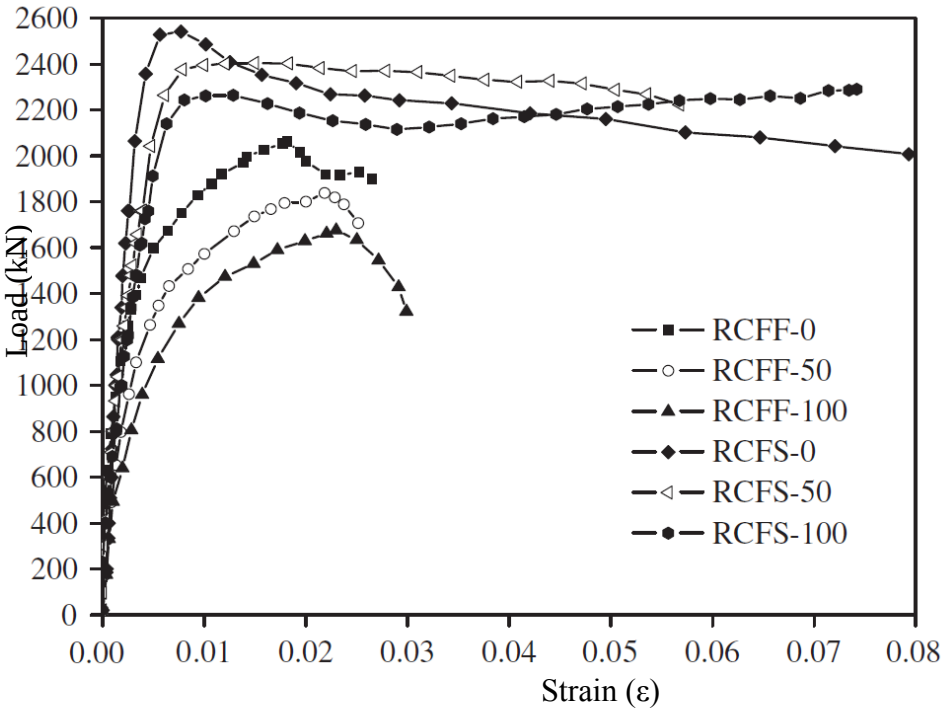

Figure 2.17. Load versus axial strain for the recycled aggregate confined concrete filled steel and fibre tubes (Xiao et al., 2012)

Yan and Ma (2013) studied the behaviour of the recycled aggregate concrete filled stainless steel tube (RACFSST) columns and beams under the combined compressive and flexural load. The experimental study included 14 beams and 14 short columns. The main parameters studied were the recycled aggregate replacement ratio, and the tube cross sectional shape. They concluded that the confinement effect of the stainless steel tube enhanced the behaviour of the recycled aggregate concrete core. The RACFSST columns and the corresponding normal aggregate concrete filled stainless steel tube columns behave in the same manner in terms of compressive and flexural behaviour.

Dong et al. (2013) carried out a series of experimental tests on ten specimens to understand the mechanical behaviour of RACFST strengthened by carbon fibre reinforced polymer

(CFRP) under axial compression load. They examined three parameters i.e. the replacement ratio of recycled aggregate (0 %, 50 %), the outer diameter to thickness ratio (D/t), and the reinforcement ratio by (CFRP) (0 %, 75 %, 100 %). Fig. 2.18 shows the CFRP arrangement adopted in this study. It was concluded that the adopted arrangement of CFRP in this study increased the bearing capacity and the stiffness of the strengthened columns, as shown in Fig. 2.19.

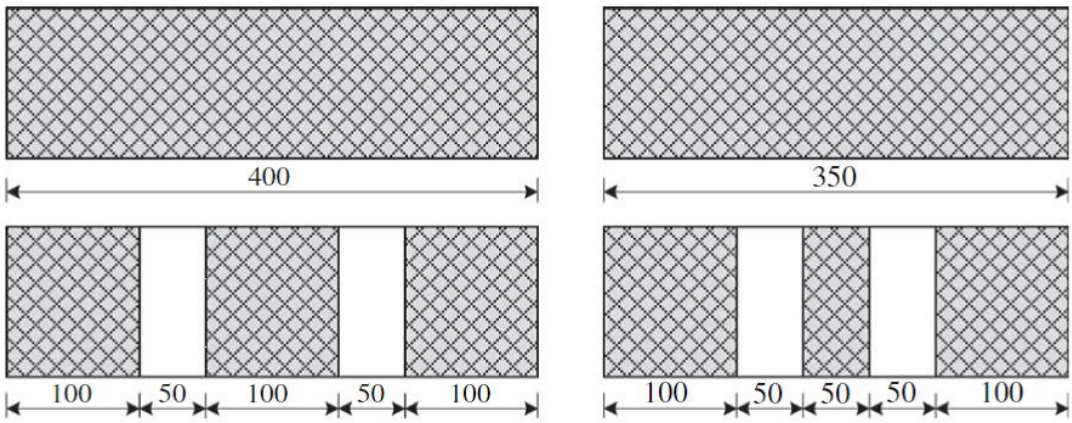

Figure 2.18. The CFRP reinforcement arrangement (Dong et al. 2013)

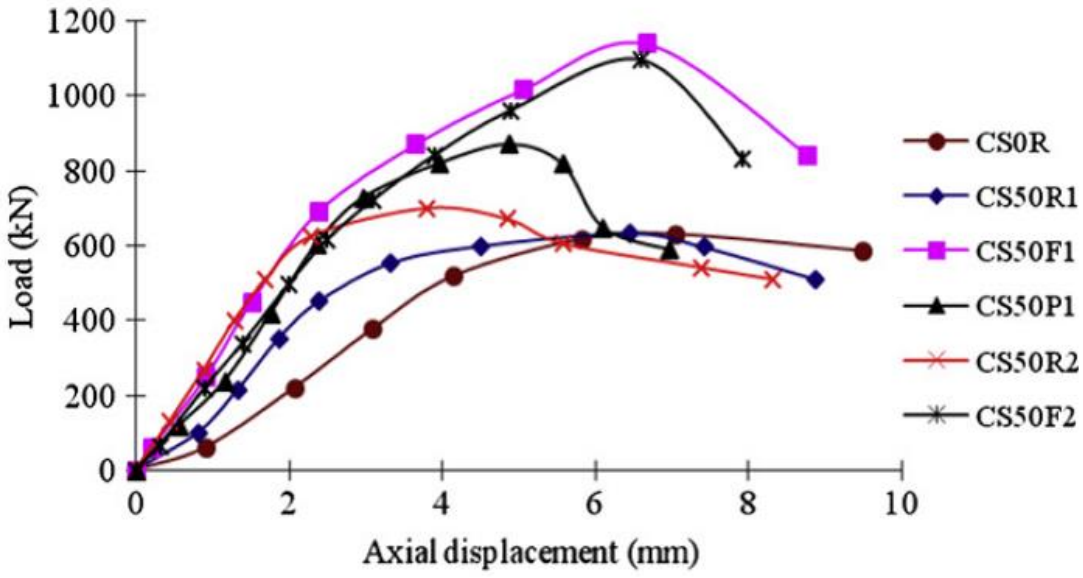

Figure 2.19. The loading-deflection curves for columns tested (Dong et al. 2013)

Chen et al. (2014) presented an experimental study on recycled aggregate concrete filled steel tubes under axial compression loading. Twenty two circular specimens and 11 square specimens were tested in this study with different replacement percentage of recycled aggregate. The adopted RA replacement percentages were 0, 10, 20, 30, 40, 50, 60, 70, 80, 90, and 100 %. The results showed that a failure mode of RACFST columns was similar to the NACFST ones and the peak stress slightly increased when the RA replacement ratio increased.

As mentioned in the previous section, limited research was carried out to study the behaviour of the RACFST columns strengthened with CFRP under eccentric axial loading. Thus, the study proposed in the current project will fill the gap left in this area with some new parameters.

2.7 Numerical modelling of CFSTs under quasi-static loading

At present with the development of digital computers and numerical techniques, the finite element method (FEM) has emerged as a powerful analytical tool for structural analysis. This enabled the engineers to model many aspects of the phenomenological behaviour encountered in CFST (Starossek et al., 2008). These aspects include the confinement effect, modelling of cracking and crushing, the behaviour of the materials after cracking and crushing and many other properties. Carrying out parametric studies experimentally consumes a lot of time and leads to high research costs. Thus, the finite element analysis is an effect approach to study the structural behaviour of the CFST columns under lateral impact loading with different parameters. Extensive research work was carried out using the FEM to study the structural response of the CFSTs under different types of loadings. The output indicates that the parametric studies using the validated models show reasonable and expected results. To create a functional and reliable model, a suitable finite element software code should be use to model the different features of the CFST, such as the interaction between the steel tube and concrete core, the failure mode and the material properties (Shams, 1997). The finite

element analysis software package (ABAQUS) has been used successfully in many numerical investigations on the CFST columns under quasi static and dynamic loadings. The results show good agreement between the numerical results and the corresponding experimental data. In addition, numerous numerical studies were conducted to investigate the behaviour of CFST with various parameters and different type of loadings using the available software programmes such as ANSYS, LS-DYNA.

Schneider (1998) presented a numerical study to investigate the behaviour of CFT under axial compression load. The ABAQUS software programme was used in this study. The concrete core was modelled with 20-node brick elements, while the steel tube was modelled with 8-node shell elements. A gap element was used to simulate the contact behaviour between steel and the concrete core. A comparison between the numerical and experimental results was made, which showed a good agreement between these results. The mechanical behaviour of circular steel-concrete stub columns was investigated by Johansson and Gylltoft (2002). The loading conditions and the bond strength between steel tube and concrete core were examined. The "smeared crack" model available in ABAQUS was used to simulate the concrete properties, while the steel tube was modelled using an elastic-plastic model. The numerical results were validated against the experimental ones. They demonstrated that the method of how the load was applied affected the mechanical behaviour of the columns. When both of the concrete section and the steel were loaded together, the behaviour was not affected by the bond strength, while the confinement effect was significantly influenced by the bond strength when only the concrete section was loaded.

The simple theoretical stress-strain model shown in Fig. 2.7 was adopted by Hu et al. (2003), Ellobody and Young (2006a and 2006b), Ellobody et al. (2006), and Dai and Lam (2010) to simulate the behaviour of the confined concrete core. The model will be explained in detail in Chapter 5 later. They studied the behaviour of circular, square, rectangular and elliptical concrete filled steel tube columns under compression loading. The model proposed

by Mender et al. (1988) considers a higher compressive strength for the confined concrete than the unconfined concrete due to the confinement effect. The numerical results were compared with the experimental ones. In general, the numerical models were successfully used to predict the compressive behaviour of concrete filled steel tubes with different cross-sectional shapes, as shown in Fig. 2.20. Dai and Lam (2010) modified the theoretical confined concrete model to be able to predict the properties of the confined concrete by an elliptical tube. Fig. 2.21 shows this modified model. It can be seen that the new model includes four stages, which are the elastic, yielding, post yielding and failure stage. The numerical model for the concrete filled steel elliptical tube is in a good agreement with the experimental results.

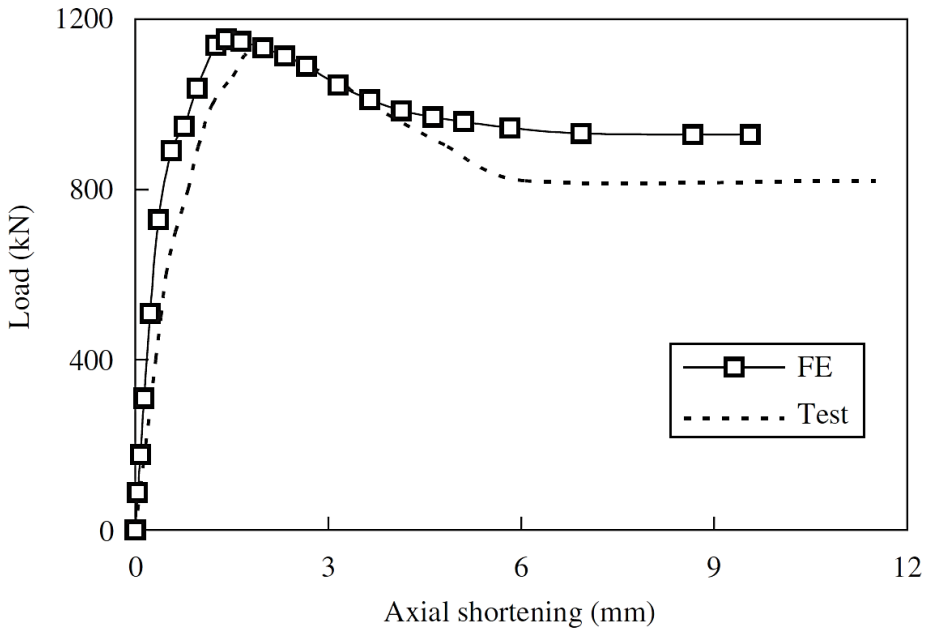

Figure 2.20. Comparison of experimental and finite element analysis results (Ellobody and Young, 2006b)

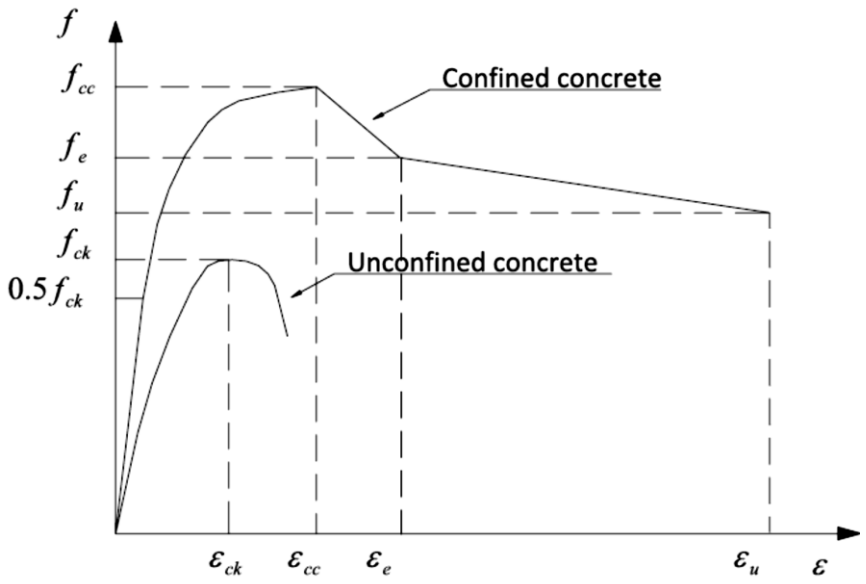

Figure 2.21. Comparison between the confined and unconfined concrete for elliptical tube (Dai and Lam, 2010)

Hu et al. (2005) presented a finite element analysis study on CFST columns under combined axial compression and bending moment. This study included modelling of three sections; circular, square, and a stiffened square section using the commercial code ABAQUS. It was concluded that the confinement effect increased the bearing capacity of the CFST columns. The stiffeners in the square tube increased the axial load carrying capacity, but the bearing capacity of the tube with the circular section was higher than those with a square section, with and without reinforcing ties.

The behaviour of concrete filled steel tubular members under constant axial compression and shear was studied numerically by Han et al. (2008). Based on the numerical results they developed a formula to predict the ultimate capacity of CFT under shear and constant compression force. The results predicted were in good agreement with the experimental data.

Dai et al. (2014) developed a finite element model using the commercial code ABAQUS to simulate the compressive behaviour of the slender elliptical concrete filled steel tube

columns. Three-dimensional 8-noded elements (C3D8) were used to mesh both the steel tube and the concrete core. The surface to surface contact was adopted in this study to define the contact between the concrete core and the steel tube with coefficient of friction of 0.3. Fig. 2.22 shows good agreement between the numerical and experimental results. Using the verified model, they conducted parametric studies to examine the effects of several parameters such as the tube length, concrete strength and the section size on the structural response of the columns. The parametric studies results were compared with those predicted using the design buckling curve available in Euro code 3 and the results showed that the Euro codes design rules for circular and rectangular are able to design the slender elliptical CFST columns.

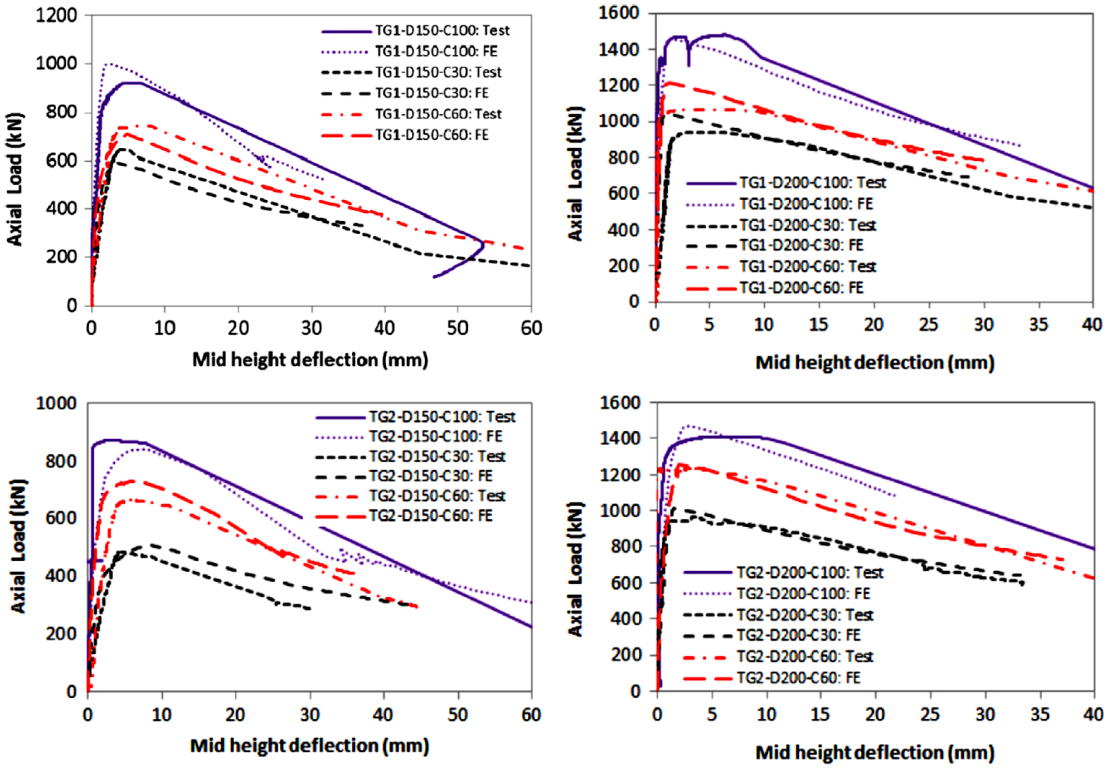

Figure 2.22. The comparison between the numerical and test results for the elliptical CFST columns (Dia et al. 2014)

Gupta and Singh (2014) presented a numerical investigation to study the confinement behaviour of circular concrete filled steel tube columns. The numerical model was built

using the finite element analysis code ABAQUS. They also used the Drucker Prager model to simulate the properties of the confined concrete, whilst the steel was modelled as an elastic perfectly plastic material. The surface to surface contact available in ABAQUS was used to model the contact behaviour between steel and concrete with a coefficient of friction of 0.25. Good correlation between the numerical models and the corresponding experimental results was obtained. Based on the validated numerical model, they studied the confining pressure provided by the steel tube and the friction between the specimen and the loading platen. It was found that there was no influence for the friction between the platen and the specimen. Non-uniform disruption was observed for the confining pressure throughout the tube length and the higher value was at the tube ends.

2.7.1 Concrete models

2.7.1.1 Concrete damage plasticity

The concrete damage plasticity (CDP) model is based on the assumption that the damage plasticity characterises the failure of concrete in both compressive crushing and tensile cracking. To represent the plastic behaviour of concrete, the CDP uses the concept of the isotropic damage evolution in combination with isotropic tensile and compressive plasticity. The strain hardening in compression and strain softening in tension as well as the damage initiation in both compression and tension can be defined in this model. The CDP model is designed to simulate concrete when it is subjected to cyclic and dynamic loadings. The adaptive meshing option can be used with the CDP model in which the analysis can be completed even with relatively high deformation rate. For example, to avoid the high distortion of the concrete elements during the impact event, the impacted area of the concrete can be re-meshed regularly during the analysis and the analysis can be completed without any distortion problem. CDP model provides capabilities to model the permanent deformation that occurs during the fracturing process as it consists of the combination of non-associated multi-hardening plasticity and isotropic damaged

elasticity. Also, the CDP model can be used for both reinforced and plain concrete in all types of structures such as beams, shells and trusses (ABAQUS 6.14). Because of these merits and advantages, the CDP model is used by many researchers to simulate the CFST columns under lateral impact loadings (Wang et al., 2013; Yousuf et al., 2012, 2013, and 2014; Han et al., 2014; Alam et al., 2015-1, 2015-2, and 2016; Yang et al., 2015; Wang et al., 2015). Thus, the CDP model is a better choice and it is adopted in this study to model the response of the confined concrete core under impact loading.

2.7.1.2 Drucker-Prager model

The Drucker-Prager (DP) model uses the modified von Mises yield criterion which is capable of capturing the increase of the shear strength due to the increase of the hydrostatic pressure. Also, it is suitable for modelling materials in which the compressive yield strength considerably higher than tensile strength. These advantages enable the DP model to simulate the concrete core of the CFST column as the concrete is confined by the steel tube and will expand as a result of increasing the hydrostatic pressure (Mollazadeh, 2015). The DP model provides an inelastic hardening mechanism to represent plastic compaction by bonding the yield surface in hydrostatic compression. The DP model also provides softening as a function of the inelastic volume increase created as the material yields on the Drucker-Prager shear failure surface. Hence, it helps to control volume dilatancy when the material yields in shear**.** This yield criterion is capable of capturing the shear strength increase as a result of the hydrostatic pressure increases, which is a unique property of the confined concrete under compression loading (Yu et al., 2010). Hence, this has meant that the Drucker-Prager model has been widely used in the finite element simulation of confined concrete in many research studies (Ellobody and Young, 2006, Mirmiran et al., 2000, Hu et al., 2003, Yu et al., 2010). In the current study, the confined concrete is mainly in compression and its failure is dominated by the compressive failure surface expanding with increasing the hydrostatic

pressure and the stresses are mostly compressive. Thus, the DP model is a reasonably good choice to model the confined concrete core of the CFST columns (Hu et al., 2003).

2.7.1.3 REL3, Winfrith and K&C concrete models

Concrete damage model (REL3) is a three-invariant model and it is the extension of the material model which was developed by Malvar et al. (1997). The REL3 includes parameters to introduce the material damage properties and the strain rate effects. This model is capable of generating the model parameters using the unconfined compressive strength of the concrete only (Schwer & Malvar, 2005).

The Winfrith concrete model (Broadhouse, 1995) was developed due to the needs of the nuclear industry in the UK to solve the reinforced concrete structures subjected to impact loading. This model utilizes (Ottosen, 1977) shear failure surface and it depends on the unconfined compressive and tensile strength of the concrete (Schwer, 2010). In addition, it has the optional inclusive of the strain rate effect.

Due to the needs to simulate the blast response of the reinforced concrete structures, Karagozain and Case (Crawford et al., 2011) proposed the K&C concrete model (KCC). This model is used to model a wide range of the concrete behaviours such as the response of the reinforced concrete structures subjected to qausi-static, blast and impact loadings and it is capable of simulating the high material damage which can result from high impact or blast loadings (Wu and Crawford, 2015). This model is able of automatically generating all the other parameters by defining only the unconfined compressive strength and the density of the concrete.

All these models are implemented in finite element analysis code LS-DYNA and they are widely used with this software to simulate the dynamic behaviour of concrete. However, all the parameters of these models are mainly generated based on the unconfined compressive strength of the concrete which can lead to an inaccurate simulation of the compression and impact response of the confined concrete studied in the current research.

2.8 Strain rate effect

The strain rate effect is a well-known parameter which may affect the results for some materials based on the value of the strain rate, the mechanical properties of the material and the test circumstances. The two materials associated with the CFST columns, i.e. concrete and steel were separately studied by many researchers to examine the effect of the strain rate. The strength of the concrete and steel can be affected by the strain rate, which can increase substantially under high rates (Bischoff and Perry, 1991; Malvar, 1998). Many theories were proposed to explain this fact. For example, the theory which suggests that the cracks propagate through the most direct route because the available time is not enough for them to find the weakest path (Bischoff and Perry, 1991). The effect of the viscosity of free water inside the concrete which is called the Stefan effect and the inertia effect were also used to explain the strain rate effect (Zheng and Li, 2004; Rossi and Toutlemonde, 1996).

The Hopkinson bar or split Hopkinson pressure bar are normally used to carry out the high strain rate tests. However, due to the difficulties of creating strain and stress profiles, the specimen geometry and the inertia effect within the specimens made the high strain rate test complicated (Bischoff and Perry, 1991).

The high strength concrete showed less strain rate sensitivity (Chan, 1986, Bischoff and Perry, 1991). It was concluded that the low strain rate dependence of concrete was shown when the strain rates below 400 s^{-1} (Grote et al., 2001). The strain rate effect became considerable for the concrete at a strain rate of 100 s^{-1} (Li and Meng, 2003). Kono et al. (2001) found that the effect of the strain rate on the confined concrete decreased with the increase of the confining stresses.

The yield strength increased with high strain rate. However, the high strength steel exhibited fewer enhancements in its strength (Chan, 1986, Jones, 2012). Dietenberger et al, (2005) found that based on the new car assessment program (NCAP), the individual parts which were made from steel and aluminum showed considerable strain rate

sensitivity under high strain rate loading. However, the overall response of the vehicle exhibited a relatively smaller effect under the high velocity crush test with a velocity of 15.6 m/s.

The impact test with velocity less than 10 m/s is considered as a low velocity test, in which the strain rate effect is negligible (Richardson and Wisheart, 1996, Wang et al., 2014). Bambach et al. (2008) experimentally calculated the strain rate for CFST with square section under lateral impact loading with an impact energy of 11532 J, the average value of strain rate was 9 s^{-1} which agreed with the fact that with low velocity test, the strain rate will not be higher than 10 s^{-1} (Zaini, 2015).

The dynamic proprieties for the rate-dependent materials can be implemented in the analytical models using a useful factor named dynamic increasing factor (DIF). The DIFs for the concrete and steel were suggested by many researchers based on the comparison of the properties of these materials under low and high strain rate (qausi-static and dynamic tests) loadings. The strain rate effect of steel can be calculated and then be used in the numerical models using the Cowper-Symonds model. The Cowper-Symonds model (Abramowicz and Jones, 1984) can be expressed as:

$$\frac{f_{yd}}{f_{ys}} = 1 + \left(\frac{\dot{\varepsilon}}{D_{cs}}\right)^{1/q} \tag{2.7}$$

where f_{yd} is the dynamic yield strength of steel, f_{ys} is the static yield strength of steel, $\dot{\varepsilon}$ is strain rate, D_{cs} and q are parameters that can be set as 6844 s^{-1} and 3.91, respectively (Abramowicz and Jones, 1984).

Some research work included the strain rate effect in their numerical models for concrete in tension and compression using the relationships below, which are given in the CEB-FIP model code (Comite Euro-International du Beton, 1993).

In compression, the CEB-FIP equations are given as:

$$\begin{cases} \frac{f_{cd}}{f_{cs}} = (\dot{\varepsilon}/\dot{\varepsilon}_s)^{1.026\dot{\alpha}_s} & for\ \dot{\varepsilon} \leq 30s^{-1} \\ \frac{f_{cd}}{f_{cs}} = \gamma_s \left(\frac{\dot{\varepsilon}}{\dot{\varepsilon}_s}\right)^{1/3} & for\dot{\varepsilon}\ > 30s^{-1} \end{cases} \quad (2.8)$$

where f_{cd} is the dynamic compressive strength, $\dot{\varepsilon}$ is the strain rate with the range of 30 x 10^{-6} s^{-1} to 300 s^{-1}, f_{cs} is the static compressive strength, $\dot{\varepsilon}_s$ is the static strain rate (30 x 10^{-6} s^{-1}), $\gamma_s = 6.156\alpha_s - 2$, $\alpha_s = (5 + 9f_{cs}/f_{co})^{-1}$, and f_{co} = 10 MPa.

Based on the CEB-FIP model, Malvar and Crawford (1998) proposed a modified a model to obtain the dynamic tensile strength of concrete (f_{td})

$$\begin{cases} \frac{f_{td}}{f_{ts}} = \left(\frac{\dot{\varepsilon}}{\dot{\varepsilon}_s}\right)^{\delta} & for\ \dot{\varepsilon}\ \leq 1s^{-1} \\ \frac{f_{td}}{f_{ts}} = \beta \left(\frac{\dot{\varepsilon}}{\dot{\varepsilon}_s}\right)^{1/3} & for\ \dot{\varepsilon}\ > 1s^{-1} \end{cases} \quad (2.9)$$

where f_{td} is the dynamic tensile strength of the concrete, $\dot{\varepsilon}$ is the strain rate with the range of 10^{-6} s^{-1} to 160 s^{-1}, f_{ts} is the static tensile strength of concrete, $\dot{\varepsilon}_s$ is the static strain rate (10^{-6} s^{-1}), $log\beta = 6\delta - 2$, $\delta = 1/(1 + 8f_{cs}/f_{co})$, and f_{co} = 10 MPa.

These models for steel and concrete were used in many studies to include the strain rate effect on the steel and concrete (Qu et al., 2011, Wang et al, 2013, Deng and Tuan, 2013, Han et al., 2014, Alam et al., 2015 and Aghdamy et al., 2015).

Other studies did not take into account the strain rate effect (Yousuf et al., 2011, 2012 and 2013, Bambach, 2011 and Wang et al., 2014). The numerical results of these studies still showed very good correlation with the experimental ones.

Some numerical studies did not consider the confinement effect but at the same time they took into account of the strain rate effect for concrete and steel (Qu et. al., 2011 and Deng and Tuan, 2013). Their results showed a reasonable agreement with the corresponding experimental data.

The carbon/epoxy and the glass/epoxy composite showed almost no strain rate sensitivity for the range studied and no strain rate effect was considered in the numerical studies (Alam et al., 2015, Alam and Fawzia, 2015).

The used models to consider the strain rate effect on steel determine the stress which is not reflect the real condition of the steel tube which confines the concrete core and neglect the composite action between the concrete and steel. Meanwhile, the models utilised to include the strain rate influence on the concrete strength in tension and compression is also used to obtain the tensile and compressive stress without considering confinement effect. Thus, these models do not necessarily reflect the real response of the steel and concrete and more research needs to be conducted to study the behaviour of concrete and steel when considering the multi-dimensional stress effects.

The influences of the strain rate effect on the CFST columns under low velocity lateral impact loading are likely to be small because of the confinement effect which increases the CFST column capacity and reduces the strain rate sensitivity. In addition, the maximum velocity for all the tests in the current study did not exceed 7.1 m/s with a corresponding strain rate of 10.1 s^{-1}. Thus, the strain rate effect will not be considered in this study for the concrete, steel tube and CFRP. Also, the compressive strength for concrete and the yield strength of the steel are relatively high. Therefore, the effect will be small and the numerical results confirm the insignificant strain rate effect for the CFST column in this study.

2.9 Review of the code practice

2.9.1 The qausi static loading

Several codes of practice included in the design and analysis of the CFST columns under axial compression loading. Eurocode, American Codes (ACI and AISC) and Japanese code (AIJ) are some of these standards and codes which deal with the CFST columns.

The Eurocode defines a concrete filled steel tube column as a composite member in EN1994-1-1 Section 6.7 and it takes into account the confinement effect of the concrete core with considering the eccentricity of loading. In addition, the EN1994-1-1 neglects the reduction factor of 0.85 for CFST column due to the protection against the environmental conditions provided by the steel tube for the concrete core (Oliveira et al., 2009).The maximum axial force of the column is:

$$P_u = A_s f_y \eta_2 + A_c f_c \left(1 + \eta_1 \frac{t}{D} \frac{f_y}{f_{cy1}}\right) \quad (2.10)$$

where A_s and A_c are the cross sectional areas of steel tube and a concrete core, respectively, f_y, f_c and f_{cy1} are the yield strength of the steel tube, the compressive strength of the concrete and the cylinder compressive strength of the concrete, respectively, D and t are the outer diameter and wall thickness of the steel tube, respectively. η_1 *and* η_2 are coefficients defined according to Eurocode with taking into account the slenderness of the column and the eccentricity of loading.

The American Concrete Institute (ACI) and Australian Standards (AS) do not explicitly consider the confinement effect on the behaviour of CFST columns under axial loading, which employ the same formula to predict the axial force as:

$$P_u = 0.85\, A_c f_c + A_s f_y \quad (2.11)$$

The AISC code design the composite section as an equivalent steel section using modified properties. The ultimate axial capacity of the CFST column can be estimated from the following equation:

$$P = \phi_c . P_n \quad (2.12)$$

where ϕ_c is the safety coefficient and it is take as 0.75. P_n is dependant value on the ratio between the ultimate capacity of the column and the elastic buckling limit P_o/P_n. The elastic buckling limit can be obtained from:

$$P_n = P_o . \left[0.658^{\frac{P_o}{P_e}}\right], if\ P_e \geq 0.44 . P_o \quad (2.13)$$

$$P_n = 0.877\,.\,P_e\,, if\ P_e < 0.44\,.\,P_o \quad (2.14)$$

The Architectural Institute of Japan (AIJ) defines the ultimate compression capacity of the CFST column based on the effective length to the outer diameter of the tube ratio L_k/D. The AIJ considers the confinement effect for the concrete core by defining a coefficient as follows

$$N_{cu1} = N_{cuc} + (1-\eta)\,N_{cus} \quad (2.15)$$

where $\eta = 0.27$ for the circular section and zero for the square section.N_{cuc} and N_{cus} are ultimate strength of the concrete and the steel tube of the column, respectively.

It can be seen that only the Eurocode considers the confinement effect for the concrete core for the CFST, whilst the AIJ code considers the confinement effect for only the circular section. However, the ACI and AISC do not take into account the confinement effect for the CFST at all.

2.9.2 The impact loading

The effects of the impact loading on buildings and bridges are considered in codes (Eurocode1, 2002, Eurocode1, 2006, ACI, 1992) and (Eurocode, 2003, Highways Agency, 2004, AASHTO, 2007). The impact load defined as an equivalent static force by introducing a specific value or presenting simplified calculations.

The Annex B of Eurocode1: Part1-1 (Eurocode, 2002) which is the only one to informatively propose an equation below to calculate the horizontal force on barriers in car parks. This equation is only valid with a maximum velocity of 4.5 m/s (16.2 km/h) and a 100 mm of vehicle deformation, which can be expressed as:

$$F = \frac{M.v^2{}_r}{2(\delta_c+\delta_b)} \quad (2.16)$$

where M is the total mass of the vehicle, v_r is velocity of the vehicle and δ_c and δ_b are the deformation of the vehicle and impacted structure, respectively.

The impact force due to vehicles and forklift trucks is defined in Sections 4.3 and 4.4 of Eurocode: Part1-7 (Eurocode, 2006) as an equivalent static force. Tables 2.3 and 2.4

show the design value of the equivalent static force based on the category of the traffic. It can be seen from these tables that the effect of the mass of the impacted structures and the vehicles as well as their stiffness are all neglected.

Table 2.3. Indicative equivalent static design forces to vehicular impact on members supporting structures over, or adjacent to roadways (Eurocode 1, 2006)

Category of traffic	Force F^{a}_{dx} (kN)	Force F^{a}_{dy} (kN)
Motorways and country national and main roads	1000*	500
Country roads in rural area	700	375
Roads in urban area	500	250
Courtyards and parking garages with access to:		
- Cars	50	25
- Lorries[b]	150	75

[a] x= direction of normal travel, y = perpendicular to the direction of normal travel.
[b] The term "lorry" refers to vehicles with a maximum gross weight greater than 3.5 tonnes.

Table 2.4. Indicative equivalent static design forces to vehicular impact on superstructures (Eurocode 1, 2006)

Category of traffic	Equivalent static design force F^{a}_{dx} (kN)
Motorways and country national and main roads	500
Country roads in rural area	375
Roads in urban area	250
Courtyards and parking garages	75
[a] x = direction of normal travel	

The Annex C of Eurocode 1: Part 1-7 (Eurocode, 2006) suggests the following equation to calculate the design action of the construction impacted by road vehicles. Two types of impact are defined in this Annex, i.e. soft impact where the structure designed to absorb the impact energy by its deformation and hard impact where the impacting body mainly

dissipates the impact energy (Eurocode, 2006). The maximum impact force can be calculated from:

$$F = v_r\sqrt{k_e.M} \quad (2.17)$$

where v_r is the velocity of the vehicle at the impact, k_e is the equivalent elastic stiffness of the impact body or the vehicle in case of the soft and hard impact, respectively and M is the mass of the vehicle.

Sections 4.7.2.1 and 5.6.2.1 of Eurocode 1: Part 2 (Eurocode, 2003) provide an equivalent static force as a design value for an accidental impact on road bridges, railway bridges and footbridges impacted by vehicle. The forces are constant of 500 and 1000 kN in the perpendicular direction to the direction of the vehicle and in the same direction of the vehicle, respectively.

In the same way, an equivalent static force of 1000 kN is suggested by the American Concrete Institute (ACI, 1992). This value is equivalent to impact of the vehicle on piers. In addition, the building code for structural concrete and commentary (ACI 318S–05, 2005) recommends considering the impact load without any further details.

2.10 Remarks and research novelty

Many experimental and numerical researches have been conducted to study the structural behaviour of the CFST columns with different parameters such as the material properties, L/D and D/t ratios, boundary conditions, the loading types (dynamic and quasi static loading). However, more experimental and numerical studies need to be carried out to gain a thorough understanding on the impact response of the CFTS columns. Based on the literature review presented here, it can be demonstrated that:

- Extensive researches have been conducted to study the compression behaviour of the NACFST columns and a limited number of studies for the ones filled with RAC.
- More studies are required to understand the behaviour of the NACFST and RACFST column strengthened with CFRP under eccentric and concentric axial

loading with different parameters such as the D/t and L/D ratios, the loading eccentricity, the cross section shape, the materials properties and the replacement ratio of the RA.

- Very limited data is available on the response of the CFST column under lateral impact loading in particular RACFST columns. In addition, only few studies were conducted to study the behaviour of the CFST column strengthened with CFRP under transverse impact loading, especially the ones filled with RAC.

Thus, to make the contribution to close the knowledge gap on the CFST column the current study will investigate

- ❖ The eccentric and concentric compression behaviour of both NACFST and RACFST columns with and without CFRP reinforcement by carrying out experimental tests and developing numerical models.
- ❖ The response of the NACFST and RACFST columns with and without CFRP strengthening under lateral impact loading with various impactor configurations. Experimental work will be conducted and numerical models will be developed and validated with the experimental results to study the behaviour of the concrete core and steel tube of the CFST column.

2.11 Summary

The compressive behaviour of the concrete filled steel tube columns has been shown through extensive previous experimental studies. Those studies have shown that the L/D ratio, D/t ratio, the strength of concrete, the loading condition and the steel yield strength have a significant influence on the behaviour of CFST columns. This chapter has also give a comprehensive review on the experimental and numerical investigations carried out on the impact behaviour of the CFST members with normal and recycled aggregate. The impact force and the lateral deflection are clearly affected by the L/D ratio, D/t ratio,

the impact location, the impact velocity and the impactor mass, as well as impactor configuration. The additional confinement by the FRP enhances the deformation resistance under impact loading. Subsequently, the research on the behaviour of the RACFST members is also reviewed. The strain rate effect on the behaviour of the CFST columns under impact loading is reviewed as well. Finally, based on the available research the knowledge gap on the structural behaviour of the CFST columns was highlighted and the types of tests and analyses to be conducted in this study were stated.

CHAPTER 3

EXPERIMENTAL

PROCEDURES

3.1 Introduction

In this chapter, an overview of the experimental procedures adopted to study the structural behaviour of the NACFST and RACFST columns under impact and compression loadings is presented. The materials and the specimen preparation are described. The details of the structural tests, including lateral impact tests and axial compression tests, are provided. The data processing to obtain the impact test results is also presented in this chapter. The lateral impact test was carried out at the University of Liverpool using the existing facilities, while the axial compression test was conducted at the School of the Built Environment of Liverpool John Moores University.

3.1.1 The motivation of the proposed experimental work

Due to the limited data available to understand the impact response of the CFST column, the experimental tests were conducted to provide an understanding of the behaviour of the CFST columns under low velocity lateral impact loading. This will provide useful data on the impact responses of the large CFST columns under vehicle or ship impact. Due to the limitation of the laboratory, the specimens are always on a small scale. However, the dimensions of the CFST specimens adopted in this study, i.e. D/t and L/D ratio were chosen within the specifications of the current design codes. Table 3.1 shows the specifications of the design codes for the D/t ratio. According to the British Standard (BS 5400, Part, 1979), the D/t ratio should be less than or equal to 47 which are calculated based on yield strength and modulus of elasticity of steel as 450 and 200,000 MPa, respectively. Nevertheless, the ratio should be less than or equal to 60 based on the Eurocode 4 requirements. The D/t ratios in this study are 32 and 38 which are within the code specifications. Morino et al. (2001) found that the L/D ratio for the CFST columns in many buildings in Japan is between 12 and 20. However, they also found that the majority of the typical storey heights for most of the buildings is between 3.5 and 4 m, while the diameter of the circular columns is in the range of 600 and 711 mm. This provides a L/D ratio between 5 and 6.6 with a height between 3500 and 4000 mm. The L/D ratios chosen in this study are 6, 9 and 13.5 for the impact test specimens and 4 for the compression test specimens due to the limitations of the laboratory

facilities. However, these ratios are still in the typical L/D ratio range. In addition, according to the Japanese standard (AIJ, 2001), the maximum L/D ratio should be less than or equal to 50 and 30 for the compression member and beam-column member, respectively. No limitation for the concrete compressive strength in the design codes for the CFST column, except for the AIJ code which set the maximum compressive strength of concrete by the limit of 60 MPa. Again, the average compressive strength of the concrete used in this study is approximately 55 MPa. Meanwhile, it can be noticed that the dimensions and the material properties for the specimens used in this project comply with design standards and the most commonly used specifications for CFST columns.

Table 3.1. The limits of the D/t ratio of the CFST column in the intentional design codes

Code	Specifications
BS 5400, Part 5	$\leq \sqrt{8E_s/f_y}$
EC4	$\leq 90(235/f_y)$
CIDECT	$\leq 90(235/f_y)$
ACI 318	$\leq \sqrt{8E_s/f_y}$
AISC-LRFD	$\leq \sqrt{8E_s/f_y}$
CAIP	$\leq 85\sqrt{235/f_y}$
AIJ	$\leq 35200/F$ [(a)]

(a) F (is the lesser of $0.7f_u$ and f_y)

(b) The yield and ultimate strength and the modulus of elasticity (f_y, f_u, E_s) are in MPa

Fixed end boundary condition is adopted in the current study to mimic the behaviour of the circular CFST column with moment resisting connection. This type of connection is very commonly used for single and multi-storey buildings (Eurocode 3, 2014).

During the service life of the structures, some column might be impacted by vehicles or ships or by falling objects due to an explosion incident. During the impact event the impacted area of the column varies with the type of the accident and the type and the surface area of the impacting object that could be small or large. Thus, it is necessary to study the effect of the configurations of the impactor on the impact force and the lateral deformation of the column. In addition, the most common impactor shapes used in the impact test are flat (circular or equiangular), wedge and spherical with different diameters such the configurations need to be examined to identify their effect on the impact response of the specimens.

The recommendation practice DNV-RP-C204 (Det Norske Vertas, 2010) mentioned that the impact force and deformation increase with increasing the contact area.

To date, no literature review is available on the effect of the impactor configuration on the impact response of the CFST column. Hence, this study includes examining the effect of the impactor shape and size.

The CFRP is a very useful material due to many advantages such as the high strength and durability. As it is a very expensive material, it is better to use the minimum quantity as long as it is effective. Thus, it is suggested to use only one layer with a length of one third of the column span to wrap the impacted area and study the effect of the additional confinement on the impact response of the CFST column. The effect of full CFRP reinforcement can be studied later using the validated numerical models.

For the compression test specimens, again only one layer of CFRP with length equal to one third of the column height was used. It is expected that the CFST column under concentric loading will exhibit a circumferential bulge at the mid height of the column. In addition, no moment will be applied on the column during the test. Thus, the mid span area of the CFST column was wrapped by CFRP layer as this area will apply high hoop stresses on the CFRP layer due to the outward buckling. Although the maximum moment is at the top end of the

CFST column strengthened with CFRP under eccentric axial loading, it is suggested that to warp the mid height area of the column by a layer of the CFRP for the comparison purposes with the ones under concentric loading.

Several attempts were conducted to check the failure mode of the column under eccentric compression loading to avoid the movement of the upper platen of the testing machine and the movement of the specimen on the bottom platen. In addition, the loading eccentricity was checked with different values to find the right one to carry out the test without any movement that may affect the test results and / or the testing machine. Eurocode 2, (2010) specifies the minimum value for the eccentricity for the short column. It is the largest of D/30 or 20 mm, where D is the outer diameter of the column. Thus, the adopted value of the eccentricity in this study is 21 mm.

As mentioned in Chapter 2, the axial force has an effect on the impact response of the CFST column. The first plan of this project was to pre-compress the CFST column and then test it under low velocity lateral impact loading. In addition, the initial plan was aimed at investigating the structural behaviour of the CFST columns under qausi-static axial (concentric and eccentric) and lateral impact loadings with the same parameters, i.e. L/D ratio, concrete type, D/t ratio and CFRP strengthening and using the compression tests results as a guide for the pre-compressed column under impact loading. However, due to the limitation of the lab equipment to test the CFST columns under compression load with different L/D ratio, the plan was amended and the study focused on only one L/D ratio and the plan of testing the axially precompressed column under lateral impact loading was also waved for the same reasons and the CFST columns were tested under lateral impact loading only.

Again, due to the laboratory limitations, no strain gauges were used in this project. No high speed data acquisition system was available to capture the strain of the materials under lateral impact loading.

3.2 Materials

There are three materials used in this study: concrete, mild steel and carbon fibre reinforced plastic (CFRP). All these materials were tested in accordance to the relevant EN and BS standards and were locally supplied.

General purpose ordinary Portland cement CEM II/42.5N complied with the requirements of British Standard BS EN 197-1 (2011) was utilized in preparation the concrete in this study. The cement was supplied by Hanson Heidelberg Cement Group. This type of cement is commonly used for general purpose concrete because it is relatively cheap and provides very good strength.

The coarse aggregate was in two categories, i.e. normal aggregate (NA) and recycled aggregate (RA). The recycled aggregate was supplied by Sloyan Doyle Demolition Company (Liverpool, England) which was obtained by crushing concrete from demolished concrete structures. The reduction of the aggregate size leads to a higher tensile and flexural strength (Akcaoglu et al., 2002; Zhang et al., 2005). Therefore, both of the NA and RA had a maximum size of 10 mm, graded according to the British Standard BS 882 (1992), this size was also selected as it is proportional with the specimen diameter. Furthermore, water absorption and density measurements were undertaken in accordance with the British Standard BS EN 1097-6 (2013) to determine the mechanical and physical properties of the coarse and fine aggregate. The density of the RA was 2435 kg/m^3 and the water absorption was 6.51%, whilst the NA had a density and water absorption equal to 2634 kg/m^3 and 0.98%, respectively. Fig. 3.1 shows the recycled aggregate used in this study.

The fine aggregate used in this investigation was normal river sand which complies with the British Standard BS 882 (1992). The water absorption and density of this sand were 4.41% and 2556 kg/m^3, respectively. The river sand is a widely available, cheap material which contributes to reduce the concrete cost for a given concrete mix.

Cold-formed steel is an available economical material (Morino et al., 2001; Morino and Tsuda, 2002). In general, the post yield strength and stiffness for the circular tubes are higher than those with square and rectangular cross sections; this is due to the high confinement offered by the circular section (Schneider, 1998; Huang et al., 2002; Kavac, 2010). Cold-formed steel tubes with a circular section were used in this research to make the specimens. To obtain the material properties of the steel tubes, standard tensile coupon tests were carried out based on the British standard BS 10002-1 (2001). Three sheet samples were cut from the steel tube with the standard dimensions. The average values of the yield strength, ultimate strength, modulus of elasticity and the elongation were 450 MPa, 530 MPa, 200 GPa and 0.31, respectively.

The bearing capacity and stiffness of the strengthened CFST columns with CFRP could be considerably enhanced (Done et al., 2013). A woven CFRP with a nominal thickness of 0.28 mm (2/2 twill), shown in Fig. 3.2, was used to strengthen the column. Tao et al. (2007) defined the ductility index (DI) to examine the effect of increase the number of the CFRP layer on the ductility of the CFST column. This index can be expressed as:

$$DI = \frac{\varepsilon_{85\%}}{\varepsilon_y}\pi r^2 \tag{3.1}$$

where $\varepsilon_{85\%}$ is the axial strain when the load falls to 85% of the ultimate load.

$\varepsilon_y = \varepsilon_{75\%}/0.75$, where $\varepsilon_{75\%}$ is the axial strain which associated with load reaches 75 % of the ultimate load. They demonstrated that the ductility decreases with increasing the layers of CFRP reinforcement. At the same time, CFRP is an expensive material. Thus, only one layer with a length equal to one-thirds of the tube length was used in this investigation. Strengthening the mid span area was adopted, as this area exhibits higher local and global displacements during the direct impact by a drop-hammer. CFRP woven was supplied by "Easycomposites" (Staffordshire, England) with a density equal to 1390 kg/m^3. An Instron 4204 testing machine was used to conduct the tensile testing on the three samples of CFRP

complied with the requirements of British Standard BS EN ISO 527-4 (1997). The tensile strength and modulus of elasticity were 550 MPa and 48 GPa, respectively.

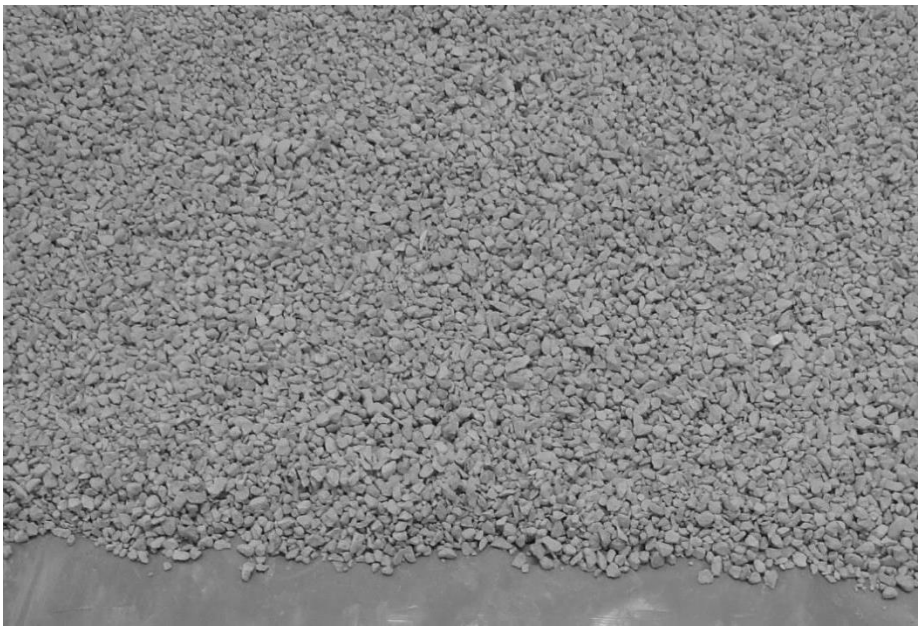

Figure 3.1. The recycled aggregate used throughout this study

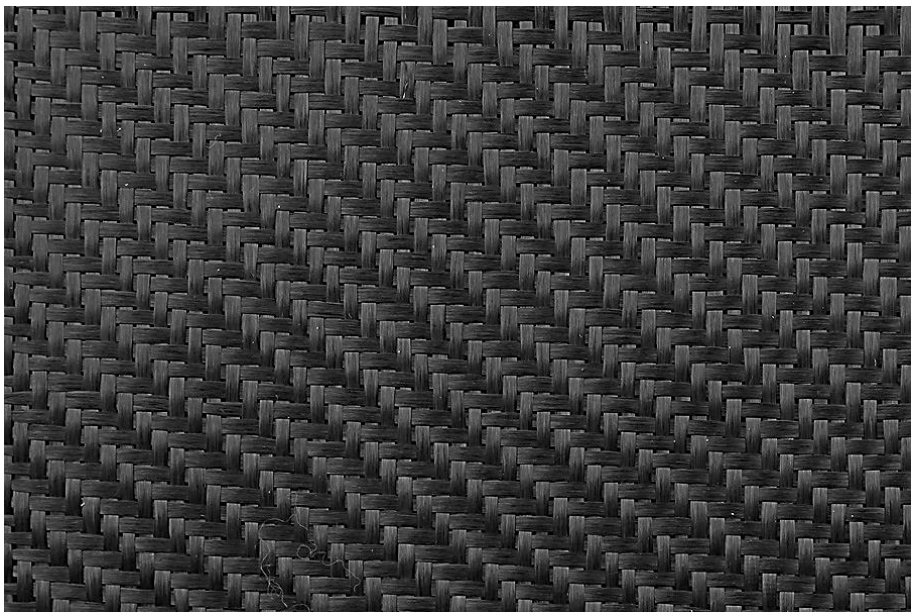

Figure 3.2. Woven carbon fibre reinforced plastic

3.3 Preparation of specimens

A structural hollow cold formed steel tube with an outer diameter (D) of 114.3 mm was used to produce the specimens for the lateral drop-hammer impact and axial compression tests. The majority part of the previous research was conducted with tube diameters less than 200mm (Giakoumelis and Lam, 2004). Here, the total number of impact specimens was 83, including 7 hollow tubes, 39 tubes filled with recycled aggregate concrete and 37 tubes filled with normal aggregate concrete. The specimens were divided into five groups with the first four groups containing 14 tubes each, of which six tubes were strengthened with CFRP. The fifth group includes 21 tubes to be subjected to impact by four different impactors without CFRP strengthening. The tubes in the first group had a 3 mm wall thickness (t), whilst that for the other groups was 3.6 mm thick to provide diameter to thickness ratio (D/t) of 38 and 32 respectively. Morino et al. (2001) mentioned that the D/t ratio for the commonly used circular tubes columns was between 17 and 65. To examine the effect of the specimen length on the impact response of the tubes, the specimens were prepared in three different lengths, i.e. 686 mm (6D), 1029mm (9D) and 1543 mm (13.5D). A considerable confinement effect was observed for the CFST column with tube length to diameter ratio (L/D) less than 15 (Shanmugam and Lakshmi, 2001). The details of the specimens manufactured are listed in Table 3.2. The letters S, M, and L in the specimen's ID refer to short, medium and long, respectively. The "50" and "0" represent 50% of the recycled aggregate and the normal aggregate concrete, respectively. The small letter "s" refers to the tubes strengthened with CFRP and the letter "H" refers to the hollow tube. To examine the effect of impactor shape on the behaviour of the CFST, two types of impactor were used in the test. The first one is the spherical impactor with three different diameters of 60 mm (BI), 40 mm (MI) and 20 mm (SI). The second type is a flat impactor with a cross-section of 40mm x 40mm (FI) section. Fig. 3.3 shows the different types of the impactors.

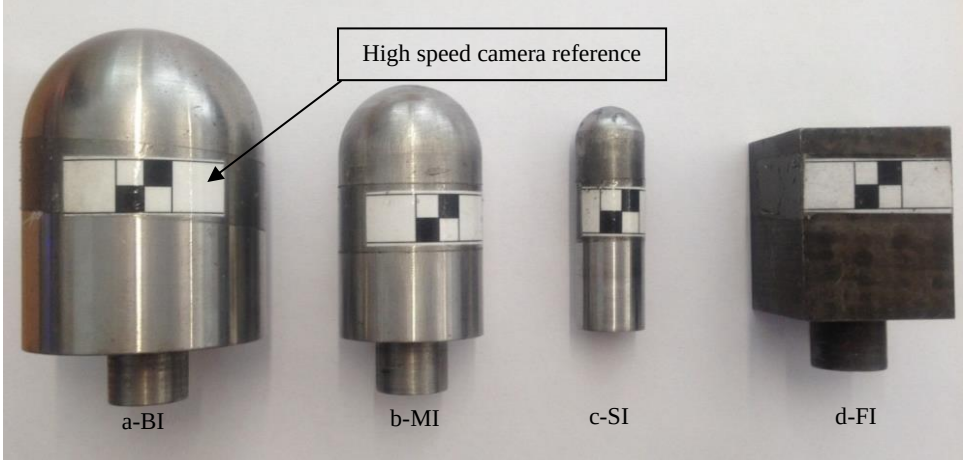

Figure 3.3. Impactor types: a) big impactor b) medium impactor c) small impactor d) flat impactor

The total number of the specimens for the compression tests was thirty tubes, divided into three groups. Half of the specimens of each group filled with recycled aggregate concrete, while the other half filled with normal aggregate concrete. The first group contains 6 tubes with wall thickness of 3.6 mm, which were fabricated to examine the effect of tube thickness on the behaviour of the concentrically loaded CFST columns. The second and third groups include 24 tubes with 3 mm wall thickness; half of them were strengthened with CFRP and they were prepared to examine the response of the CFST columns under concentric or eccentric axial loading. The length of the compression test specimens is 457 mm (4D). The details of the specimens are listed in Table 3.3. The letters C and E in the specimen's ID refer to concentric and eccentric loading, respectively. Again, the "50" and "0" represent 50% of the recycled aggregate and the normal aggregate concrete, respectively. The small letter "s" refers to the strengthened tubes with CFRP, while the small letter "i" refers to the tube with wall thickness of 3.6 mm.

3.3.1 Concrete mix design

The concrete mix was designed in accordance with the British Standard BS 5328 (1997). Several trial mixes were conducted to obtain the anticipated mix design. The free water-

cement ratio was 0.46 for both mixes and the adopted replacement ratios of recycled aggregate in this study were 0% and 50% of the total weight of coarse aggregate. It is applicable to utilize the CFST columns filled by recycled aggregate concrete with 50% replacement ratio (Yang et al., 2009). Table 3.3 shows the details of the mix proportions for the normal and recycled aggregate concrete.

3.3.2 Mixing

The pan mixer of capacity 0.1 m^3 was used to mix the concrete materials, as shown in Fig. 3.4. The dry materials were weighed and then added into the mixer and mixed according to the British Standard BS 1881-125 (2013) to ensure the concrete homogeneity. Recycled aggregate is required to be treated by increasing its humidity before using it with concrete mix, due to its effects on concrete workability (Etxeberria et al., 2007). To minimize the effect of the high water absorption of the RA on the workability and the strength of the concrete mix, the RA was pre-soaked for 24 hours before the concrete mixing in an amount of water equals to 5.53% of the total weight of the RA. This percentage of water is calculated from the difference between the water absorption of the RA and NA i.e., 6.51% and 0.98%, respectively. The slump tests were carried out. The average slump values for the concrete mixes with normal and recycled aggregate are shown in Table 3.4.

3.3.3 Casting and compaction

Before the casting, the interior surface of each tube was cleaned by steel wire brush to remove any rust or dust. The base of the compression test tubes was welded to 200 x 200 mm square steel plate with 12.5 mm thickness, while the base of the impact test tubes was closed by a wooden plate, as shown in Fig. 3.5 and Fig. 3.6, respectively. Each tube was filled with the concrete in layers and then compacted using a poker vibrator and vibrating table. Nine 100 mm cubes were prepared and cast with each concrete batch to determine the corresponding compressive strength of the concrete at 7 and 28 days. After the compaction, all tubes and cubes were covered by a damp hessian and polythene sheets for 24 hours, this was followed by covering each specimen with cling film to retain the necessary moisture to

ensure complete hydration, as shown in Figs. 3.7 (a) and (b), respectively. The gap resulting from shrinkage at the top surface of the concrete was filled with cement mortar. Before conducting the compression test, the top end of each specimen was welded with a 12.5 mm thick square steel plate. The complete results of the cube tests are tabulated in Appendix A

Table 3.2. Details of the impact test specimens

Specimen ID	D (mm)	L (mm)	t (mm)	Clear Span (mm)	Compressive strength (MPa)	No. of specimens
S0	114.3	686	3	525	56.7	3
S50	114.3	686	3	525	54.3	4
S0s	114.3	686	3	525	56.7	3
S50s	114.3	686	3	525	54.3	3
SH	114.3	686	3.6	525	-	3
S0-BI	114.3	686	3.6	525	56.7	3
S50-BI	114.3	686	3.6	525	53	3
S0-MI	114.3	686	3.6	525	56.7	5
S50-MI	114.3	686	3.6	525	53	4
S0s-MI	114.3	686	3.6	525	56.7	3
S50s-MI	114.3	686	3.6	525	53	3
S0-SI	114.3	686	3.6	525	56.7	3
S50-SI	114.3	686	3.6	525	53	5
S0-FI	114.3	686	3.6	525	56.7	3
S50-FI	114.3	686	3.6	525	53	3
MH	114.3	686	3.6	525	-	2
M0	114.3	1029	3.6	860	55.97	4
M50	114.3	1029	3.6	860	52.2	4
M0s	114.3	1029	3.6	860	55.97	3
M50s	114.3	1029	3.6	860	52.2	3
LH	114.3	1543	3.6	1365	-	2
L0	114.3	1543	3.6	1365	54.2	4
L50	114.3	1543	3.6	1365	50.57	4
L0s	114.3	1543	3.6	1365	54.2	3
L50s	114.3	1543	3.6	1365	50.57	3

Table 3.3. Details of the compression test specimens

Specimen ID	D (mm)	t (mm)	Effective height (mm)	Compressive strength (MPa)	No. of specimens
C0i	114.3	3.6	457	56.7	3
C50i	114.3	3.6	457	54.3	3
C0	114.3	3	457	56.7	3
C50	114.3	3	457	54.3	3
C0s	114.3	3	457	56.7	3
C50s	114.3	3	457	54.3	3
E0	114.3	3	457	56.7	3
E50	114.3	3	457	54.3	3
E0s	114.3	3	457	56.7	3
E50s	114.3	3	457	54.3	3

Table 3.4. Mix proportions of recycled and normal aggregate.

Concrete type	Replacement ratio (%)	Cement (kg)	Water (kg)	Sand (kg)	NA (kg)	RA (kg)	Slump (mm)
Normal	0	438	203	710	977	0	96
Recycled	50	438	203	710	488.5	488.5	89

Figure 3.4. The concrete materials in a pan mixer

Figure 3.5. The tubes for compression test specimens

Figure 3.6. Impact test specimens

(a) Post casting curing during the first 24 hours

Figure 3.7. Post casting process to maintain the moisture content of the specimens

(b) Maintain the moisture content by covering the tube ends with cling film

Figure 3.7 (continued) . Post casting process to maintain the moisture content of the specimens

3.3.4 Compression test

Fig. 3.8 shows the Tonipact 3000 KN compression testing machine used to test the 100 mm concrete cubes at ages of 7 and 28 days to monitor the consistency of the concrete mixing for all concrete batches by the compressive strength of the cubes. The average 28-day compressive strength of the normal and recycled aggregate concrete cubes, in accordance with BS EN 12390-3 (2009), were 55.76 MPa and 53.05 MPa, respectively.

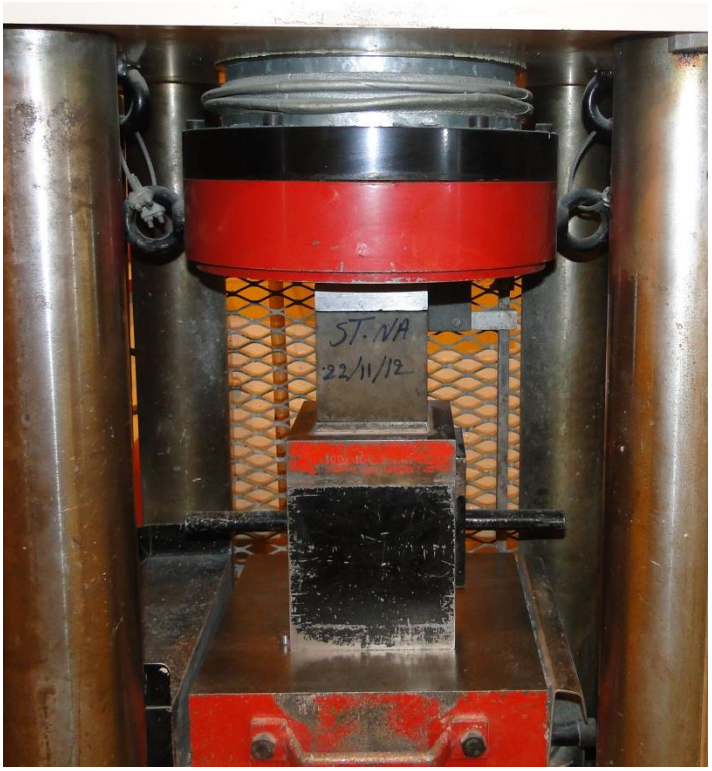

Figure 3.8. Tonipact compression testing machine

3.3.5 CFRP strengthening

To obtain a better bond and ensure good adhesion between the surface of the tube and the CFRP, the external surface of the steel tubes was treated by rough aluminium oxide paper and then it was cleaned by dry tissue to remove dust, as shown in Fig 3.9 (a). EL2 epoxy laminating resin with a 100:30 mixing ratio, i.e., 100 parts resin to 30 parts hardener by weight was used. The properties and any other specifications of the resin were listed in Appendix A. To ensure that the thickness of the resin is equal on the specified surface area of the tube, the same volume of resins was used for the same area and it was applied to the surface of the tube using a small brush. Only one layer of the CFRP woven was placed around the external surface at the mid-height of the tube with the length equal to one-third of the span of the tube. To ensure the circumferential continuity of the CFRP layer, the CFRP layer was overlapped by 150 mm from the finishing end of the sheet. After the woven and resin were placed on the tube, a small roller was used to press the fibre sheet to distribute the resins uniformly on the whole bonding area and move the air out. Later, it was tightly

wrapped by a high shrink composite tape to consolidate the strengthening. A post cure in an oven at up to 60° C for 8 hours was applied to help settlement for the one layer of the reinforcing material as recommended by the manufacturer. Fig. 3.9 (b) shows the strengthening process with CFRP.

(a) Preparing the tube surface

(b) The impact test specimens strengthened with CFRP

Figure 3.9. Strengthening process with CFRP

3.4 Impact test

3.4.1 Impact rig

The specimens were tested under lateral impact load using an impact rig, shown in Fig. 3.10 (a). The maximum height of the rig is 2.6 m. The mass of the drop-hammer is 106, 106.5, 107, and 107.5 kg for SI, MI, FI, and BI, respectively. The maximum mass can be carried by the impact rig is 107.5 kg and it is varied from 106 to 107.5 kg due to the difference of the impactor weight. The average theoretical velocity for the tests in this study is 7.1 m/s. The theoretical impact energies are 2672, 2685, 2697 and 2710 J with the mass of 106. 106.5, 107 and 107.5 kg, respectively. The impact rig includes three main components, i.e. the drop-hammer rail that is a 150 x 90 C-channel column, the winch that is used to lift the drop-hammer and the release locking pin that is connected to the switch panel. A steel plate strip is fastened to each internal side of the C-channel to align the drop-hammer. The schematic of the test impact rig with average velocity and impact energy and the expected lateral displacements are shown in Fig. 3.10 (b).

3.4.2 High speed video camera

In this study, two types of displacements were captured, i.e. the total and global displacement as shown in Fig. 3.11 (a). The total displacement (or the top surface displacement) represents the local indentation and the global displacement of the tube, while the global displacement (or the displacement of the bottom surface of the column) is the global movement of the tube. To capture the total and the global displacements, velocity and the mode of failure of the specimen, a high speed camera (HSC, MotionPro X4, model no. X4CU-U-4) with 10000 frames per second resolution, was used with two high voltage lights, as can be seen in Fig. 3.11. A frequency of 5000 frame per second was set for the HSC because the captured area was large, in order to maintain enough time to record all the impact period, as the recording time reduces with increasing the HSC resolution. Two targets were attached on the impactor and at the mid span of the specimen, as shown in Fig. 3.11 (c), to track their movement during the impact event. To record the frames into a video file, MotionPro software, version 2.30.0, was used in this study. ProAnalyst software was

adopted for the image processing and calibration to obtain the required velocity and displacement.

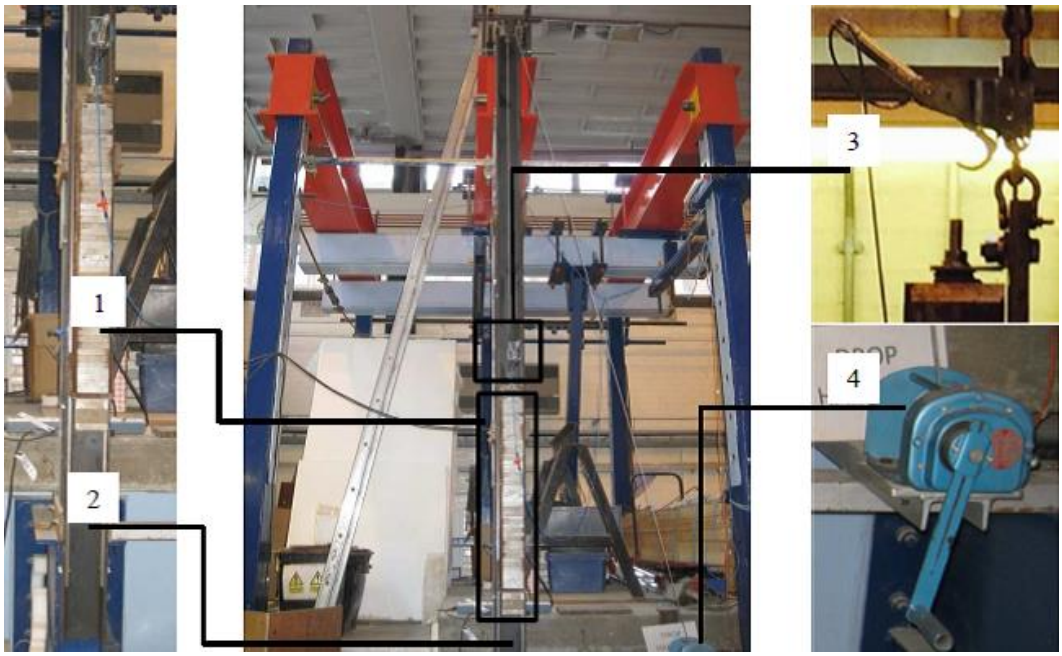

(a) The impact rig components: (1) Drop-hammer, (2) Rail, (3) Locking pin, (4) Winch

Figure 3.10. The impact test frame

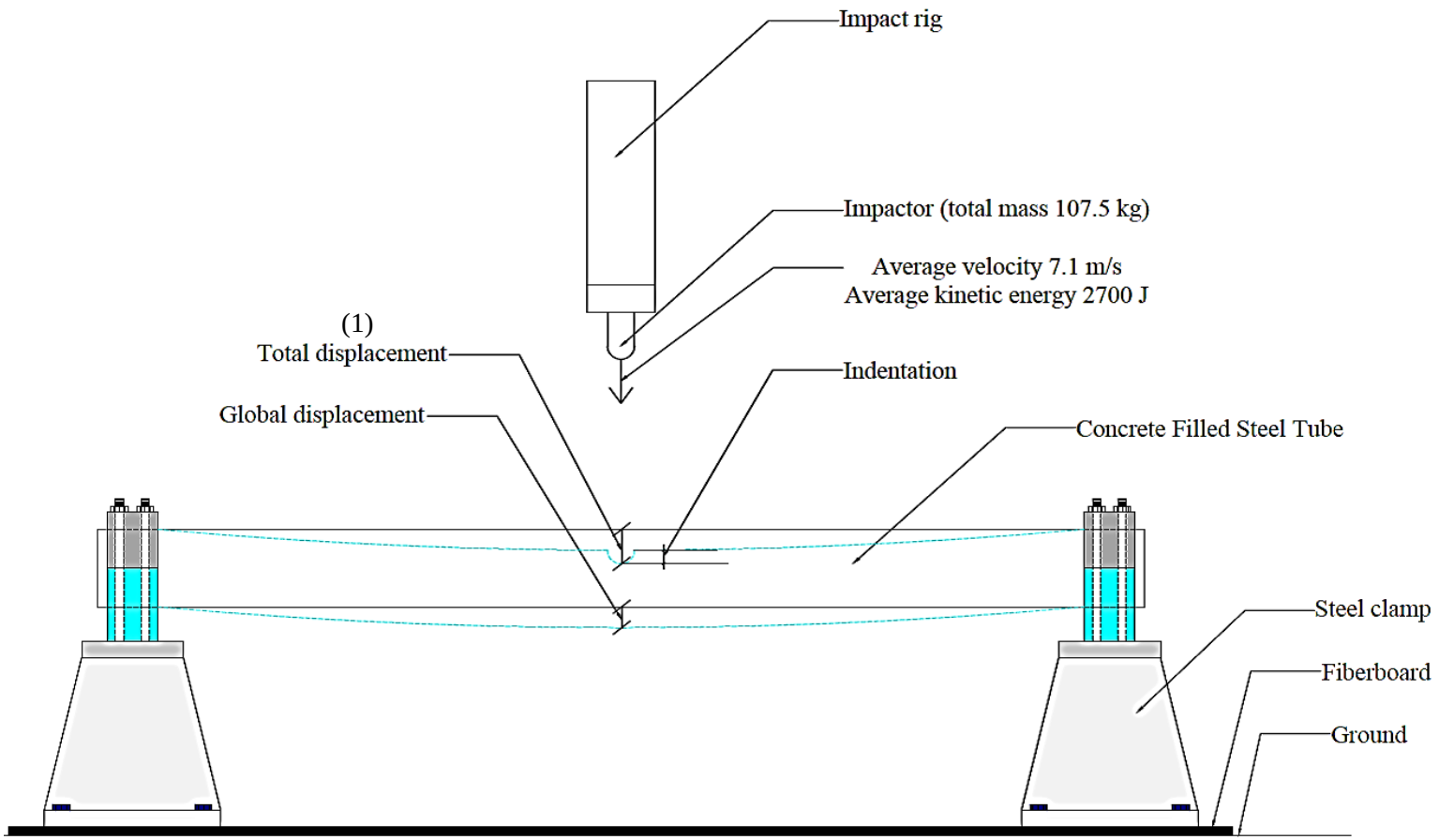

(b) The schematic of the test impact rig

Figure 3.10 (continued). The impact test frame

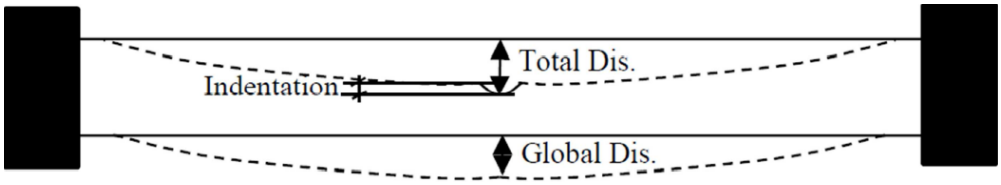

(a) Local and global displacement with the indentation caused by an impact with spherical impactor

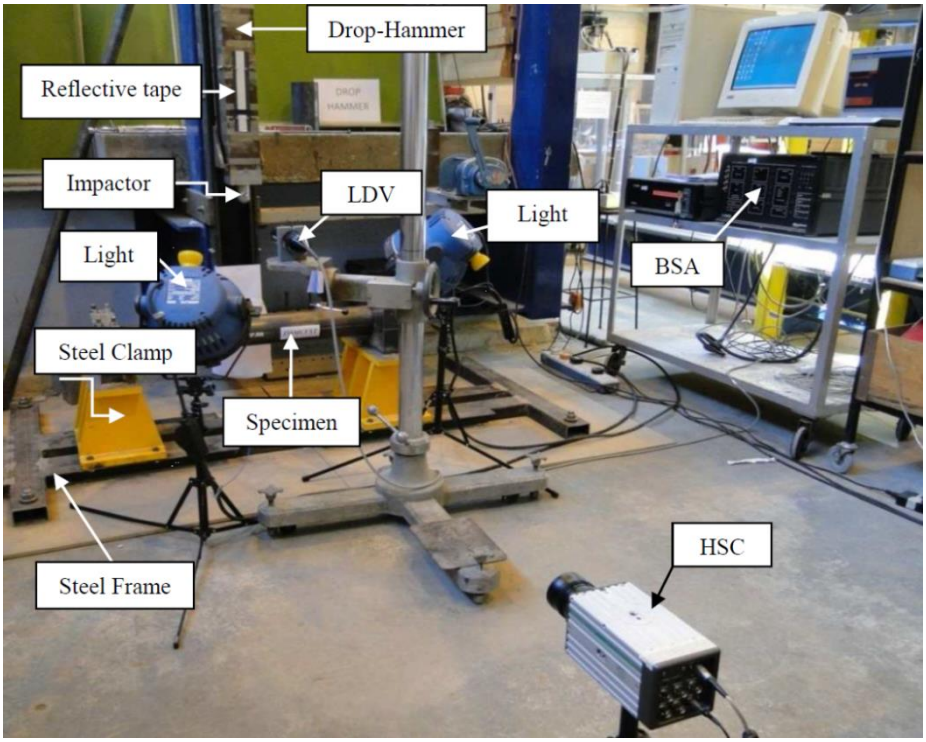

(b) General set-up

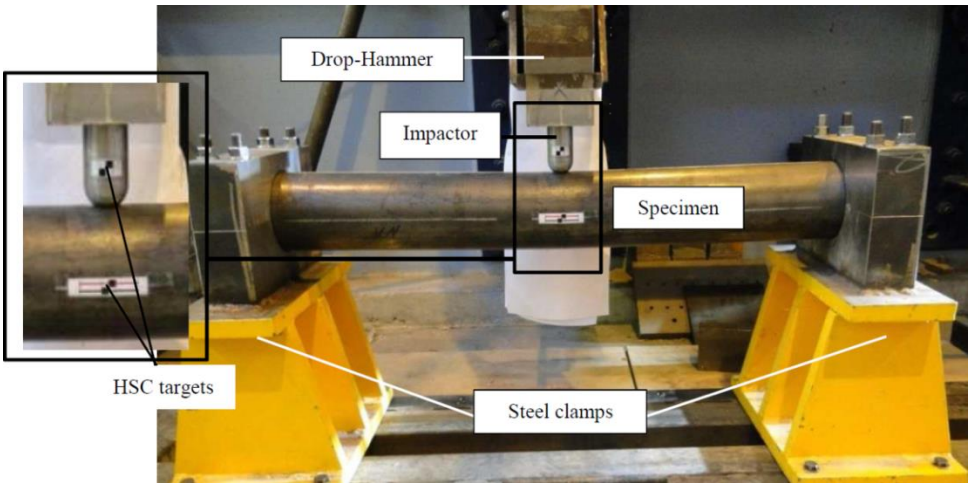

(c) Close up image

Figure 3.11. Set up of the impact test

3.4.3 Laser Doppler Velocimeter

A Laser Doppler Velocimeter (LDV) was used to obtain the impact force and the total displacement based on the velocity-time history. The LDV does not affect the system and is not affected by it, since there is no contact between the specimens tested and the LDV (Birch and Jones, 1990). The Dantec Flowlite LDV system was adopted in this study. This system includes a Burst Spectrum Analyser enhanced (BSA) signal processor model 57N21, which was linked to a computer via an interface card, optic unit, and a fibre optic cable. When the impactor hits the tube, the system will be triggered and the data will be captured over the impact period. Before the impact test, the BSA setting was performed by using the BSA flow software. A reflective tape shown in Fig. 3.11 (b) was placed on the drop-hammer with 250 mm length and 25mm width. This tape reflects the two red colour laser beams which impinge the impactor and then the LDV will process the reflected beams to produce the velocity-time history. The details of the LDV system are shown in Fig. 3.12. Table 3.5 shows the adopted BSA settings, which are used in accordance to the user's guide manual recommendations (DANTEC, 2000).

Table 3.5. BSA general setting

	Parameter	Value
BSA data collection/buffering	Data collection mode	Continuous
	Output buffer mode	Burst
	Number of burst	60000
	Measurement intervals	10
	Duty cycle	100%
BSA range/gain	Velocity centre	3.31 m/s
	Velocity span	13.2 m/s
	Record length	16
	High voltage	848 V
	Signal gain	35 dB
	Calibration	6.61 m/s

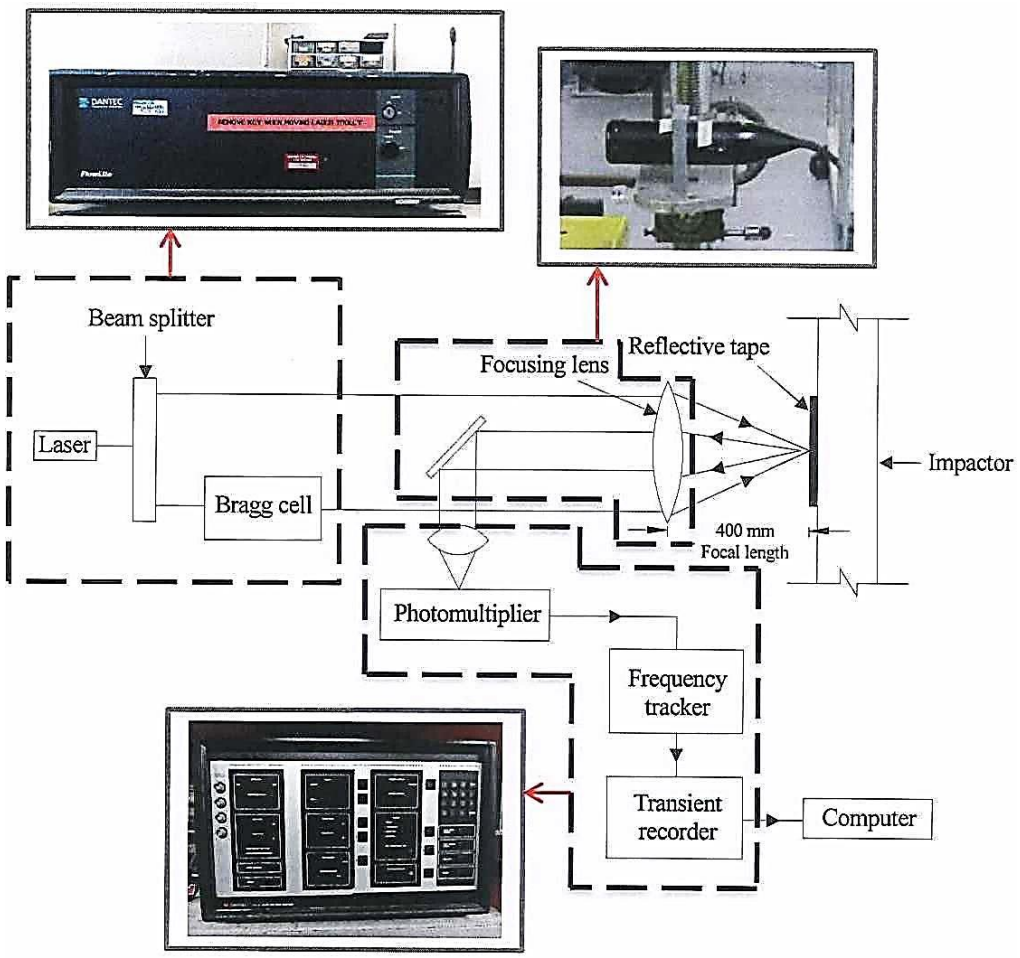

Figure 3.12. Schematic arrangement of the LDV (Zaini, 2015)

3.4.4 Impact test procedures

Fig. 3.13 shows the details of the high strength steel clamp which was used to provide fixed ends of the specimens to mimic the fixed boundary conditions of the column ends. In order to reduce the vibration resulting from the high energy impact, a steel frame was used to fix the steel clamp to the ground with 12 mm thick fiberboard. The clamps were adjustable on the steel frame to change the tube setting in accordance with the tube length. To provide an equal fixity for both ends of the tube and secure them with the clamp, a 120 N.m torque was applied on all the eight studs of the clamp. The LDV was positioned in the front of the reflective tape on the impact rig with 400 mm ±10 mm distance, to secure the signal strength. The HSC was setup opposite to the mid span area of the tube to track the movement of the impactor and the tube. The overall setup of the impact test is shown in Fig.

3.11. All the impact tests were carried out with the same initial impact energy, which was 2650 J ± 100 J depending on the weight of the impactor and the initial impact velocity. During each test, the measurements of the velocity-time history and the deformation were recorded, and then the global displacement, total displacement and the contact force were derived from the HSC and LDV. The permanent indentation was also measured using a Vernier caliper and steel strip. To inspect the damage mode of the tested specimens, digital photos were taken. To obtain consistent results, three specimens were tested for each single parameter. The total displacement (or the top surface displacement) represents the local indentation and the global displacement of the tube, which was captured using both the HSC and LD, as shown in Fig. 3.11 (a). The global displacement (or the bottom surface displacement) is the global movement of the tube, which was recorded using the HSC.

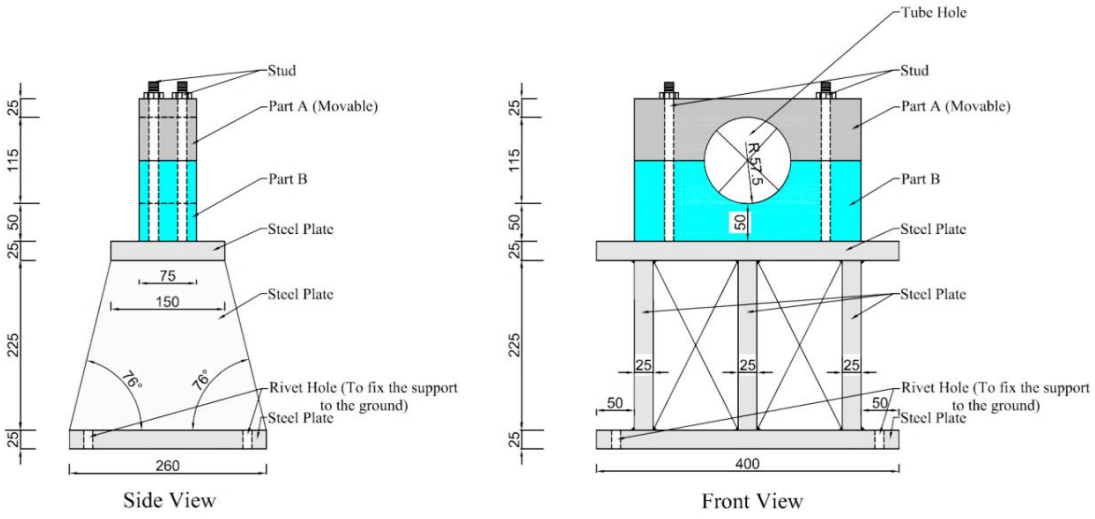

Figure 3.13. High strength steel clamp details

3.5 Data processing

The Dantec Flowlite LDV system was used to provide the impact velocity-time history in this study. Many methods and filter types are available and each one of them has associated advantages and disadvantages. Low pass, High pass, Band pass and Notch pass are the commonly used filter types, while Chebyshev, Butterworth and Bessel are the well-known filtering methods. The Low pass Butterworth filter with the fourth order was chosen in this

study, which was adopted in some low impact velocity investigations (Ziani, 2015). The LDV signals were processed using the digital filter software imPRESSion 6 (Nicolet Technology, 2002), as shown in Fig. 3.14. It can be seen from Fig. 3.14 that there are three stages in the velocity-time history. In the first stage, the impactor hits the CFST column with its maximum velocity which is about 7.1 m/s. In the second stage, the impactor and the CFST column move downward together up to the maximum displacement of the column. In this stage the velocity of the impactor decreases and the lateral displacement increases up to the maximum lateral displacement. The third stage includes the bouncing back of the CFST column and the impactor due the elastic energy (recovering energy). No rebound was captured within the period from the first contact between the column and impactor to the time when the column reaches its maximum lateral displacement.

The raw data for each test was reduced to be within the period of the first contact and the rebound. The time steps are equaled by obtaining the linear interpolation using the impression software and then, the data filtered using the Low pass Butterworth filter. The impact force can be obtained by multiplying the mass of the drop-hammer by the acceleration which was evaluated from the differentiation of the impact velocity with respect to time, while the integration of the LDV signal provided the local displacement on the tube column. A comparison between the results obtained from the HSC and those calculated from the LDV signals has been made to check the agreement between the two different sources of data. Fig. 3.15 shows a very good agreement between the HSC and the LDV results for the velocity-time and local displacement-time history, respectively. In order to examine the accuracy of the filtered results of the LDV, the theoretical kinetic energy was compared with the experimental impact energy. Well correlated values were obtained; the calculated energy for one of the NACFST specimens was 2699 J, while the one obtained from experimental results was 2687 J, as can be seen in Fig. 3.16. The area below the force – total displacement curve was used to calculate the total and observed energies. The maximum lateral displacement (1) shown in Figs. 3.10 (b) and Fig. 3.16 with the corresponding impact force

used to calculate the total impact energy. The total impact energy includes the energies absorbed by the steel tube and the concrete core. The energy observed by each element will be obtained later using the validated finite element models. The total observed energy obtained from the area below the impact force-lateral displacement trace from (0, 0) point to the point when the impact force equals to zero with associated lateral displacement (2) as shown in Fig. 3.16.

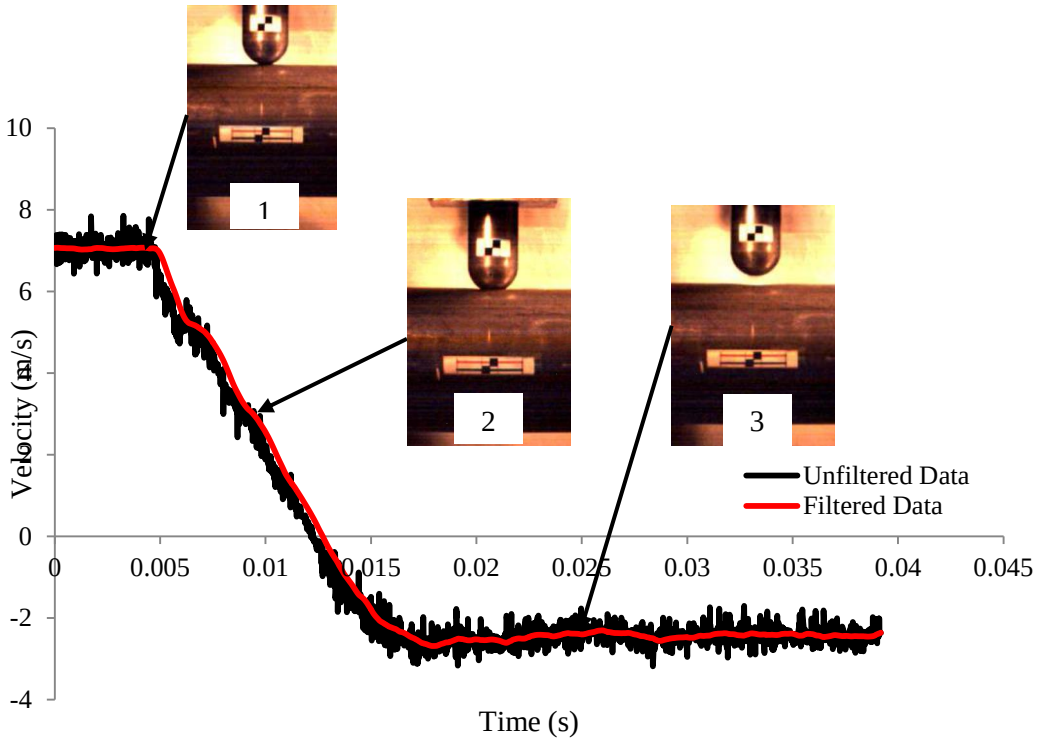

Figure 3.14. Typical filtered velocity-time histories of the impact test for specimen L0

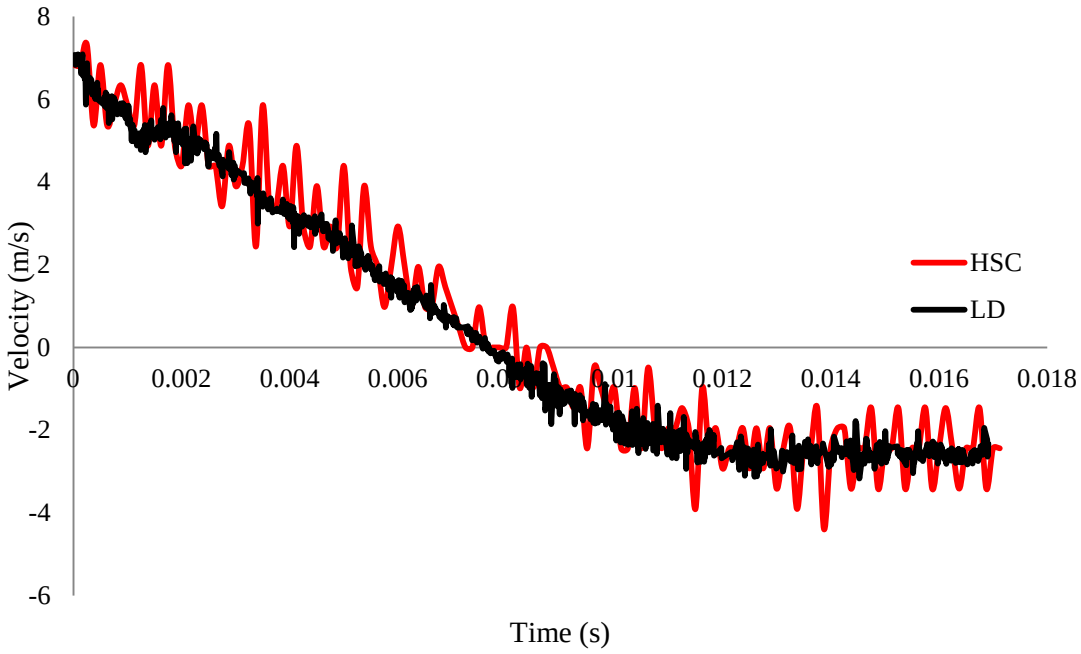

(a) Velocity versus time curves

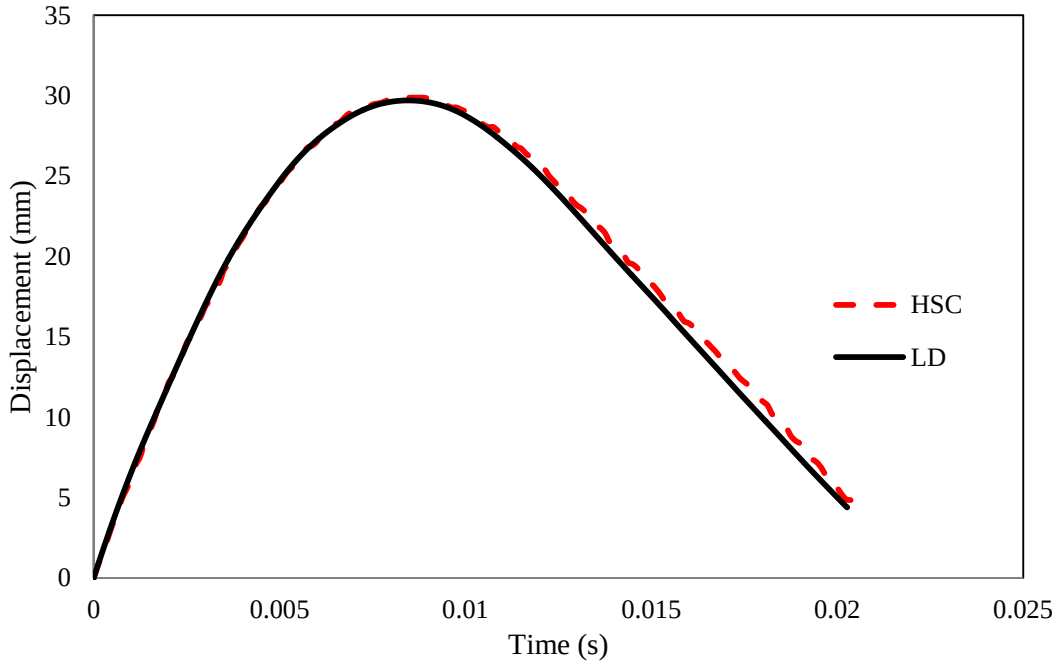

(b) Displacement versus time curves

Figure 3.15. The comparison between the high speed camera and the laser Doppler results

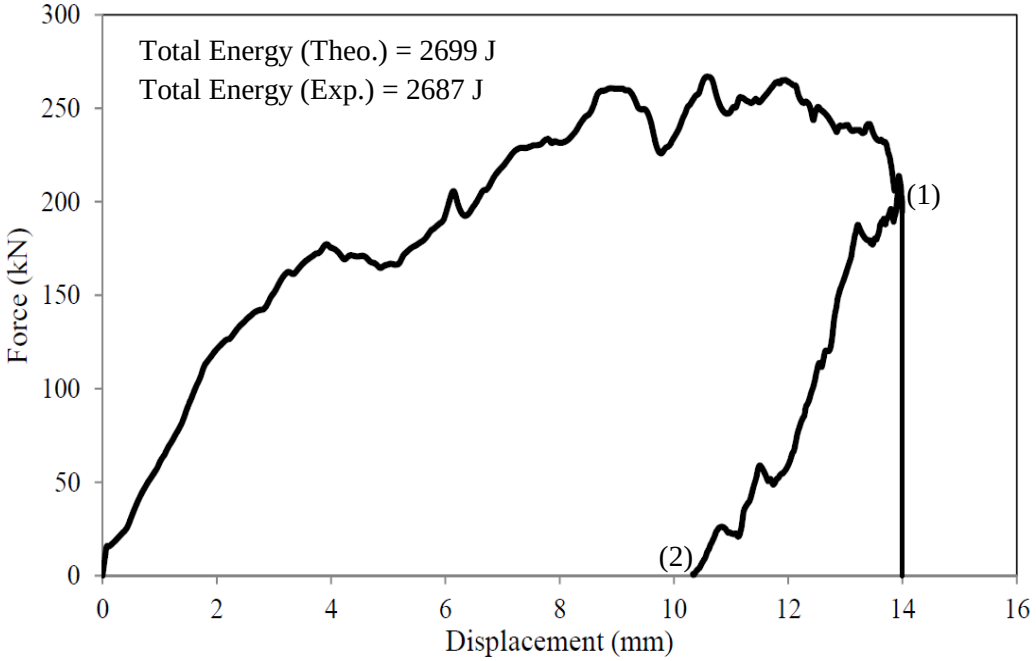

Figure 3.16. Comparison between the calculated and experimental impact energy

3.6 Compression tests

3.6.1 Instrumentation

The compression tests were carried out using the facilities of the Built Environment School laboratory at Liverpool John Moores University. The specimens were tested using an AUTOMAX 5 compression testing machine, (model 50-C6652) with 4000 kN maximum capacity, which is shown in Fig. 3.17. This machine is connected to a control unit which links to a lap top computer with special software to record the load with respect to time. Data Manger software supplied by Controls was used to obtain the load-time history.

The displacement-time history was captured by two linear displacement transducers with 25 mm maximum stroke. These transducers were connected to a PC via instruNet data acquisition. The transducer and instruNet are shown in Fig. 3.18.

Figure 3.17. Automax compression testing machine

(a) Linear displacement transducer (b) instruNet data acquisition

Figure 3.18. Displacement capturing devices

3.6.2 Test procedures

Figs. 3.19 (a) and (b) show the compression test setup for the axial concentric and eccentric loading tests, respectively. To apply eccentric loading on the specimens, a steel bar with 20 mm diameter was welded to the top plate of the specimens. The distance between the steel bar centre and the centre of the tube was 21 mm, which is the eccentricity, adopted in this study. The main test parameters were the concrete type, i.e. normal and recycled aggregate concrete, loading condition, tube thickness and the CFRP reinforcement. Three specimens were tested to examine each parameter.

Both types of specimens, i.e. concentric and eccentric loaded specimens were placed between the platens and loaded uniformly with a consistent loading rate of 100 N/min. A personal computer was connected to the machine to capture the load-time history. Magnetic holders were used to place the transducer vertically on the bottom platen which moves upward to apply the compression loading on the specimens. All the specimens were loaded up to failure and the machine was stopped manually to avoid damaging the transducers due to the high axial deformation. The load and displacement versus time were recorded and then combined together to draw the load-displacement traces. Photos were taken using a digital camera after the test to inspect the failure mode of the tubes tested.

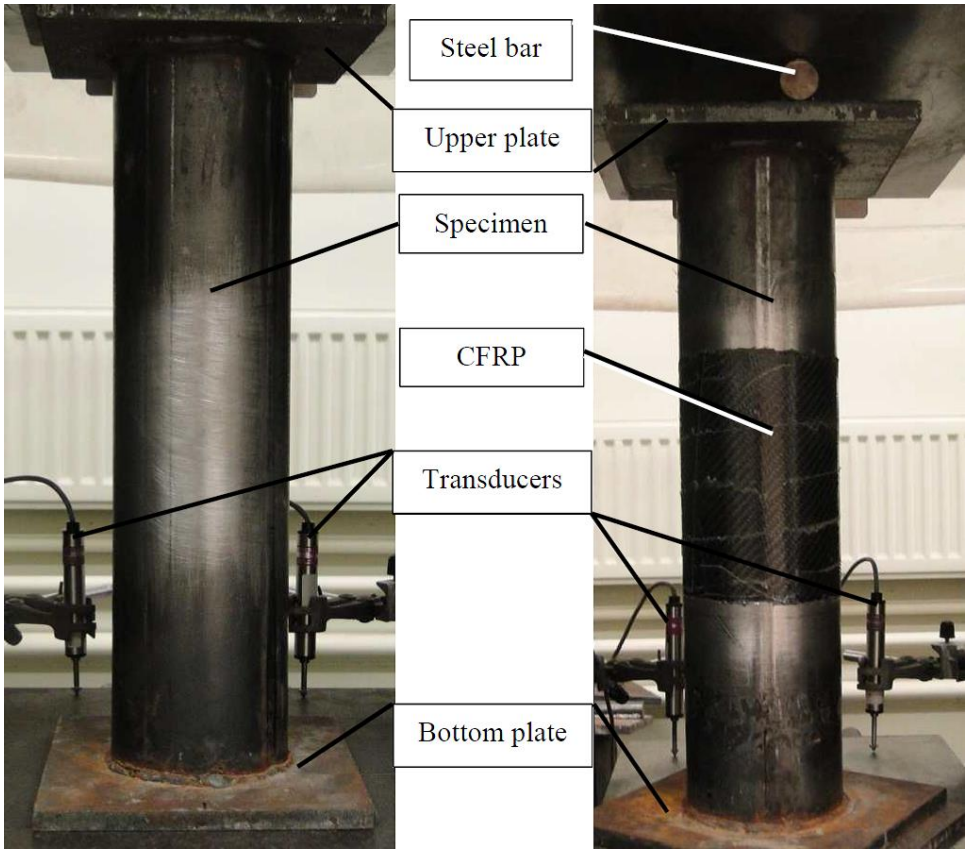

(a) Concentric test setup (b) Eccentric test setup

Figure 3.19. Compression test setup

3.7 Summary

The details of the impact and compression tests were presented in this chapter, including the sample preparation and test procedures. The main tests to obtain mechanical properties of the materials used were undertaken. The same water-cement ratio was used for both types of concrete, i.e. recycled aggregate and normal aggregate concrete. The specimens were wrapped by one layer of CFRP at the mid span area to examine the effect of CFRP reinforcement on the structural response of CFST columns. The instrumentation used for both tests were presented. The impact behaviour of the CFST columns with different parameters was investigated. The LDV data processing was also presented in this chapter including the validation with HSC results. Finally, the compression tests were carried out to determine the compression capacity and failure mode of the CFST columns under concentric and eccentric loading.

CHAPTER 4
EXPERIMENTAL RESULTS AND DISCUSSION

4.1 Introduction

This chapter presents the experimental results on CFST columns subjected to lateral impact loading. The effects of the concrete filling on the impact response and the failure mode of the hollow tube columns will be discussed. Following this, the outcomes of the specimens tested with different parameters, i.e. L/D, D/t, CFRP reinforcement, and impactor configuration will be evaluated and analyzed. Subsequently, this chapter covers the results of the compression tests of the CFST columns under eccentric and concentric axial loading. The damage modes of the CFST specimens due to the compression loading will be observed and compared.

4.2 Lateral impact test

Eighty-three specimens were tested under lateral impact loading with a maximum weight of 107.5 kg and initial impact energy of 2650 J ± 100 J. When the impactor hits the tube with an initial velocity, the deformation will start with a local indentation as explained earlier in Section 3.4.4 which is equal to the deference between the displacement on the top surface (or the total displacement) "δ_{max}" and the displacement on the bottom surface (or the global displacement).

4.2.1 The influence of the concrete filling on the impact behaviour of the hollow steel tube with different L/D ratios

4.2.1.1 Load-displacement relationships

For each test, only the raw data within the period from the first contact between the tube and the impactor to the time of the rebound was adopted in this study. As mentioned in Chapter 3, the linear interpolation was used to equalize the time steps and the Low pass Butterworth filter was used to filter the data using the Impression software. The impact force was obtained by multiplying the mass of the drop-hammer by the acceleration from the differentiation of the impact velocity with respect to time. The integration of the velocity from the LDV signal provided the total displacement of the tube column. The global displacement and the deformation shape were recorded using the HSC.

Figs. 4.1 (a) and (b) show the impact force-total and global displacements curves, respectively for the hollow short, medium and long steel tube columns. It can be seen that although the raw data of the LDV were filtered initially, the curves still include oscillations. These oscillations are excited by the natural frequency of the test rig. Hence, filtering the force–total and global displacements traces again results in smooth curves which do not show fluctuation. However, the second filtering process causes a distortion for the data as can be noticed from Fig. 4.2. The filtering process caused an increase of the total displacement from 57 mm to 69 mm, which was a discrepancy with the captured data of the HSC in which the total displacement was 58 mm. Accordingly, these oscillations under dynamic conditions reflect the effect of the vibration of the test rig. Thus, under dynamic conditions, the fluctuation is a normal phenomenon, especially for low stiffness specimens. As can be seen later, these oscillations disappear or just a few of them appear with force-total and force-global displacement traces for the concrete filled tubes which exhibited higher stiffness and deformation resistance.

Fig. 4.1 shows that for tubes with different L/D ratios, the force and displacement increased steadily up to the maximum level and then the force decreased to zero and the displacement retreated slightly to the permanent value when the impactor rebound back from the tube surface. Here, the elastic recovery was small and it decreased with increasing the L/D ratio due to the high impact energy dissipation which is represented by the permanent plastic deformation of the tube. It can be noted that the maximum force increased from 64.74 kN to 83.97 kN, while the total displacement decreased from 68.7 mm to 52.1 mm from the long to short tubes. The global displacement for the hollow long tube was 30.3 mm, whilst the global displacement reduction for the medium and short tube compared with the long one, was 38.3 % and 68.5 %, respectively, as shown in Fig. 4.1 From these results it can be seen that with increasing tube length, the total and global deformation increased and the impact force decreased due to the reduction of the tube stiffness, as expected.

In order to compare the impact response of the hollow tube and the concrete filled tube columns, the latter are displayed with the former. Figs. 4.3-4.5 show that the filling of the tubes with concrete enhances the local deformation resistance for CFST with L/D ratio of 6, 9 and 13.5, respectively. In general, it can be seen that the impact force for all tubes would be divided into three stages. During the first stage (initial stage), the force increased quickly, which was corresponding to a relatively small displacement. The second stage (plateau stage) included some fluctuations which relate to the structural response of the tubes. Throughout this stage the displacement increased steadily with little increase on the impact force for the tubes with L/D ratios of 6 and 9 except for the tube with L/D ratio of 13.5 in which the impact force decreased to about 10 kN and then rose again to a certain value. The HSC records did not show any rebound or separation between the impactor and the surface of the tube for all columns regardless the tube length as can be seen later in Fig. 4.46. The third stage shows that the impact force fell to zero resulting from the rebound, whilst the total displacement reduced to a certain level due to the elastic recovery. All these stages will be discussed in more details in Section 4.2.8. These figures also reveal that the maximum force decreased when the tube length increased, as expected. The concrete filling contributes to increasing the maximum force by 217 %, 182 % and 157 % respectively for the short, medium and long tube. Furthermore, the concrete filling caused a significant reduction in the total and global displacements. For the short tube, the global and total displacements were reduced by 31 % and 75 %, respectively. The total displacements decreased by 68 % for the tube with L/D ratio of 9 while it decreased by 75 % for the one with L/D ratio of 13.5. All the test results plotted and discussed in this chapter are summarised in Table 4.1.

4.2.1.2 Mode of failure

Figs. 4.6 (a), (b), and (c) show that the hollow steel tubes failed in a similar manner with L/D ratios of 6, 9 and 13.5, respectively. The HSC record shows that the deformation started with an indentation at the contact area and then it buckled locally with two arched edges as shown in Fig. 4.7. In the meantime, the tube begins to buckle globally and the bending

continued at this stage up to a certain level of global deformation based on the stiffness of the tube and the boundary conditions. However, Fig. 4.6 also shows that the local and global deformation increased with increasing the L/D ratio due to the reduction of the stiffness of the tube column. It can be seen that the overall size of the local buckling along the axial direction increased from 125 mm to 170 mm and the total displacement increased from 52.2 mm to 68.7 mm when the L/D ratio increased from 6 to 13.5. Based on these results, the local and global deformations are proportional to the tube length (L) and the deformation becomes more localized with shorter tubes. Filling the tube with concrete plays a vital role in changing the deformation mode of the specimens, with reducing the local indentation and the global displacements as well as avoiding local buckling due to the composite action of the concrete core and steel tube. The concrete filling sustained a substantial deformation resistance which reduced the local indentation significantly for the short, medium and long steel tube. The absorbed energy in the hollow tubes mainly relates to large local and global deformations, while in the CFSTs it was represented by the local indentation in the steel tube and concrete core, the global bending for the tube and concrete, as observed from Figs. 4.8 (a), (b) and (c), respectively.

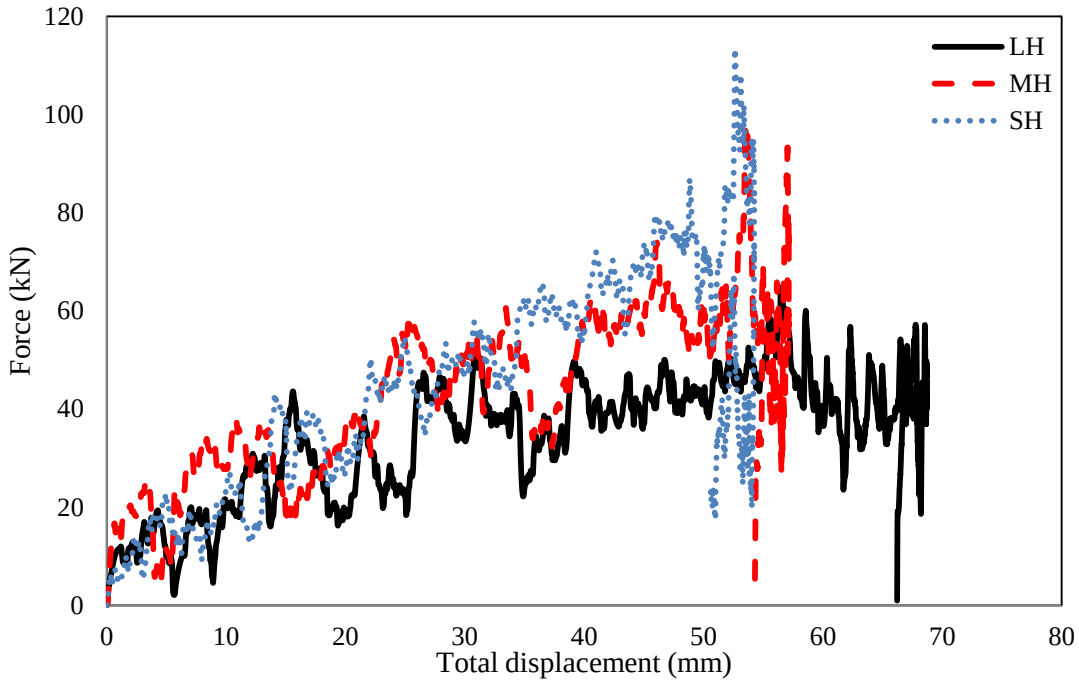

(a) The force-total displacement curves

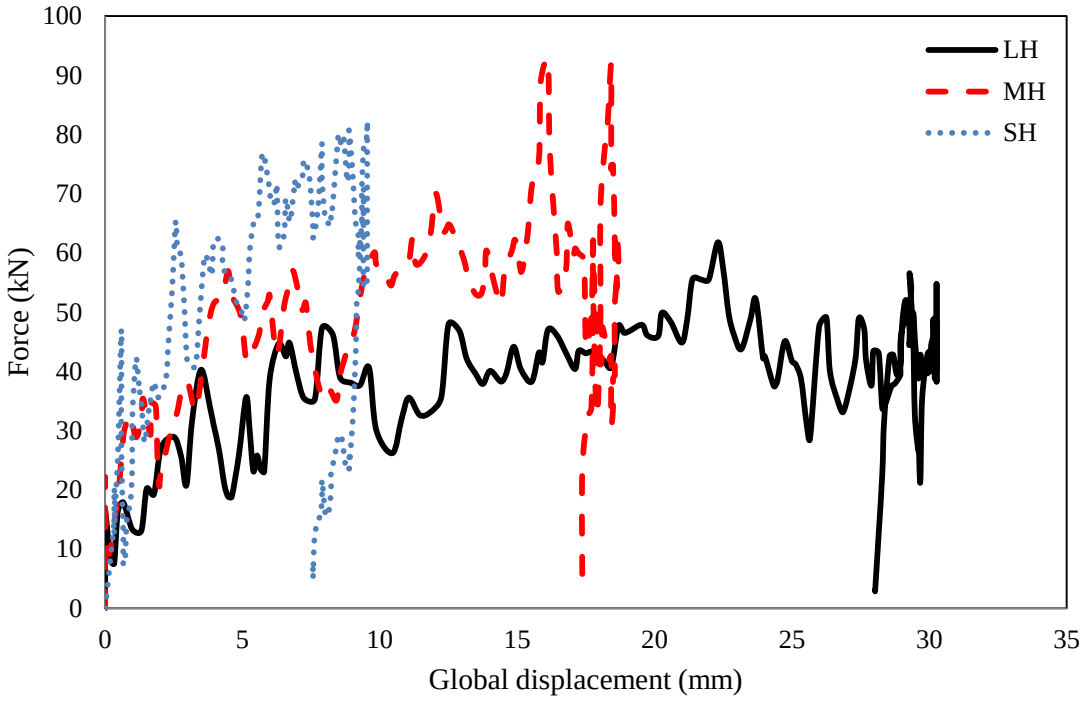

(b) The force-global displacement curves

Figure 4.1. The force - displacement traces for the hollow tubes with different lengths

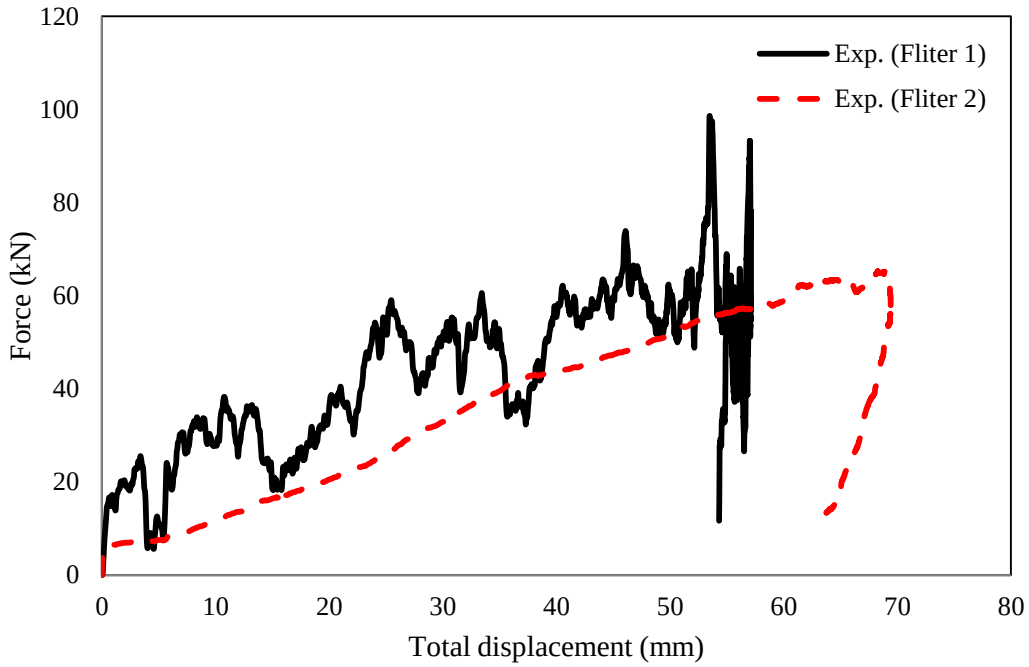

Figure 4.2. The effect of the second filtration process on the force-total displacement trace of the hollow tube with L/D ratio of 9

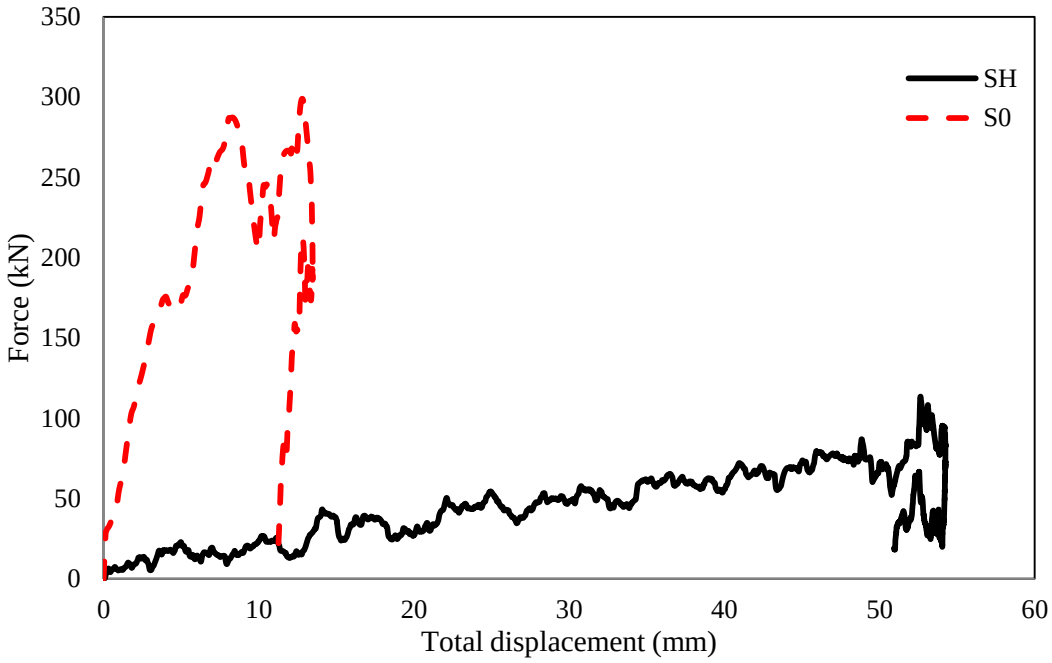

Figure 4.3. The force-total displacement curves for the hollow and concrete filled short steel tubes

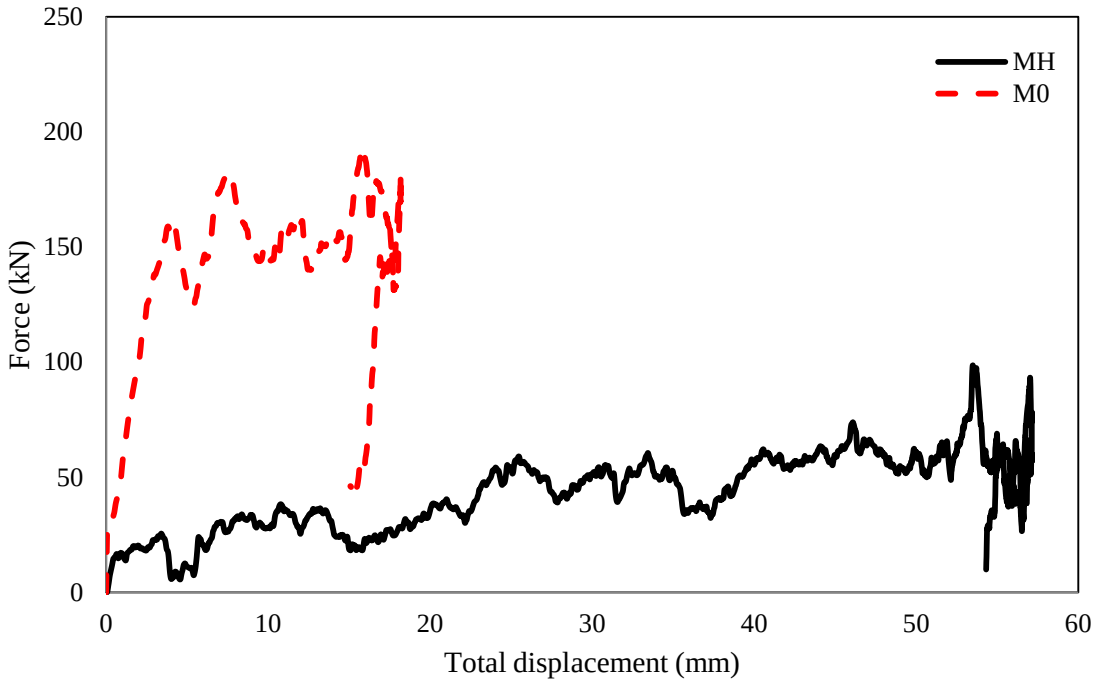

Figure 4.4. The force-total displacement curves for the hollow and concrete filled medium steel tubes

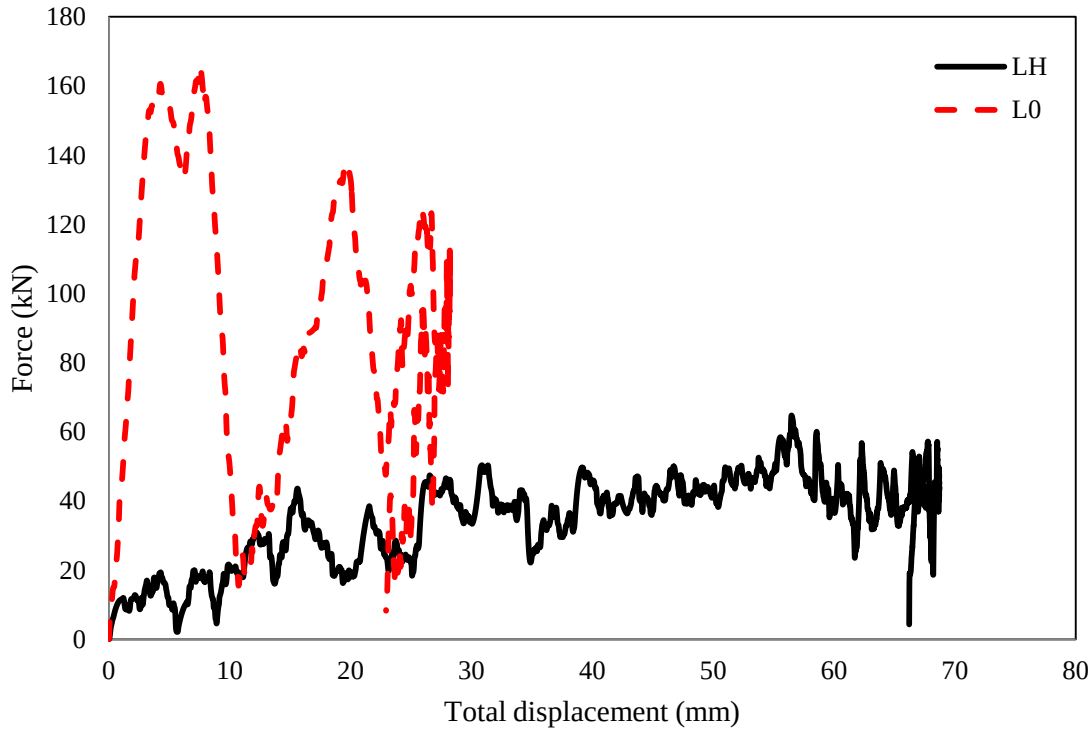

Figure 4.5. The force-total displacement curves for the hollow and concrete filled long steel tubes

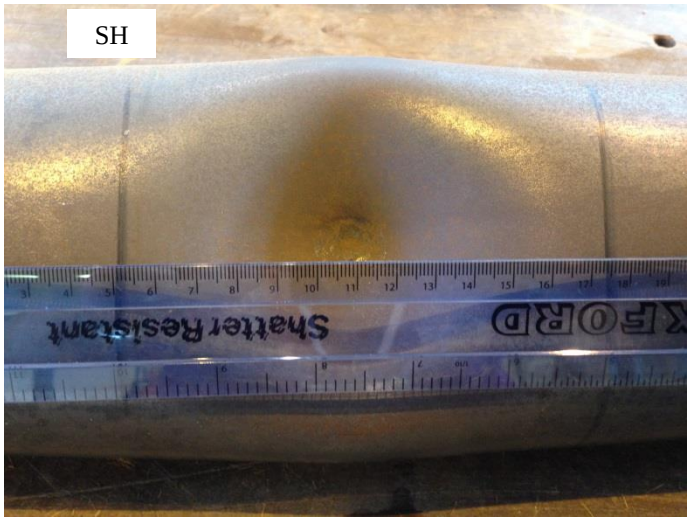

(a) Short hollow tube

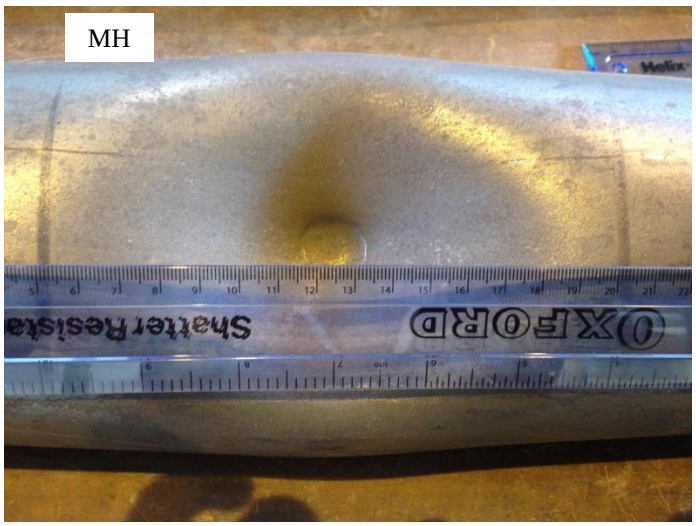

(b) Medium hollow tube

(c) Long hollow tube

Figure 4.6. The effect of the specimen length on the failure mode of the hollow tubes

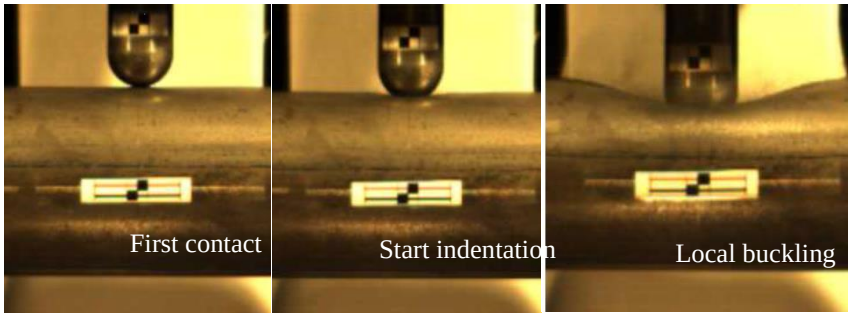

Figure 4.7. The HSC record for the deformation of the hollow tube

(a) hollow (left) and concrete filled short tube (right)

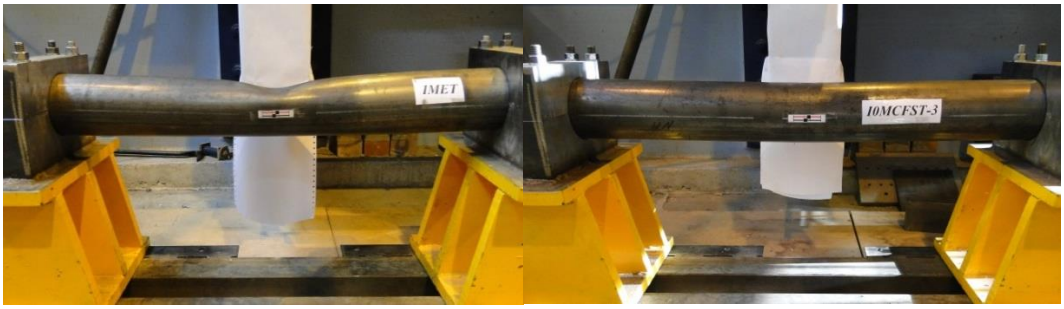

(b) hollow (left) and concrete filled medium tube (right)

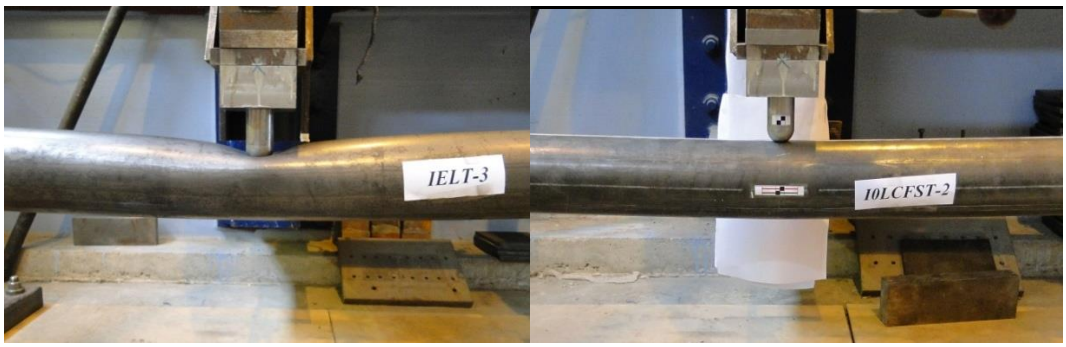

hollow (left) and concrete filled long tube (right)

Figure 4.8. The influence of the concrete filling on the deformation shape of the hollow steel tube with different L/D ratio

Table 4.1. The impact test experimental results

Specimen ID	Maximum force (kN)	Global dis (mm)	Indentation (mm)	Total disp. (mm)	Total Energy (J)	Absorbed Energy (J)	Rc (mm) Exp.	Rc (mm) Theo.	% *
S0	217.3	6.1	12.7	19.4	2655	2460	20	21.3	6.7
S50	195.7	6.3	12.8	20.5	2670	2472	20	21.3	6.4
S0s	229.4	5.3	14.1	20.8	2661	2455	20	20.2	1.1
S50s	187.4	6	13.7	19.9	2578	2422	20	20.6	2.9
SH	84	9.5	-	52.2	2442	2268	-	-	-
S0-BI	286.3	6.8	4.9	12.9	2478	2152	29	28.3	2.3
S50-BI	259.3	7.1	5.5	13.4	2481	2217	30	29.8	0.5
S0-MI	266	6.6	6.4	14	2687	2340	24	25.3	5.3
S50-MI	250	6.6	6.6	14.6	2659	2314	25	25.6	2.4
S0s-MI	274	6.6	7.1	13.6	2522	2247	24	26.3	9.8
S50s-MI	253	6.3	7.1	13.5	2486	2199	25	26.3	5.4
S0-SI	220.1	5.8	10.2	16.4	2546	2308	19	17.2	9.3
S50-SI	216	5.6	10.4	15.6	2527	2277	19	17.2	9.3
S0-FI	319	8.6	2.2	11.2	2455	2191	-	-	-
S50-FI	317.8	8.2	2.2	11.4	2509	2214	-	-	-
MH	68.7	18.7	-	57.1	2460	2336	-	-	-
M0	194	14.5	4.9	18.2	2616	2182	21	22.6	7.7
M50	181.1	14.5	5.1	19.2	2653	2229	22	23.0	4.5
M0s	204	13.2	5.6	17.4	2470	2060	22	23.9	8.8
M50s	179.7	13.5	5.2	18.5	2445	2013	22	23.2	5.4
LH	64.7	30.3	-	68.7	2351	2253	-	-	-
L0	166	24.3	3.9	28.2	2643	2257	18	20.5	13.6
L50	164.1	25	4.3	29.8	2729	2449	19	21.4	12.4
L0s	132.5	22.4	5.3	27	2464	2095	23	23.4	1.7
L50s	142.1	22.4	5.1	27.8	2449	2084	23	23.0	0.0

* [(Exp.-Theo.)/Exp.)*100

4.2.2 The impact behaviour of the CFST column with different L/D ratios

4.2.2.1 Load-displacement traces

At the contact point, the column underwent to a sudden descending momentum during the impact event and then rebounded back due to the elastic energy. As explained earlier, the force-displacement traces included three stages which are the initial, plateau and final (unloading) stages, in which the displacement and impact force vary according to the columns stiffness. Here, to investigate the effect of the L/D ratio on the impact response of the CFST columns, the boundary conditions, the tube thickness, the shape and diameter of projectile, the concrete type and the impact energy were kept constant for each batch of the concrete type. Thus, the total and global displacements, indentation depth, the impact force and the absorbed energy were affected only by the tube stiffness. To avoid the repetition, all the impact event stages will be explained in details in Section 4.2.8. In general, for the specimens filled with recycled aggregate concrete, the maximum force was slightly lower than for those filled with normal aggregate, whilst the displacement was slightly higher. This is due to the lower mechanical properties of the recycled aggregate which leads to the slight reduction of the load carrying capacity of the concrete. The comparison between the long tubes filled with normal and recycled aggregate are shown in Fig. 4.9. The maximum force for the tube filled with normal aggregate was 166.3 kN, while it was 164.1 kN for those filled with recycled aggregate, also the displacement increased from 28.2 mm to 29.8 mm with 50 % of RA replacement. The recycled aggregate has the same effect on the medium and short tube, as shown in Figs. 4.10 and 4.11, respectively. The contact force for the medium tube was reduced by 5.1 %, whilst the reduction for the short tube was 6.45 %. Figs 4.9 to 4.11 indicate that the tubes filled with normal and recycled aggregate concrete are affected by the L/D ratio. For the NACFST columns, the force decreased from 299 kN to 166.3 kN and the displacement increased from 13.5 mm to 28.2 mm, when the L/D increased from 6 to 13.5. For the RACFST columns with the same L/D ratios, the force decreased by 42 % and the displacement increased by 116 %. Fig. 4.12 shows that the global displacement for the RACFST column is slightly higher than the one filled with NA

concrete. However, Figs 4.13 and 4.14 show that both NACFST and RACFST columns were deflected by the global displacements of 14.5 mm and 6.6 mm with L/D ratios of 9 and 6, respectively. The above results indicate the impact responses of NACFST and RACFST columns are comparable, which suggests that the RACFST columns can be used in the new construction with suitable quality control. It can be seen from Figs 4.12-14 that the initial displacement is almost zero with increasing contact force. This is because the initial local indentation is not being taken into account in the global displacement, which gives much higher initial stiffness on the load versus global displacement plots.

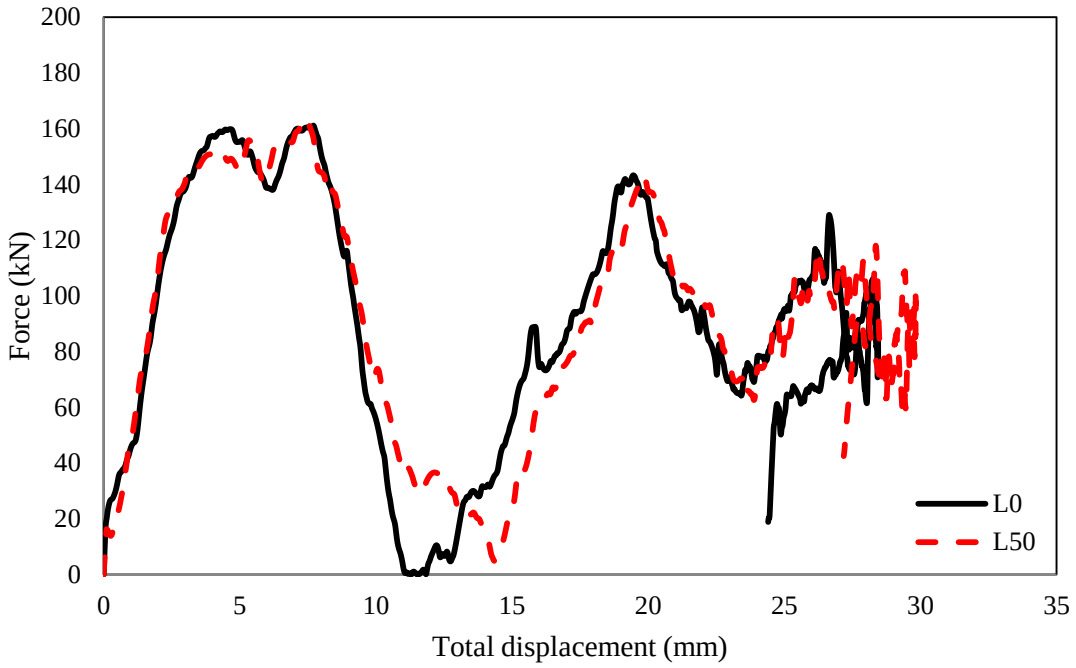

Figure 4.9. The force-total displacement curves for the long steel tube filled with normal and recycled aggregate concrete

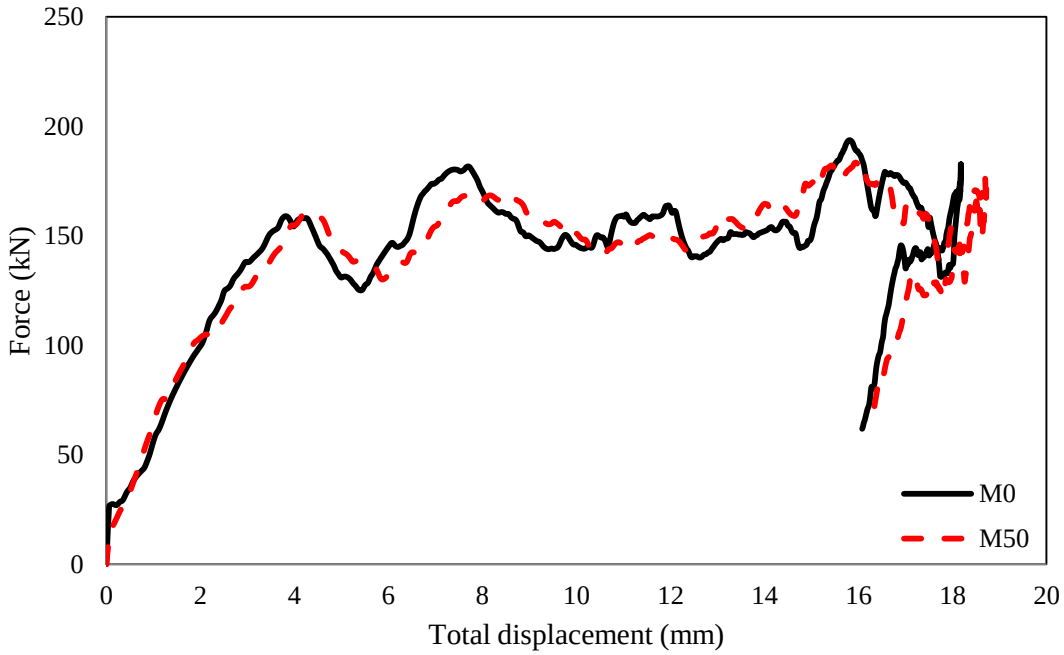

Figure 4.10. The force-total displacement curves for the medium steel tube filled with normal and recycled aggregate concrete

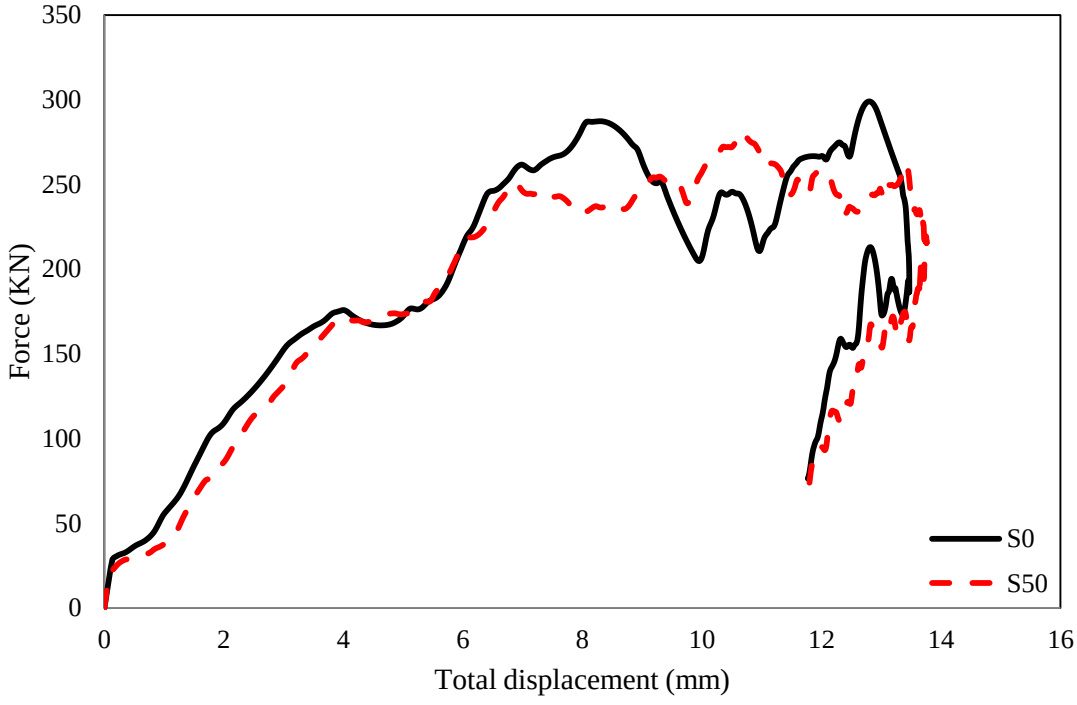

Figure 4.11. The force-total displacement curves for the short steel tube filled with normal and recycled aggregate concrete

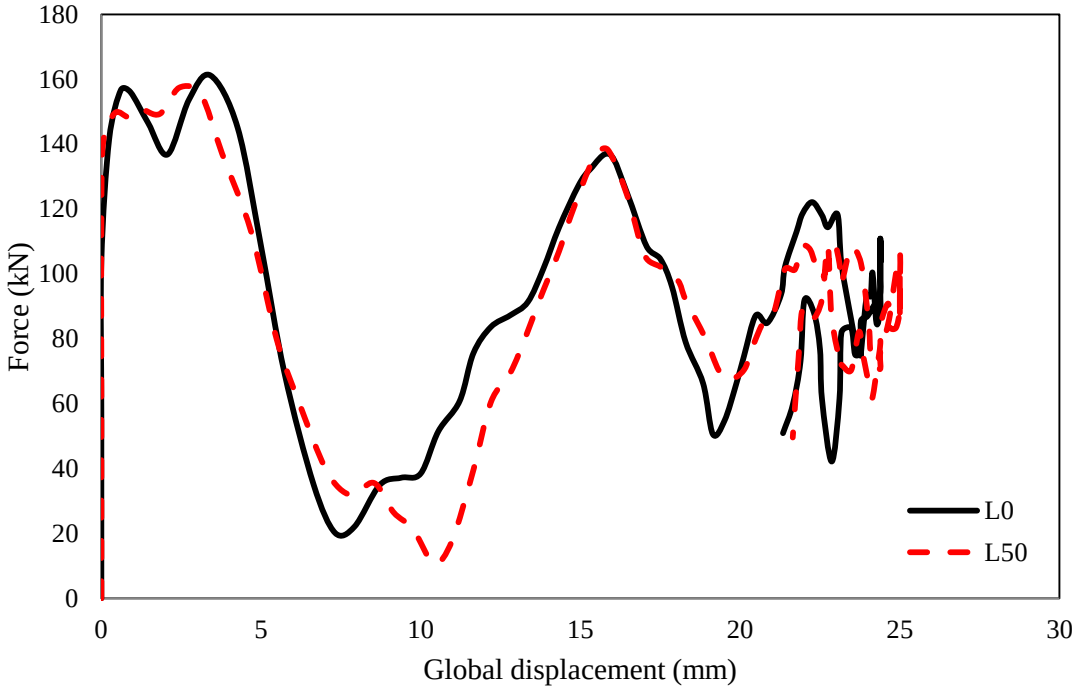

Figure 4.12. The force-global displacement curves for the long steel tube filled with normal and recycled aggregate concrete

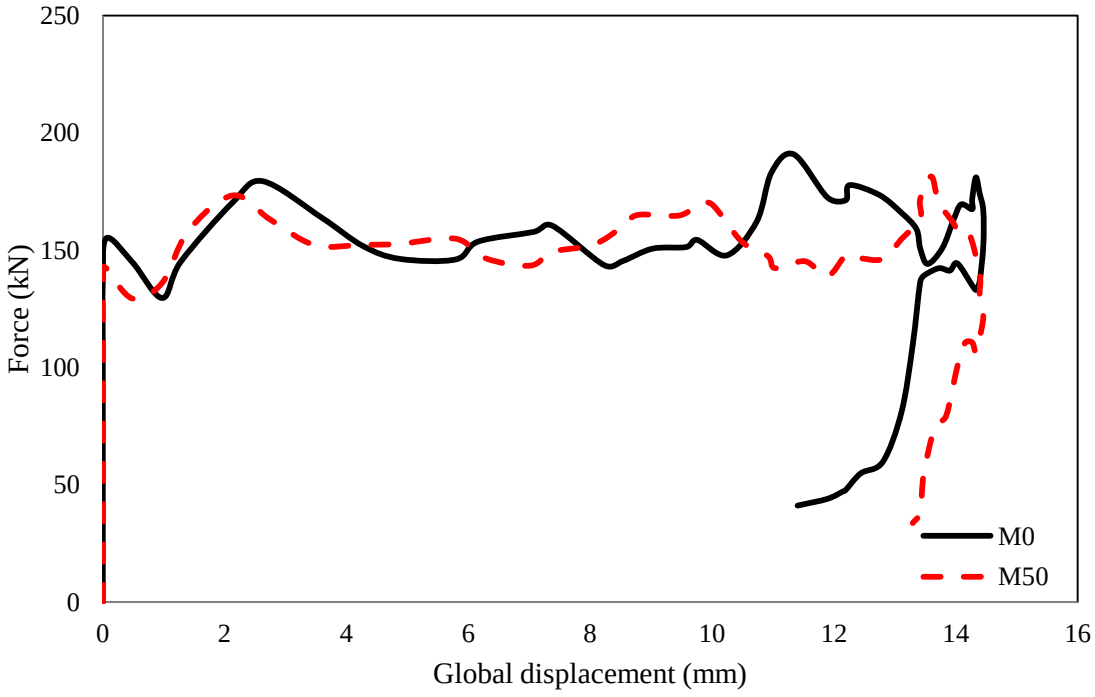

Figure 4.13. The force-global displacement curves for the medium steel tube filled with normal and recycled aggregate concrete

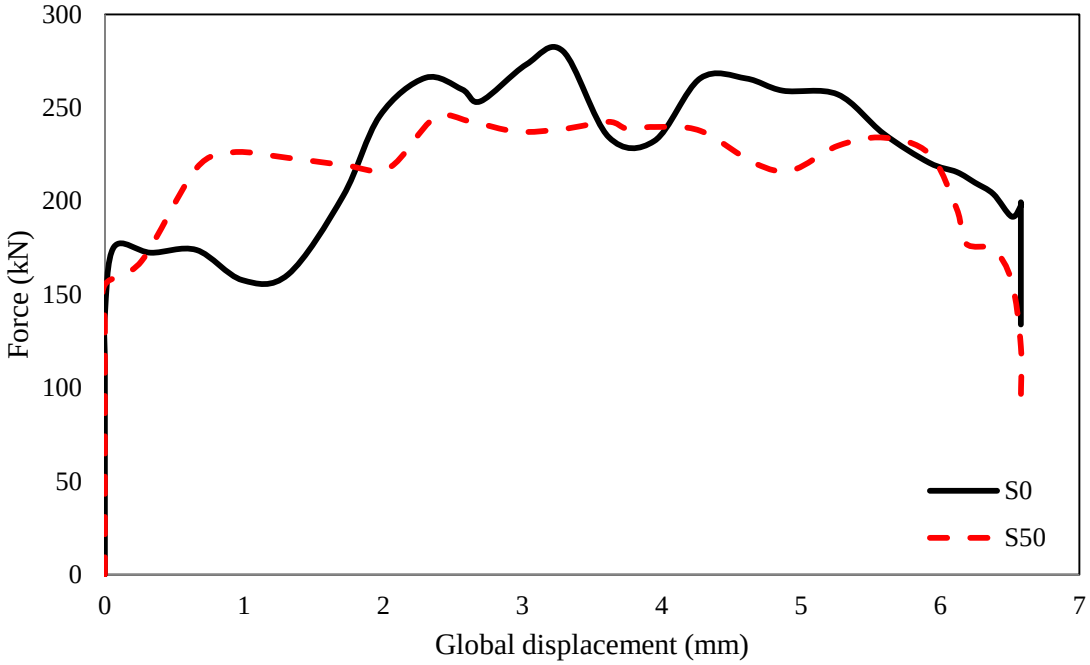

Figure 4.14. The force-displacement curves for the short steel tube filled with normal and recycled aggregate concrete

4.2.2.2 Deformation pattern

Despite the columns being tested with three different L/D ratios, RACFST and NACFST columns failed with a similar deformation mode. In this study, the columns did not fail completely under the applied impact energy but they deformed in the following sequence as shown in Figs 4.15 (a), (b) and (c) and 4.16: (1) local indentation at the contact area starts with the first contact between the impactor and the column; and (2) global deformation at the mid-span of the column begins when the impact energy exceeds the local deformation energy. It can be seen from Fig 4.17 that, with the same spherical impactor, the indentation diameter decreases with increasing specimen length, which are 18 mm for the long tube (L), 21 mm and 24 mm, for the medium (M) and short (S) tubes, respectively. The indentation depth was also measured with the averaged depth for the short tubes filled with NA and RA concrete as 6.6 mm and 6.4 mm, respectively. Table 4.1 shows that the indentation decreased from 4.9 mm to 3.9 mm when the L/D ratio increased from 9 to 13.5 for the NACFST columns, whilst for those filled with RA concrete, it decreased from 5.1 mm to 4.3 mm. It can be concluded that the initial indentation increases with increasing tube stiffness

which is dependent on the length of the specimen. Both of the short RACFST and NACFST columns have the same mode of failure with two different impactor shapes, as demonstrated in Fig. 4.16.

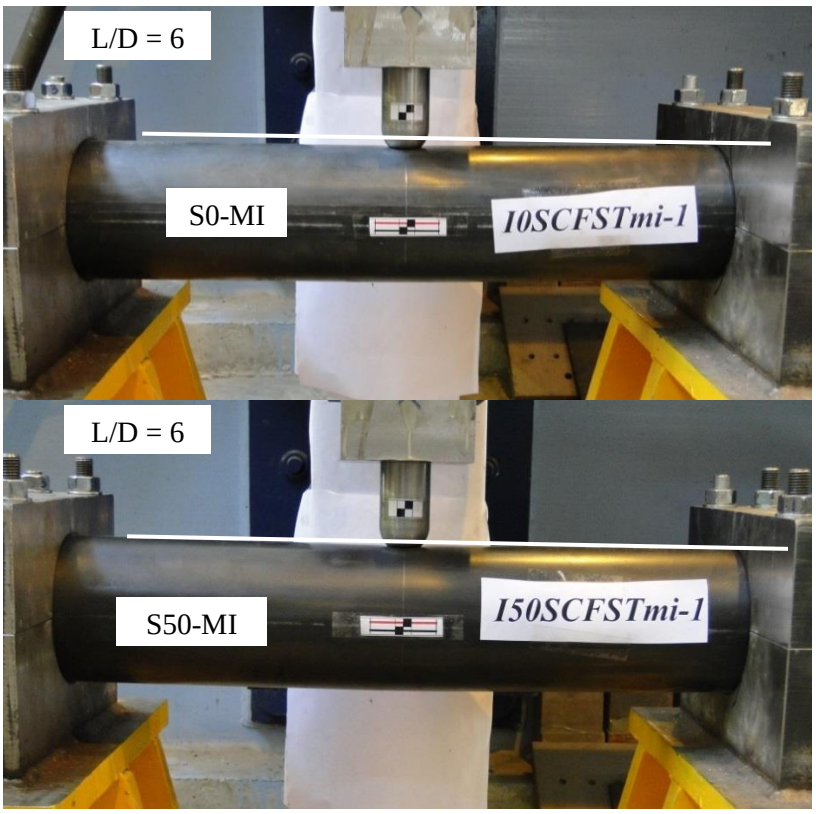

(a) Short tube

Figure 4.15. The deformation mode for NACFST and RACFST columns with different L/D ratio

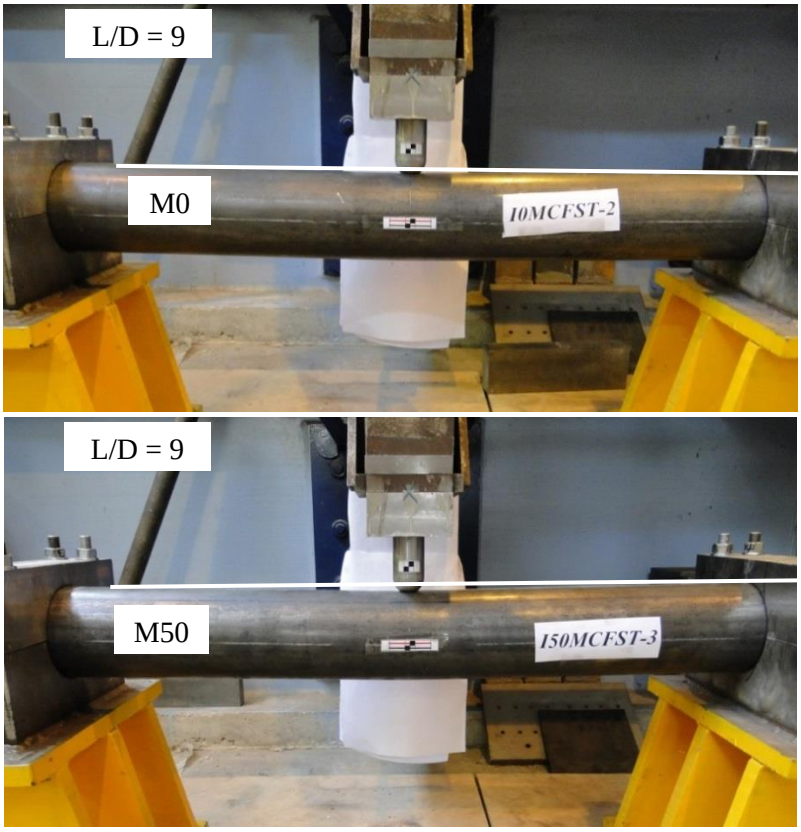

(b) Medium tube

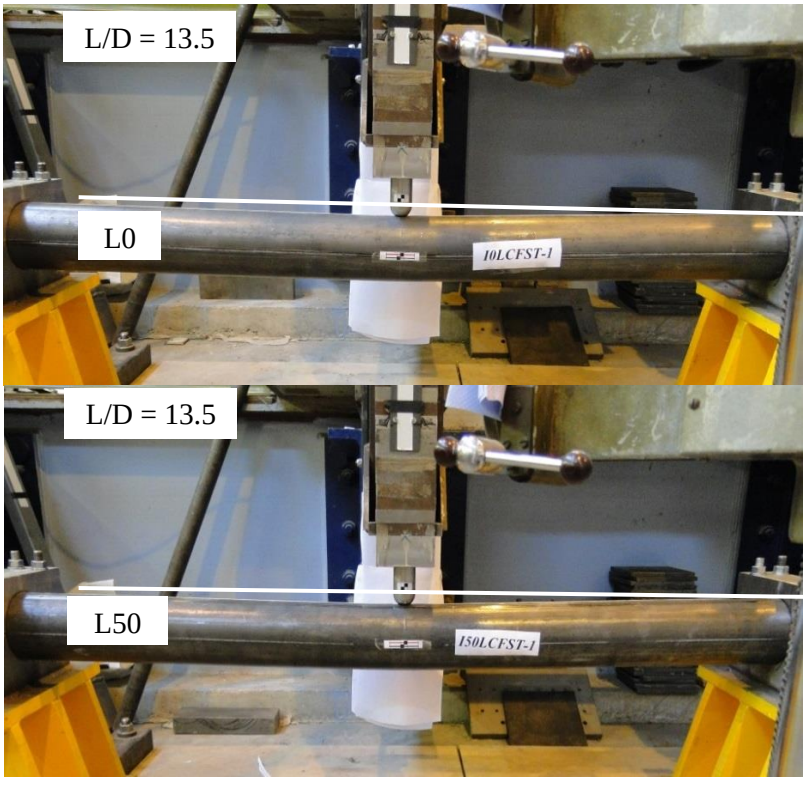

(c) Long tube

Figure 4.15 (continued). The deformation mode for NACFST and RACFST columns with different L/D ratio

Figure 4.16. The deformation mode for NACFST and RACFST columns with (1) flat impactor (40x40) mm and (2) spherical impactor 20 mm diameter

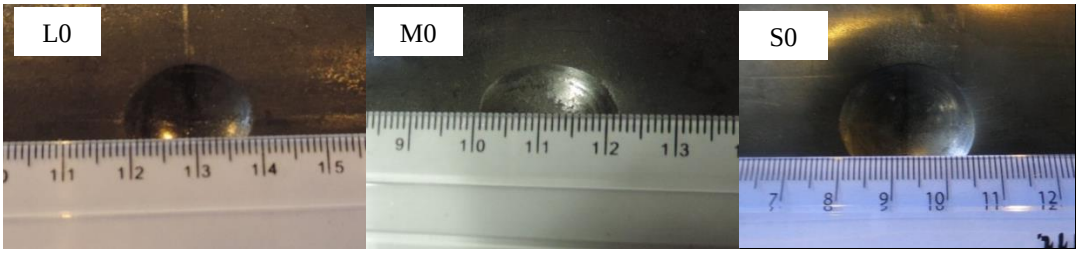

Figure 4.17. The influence of the L/D ratio on the local deformation of the tube

4.2.3 The effect of the impactor configuration on the impact behaviour of the CFST columns

4.2.3.1 Load-displacement relationships

The effect of the impactor shape on the impact behaviour of the CFST columns was examined. The experimental findings for these tests are the impact force, the total displacement, global displacement and the deformation pattern. The impact force and the total and global displacements are discussed here and the deformation shape is to be discussed in the next section. The results show that with increasing size of the impactor, the contact force increased and the total displacement decreased for both types of concrete, as anticipated. This is due to the fact that the big contact area will have a global dominant

response from the CFST column to resist the applied loading at the contact moment rather than the localised one under the impactor. This is clearly reflected by the depth and the diameter of the indentation for the columns hit by impactors with different sizes as discussed later in the next section. Again, the impact event can be divided into three phases, i.e. the initial phase in which the impact force increases steadily, the plateau phase when the lateral displacement increases with a slight increase of the impact force and the final phase which starts when the velocity of the impactor and the CFST column reaches zero and the elastic recovery begins to act. Fig. 4.18 shows that the increase of the diameter of the impactor from 20 mm to 60 mm leads to an increase of the contact force from 220 kN to 286 kN due to a larger contact area, while reducing the total displacement from 16.3 mm to 13 mm. The RACFST specimens give a lower bearing capacity than that of the NACFST specimens with different impactor shape and diameter, which is shown in Fig. 4.19. The load capacity of the RACFST specimen tested with the small impactor (SI) is reduced slightly from 220 kN to 216 kN, whilst those tested with medium impactor (MI) reduced from 267 kN to 259 kN. In contrast, the global displacement increases with increasing the impactor size, as shown in Fig. 4.20. This indicates that the large contact area between the impactor and the tube leads to reducing the energy dissipation due to lowering the local indentation but increasing the energy absorption due to the increased global deformation. The global displacement is increased by 17.2 % when the impactor diameter increased from 20 mm to 60 mm. The maximum force and the global displacement for the specimens tested are summarised in Table 4.1.

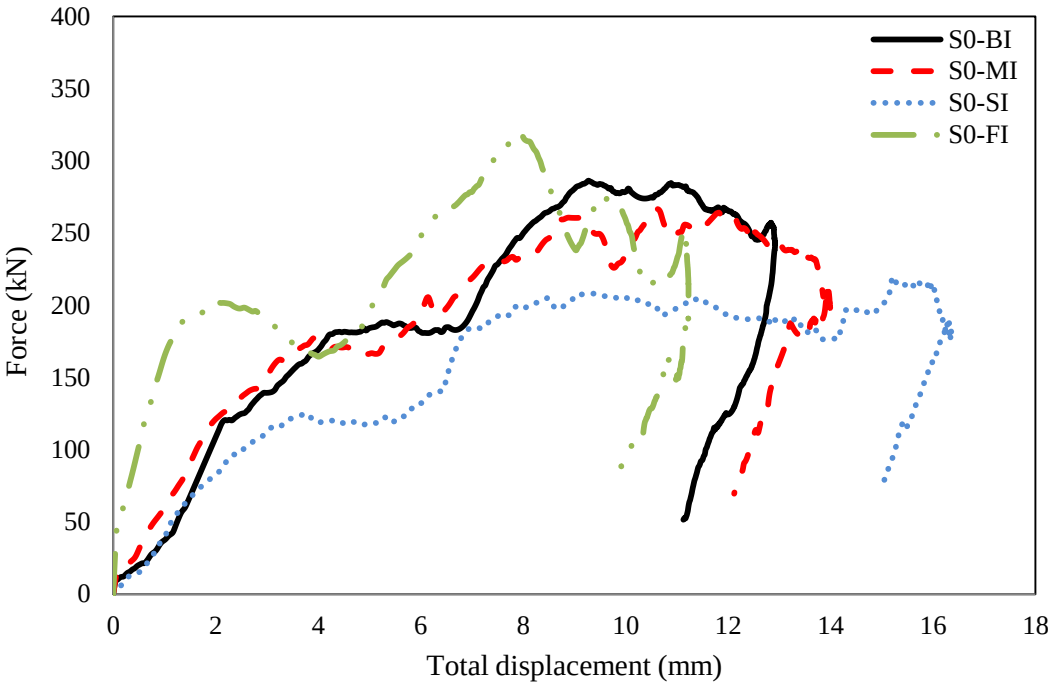

Figure 4.18. The force-total displacement curves for the short NACFST tubes with different impactor configurations

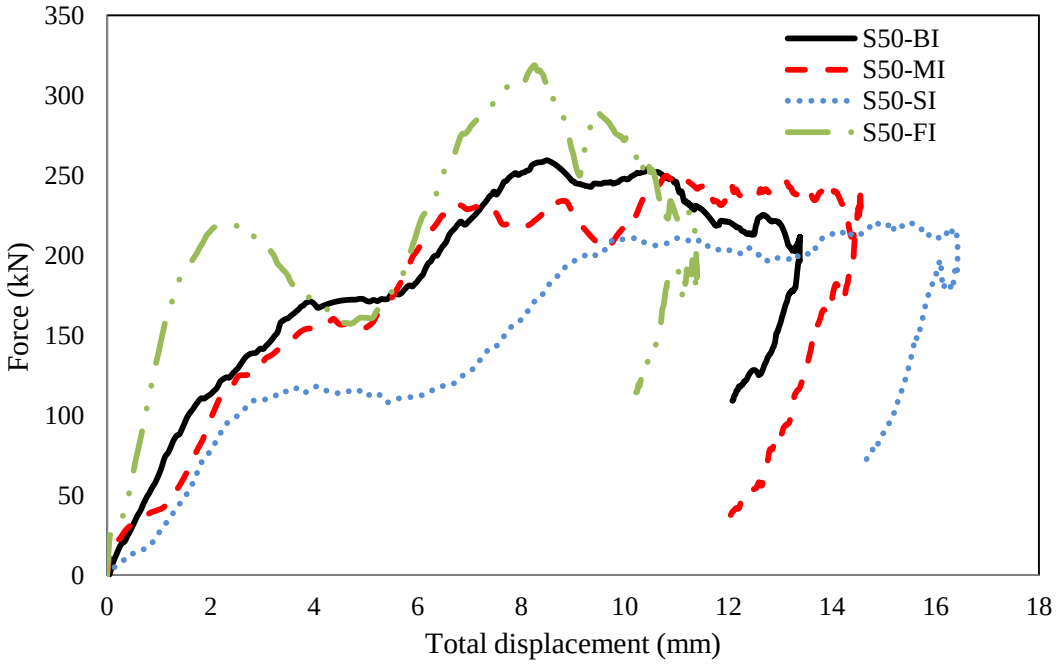

Figure 4.19. The force-total displacement curves for the short RACFST tubes with different impactor configurations

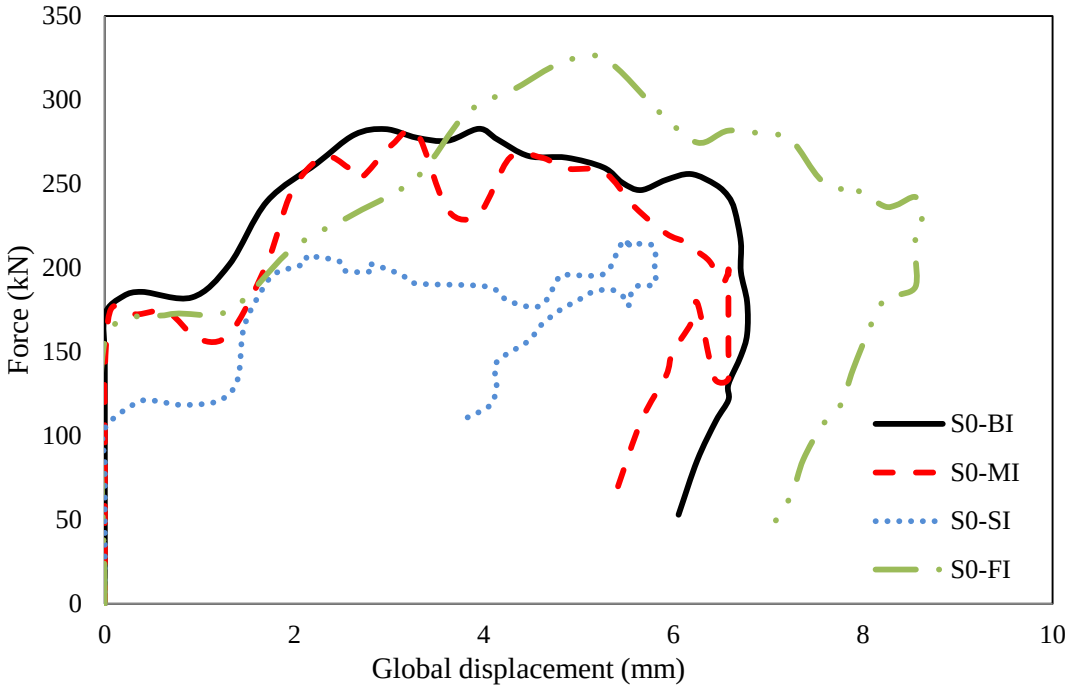

Figure 4.20. The force-global displacement curves for the short NACFST tubes with different impactor configurations

4.2.3.2 Failure modes

For the spherical impactors with different diameters, the diameter of the indentation increases with increasing impactor diameter as expected, whilst the indentation of the flat impactor has the same dimensions and shape as the impactor. Fig. 4.21 shows that the diameter of the indentation for the big impactor (BI) is 29 mm, whilst it is 24 mm and 19 mm for the medium and small impactor, respectively. Fig. 4.20 also demonstrates that both RACFST and NACFST columns have a similar deformation mode, irrespective of the impactor configuration. For the NACFST columns, the indentation depths of the small and medium impactors are 10.2 mm and 6.4 mm respectively, whilst that for the big impactor is 4.9 mm and for the flat impactor is only 2.2 mm. There is a slightly higher indentation depth for the tubes filled with RA concrete regardless of the impactor configuration, as noted in Table 4.1.

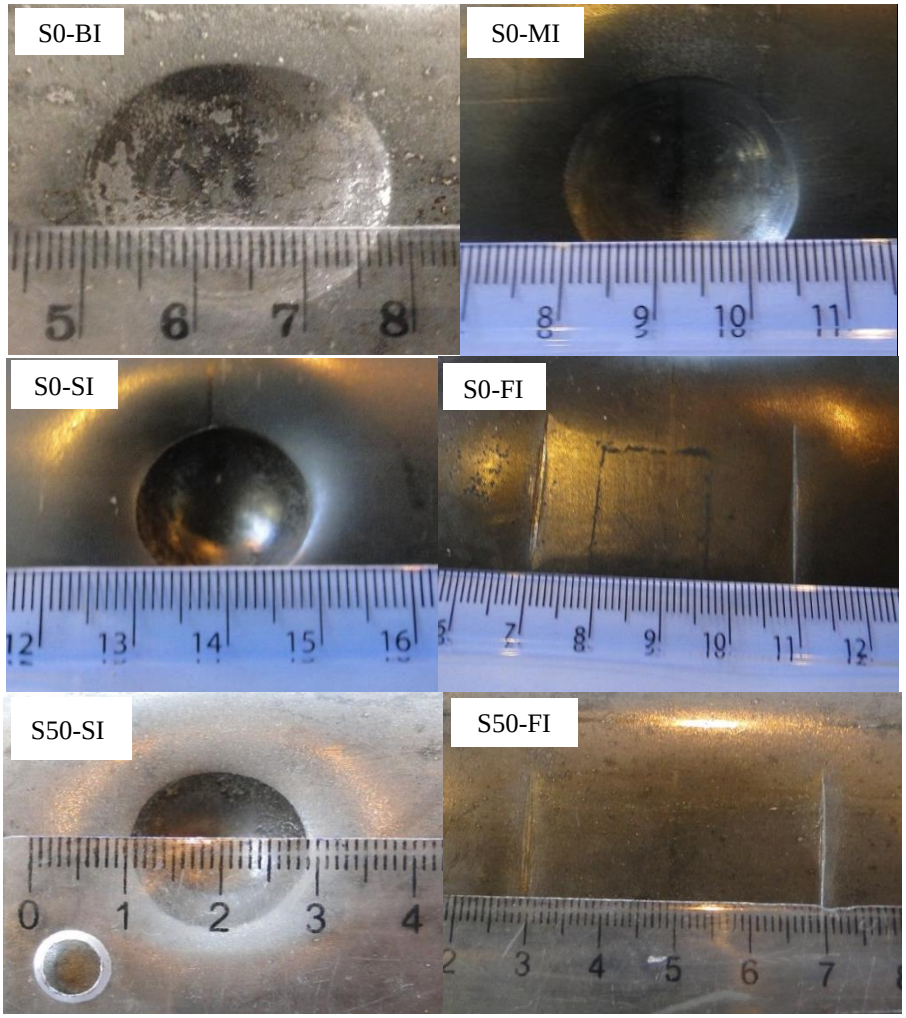

Figure 4.21. The effect of the impactor shape on the failure modes of specimens

4.2.4 The influence of the CFRP reinforcement on the impact response of the CFST columns

4.2.4.1 Load-displacement curves

The strengthened NACFST and RACFST specimens with CFRP show a similar impact response and the contact forces for the strengthened specimens are less than those of the unstrengthened ones during the first stage of the test, as can be observed in Figs 4.22- 4.27. In general, the impact response of the CFST columns strengthened with one CFRP layer is similar to those without CFRP strengthening regardless of the L/D ratio. In general, as mentioned in the previous section, the same three stages can be observed within the impact events for these figures. However, the force degrades to almost zero for the CFST column

with L/D ratio of 13.5 during the second stage of the impact event. This will be discussed in Section 4.2.8 to avoid repetition. These figures demonstrate that the strengthened columns show slightly higher initial stiffness than the unstrengthened columns, irrespective the type of concrete filling. In terms of the contact force, the use of one layer of CFRP causes a reduction of the contact force. This layer of the CFRP minimized the contact interaction and reduced the frequency of the columns tested, which in turn caused the reduction of the maximum force in the first cycle. Following this, it can be seen that the maximum force was reduced for the long NACFST specimens from about 160 kN down to as low as 10 kN (Fig. 4.22). This is attributed to the conjoined motion between the impacting mass and the CFST column. However, the contact forces associated with the CFRP strengthened tubes were less than those of the unstrengthened specimens because of that the contact stiffness of the CFRP through its thickness is much smaller than that of the steel tube or the concrete core. Initially, the impactor hits the CFRP layer which has a lower contact stiffness. Thus, the contact force is relatively low until the impactor penetrates the CFRP layer and hits the steel tube. Once the impactor is in contact with the steel tube, contact stiffness increases due to high stiffness of the steel tube as well as the high stiffness of the composite section of the steel tube and the concrete core. Here, the modulus of elasticity of CFRP through the thickness is only 10 GPa, whilst it is 200 GPa for the steel tube. The results from other researchers also showed that the CFRP layer reduces the impact force due to the low contact stiffness of the CFRP in comparison with the steel tube and the concrete (Wang et el., 2015; Chen et al., 2015 and Alam et al., 2016). The contact force for the long strengthened NACFST column was 146.3 kN, while it was 166.2 kN for the corresponding unstrengthened column. The strengthened RACFST specimens exhibited similar behaviour to those with normal aggregate as shown in Figs 4.23, 4.25 and 4.27. The corresponding contact forces were reduced by 3.4 % and 1.1 % for the long and medium RACFST columns, respectively.

The total displacement was slightly affected by the strengthening, which was decreased for most columns with different L/D ratios and recycled aggregate replacement. The reduction of the total displacement was 4.3 %, 4.4 % and 2.9 % for long, medium and short NACFST columns, respectively. The RACFST columns showed higher reduction in the total displacement. For the columns with L/D of 6, the total displacement decreased by 7.5 %, while it reduced by 7.3 % and 6.7 % for the columns with L/D ratio of 9 and 13.5, respectively. However, the local indentation depth for the strengthened columns with CFRP was higher than those without a CFRP jacket with the same spherical impactor diameter. This is because the higher stiffness induces the column to exhibit a higher global resistance and increase the local energy absorption. The indentation depth for the strengthened long NACFST column increased by 36 %, and it increased by 14.3 % and 11 % for the strengthened medium and short NACFST columns, respectively. For the strengthened RACFST column with L/D ratio of 6, the indentation depth increased from 6.6 mm to 7.1 mm, whilst it increased from 4.3 mm to 5.1 mm for the strengthened RACFST with a 13.5 L/D ratio.

The global displacement evaluated from the HSC for the strengthened NACFST and RACFST indicates that the CFRP has a reasonable effect on the global displacement of the tube. Fig. 4.28 reveals that one layer of CFRP reduces the global displacement by about 10.4 % for the long RACFST column. Figs. 4.29 and 4.30 show that the global displacement decreased from 14.5 mm to 13.2 and from 6.6 mm to 6.3 mm for the medium NACFST and short RACFST columns, respectively. It can be concluded that the CFRP reinforcement has a stronger influence for the columns with high L/D ratios.

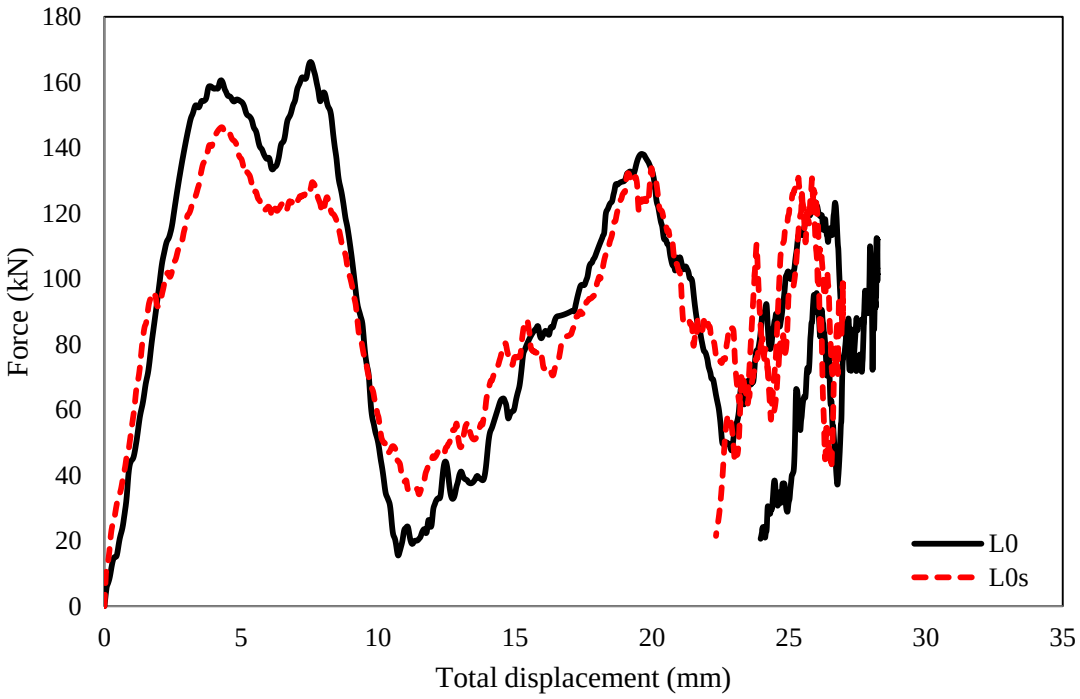

Figure 4.22. The force-total displacement curves for the strengthened and unstrengthened long NACFST columns

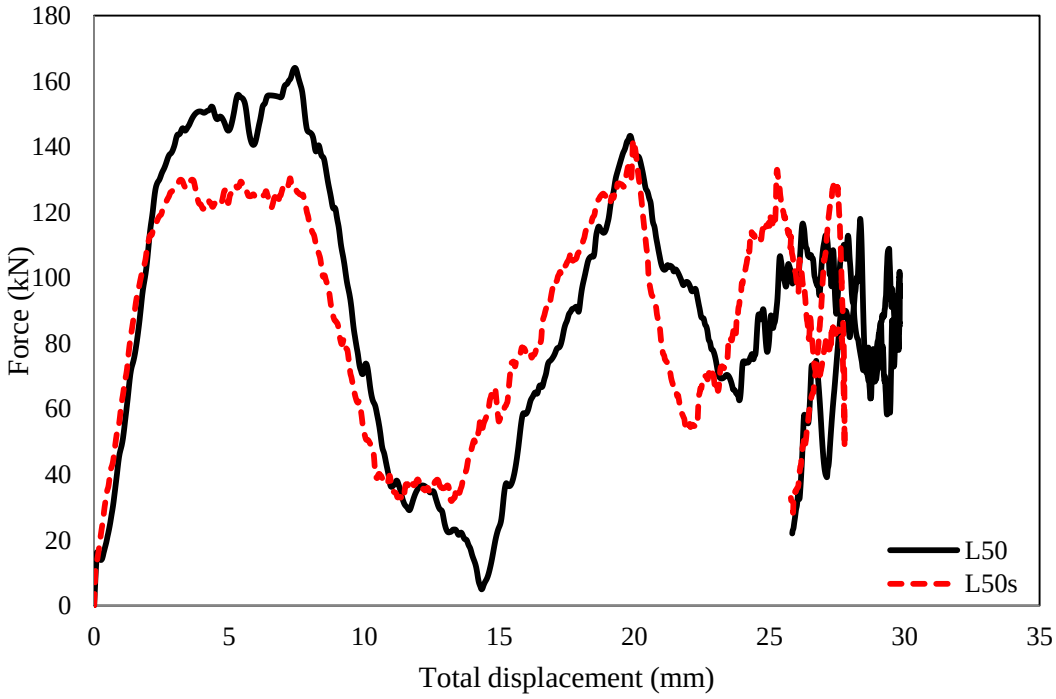

Figure 4.23. The force-total displacement curves for the strengthened and unstrengthened long RACFST columns

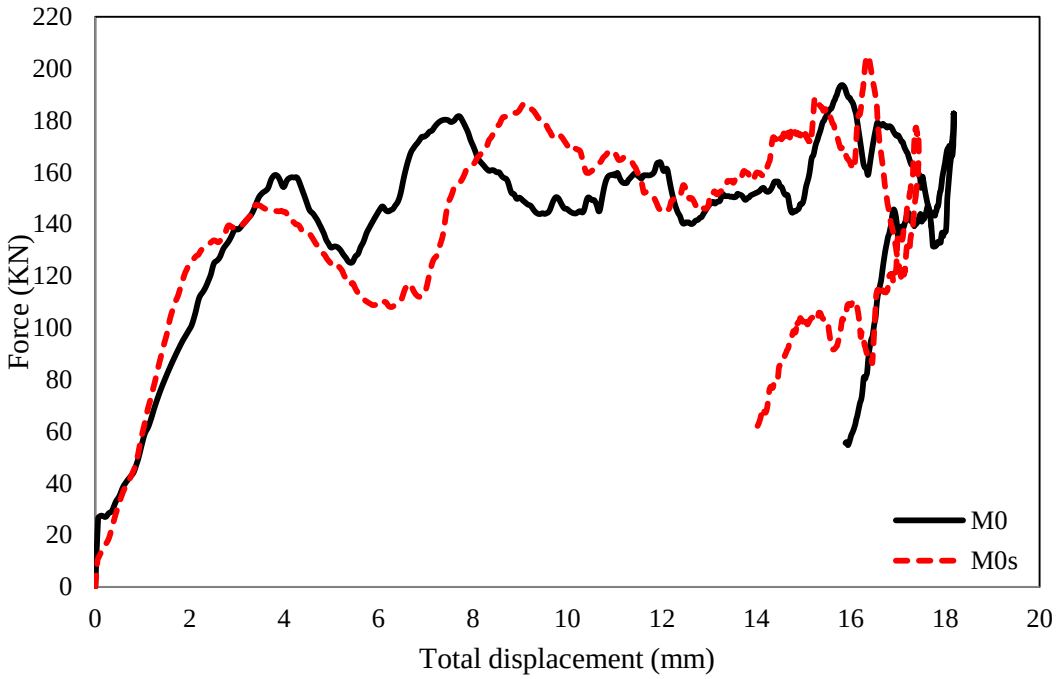

Figure 4.24. The force-total displacement curves for the strengthened and unstrengthened medium NACFST columns

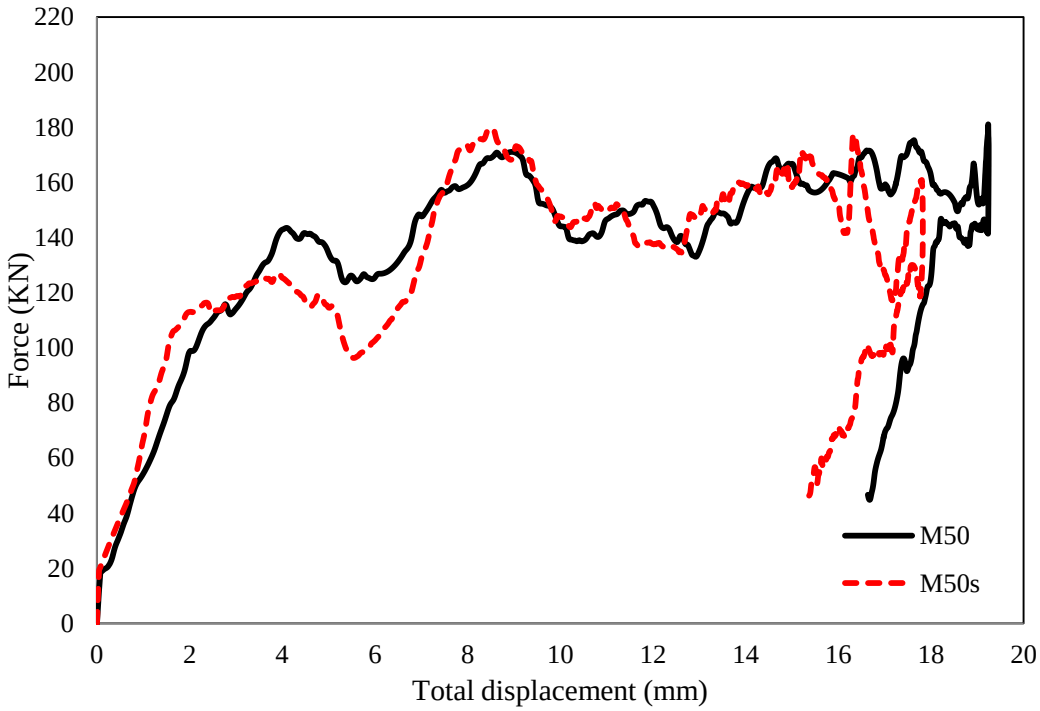

Figure 4.25. The force-total displacement curves for the strengthened and unstrengthened medium RACFST columns

Figure 4.26. The force-total displacement curves for the strengthened and unstrengthened short NACFST columns

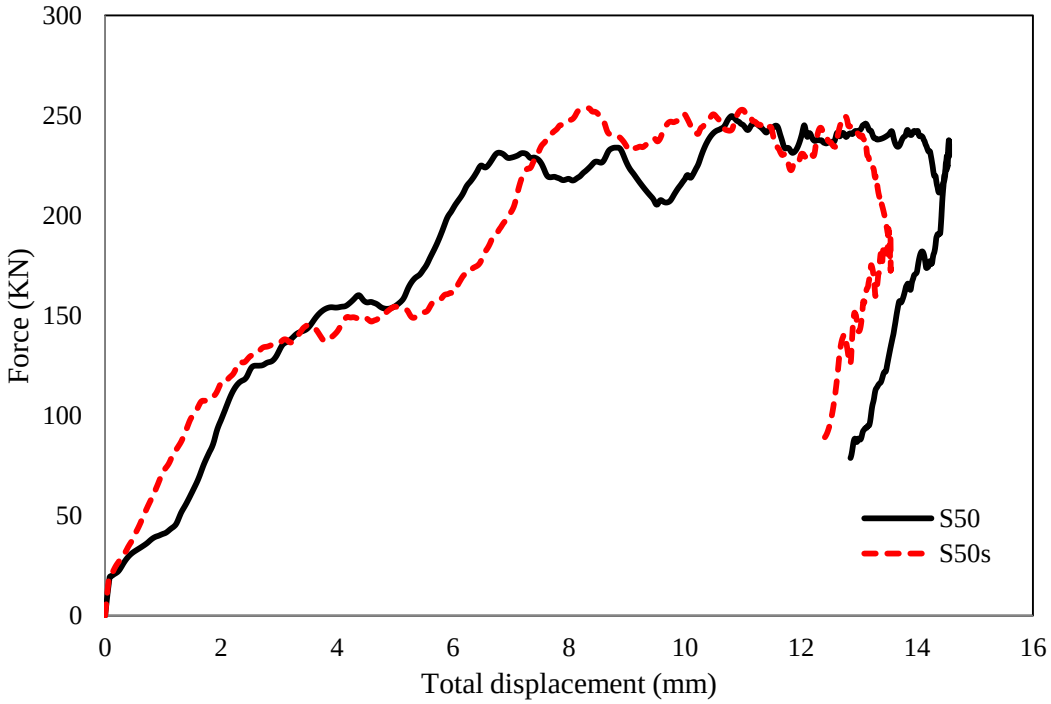

Figure 4.27. The force-total displacement curves for the strengthened and unstrengthened short RACFST columns

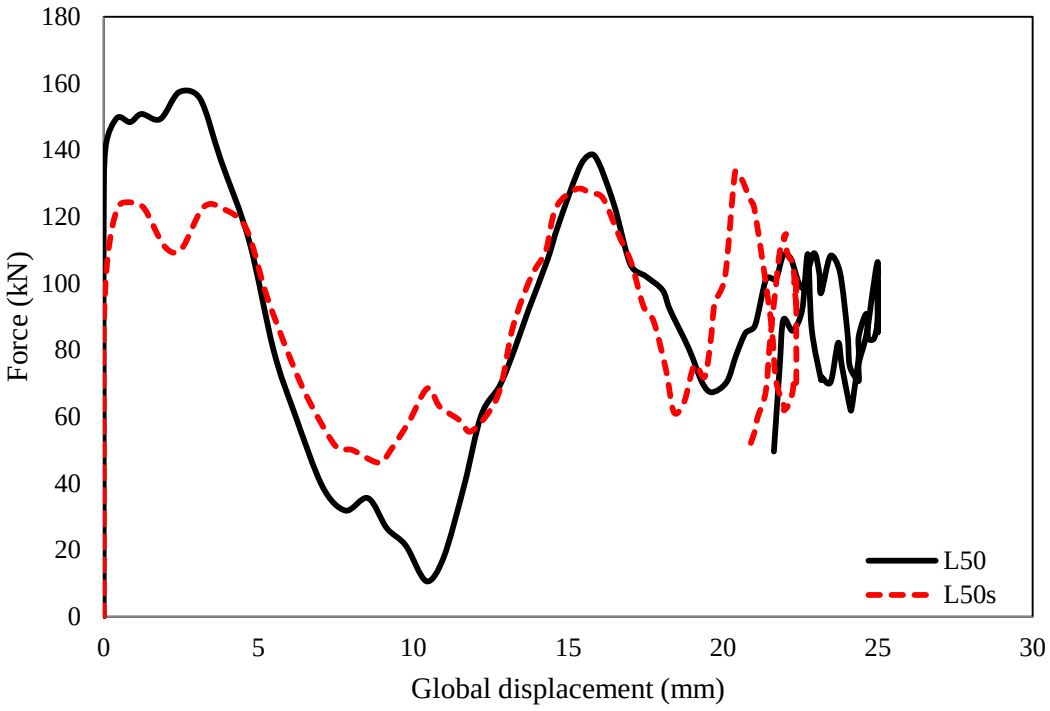

Figure 4.28. The force-global displacement curves for the strengthened and unstrengthened long RACFST columns

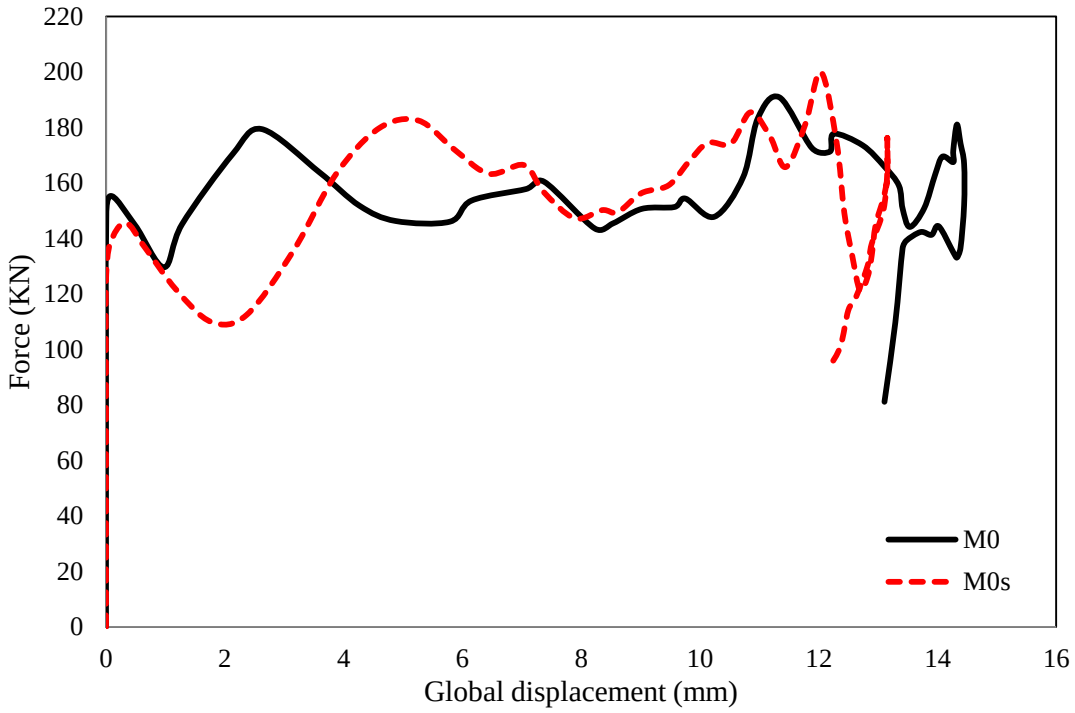

Figure 4.29. The force-global displacement curves for the strengthened and unstrengthened medium NACFST columns

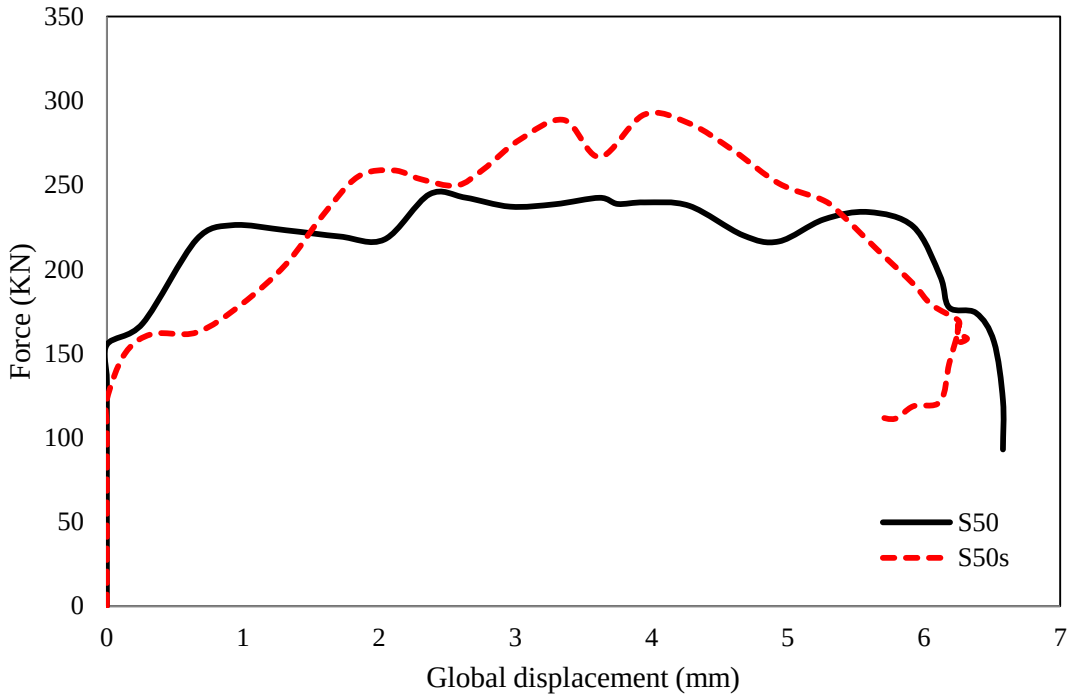

Figure 4.30. The force-global displacement curves for the strengthened and unstrengthened short RACFST columns

4.2.4.2 Deformation mode of the indentation

For the specimens strengthened with CFRP, the failure was initiated with a crack at the bottom of the section in the mid-span and around the centre of the indentation. The contact area of the CFRP layer with the impactor was totally smashed. However, there was no obvious separation observed between the CFRP layer and the steel tube, as shown in Fig. 4.31. The effect of the sample length on the damage of CFRP can be clearly seen, with the crack width increased from 1 mm for the short NACFST column to 5 mm for the long one, whilst the crack width for the medium NACFST was about 2 mm. Table 4.1 reveals that with one layer of CFRP reinforcement the indentation depth increased slightly for a given tube length, due to enhancement of the stiffness of the tube which gives a higher resistance to the global deflection.

Fig. 4.32 manifests that the strengthened RACFST columns with different L/D ratios exhibit the similar deformation shape to that of NACFST columns. The crack width increased from

about 1 mm to 5 mm when the L/D ratio increased from 6 to 13.5. However, these cracks did not affect the bond between the CFRP layer and the steel tube, as no de-bonding was noticed during the test.

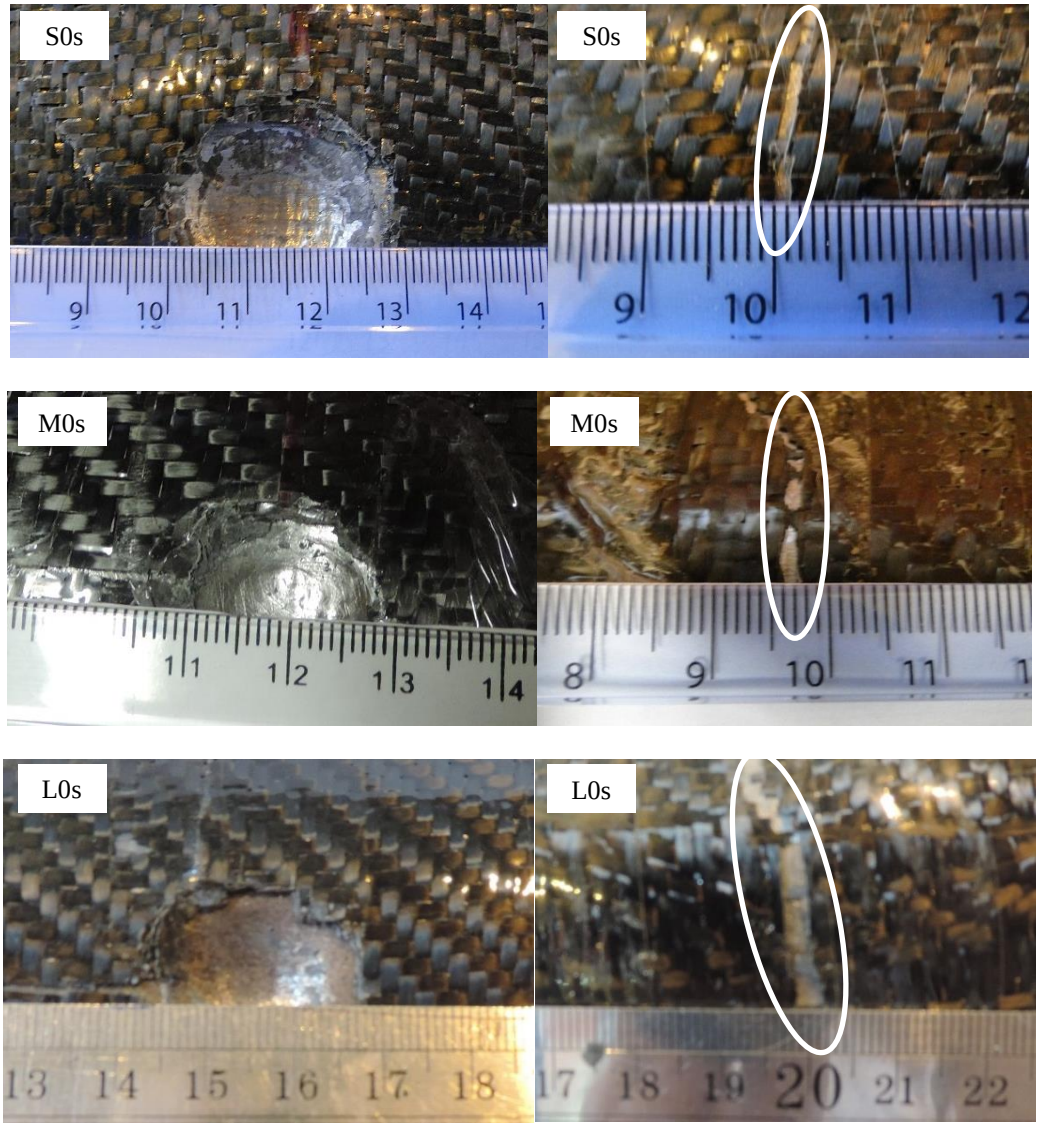

Figure 4.31. The mode of failure of the NACFST columns strengthened with FRP with different L/D ratio

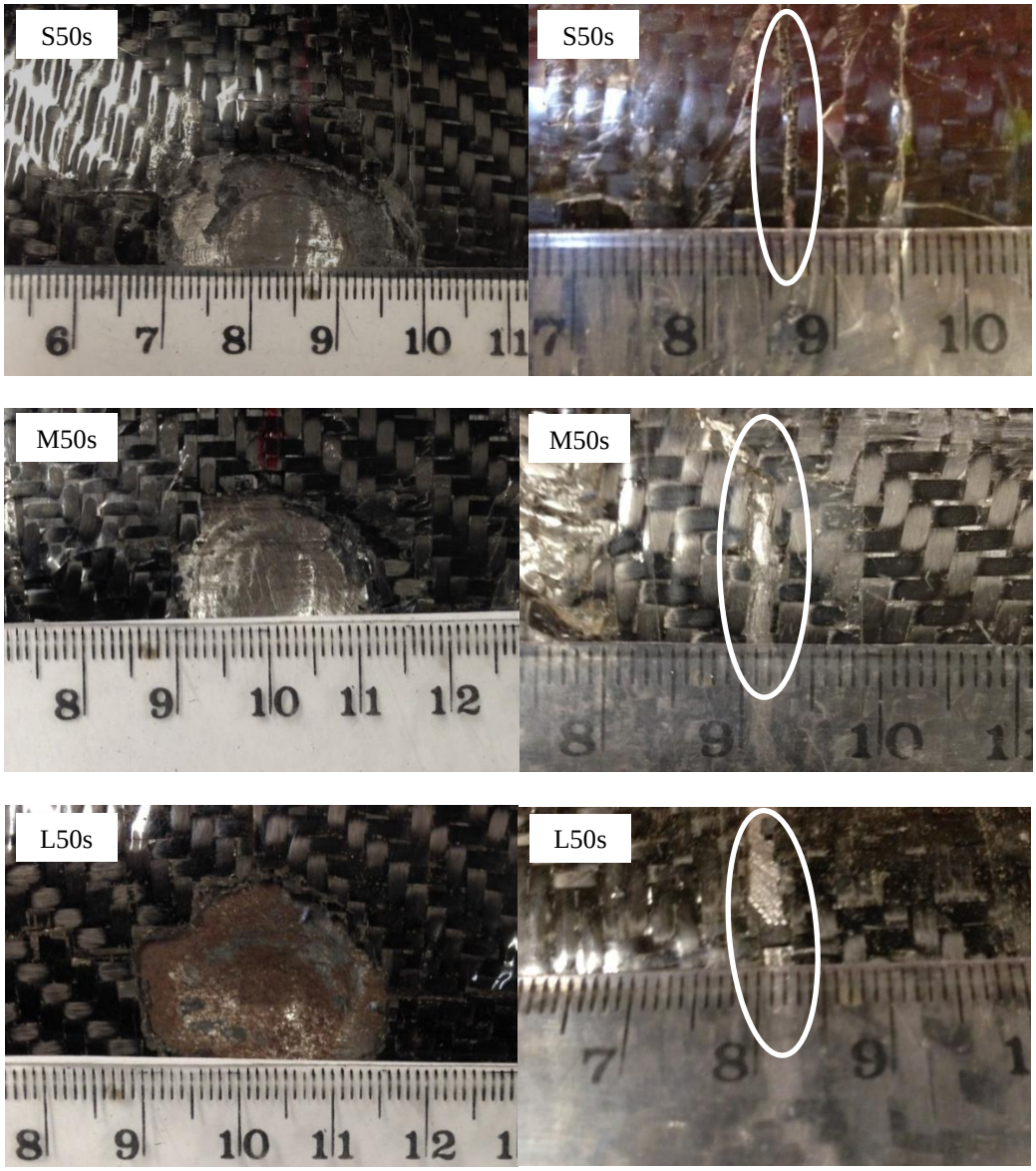

Figure 4.32. The mode of failure of the RACFST columns strengthened with FRP with different L/D ratio

4.2.5 The effect of the D/t ratio on the behaviour of the CFST columns

The D/t ratio has a significant effect on the impact behaviour of the NACFST and RACFST columns, as indicated in Figs. 4.33 and 4.34. These figures also show the three stages of the impact event and present the impact force and total displacement traces. Regardless of the D/t ratio, when the impactor hits the steel tube with an impact velocity, the impact force raises from zero to a certain level within the initial stage of the period of impact. Then, during the plateau stage the impact force keeps increasing slightly with increasing lateral displacement as well. Once the impact velocity reaches zero in the third stage, the CFST column starts to recover due to the elastic energy and the force begins to decrease towards zero when the impactor bounces from the tube. These figures reveal that with a D/t ratio of 38, both of the NACFST and RACFST columns exhibited lower stiffness than those with a D/t ratio of 32 when they were impacted using the same spherical impactor with a diameter of 20 mm (SI). This is due to less confinement between the concrete core and steel tube as it increases with lower D/t ratio. The confining pressure for the confined concrete can be calculated from equations 4.1 to 4.3 which were proposed by Mander et al. (1988). It can be seen that the confining pressure is related to D/t ratio. With a increasing D/t ratio, the confining pressure decreases, which agrees with the experimental results. When the D/t ratio increased from 32 to 38, the total displacement increased by 20.2 % and by 27.3 % for the NACFST and RACFST columns, respectively. Furthermore, the global displacement decreased by 5.7 % for the NACFST columns and 18 % for RACFST columns with the same reduction of D/t ratio, as shown in Fig. 4.34.

$$f_l = \frac{2\sigma_\theta t}{D} \tag{4.1}$$

where f_l is the confining stresses and the value of σ_θ is equal to $0.1f_y$. f_y is the yield strength of the steel tube

$$f_l/f_y = 0.043646 - 0.000832(D/t) \qquad for\ 21.7 \le D/t \le 47 \tag{4.2}$$

$$f_l/f_y = 0.006241 - 0.0000357(D/t) \qquad for\ 47 \leq D/t \leq 150 \tag{4.3}$$

A relationship between the indentation depth and diameter with D/t ratio is proposed in this study. The proposed model can be written as:

$$R_c = \sqrt{((2 * R_i * d) - d^2)} * \left(0.082 * \frac{D}{t} - 0.9\right) \tag{4.4}$$

where R_i is the radius of the impactor and R_i and d are the radius and the depth of the indentation, respectively.

The comparison between the predicted and experimental results is tabulated in Table 4.1. It can be seen that the diameter of the indentation is very well predicted for most of the CFST columns with different parameters such as the L/D ratio and the concrete type.

The low stiffness of the columns with a D/t ratio of 38 caused a failure by local indentation with steel tube cracking. S0 and S50 are the NACFST and RACFST columns, respectively, with a D/t ratio of 38, whilst the S0-SI and S50-SI are the NACFST and RACFST columns with a D/t ratio of 32. It can be seen from Table 4.1 that the indentation depth was influenced by the stiffness reduction and it increased from 10.2 mm to 12.7 mm for the NACFST columns, whilst increasing from 10.4 mm to 12.8 mm for the RACFST columns when the D/t ratio increased from 32 to 38. However, the shape and diameter of the indentation were not affected by the D/t ratio alteration for both columns with 0 % and 50 % RA replacement, as shown in Fig. 4.35.

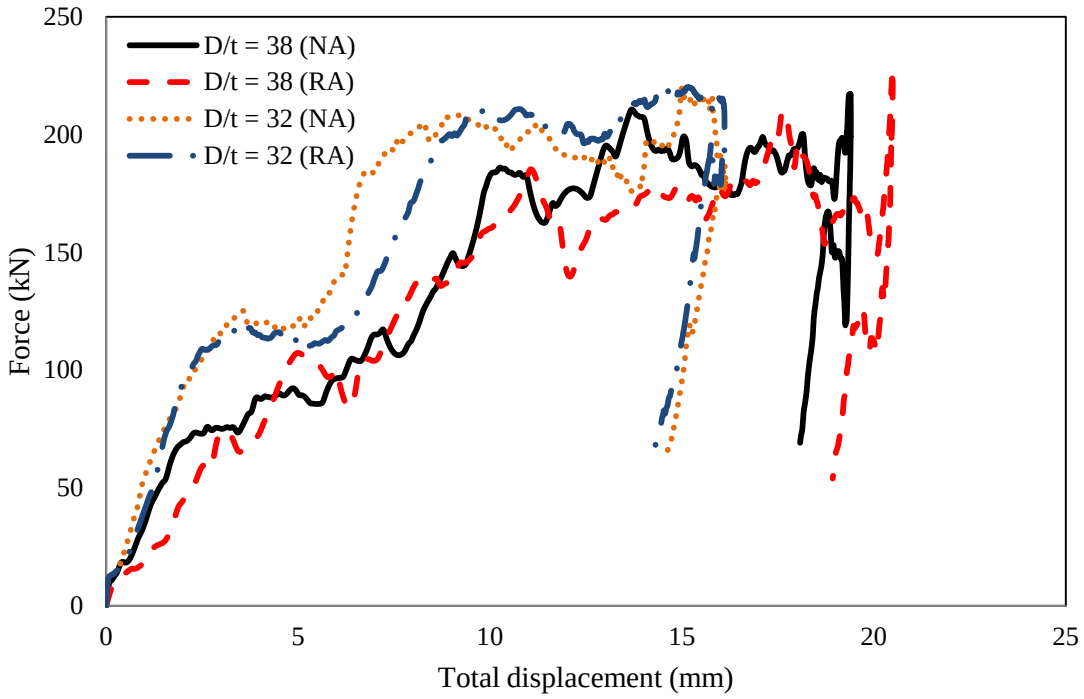

Figure 4.33. The force-total displacement curves for the short NACFST and RACFST columns with different D/t ratio

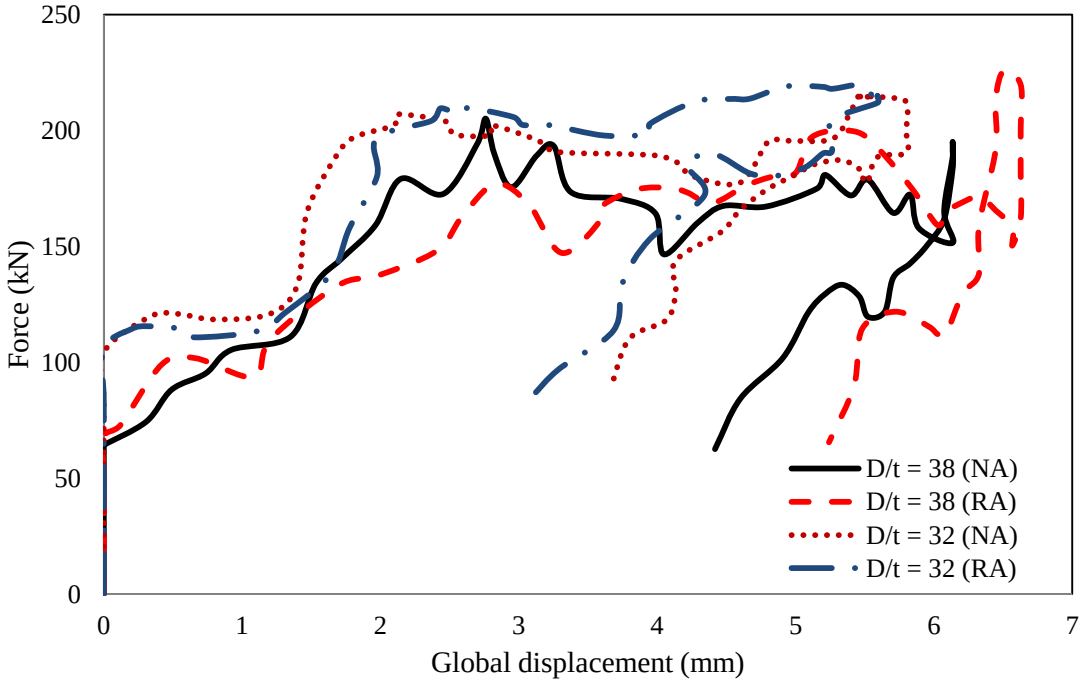

Figure 4.34. The force-global displacement curves for the short NACFST and RACFST columns with different D/t ratio

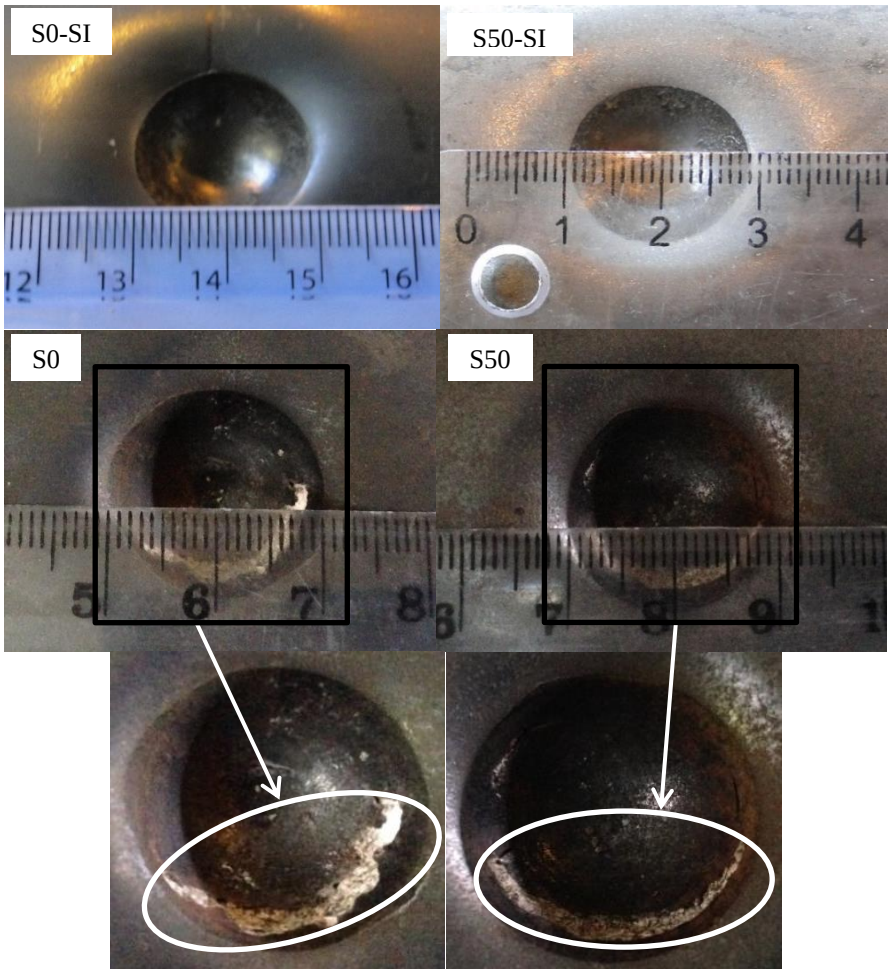

Figure 4.35. The effect of the impactor shape on the failure modes of specimens

4.2.6 The confinement effect on the failure mode of the concrete

The concrete core inside the steel tube was observed by removing the steel tube. The CFST columns were fixed on a bench using timber beams to avoid any movement during cutting of the steel tube. To avoid damaging the CFST columns, the tube was cut laterally into two halves as shown in Fig. 4.36. Once the cutting was completed, the top skin of the steel tube was removed and some images were taken of the indentation. Then, the concrete core was covered again by the top skin to hold the concrete core and the tube was rotated carefully to remove the bottom skin of the steel tube and then some images were taken of the cracks in the concrete core. Although concrete is a brittle material, the confinement effect allows the concrete to behave like a ductile material and the deformation resistance of the concrete core is considerably enhanced by the steel tube. Here, Fig. 4.37 shows the indentation diameter and shape of the concrete core. For all columns, the cracks were initiated at the mid span of the concrete core opposite to the indentation side. With increasing the tube length, the crack width and the number of cracks were also increased with a larger deflection due to the degradation of the lateral resistance. Fig. 4.38 shows the impactor configuration effect on the failure mode of the concrete core, i.e. with increasing the diameter of the spherical impactor the number and the width of cracks increased at the bottom surface. The flat impactor was noticed to cause more cracks due to the big contact area between the impactor and the column. The impact face of the concrete failed with formation of a spherical and rectangular cap for the columns hit by the corresponding impactors, respectively.

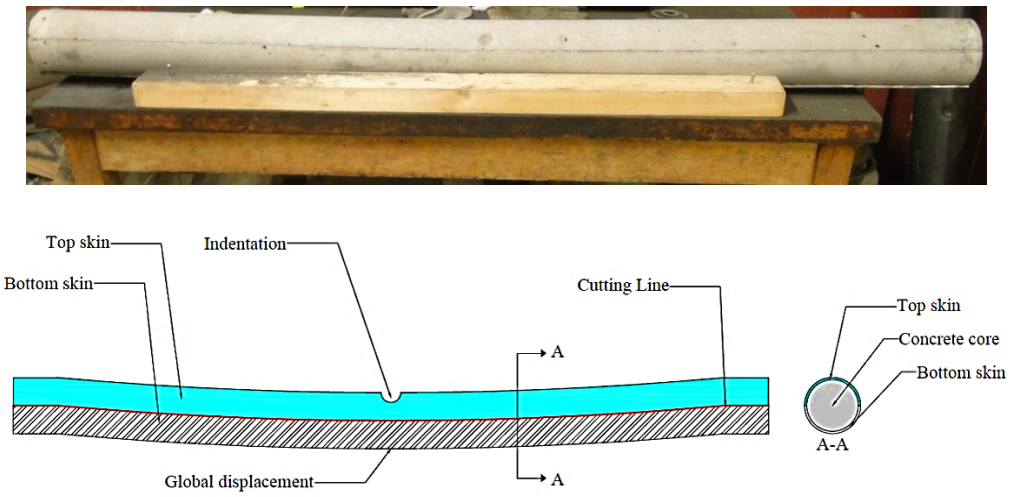

Figure 4.36. Concrete core after the steel tube is removed form a CFST column

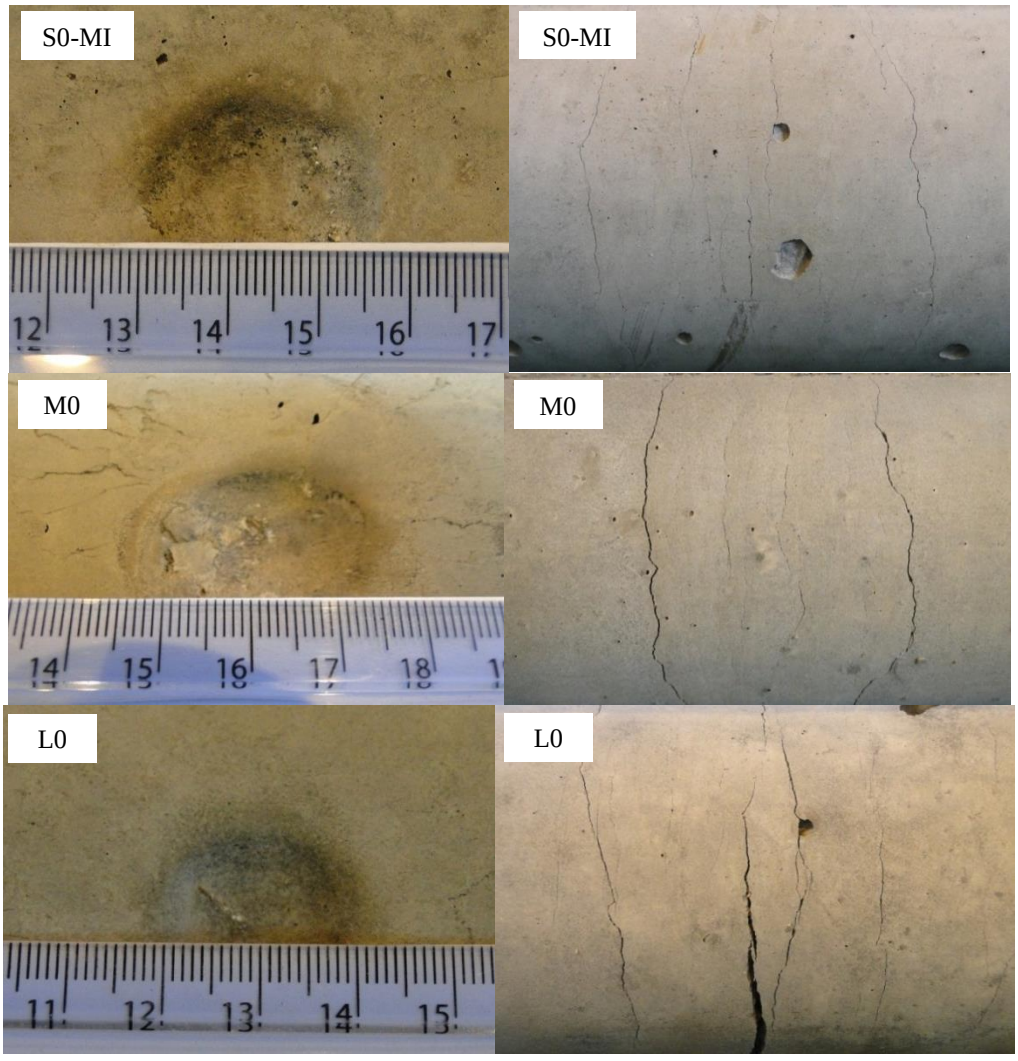

Figure 4.37. The effect of the specimen length on the failure mode of the concrete core of the CFST specimens

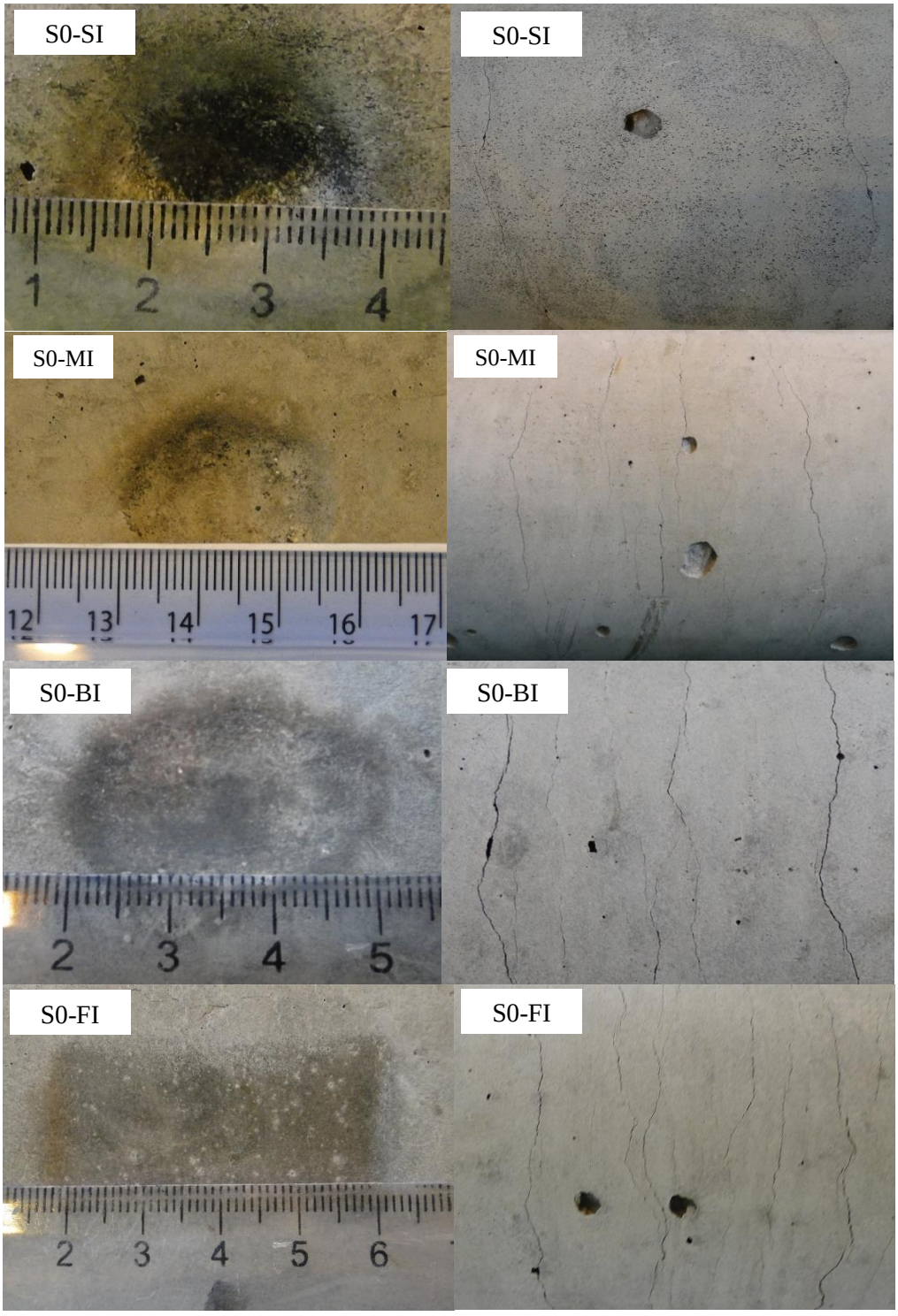

Figure 4.38. The effect of the impactor configuration on the failure mode of the concrete core of the CFST specimens

4.2.7 Energy absorption

The area beneath the total displacement-force curve was calculated to obtain the total and absorbed energy, as can been seen in Fig. 4.39. The results are also tabulated in Table 4.1. Figs. 4.40 to 4.43 are presented to show the effect of the CFST strengthening on the energy absorption of the CFST columns under the lateral impact loading, which shows the complete set of data for the NACFST and RACFST columns with and without CFST strengthening with different L/D ratios. Fig. 4.40 and Fig. 4.41 show the energy absorption for the CFST columns based on the total displacement, whilst Fig. 4.42 and Fig. 4.43 show the energy absorption based on the global displacement. In general, both the concrete core and the steel tube absorb the impact energy but with different proportions based on the stiffness and strength of each one of them. The validated numerical models for the CFST columns were used to calculate this proportion, which will be presented and discussed in Chapter 5. According to the test results, the total absorption energy was highly affected by the CFRP. The total energy absorption decreased from 2340 J to 2247 J for the short tubes without and with CFRP, whilst the reduction for the medium and long tubes were 6 % and 8 %, respectively. This is due to the increased specimen stiffness, as a result of the additional confinement of one layer of CFRP. The effect of the D/t ratio on the energy absorption is clearly observed. The total energy absorbed by the short NACFST specimen with a D/t of 38 is 6.5 % higher than that with a D/t ratio of 32, while the RACFST column with a D/t ratio of 32 absorbed 7.9 % less energy than that with a D/t ratio of 38. In general, the absorbed energy for the specimens filled with recycled aggregate concrete was slightly higher than those filled with normal aggregate concrete. The energy absorbed by the long tube with RA was 8.5 % higher than those with NA. It can be seen from Figs 4.42 and 4.43 that the absorbed energy calculated based on the global displacement is less than the one calculated based on the total energy for all CFST columns. This is because the global displacement is measured from the bottom of the CFST column neglecting the indentation of the CFST column. However, it is difficult to say that the difference between the two types of absorbed energies, i.e. the total and global, as the absorbed energy by the indentation is also

associated with the global movement. The difference between the two types of energies reduced with increasing the L/D ratio due to the reduction of the indentation depth of the CFST which resulted from the stiffness degradation of the columns with increasing the span length of the columns. The difference reduced from 40 % to 16 % and from 39 % to 22 % when the L/D ratio increased from 6 to 13.5 for NACFST and RACFST columns, respectively.

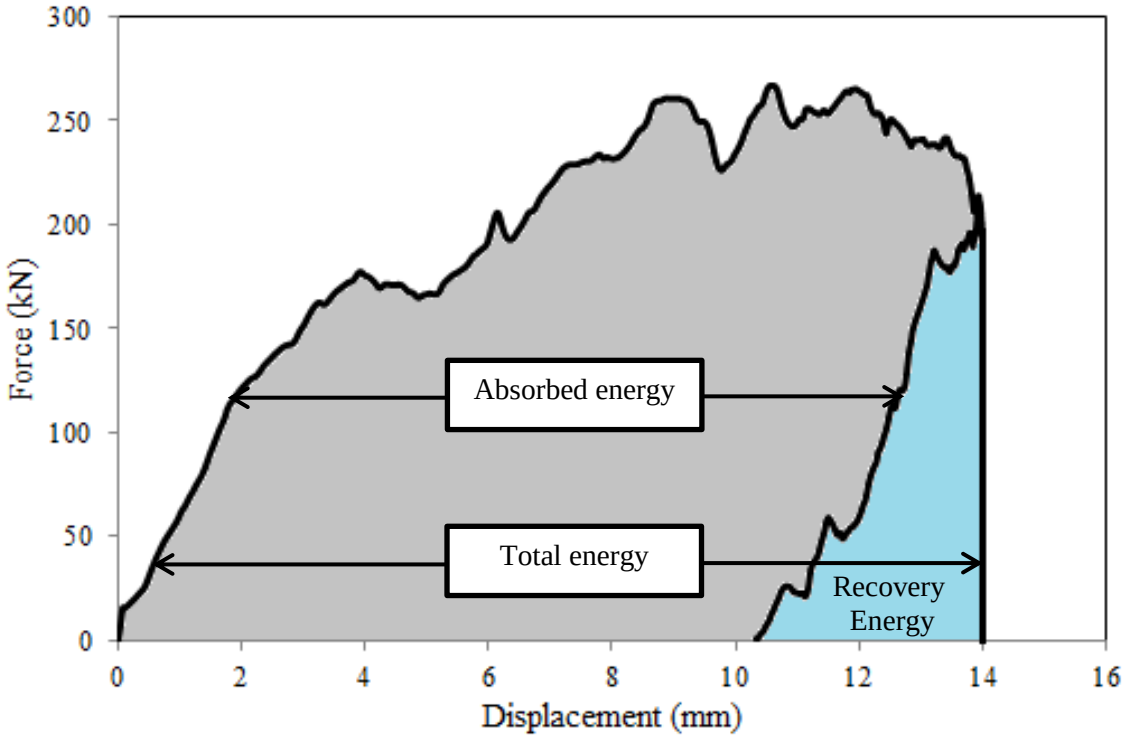

Figure 4.39. The total and absorbed energy calculation for the short NACFST column

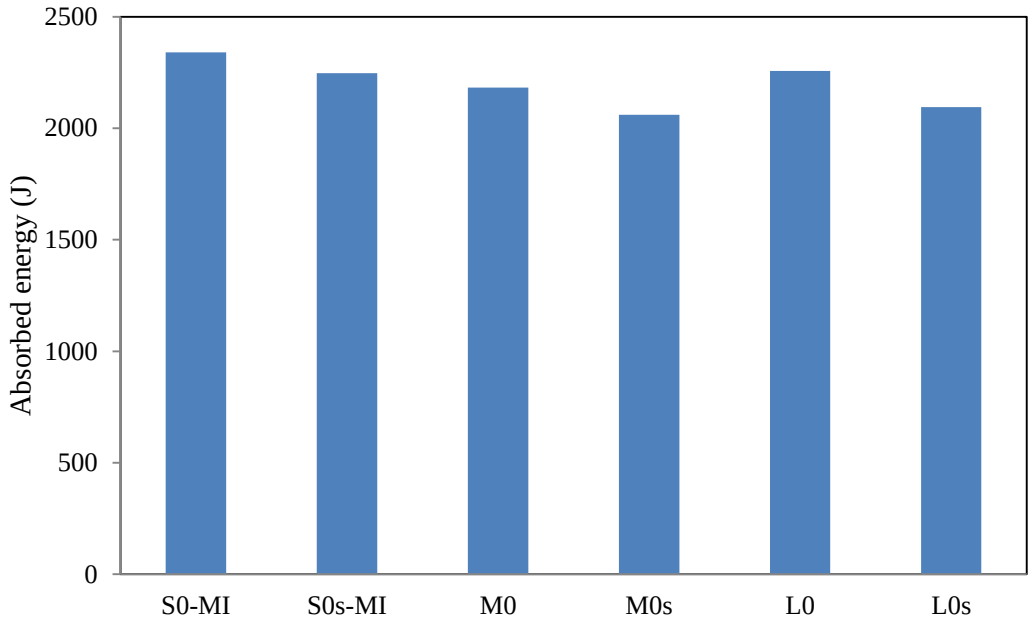

Figure 4.40. The effect of the CFRP on the energy absorption of the NACFST columns

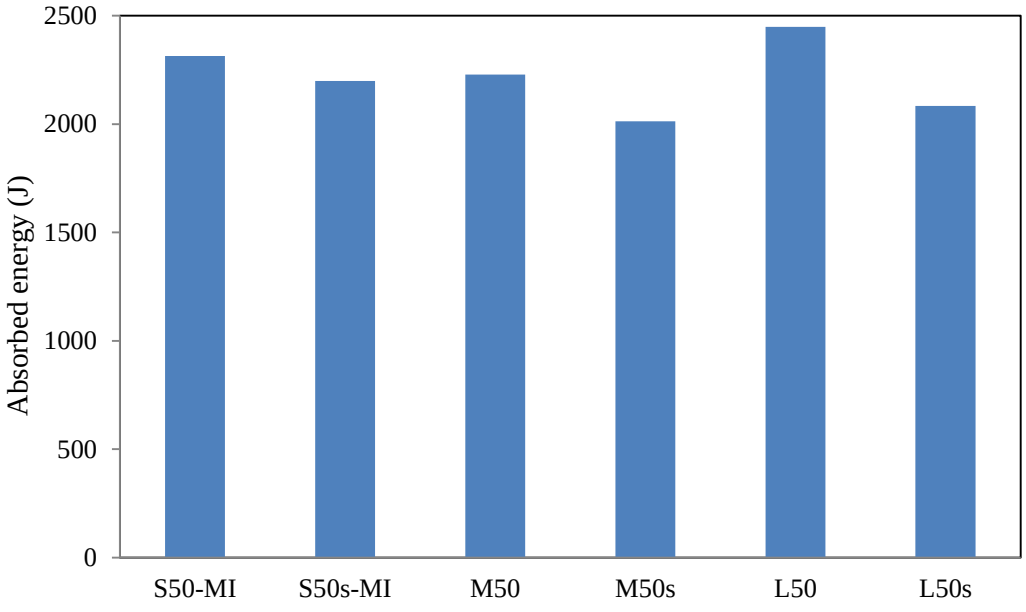

Figure 4.41. The effect of the CFRP on the energy absorption of the RACFST columns

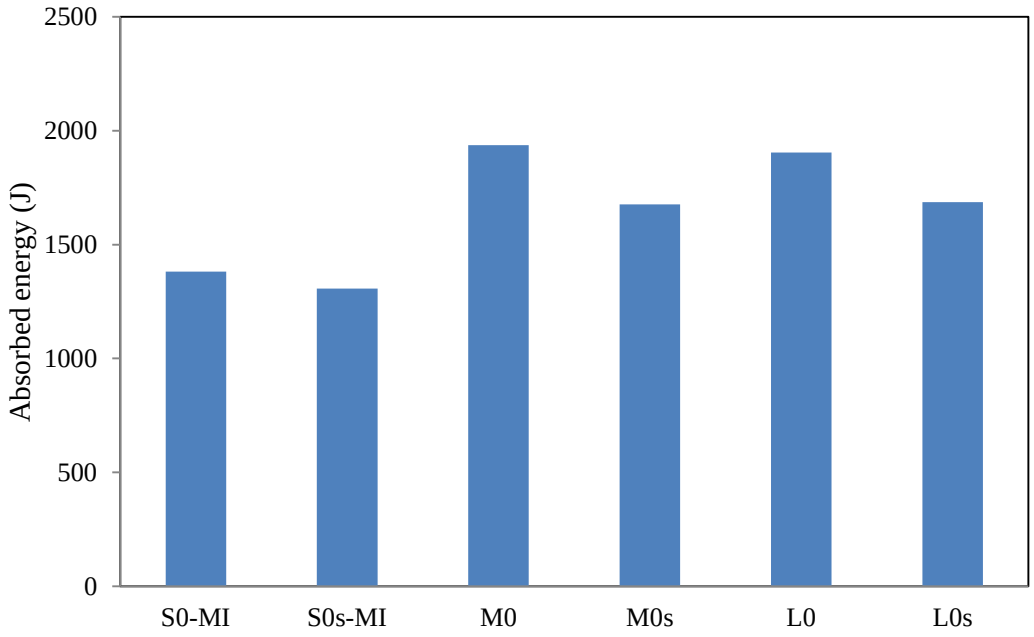

Figure 4.42. The effect of the CFRP on the energy absorption of the NACFST columns based on global displacement

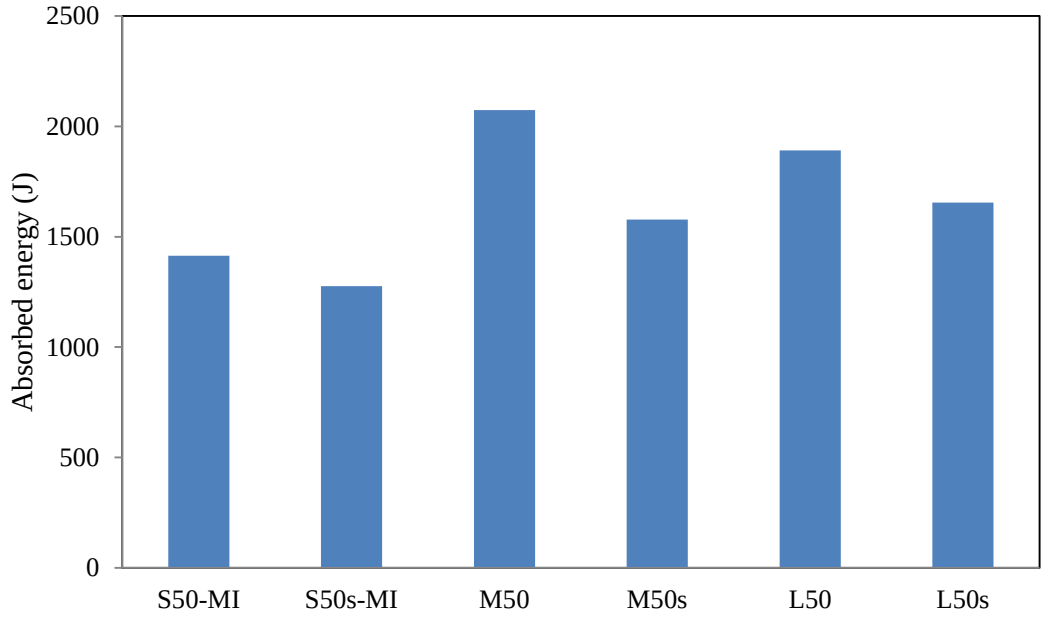

Figure 4.43. The effect of the CFRP on the energy absorption of the RACFST columns based on the global displacement

4.2.8 Discussion of the integrated results

Figs. 4.44 and 4.45 show the force-time history for the NACFST and RACFST specimens, respectively with and without CFRP strengthening with three different L/D ratios. The results from the HSC and LDV were observed and based on this observation the impact event can be again divided into three stages as follows:

- Stage 1 in which the impact force increases rapidly with a small relative lateral displacement. In this stage, the impactor hits the CFST column with its maximum velocity and then the velocity begins to decrease with a deceleration dependent on the deformation resistance of the columns which is related to the material properties, boundary conditions, D/t ratio, L/D ratio and the contact area. In addition, the indentation is initiated once the impactor strikes the tube.
- Stage 2 in which the impact force is stabilizing in a level with some fluctuations because of the yielding of the steel tube and the cracking of the concrete core as can be seen later in Chapter 5. The velocity of the impactor and CFST columns decreases and the total and global displacement increase. At the end of this stage, both the local and global deformations arrive at the maximum values.
- Stage 3 in which the impactor rebounds due to the elastic energy but keeps in contact with the CFST column up to a certain point until it disengages from the column. The impact force decreases to zero and the lateral displacement decreases to its permanent value.

The impact duration increases with increasing the tube length due to the reduction of the column stiffness which led to increasing the lateral displacement. The impact time for the long specimen was 13.2 x 10^{-3} s, whilst it was 8.7 x 10^{-3} s for the medium specimen and 5.7 x 10^{-3} s for the short one. It can be seen that there are two peak forces during the first two milliseconds, especially for the long and medium columns. The first peak force was recorded approximately at 6x10^{-4} s for all specimens, irrespective of the L/D ratio, the type of the concrete filling and the CFRP reinforcement. For all specimens, when the steel tube reached its yield strength at the contact area, the force decreased to a certain level and then it

rose again to the second peak, as the load was transferred from the steel tube to the concrete core which reserves a good local deformation resistance. The HSC records did not show any rebound during the impact event for all CFST columns as can be seen in Fig. 4.46. Once the impactor struck the CFST column, the column deformed with an indentation and then it moved together with the impactor causing the associated lateral displacement. When the column reached its maximum displacement, the impactor and the column bounced back due to the elastic energy of the tube, which can be seen from the final phase of the force-total displacement trace with the force being reduced to zero. The validated numerical models for the CFST columns show that at the first peak load, the stresses at the contact area of the steel tube were equal or higher than the yield strength of steel due to hardening. The numerical results will be presented and discussed in Chapter 5. At the beginning of Stage 2, the trend of the force-displacement curve changes dependent on the L/D ratio. For the short tube which is believed to sustain a very good global resistance and modest local stiffness, Stage 2 is short and the force fluctuates and reaches it maximum value due to the vibration and the movement of the impactor and the tube which affects the confinement pressure as can be seen later in Chapter 5. While the long column exhibited a higher global deformation than the local one, the force was degraded to a very low value. Again, the vibration and the movement of the tube and the impactor are the main reason for this phenomenon. The HSC records did not show any separation between the impactor and the CFST column. However, they were very close to splitting because of the velocity of the CFST column was slightly higher than the impactor velocity during this stage as can be seen later in Chapter 5 from the numerical results. In addition, the cracks of the concrete core and yielding of the steel tube led to a reduction of the confining pressure between the concrete core and the steel tube. Again, this will be presented and explained in Chapter 5. The flexural capacity for the concrete core is less than the steel tube and therefore, at this stage the concrete core will exhibit cracks which led to rapid resistance reduction. The cracks induce the concrete core to expand by forming voids and gaps, which, in turn, increases the internal pressure on the steel tube. Once that happens, the flexural capacity of the column will increase due to

increasing the confinement effect of the steel tube. However, this increase in the flexural capacity will not be high and it will be limited to short periods as can be seen later from the confining pressure-time history of the numerical models in Chapter 5. Thereafter, the force increased again due to the combined action between the concrete core and steel tube. The measured indentation depth and the cracks at the bottom extreme fibre of the concrete core provide evidence of this explanation in which the short columns did not show wide cracks, whilst the long one exhibited more and wider cracks. Thus, the consecutive concrete core crushing and cracking appeared as alterations in the force-time traces. This can be clearly seen from the numerical models presented in Chapter 5. Furthermore, the fast variation of the contact area between the column and the impactor induces these fluctuations in the impact force value. These changes were caused by the robust vibration which is resulted from the rapid increase of the impact force at the initial stage of the impact. (Liew et al., 2009; Wang et al., 2014; and Wang et al., 2015). Therefore, the CFRP jacket sustains substantial global resistance for the long column due to the additional confinement provided, as can be seen in Figs. 4.44 and 4.45. However, for the short specimens the effect of the CFRP layer was not significant. This evidence suggests that for the columns with high L/D ratio additional confinement should be provided to increase the impact resistance. Fig. 4.45 demonstrates that the influence of the CFRP layer on the response of the long RACFST column after the sudden reduction of the impact force was higher than that without CFRP reinforcement and 0 % RA replacement ratio.

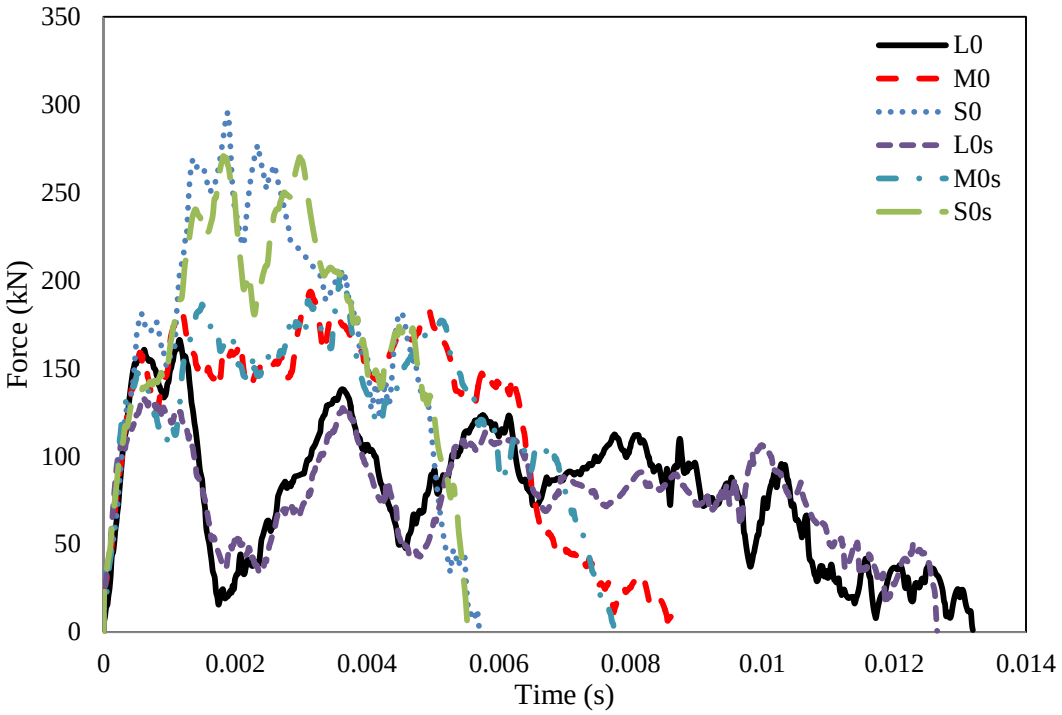

Figure 4.44. Comparison between the force-time histories between the strengthened and unstrengthened NACFST columns with different length

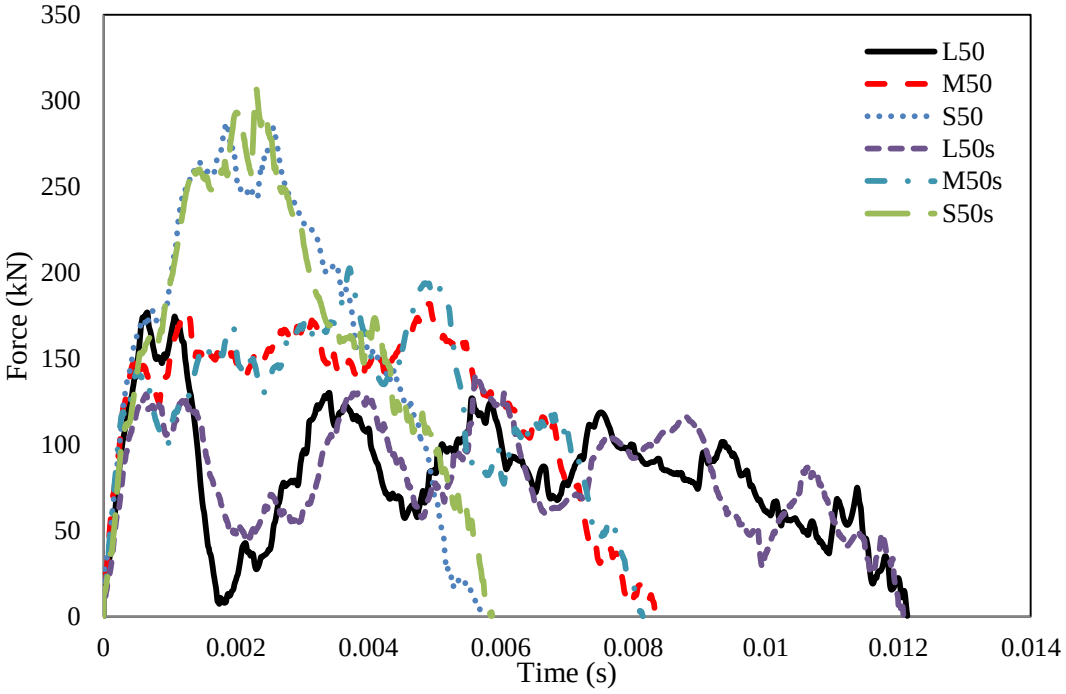

Figure 4.45. Comparison between the force-time histories between the strengthened and unstrengthened RACFST columns with different length

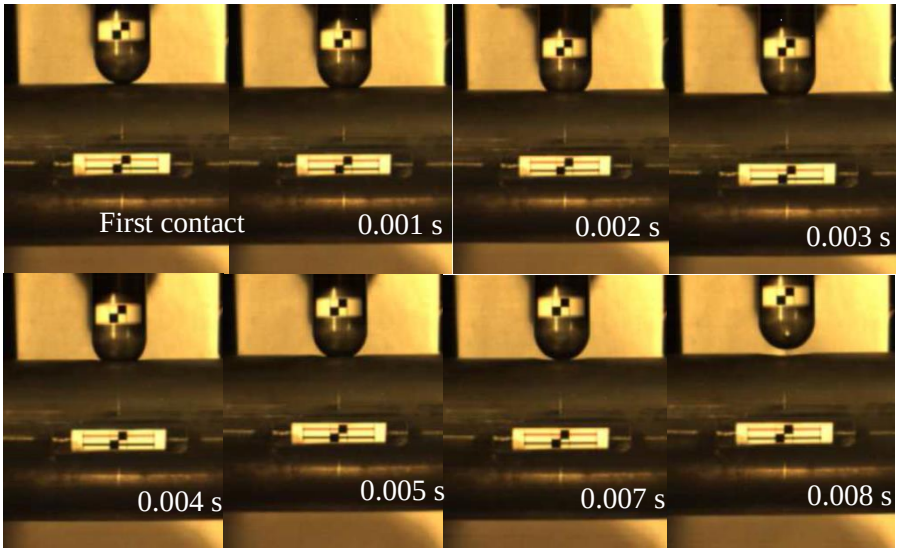

(a) Short Tube

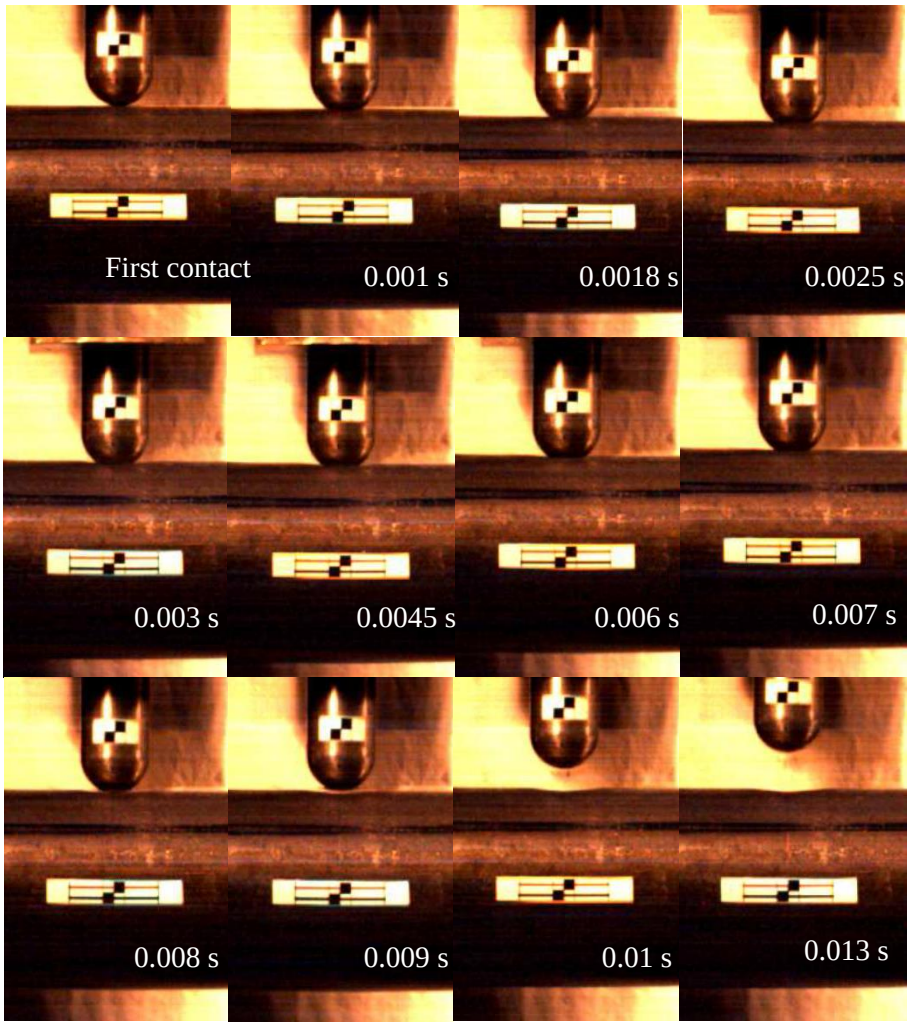

(b) Medium tube

Figure 4.46. The HSC record for the CFST columns with different lengths

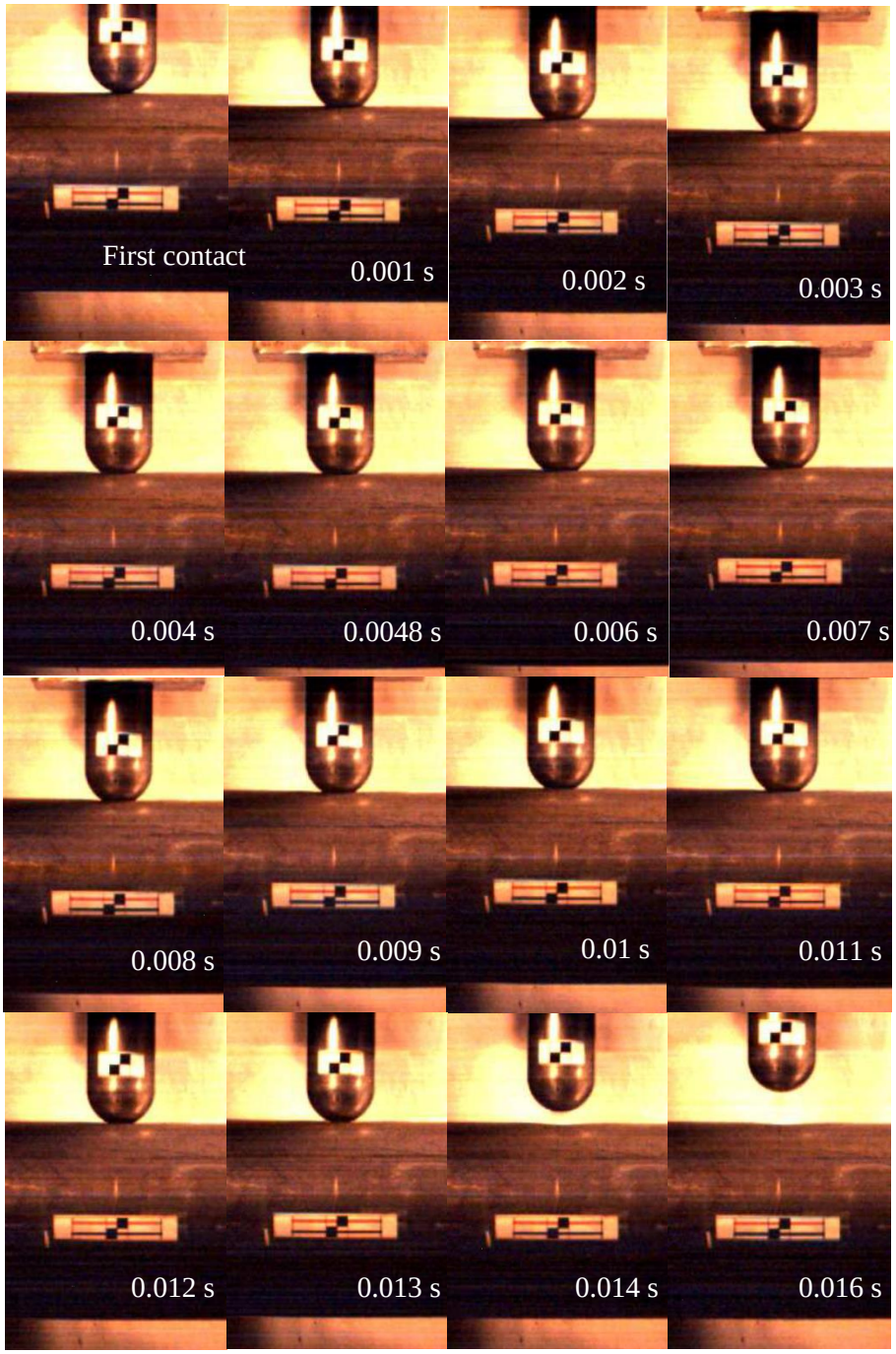

(c) Long tube

Figure 4.46 (continued). The HSC record for the CFST columns with different L/D ratio

4.3 Axial compression test

Thirty concrete filled steel tube specimens, with 0 % or 50 % RA replacement ratios, were tested under eccentric and concentric axial loading. The main experimental parameters are the loading condition i.e. eccentric and concentric, the strengthening with CFRP and the wall thickness of the steel tube. The load-displacement curves and the modes of failure of the specimens tested are presented and discussed here.

4.3.1 Concentric compression loading

Fig. 4.47 shows that with 50 % RA replacement ratio the ultimate compression capacity was slightly affected under concentric axial loading. The maximum force for the NACFST column was 2 % higher than the corresponding RACFST column, due to the lower mechanical properties of the RA concrete. Furthermore, no obvious difference was recorded between the displacement of the NACFST and RACFST columns. Fig. 4.47 reveals that the post yielding behaviour of the RACFST columns was similar to that of the corresponding NACFST, which is typical softening or stiffness degrading behaviour.

Both of the NACFST and the RACFST columns show the same mode of failure, as can be seen from Fig. 4.48. The failure mode is characterized with two bulges, the first one is close to the top end which was formed earlier, while the other one was formed on the other face near the mid height of the specimen. After the specimen reached its maximum capacity, the lateral displacement increased and the bulge grew until the loading was stopped. Some specimens failed with a different failure mode, which included only one outward local buckling and small global deformation, as can be seen in Fig. 4.48 (b). No global buckling was noticed for the other specimens due to the low L/D ratio.

Table 4.2. The compression test experimental results

Specimen ID	Max. force (kN)	Max.dis. (mm)
C0i	1167	16.7
C50i	1158	17.5
C0	1092	20.2
C50	1074	20.5
C0s	1147	16.5
C50s	1117	17.6
E0	934	15.5
E50	866	15.5
E0s	966	15.4
E50s	928	15

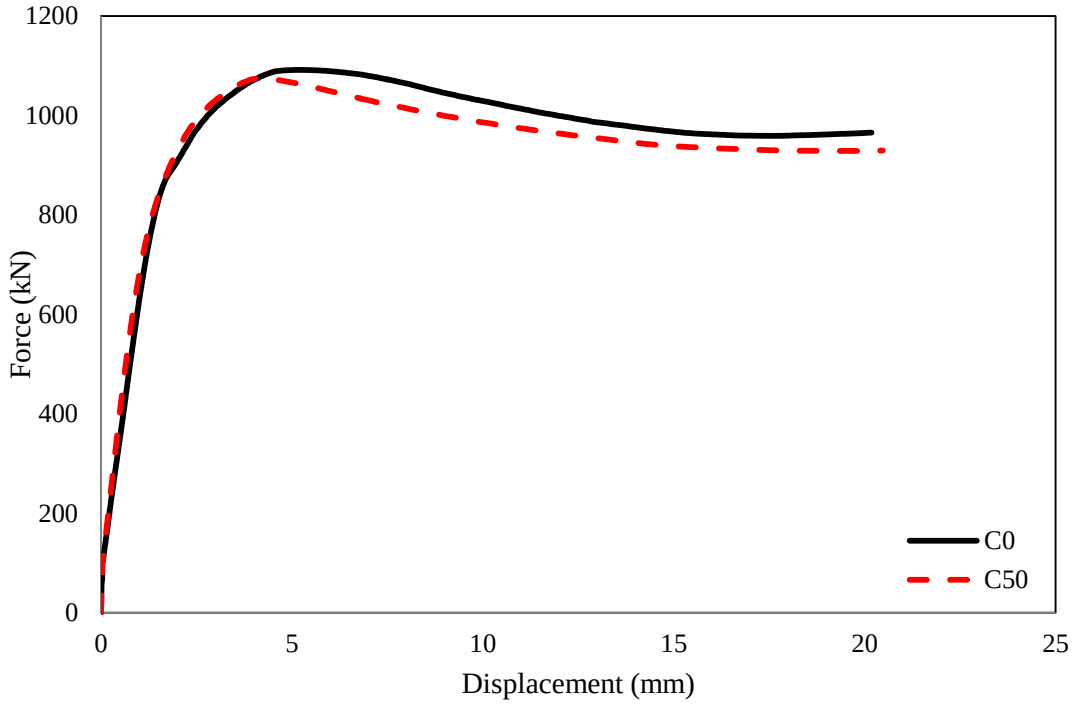

Figure 4.47. Comparison between the force-displacement curves for the NACFST and RACFST columns with D/t ratio of 32 under concentric loading

(a) Comparison between the failure mode of the NACFST and RACFST specimens

(b) Different mode of failure

Figure 4.48. The failure mode of the NACFST and RACFST columns under concentric axial loading

With the CFRP jacketing, the specimens show a higher stiffness during the elastic stage. The results indicate that the limited CFRP reinforcement increases both the initial stiffness and the maximum force and reduces the axial shortening, regardless of the RA replacement ratio. Figs. 4.49 and 4.50 show that the axial displacement was reduced by 18 % and 14 %, whilst the maximum force was increased by 5 % and 4 % for the NACFST and RACFST columns, respectively. It can be seen that the load displacement response of the CFST column with CFRP strengthening is slightly different from the one without strengthening. This is because of the additional confinement by the CFRP layer which increased the load carrying capacity of the column up to a certain level when the CFRP layer ruptured. The load then decreased steadily due to the sudden failure of the CFRP. The results also show that the post yielding behaviour of the strengthened specimens is mainly dominated by the almost perfectly-plastic response. The effectiveness of the CFRP reinforcement can be examined by calculating the column stiffness using the maximum force and the associated axial displacement. The CFRP arrangement adopted in this study enhanced the secant stiffness (i.e. measured from the peak force and the corresponding displacement) of the NACFST and RACFST columns by 62% and 87%, respectively in comparison with the ones without CFRP strengthening.

For the NACFST and RACFST specimens with a single layer of CFRP, the failure was initiated with an outward indent near the top end. With an increase of the applied load, the bulge gradually swelled and the second outward local buckling was also developed at the mid height of the column. At the same time, the crack on the CFRP layer was initiated and the crack width increased with the expanding of the bulge until it ruptured. A loud noise was heard, due to the cracking and de-bonding of the CFRP layer. For all specimens the CFRP fracture occurred in the same direction as the outward local deformation, which hardly exhibited any sign of the global deformation, as can be seen from Figs. 4.51 (a) and (b).

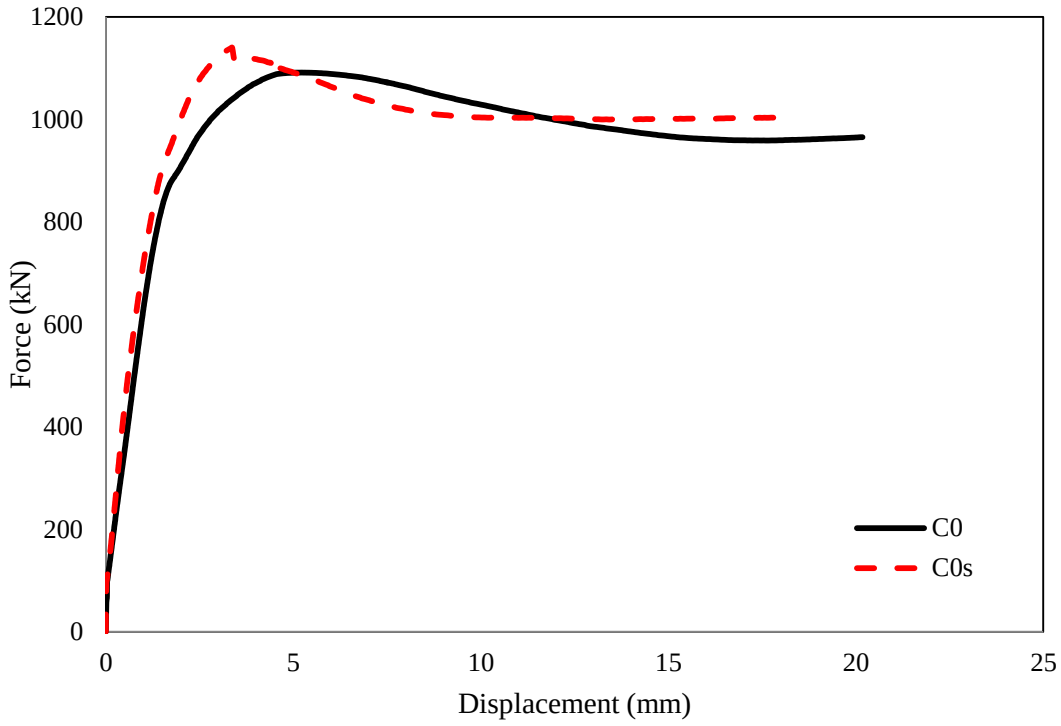

Figure 4.49. The influence of the CFRP on the compression capacity of the NACFST columns under concentric loading

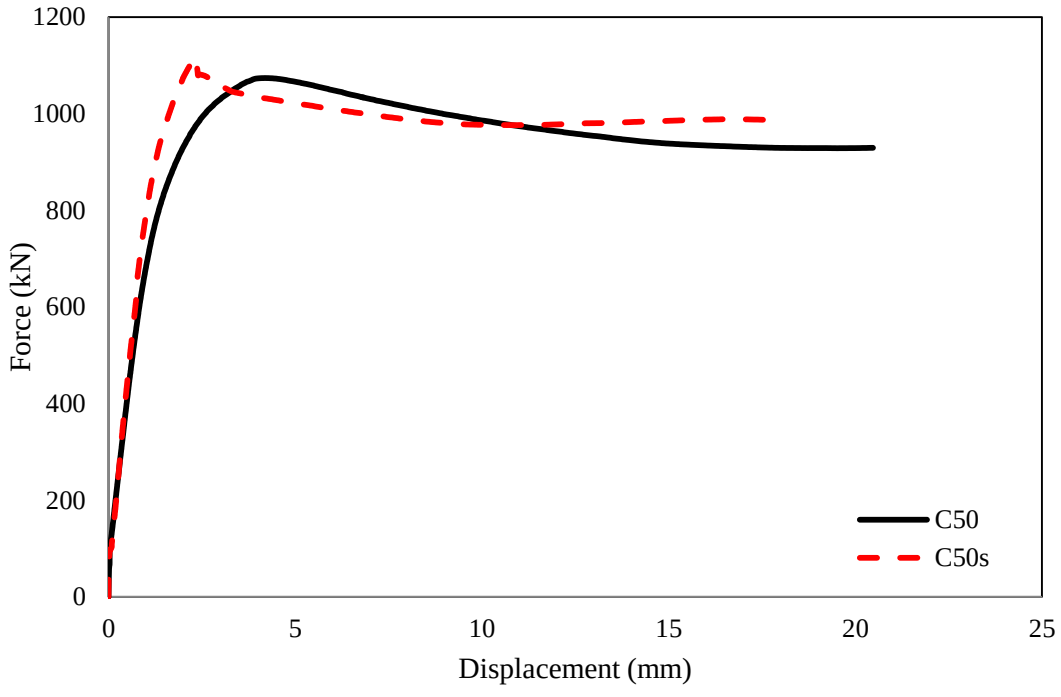

Figure 4.50. The influence of the CFRP on the compression capacity of the RACFST columns under concentric loading

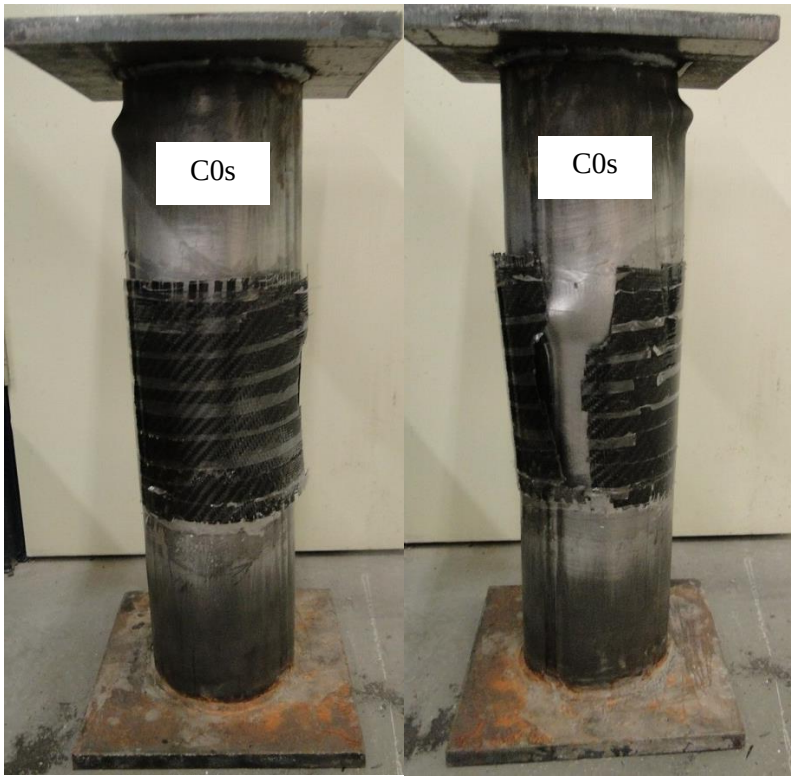

(a) The failure of the strengthened NACFST specimen

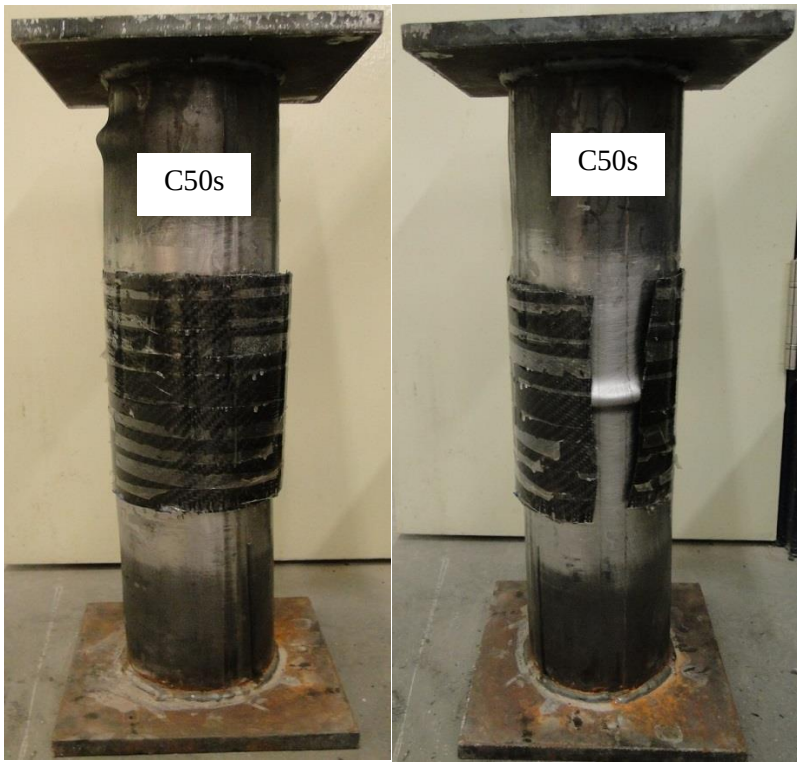

(b) The failure of the strengthened RACFST specimen

Figure 4.51. The deform shape of the NACFST and RACFST columns under concentric axial loading

4.3.2 Eccentric axial loading

Fig. 4.52 shows the plot of the force versus the axial displacement for the NACFST and RACFST specimens subjected to eccentric axial loading. In general, all specimens showed a similar behaviour, which may be characterized as an elastic-perfectly plastic response. The eccentricity loading significantly influenced the bearing capacity of the all specimens, as can be seen in Table 4.2. The maximum force was reduced by 14.5 % and 19.4 %, while the axial shortening reduction was 23.3 % and 24.4 % for the NACFST and RACFST columns, respectively. This is because of the eccentricity of loading. The columns tested are considered as short stocky columns as the L/D ratio is only 6. Thus, the slenderness effect is omitted here. The applied loading with an eccentricity induces a bending moment at the cross section of the column, which, in turn causes a lateral deflection for the column. The column under concentric loading exhibits a higher load carrying capacity due to the high compressive strength of concrete which results from the confinement effect of the steel tube. The comparison between the NACFST and the RACFST specimens under eccentric loading shows that the ultimate compression force was decreased from 934 kN to 866 kN when 50 % of the normal aggregate was replaced by recycled aggregate. However, the axial displacement was not affected by the type of the concrete filling.

The typical mode of failure of the NACFST and RACFST specimens are depicted in Figs. 4.53 (a) and (b), respectively. The failure began by developing a bulge close to the top end on the same side as the eccentric loading steel bar. With expanding of the bulge, the top plate rotated around the major rotational axis and induced the specimen to bow near the top end, as can be seen in Fig. 4.53. The top plate continued to bend and other outward buckling developed below the first one due to increasing applied loading. At the same time, the axial shortening increased and the bearing capacity decreased. However, some of the columns only exhibited one outward indent or two close bulges, as shown in Fig. 4.53 (b). The bowing of the specimens loaded eccentrically causes a reduction in the confinement between the concrete core and the steel tube, which causes the concrete to crack on the tension side. In contrast, with the specimens loaded concentrically, the concrete core would be fully

confined by the steel tube and it would not exhibit any tensile crack, as long as no flexural failure occurs.

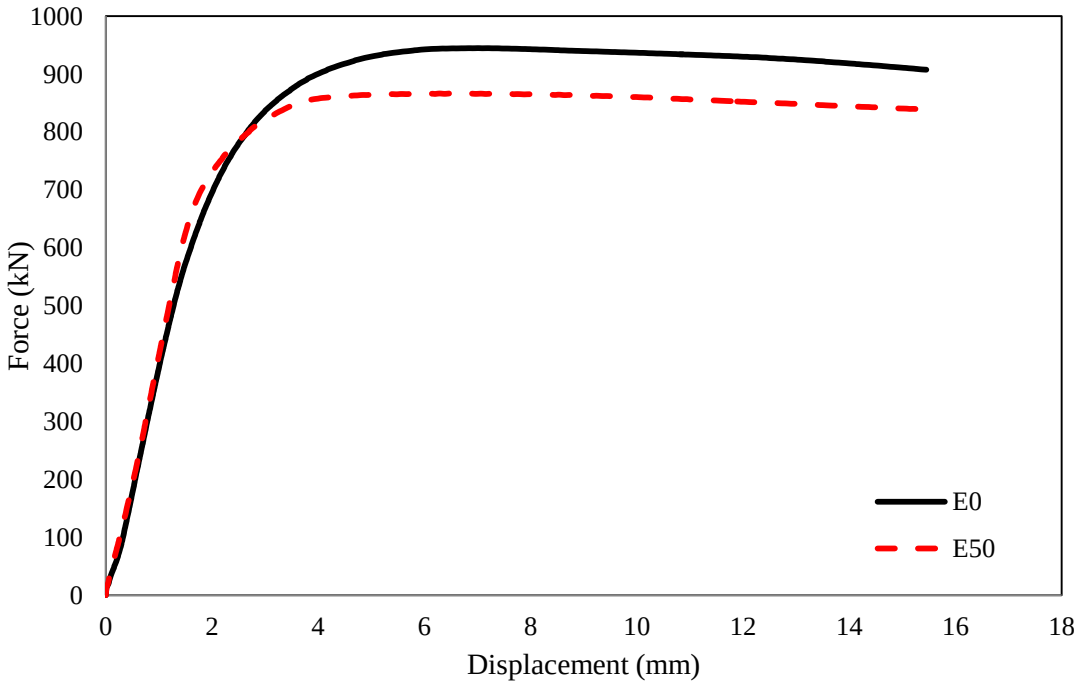

Figure 4.52. Comparison between the force-displacement curves for the NACFST and RACFST columns under eccentric loading

(a) Comparison between the failure mode of the NACFST and RACFST specimens

(b) Different failure modes

Figure 4.53. The deform shape of the NACFST and RACFST columns under eccentric axial loading

The strengthened NACFST and RACFST columns were also examined under eccentric axial loading. It was found that the CFRP jacket sustained the modest bearing capacity with almost elastic-perfectly plastic behaviour for the NACFST and RACFST columns, as shown in Figs. 4.54 and 4.55, respectively. The additional confinement provided by the CFRP increased the ultimate capacity for the NACFST column by 3.4 %, whilst the maximum force was elevated from 866 kN to 928 kN for the RACFST column.

The failure mechanisms of the strengthened specimens under eccentric loading were similar to those of the unstrengthened columns, irrespective of the type of concrete filling. The CFRP layer began to crack when the bowing increased and the outward local buckling enlarged. However, the full rupture of the CFRP jacket did not occur but a cracking noise was heard during the final stage of the test. Figs. 4.56 (a) and (b) demonstrate that both of the NACFST and RACFST columns with CFRP reinforcement have similar deformation shapes.

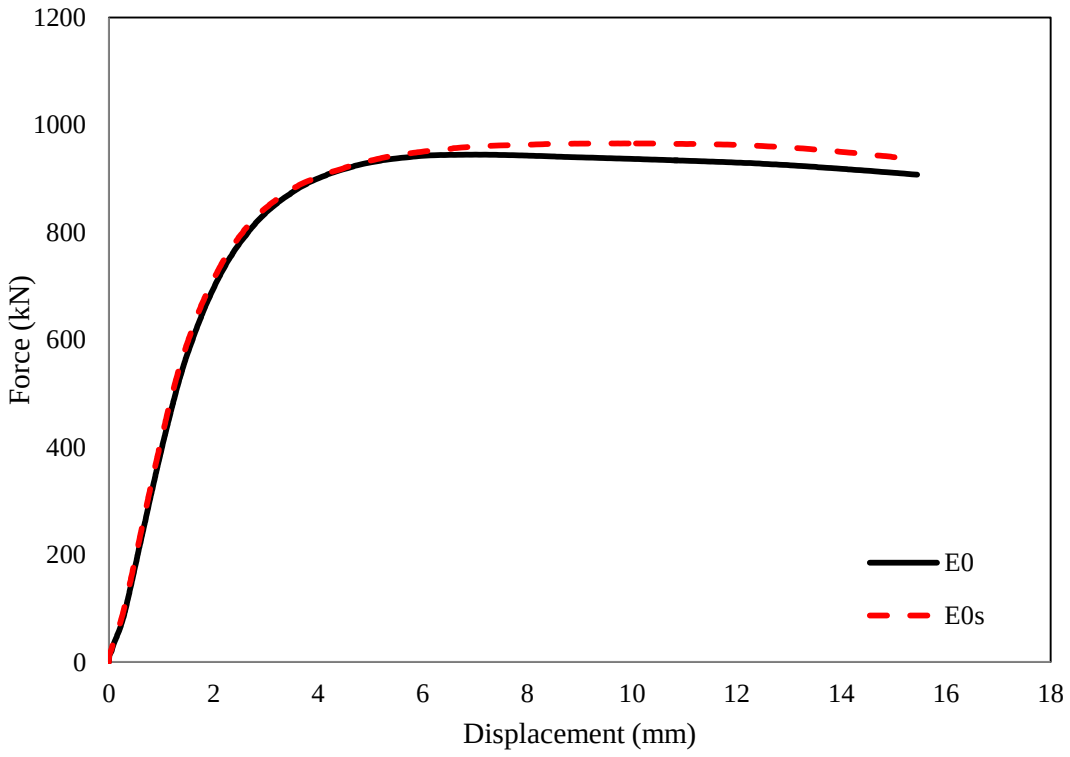

Figure 4.54. The influence of the CFRP on the compression capacity of the NACFST columns under eccentric loading

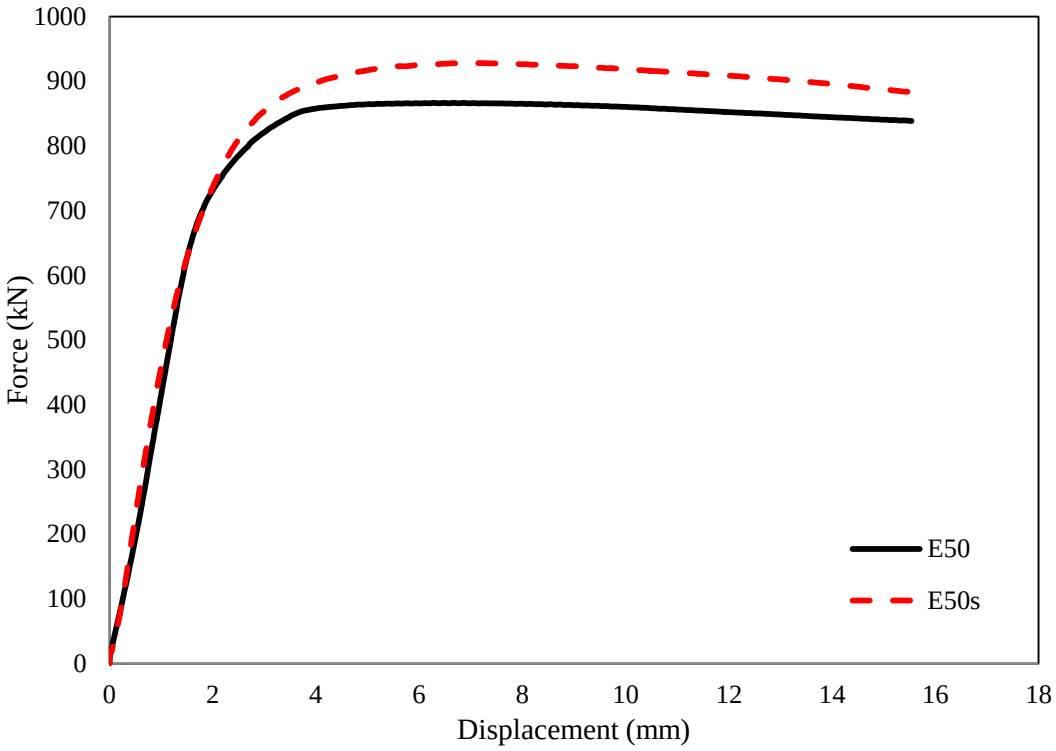

Figure 4.55. The influence of the CFRP on the compression capacity of the RACFST columns under eccentric loading

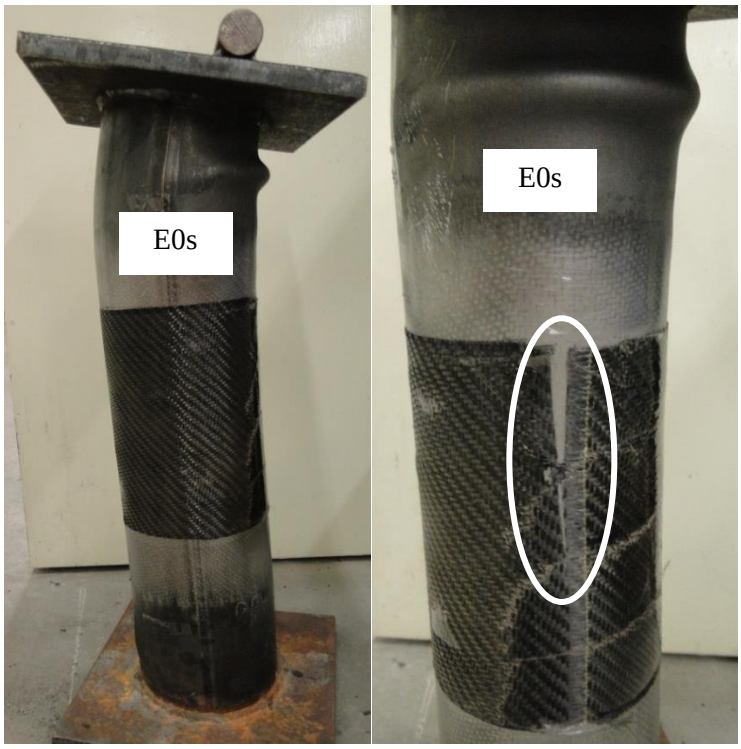

(a) The failure of the strengthened NACFST specimen

Figure 4.56. The deform shape of the NACFST and RACFST columns under eccentric axial loading

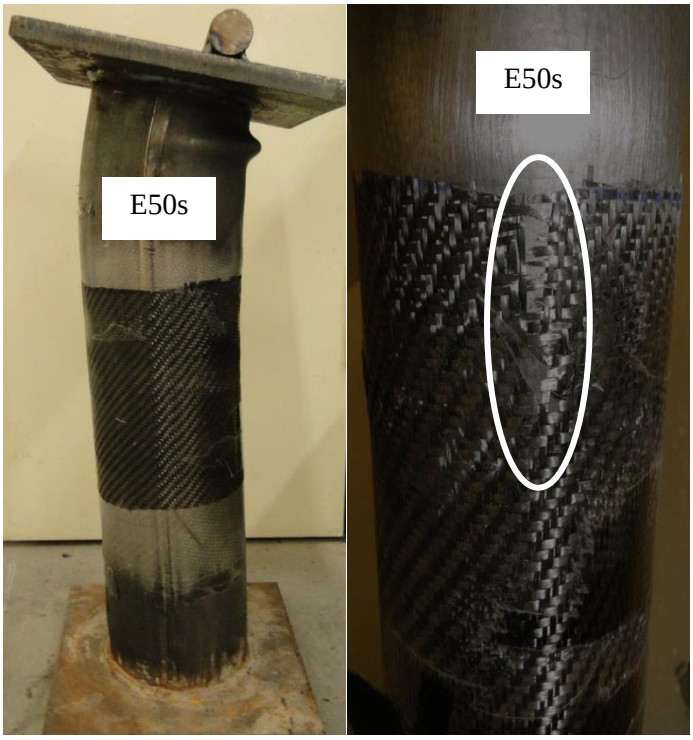

(b) The failure of the strengthened RACFST specimen

Figure 4.56 (continued). The deform shape of the NACFST and RACFST columns under eccentric axial loading

4.3.3 The effect of the D/t ratio on the compression behaviour of the CFST column

Fig. 4.57 shows a comparison of the compression behaviour of the NACFST and RACFST specimens with tube wall thickness of 3.6 mm. It is clear that the maximum capacity of the RACFST column is slightly less than the corresponding NACFST column. The reduction of the ultimate force was only 0.8 %, whilst the increase of the axial displacement was 5 %. The D/t ratio showed a significant influence on the bearing capacity of the CFST column regardless the RA replacement ratio. It was found that with the reduced D/t ratio from 38 to 32 the maximum force increased from 1092 kN to 1167 kN and from 1074 kN to 1158 kN for the NACFST and RACFST specimens, respectively. Moreover, the axial shortening decreased by 17.3 % for the NACFST column and by 15 % for the RACFST column as can be seen in Figs 4.58 and 4.59. The post yielding behaviour of the column with RA concrete filling may be classified between the stiffness degrading and a mild strain hardening, whilst the behaviour of the column filled by NA concrete appeared to be elastic-perfect plastic.

The deformation shape for the NACFST and RACFST specimens with a D/t ratio of 32 is shown in Fig. 4.60. The figure reveals that both columns failed with the same failure mechanism in which the bulge was developed at the top end of the tube. This deformation shape is known as an elephant's foot failure mode. With increasing the applied loading, the column exhibited other outward local buckling on the opposite side of the first bulge. However, all specimens did not show any global buckling during the test.

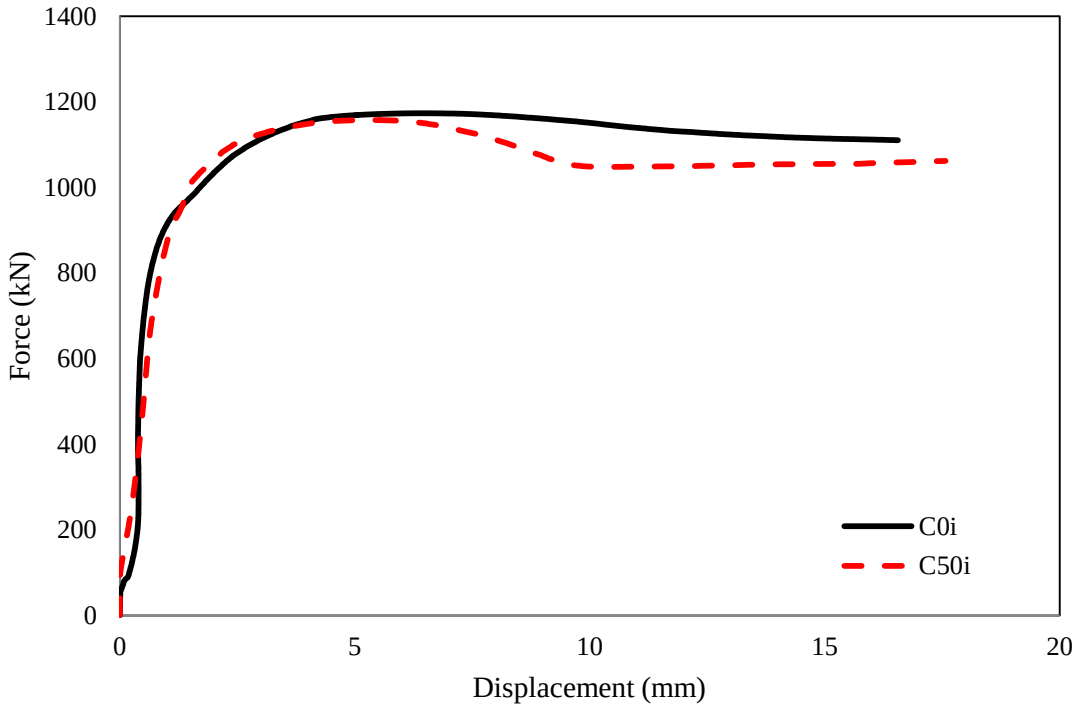

Figure 4.57. Comparison between the force-displacement curves for the NACFST and RACFST columns with D/t ratio of 32 under concentric loading

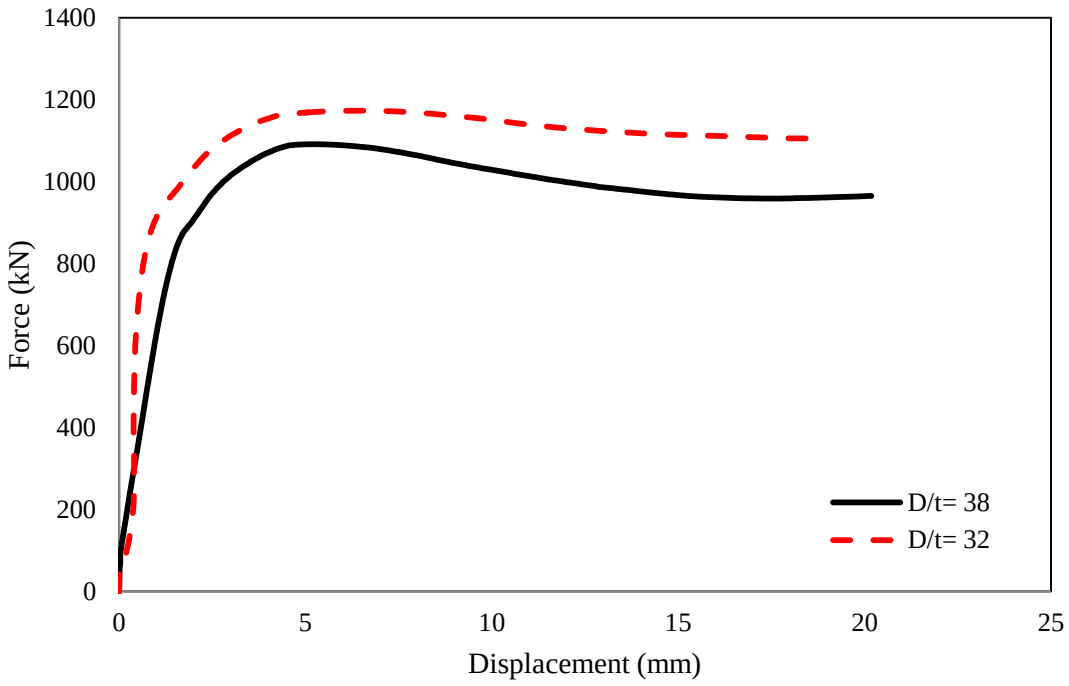

Figure 4.58. Comparison between the force-displacement curves for the NACFST columns with different D/t ratio

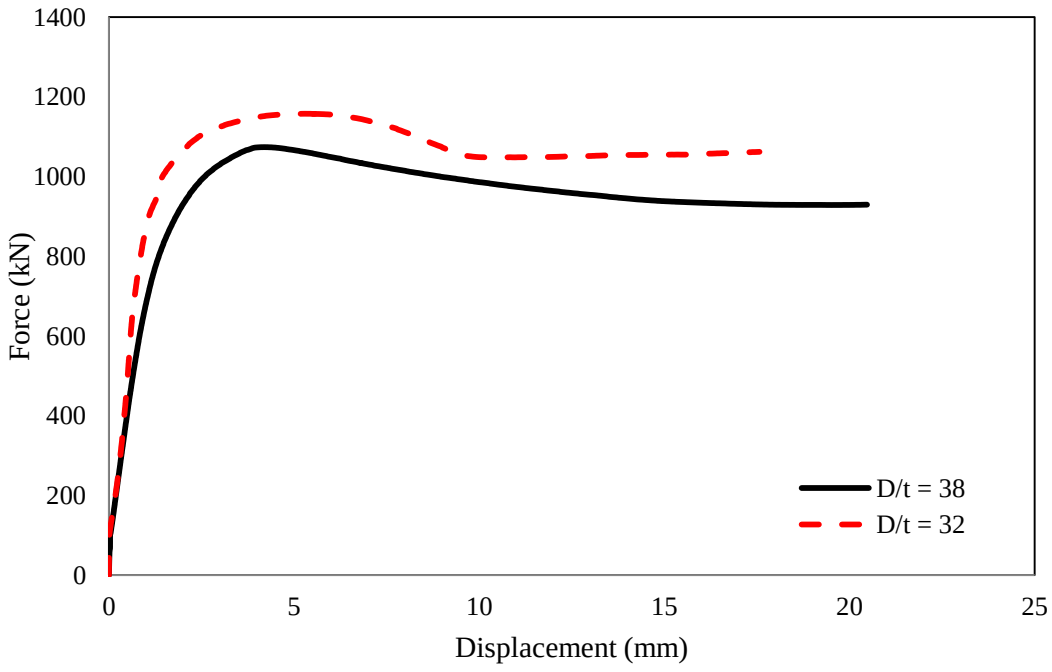

Figure 4.59. Comparison between the load- displacement curves for the RACFST columns with different D/t ratio

Figure 4.60. The deformation shape of the NACFST and RACFST columns with D/t ratio of 32

4.4 Summary

4.4.1 Lateral impact tests

The comparison between the impact forces for the hollow and concrete filled tubes has showed that the concrete filling creates substantial local and global deformation resistance and increases the impact force for the specimens with different L/D ratios. For the short columns the force has increased by 217 %, whilst for the medium and long specimens the force has increased by 182 % and 157 %, respectively. The results have demonstrated that the RACFST columns show a very good response under lateral impact loading with various test parameters. The peak forces are slightly lower compared with the NACFST columns. In addition, the failure patterns are quite similar to those of the columns without RA replacement. These results suggest that it is viable to use the RACFST columns in construction.

The contact area between the impactor and the tube has significant effects on the impact response particularly for the columns with low L/D ratios. The peak force increased by 30.1 % with increasing the diameter of the spherical impactor from 20 mm to 60 mm.

The L/D ratio also has a considerable influence on the impact behaviour of the CFST columns. For the NACFST columns, the force is reduced from 299 kN to 166.3 kN and the displacement is increased from 13.5 mm to 28.2 mm, when the L/D is increased from 6 to 13.5. For the RACFST columns with the same L/D ratios, the force is decreased by 42 % and the displacement increased by 116 % when tube length reduced from 1543 mm to 686 mm.

The test data reveals that the D/t ratio has a significant influence on the impact behaviour of the CFST columns, irrespective of the type of the concrete filling. When the D/t ratio is increased from 32 to 38, the total displacement is increased by 20.2 % and 27.3 % for the NACFST and RACFST columns, respectively. Furthermore, the global displacement is decreased by 5.7 % for the NACFST columns and 18 % for RACFST columns with the same reduction of D/t ratio.

The additional confinement provided by the CFRP jackets also has a significant influence on the impact behaviour. One layer of CFRP reduces the initial peak force for all specimens, which also provides a reasonable global deformation resistance particularly for the columns with high L/D ratios. Furthermore, the contact force for the long strengthened NACFST column is 146.3 kN, while it is 166.2 kN for the corresponding unstrengthened column.

4.4.2 Compression tests

The RACFST columns showed similar compressive behaviour compared with the NACFST columns, in terms of the failure pattern and the ultimate force. The maximum force for the NACFST column is only 2 % higher than the corresponding RACFST column, due to the slightly lower mechanical properties of the RA concrete.

The effectiveness of the CFRP reinforcement has been examined by calculating the column stiffness using the maximum force and the associated axial displacement. The CFRP arrangement adopted in this study has enhanced the stiffness of the NACFST and RACFST columns by 25 % and 90 %, respectively.

The eccentricity of the loading significantly affects the bearing capacity of the all specimens. The ultimate force is decreased by 14.5 % and 19.4 %, while the axial shortening reductions are 23.3 % and 24.4 % for the NACFST and RACFST columns, respectively.

The additional CFRP confinement increased the ultimate capacity for the NACFST column by 3.4 %, while the maximum force was raised from 866 kN to 928 kN for the RACFST column.

The D/t ratio showed a significant influence on the bearing capacity of the CFST column regardless the RA replacement ratio. It was found that the reduction of the D/t ratio from 38 to 32 increased the maximum force from 1092 kN to 1167 kN and from 1074 kN to 1158 kN for the NACFST and RACFST specimens, respectively.

CHAPTER 5

FINITE ELEMENT MODELLING

5.1 Introduction

This chapter presents the numerical procedures and techniques that are employed to simulate the behaviour of the concrete filled steel tube columns under both dynamic and quasi-static loadings. Here, the commercial finite element analysis code, ABAQUS/Explicit and ABAQUS/Standard are used to develop numerical models to help understand the performance and the structural behaviour of the CFST columns under lateral impact and axial compression loadings, respectively. There are two constituent materials considered to model the impact behaviour of CFST column, i.e. the concrete core and the steel tube. In addition, the contact type and the contact properties between the steel tube and the concrete core are also very important to simulate the CFST appropriately. The details of the constitutive models of the CFST columns are included here. The "Concrete Damage Plasticity" model is used to simulate the impact behaviour of the confined concrete, while the "Drucker Prager" model is adopted to model the confined concrete under quasi-static concentric and eccentric loadings. The mild steel tube is modelled as an isotopic elasto-plastic material. The damage of CFRP is simulated using the Hashin's failure criteria. Subsequently, the finite element (FE) modelling results are also given in this chapter. The numerical models are validated against the experimental data presented in Chapter 4, which will be further used to conduct parametric studies in Chapter 6. The comparison between the numerical and experimental force-displacement traces for the CFST column under lateral impact and quasi-static loading is presented. The deformation mode and energy absorption are also discussed.

5.2 Modelling of CFST columns under lateral impact loading

5.2.1 Element type and mesh size

Full three-dimensional models were developed to simulate the impact behaviour of all the unstrengthened CFST columns with different L/D ratios, D/t ratios, concrete types and impactor configurations. However, the CFST column with CFRP strengthening was modelled using a quarter model to reduce the computational time by using the symmetry boundary conditions along the symmetry planes, as shown in Figs 5.1 (a) and 5.1 (b),

respectively. The element behaviour can be defined using an element's formulation which refers to the mathematical theory.

All of the solid elements in ABAQUS (ABAQUS documentation, 2015) except for the infinite elements are written to include finite strain effects. The strains are calculated as

$$\varepsilon = sym\left(\frac{\partial \boldsymbol{u}}{\partial \boldsymbol{x}}\right) \tag{5.1}$$

where $\boldsymbol{u}$ is the total displacement and $\boldsymbol{x}$ is the spatial position of the point under consideration in the original configuration.

When the elements are used for geometrically nonlinear analysis with any other material definition (at finite strain this means the material has some inelastic behaviour the strains are calculated as the integral of the rate of deformation,

$$D = sym\left(\frac{\partial v}{\partial x}\right) \tag{5.2}$$

where v is the velocity at a point and x are the current spatial coordinates of the point.

If the local orientation is specified for an element, stress and strain components are given as physical components referred to the global spatial directions, otherwise, the solid elements will report stress as the "true" (Cauchy) stress in all other cases.

The interpolation function for the 8-noded brick element can be written as: (ABAQUS Theory Manual, 2015)

$$\begin{aligned} u = {} & \frac{1}{8}(1-g)(1-h)(1-r)u_1 + \frac{1}{8}(1+g)(1-h)(1-r)u_2 \\ & + \frac{1}{8}(1+g)(1+h)(1-r)u_3 + \frac{1}{8}(1-g)(1+h)(1-r)u_4 \\ & + \frac{1}{8}(1-g)(1-h)(1+r)u_5 + \frac{1}{8}(1+g)(1-h)(1+r)u_6 \\ & + \frac{1}{8}(1+g)(1+h)(1+r)u_7 + \frac{1}{8}(1-g)(1+h)(1+r)u_8 \end{aligned}$$

where u_1, u_2, …u_8 are the displacements on 8 nodes.

For the 8-node brick elements the interpolation function given above can be rewritten as

$$\mathbf{u} = N^I(g,h,r)\mathbf{u}^I \text{ sum on } I. \tag{5.3}$$

The isoparametric shape functions N^I can be written as:

$$N^I(g,h,r) = \frac{1}{8}\Sigma^I + \frac{1}{4}g\Lambda_1^I + \frac{1}{4}h\Lambda_2^I + \frac{1}{4}r\Lambda_3^I + \frac{1}{2}hr\Gamma_1^I + \frac{1}{2}gr\Gamma_2^I + \frac{1}{2}gh\Gamma_3^I + \frac{1}{2}ghr\Gamma_4^I, \tag{5.4}$$

where

$$\Sigma^I = [+1,+1,+1,+1,+1,+1,+1,+1],$$

$$\Lambda_1^I = [-1,+1,+1,-1,-1,+1,+1,-1],$$

$$\Lambda_2^I = [-1,-1,+1,+1,-1,-1,+1,+1],$$

$$\Lambda_3^I = [-1,-1,-1,-1,+1,+1,+1,+1],$$

$$\Gamma_1^I = [+1,+1,-1,-1,-1,-1,+1,+1],$$

$$\Gamma_2^I = [+1,-1,-1,+1,-1,+1,+1,-1],$$

$$\Gamma_3^I = [+1,-1,+1,-1,+1,-1,+1,-1],$$

$$\Gamma_4^I = [-1,+1,-1,+1,+1,-1,+1,-1],$$

and the superscript *I* denotes the node of the element. The last four vectors, Γ_α^I(α has a range of four), are the hourglass base vectors, which are the deformation modes associated with no energy in the 1-point integration element but resulting in a non-constant strain field in the element.

In the finite element analysis, the numerical (full or reduced) integrations are used to calculate the stiffness and the mass of the element. The reduced integration (primarily used by ABAQUS/ Explicit) (ABAQUS documentation, 2015) means using lower order integration to form the element stiffness. Thus, the running time will be reduced, especially for the three dimensions elements. For example, the element assembly is about 3.5 times more costly for C3D8 than that for C3D8R. In addition, with the reduced integration elements, the stresses and strains are calculated at the locations that provide optimal accuracy. The 8-node element is very active for solving the problems including contact-impacts (Belytschko et al., 2000). In ABAQUS/ Explicit, the full and reduced integrations options are available for the hexahedral elements, whilst the reduced integration option is available only for the first order quadrilateral elements. For quadrilateral and hexahedral elements in ABAQUS/ Standard, both of the full and reduced integration options are available.

In practice, the C3D8R element is not very useful without hourglass control which is automatically activated for this type of element. In stress/displacement analyses, hourglassing can be a problem with the first order and reduced integration elements such as CPS4R, CAX4R and C3D8R. Hourglassing is a spurious deformation mode of the finite element mesh that appears as a patchwork of zigzag or hourglass like element shapes and it is basically due to the excitation of the zero energy degrees of freedom. Since the C3D4R elements have only one integration point, it is possible for them to distort in such a way that the strains calculated at the integration point are all zero, which, in turn, leads to uncontrolled distortion of the mesh.

For solid and shell elements, ABAQUS/Explicit only offers the linear first order interpolation to calculate the internal stresses and strains at any point in the element. In general, when large strains or very high strain gradients are expected, it is recommended to use first order elements. In addition, many numerical studies used the linear elements with

reduced integration to solve the structural impact problems (Yu and Jones, 1979; Zeinoddini et al., 2008; Dorogoy and Rittel, 2008; Thilakarathna et al., 2010; and Al-Thairy, 2012). Thus, first order eight-noded solid elements with reduced integration (C3D8R) were used to mesh the concrete core, as shown in Fig 5.2. Each node of this element contains three translational degrees of freedom with the reduced integration to minimize the analysis time. Using the shell element to simulate the steel section will affect the accuracy of the simulation of the contact interaction between the concrete and the steel tube and the confinement of the concrete. Thus, the eight-noded solid element would be better to be used to reflect the through-thickness deformation characteristics of the tube (Dai and Lam, 2010). Therefore, C3D8R elements were also adopted in this study to model the steel tube, as can be seen in Fig. 5.2 (c). Three and four layers of elements were defined within the tube wall thicknesses of 3 mm and 3.6 mm, respectively.

The impactor was modelled as a rigid body because it is made from high strength steel and its deformation is very small or it is almost nonexistent which can be neglected. The rigid body is a collection of nodes and elements whose motion is governed by the motion of a single reference point that has both rotational and translation degrees of freedom. The geometry, mass, rotational inertia of the rigid body is accurately represented by the rigid bodies' simulation. In addition, accurate visualisation and post-processing of the model can be provided by the rigid bodies. To define the rigid body an appropriate rigid element should be used. Since, all the models are modelled as full three dimensions models, the 4-noded 3D bilinear rigid quadrilateral elements (R3D4) Rigid elements was used to simulate the rigid body, i.e. the impactor. The rigid elements can be used to define the rigid bodies for multi-body dynamic simulations as well as to define the surfaces of the rigid bodies for contact. The rigid elements do not use numerical integration points because they are unreformed elements. Thus, the 4-noded 3-D bilinear rigid quadrilateral elements (R3D4) were chosen to model the impactor. The steel clamps were modelled using the C3D8R elements as well. The CFRP layer was simulated using 8-noded quadrilateral in-plane general-purpose

continuum shell elements, with reduced integration and hourglass control (SC8R), as shown in Fig. 5.2 (d). No over constraint will occur at the kinematic relationship of displacement in the interface between the solid and shell element, if the continuum shell element SC8R are being used, instead of the shell element (S4R) (Rejab, 2013). To predict the failure of the CFRP, the SC8R element is used by many researchers to model the CFRP due to its capability to capture the shear stress through the thickness (Al-Mosawe et al., 2016).

The element size for the tube and concrete was determined based on the mesh sensitivity study. Fig. 5.3 shows that the numerical model of the CFST short column with element size of 10 mm exhibited stiffer behaviour with the higher impact force and less total displacement than the corresponding experimental results. With reducing the element size, the accuracy of the model was enhanced. The mesh with element size of 5 mm showed a reasonably good agreement with the experimental data. However, reducing the element size to 3 mm and then to 1mm did not effectively improve the accuracy of the numerical results, especially for the first stage of the force-total displacement trace. Also, the computational time increased with decreasing the element size, as expected. Therefore, the element size of 5 mm was adopted in this study for the concrete core, steel tube and CFRP layer. The impactor, as a master surface, was modelled with an element size of 2 mm, while the steel clamp was simulated using 12 mm size of element.

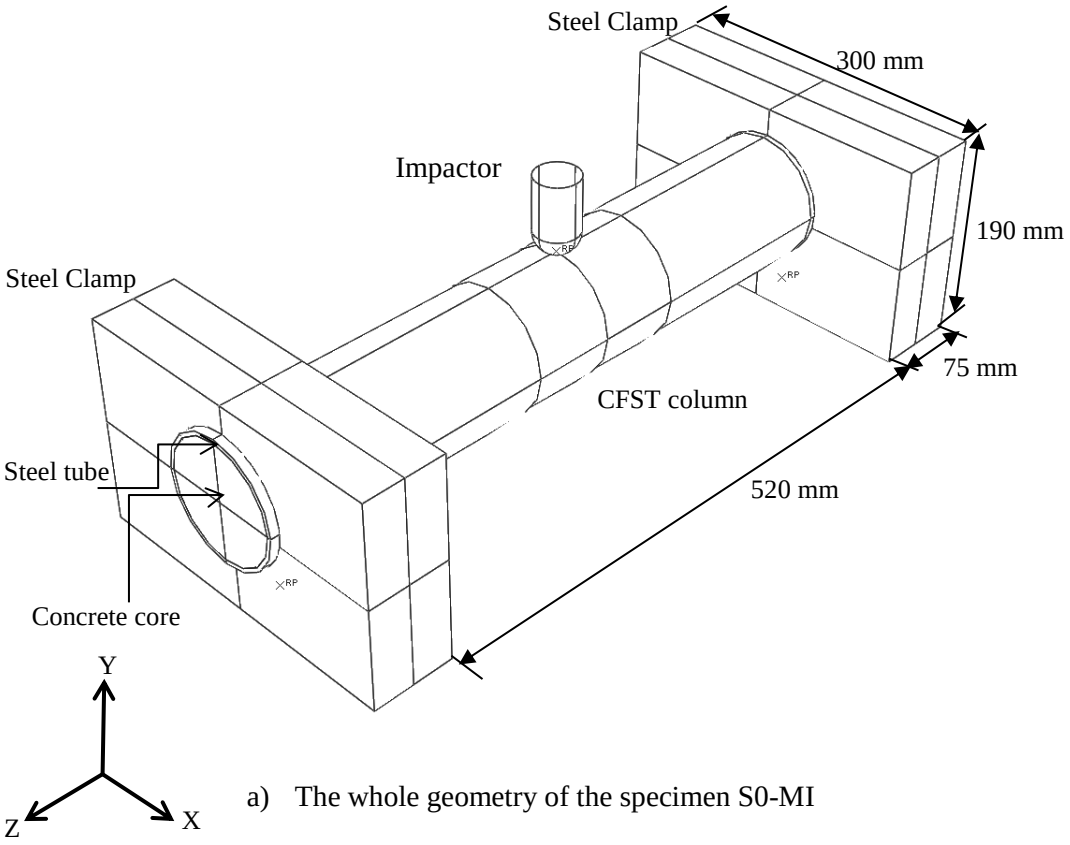

a) The whole geometry of the specimen S0-MI

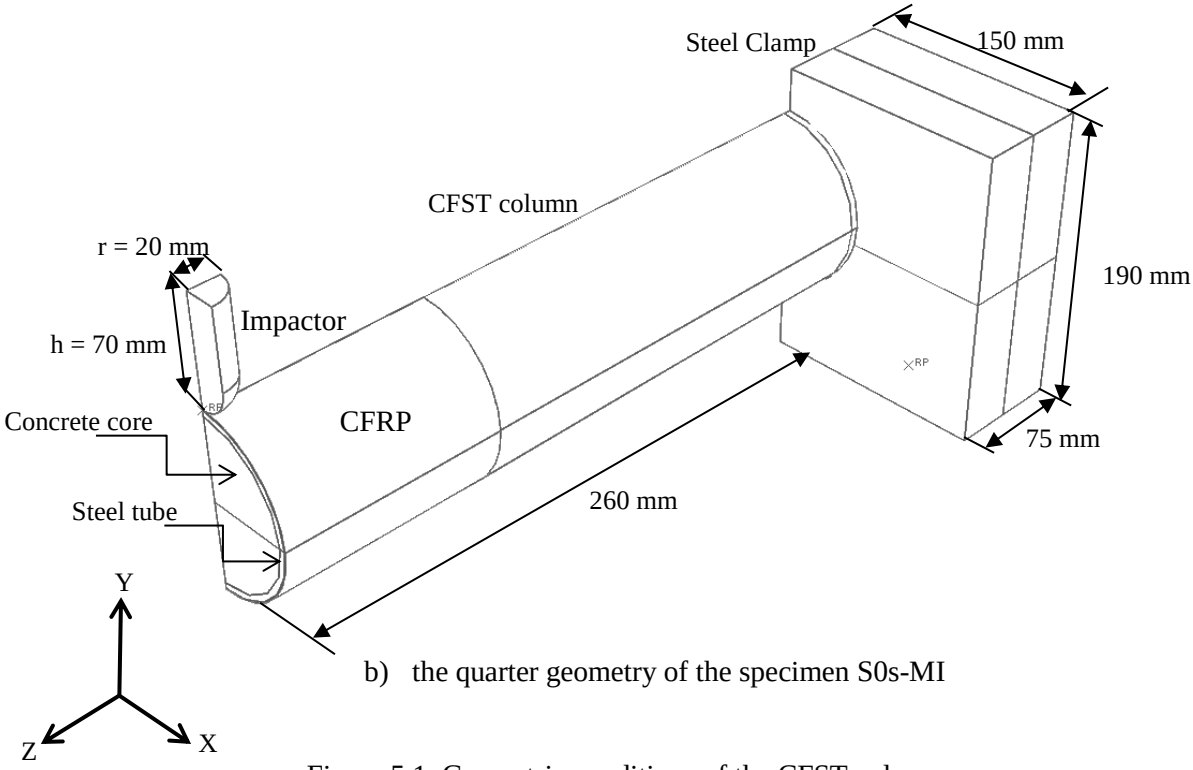

b) the quarter geometry of the specimen S0s-MI

Figure 5.1. Geometric conditions of the CFST columns

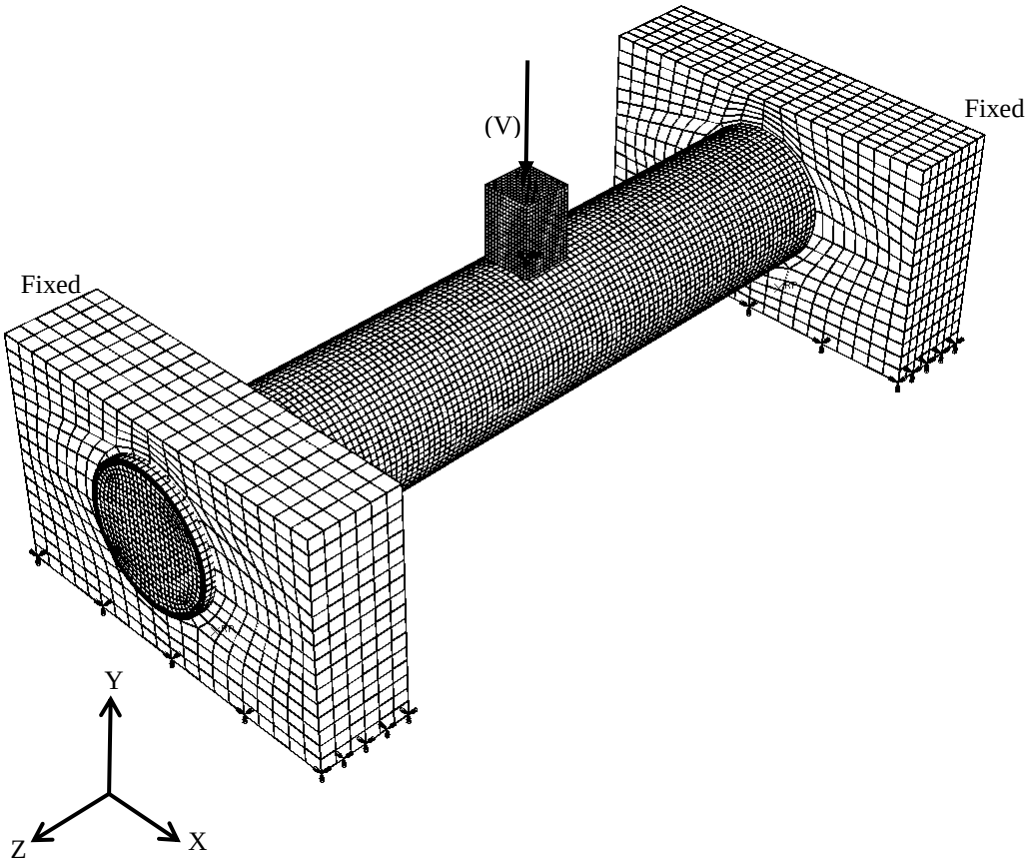

a) the mesh, boundary and loading conditions of the S0-FI

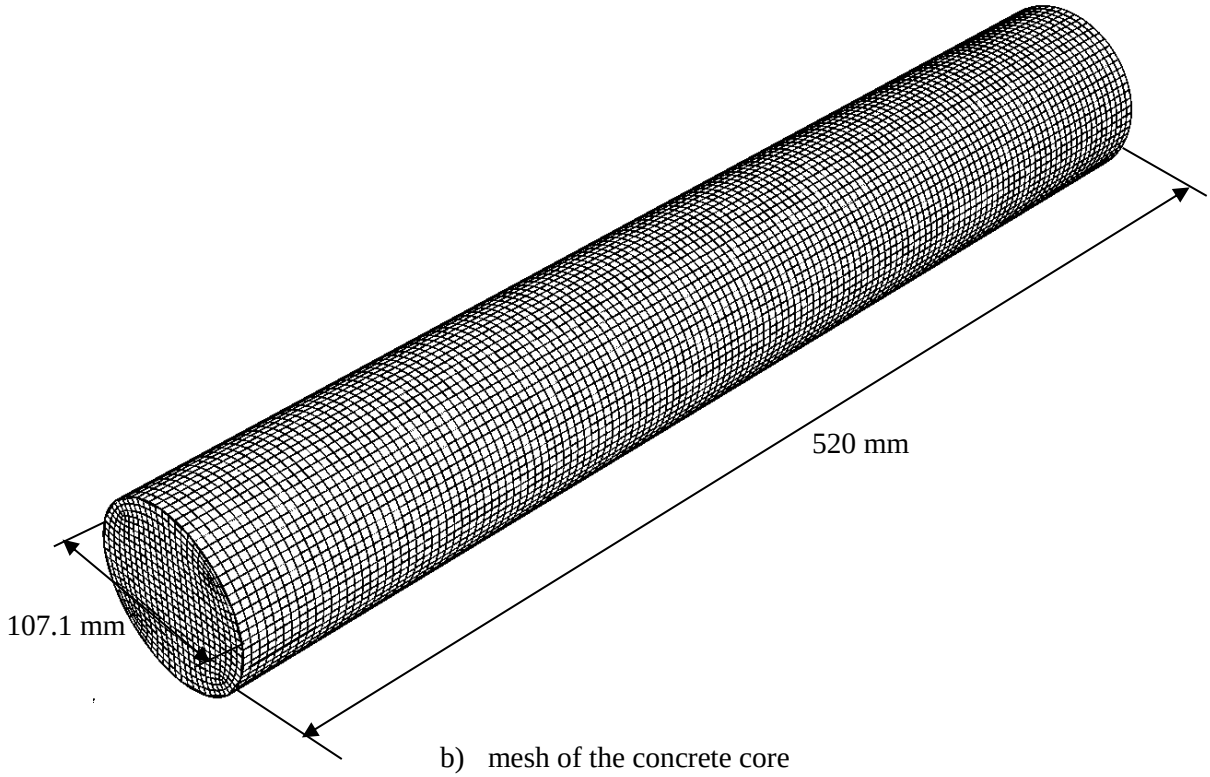

b) mesh of the concrete core

Figure 5.2. The mesh, boundary and loading conditions of the CFST column

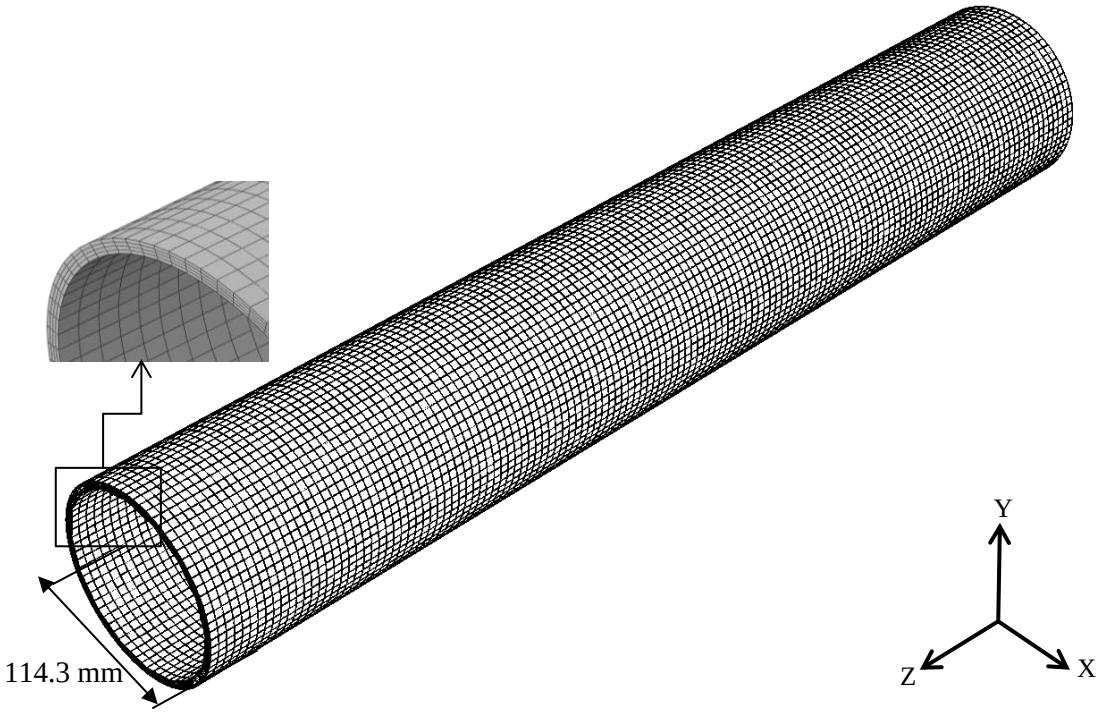

c) mesh of the steel tube

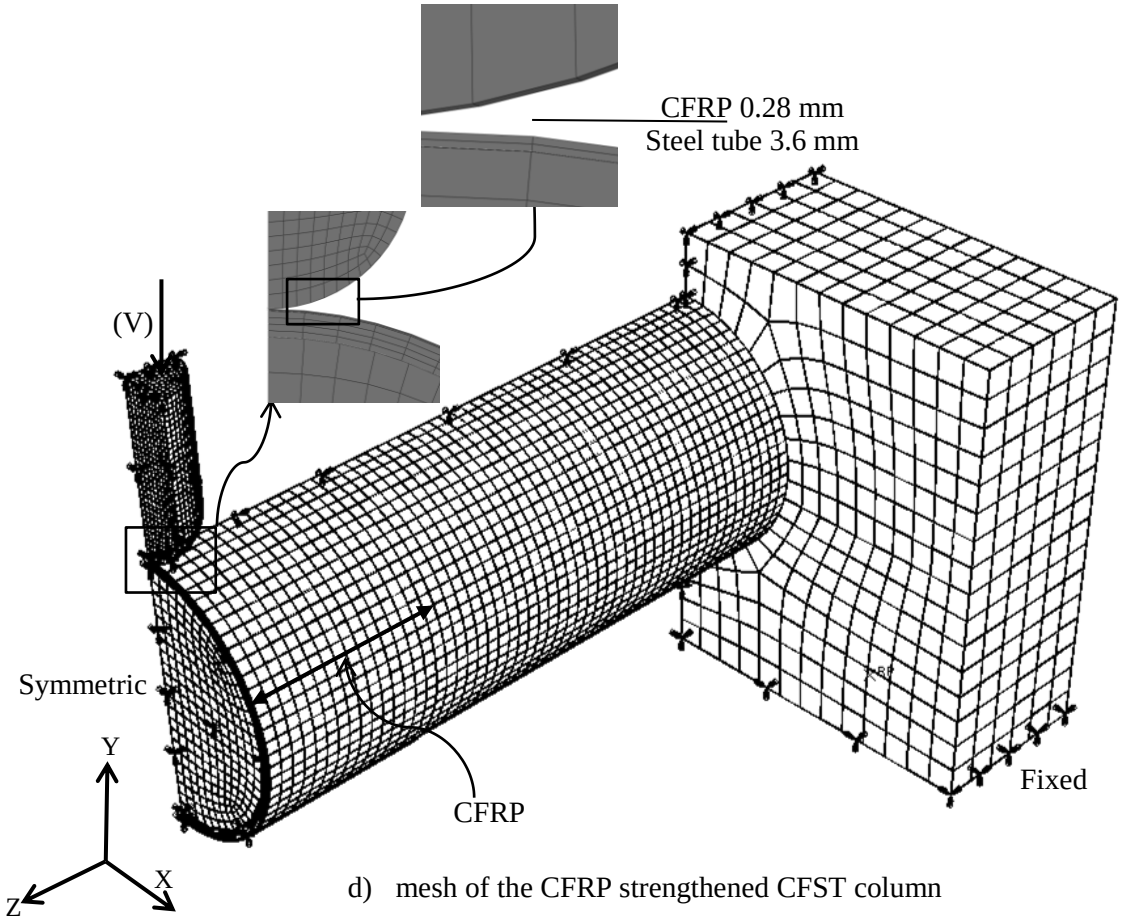

d) mesh of the CFRP strengthened CFST column

Figure 5.2 (Continued). The mesh, boundary and loading conditions of the CFST columns

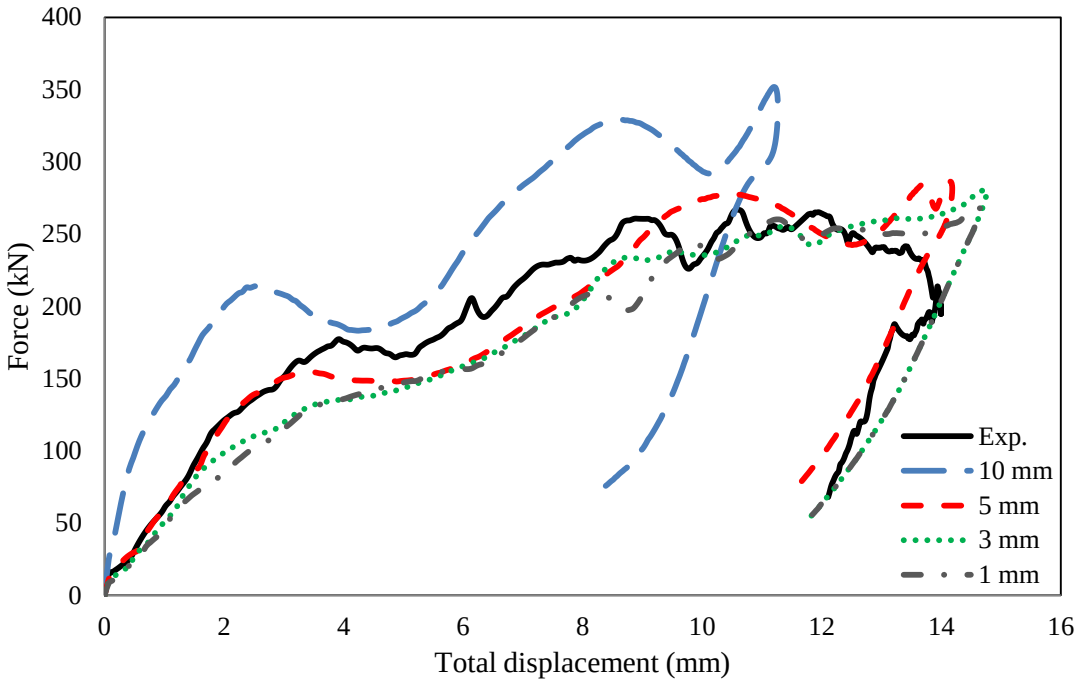

Figure 5.3. The element size effect on the accuracy of the numerical model

5.2.2 Boundary conditions and loading

To simulate the experimental test conditions, the bottom face of the steel clamp was restrained in all directions to provide a fully fixed end which mimics the experimental conditions, while the tube ends were free, as shown in Fig. 5.2 (a). The impactor was restrained against all degrees of freedom, except for the vertical displacement, i.e. Ux = Uz = URx = URy = URz = 0 and Uy ≠ 0. As mentioned earlier, only a quarter of the strengthened CFST columns were modeled. Thus, the impactor, steel clamp, concrete core, steel tube and CFRP were restrained in the x-y plane and y-z plane as symmetric conditions, as shown in Fig. 5.2 (d). The impactors were modelled with masses of 106, 106.5, 107, and 107.5 kg for samples of SI, MI, FI, and BI, respectively. The initial velocity which was calculated based on the initial impact energy from the experimental tests was applied to the impactor, with an only degree of freedom in the y direction. The dynamic step time was set according to the experimental test data for each test, i.e. 12, 16, and 20 ms for the short, medium and long tubes, respectively.

5.2.3 Interaction and contact condition

The interaction between the steel tube and the steel clamp was defined as surface to surface contact with penalty contact properties. The contact was assumed "hard" with separation possibility after getting into contact and the tangential behaviour adopted with a coefficient of friction of 0.01. The influence of the coefficient between the steel tube and the clamp was studied and the results will be discussed later in Section 5.4.2. The same contact properties were used for the interaction between the steel tube and the impactor and between the impactor and the CFRP layer. Figs. 5.4 and 5.5 show the effect of the coefficient of the friction between the impactor and the steel tube and between the CFRP and the impactor, respectively. It can be seen that with increasing the friction coefficient, the impact force and the total displacement increased slightly. However, the numerical results with the coefficient of frictions of 0.01 appear to have a reasonable agreement with the experimental data.

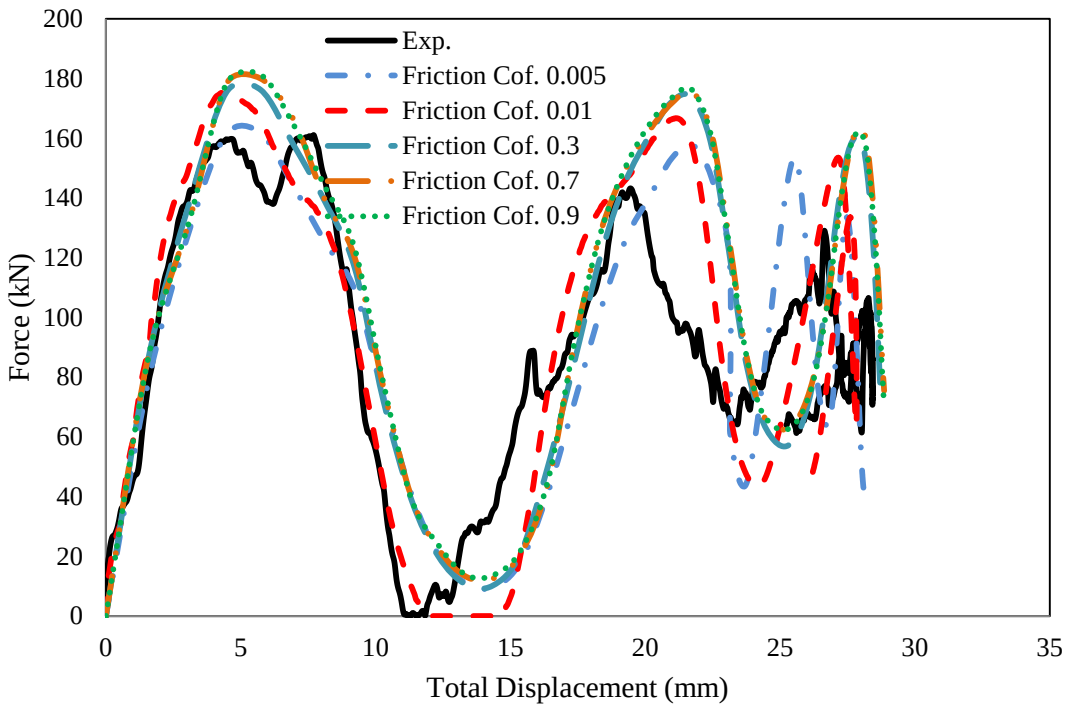

Figure 5.4. The influence of the coefficient of friction between the impactor and the steel tube on the behaviour of the CFST columns

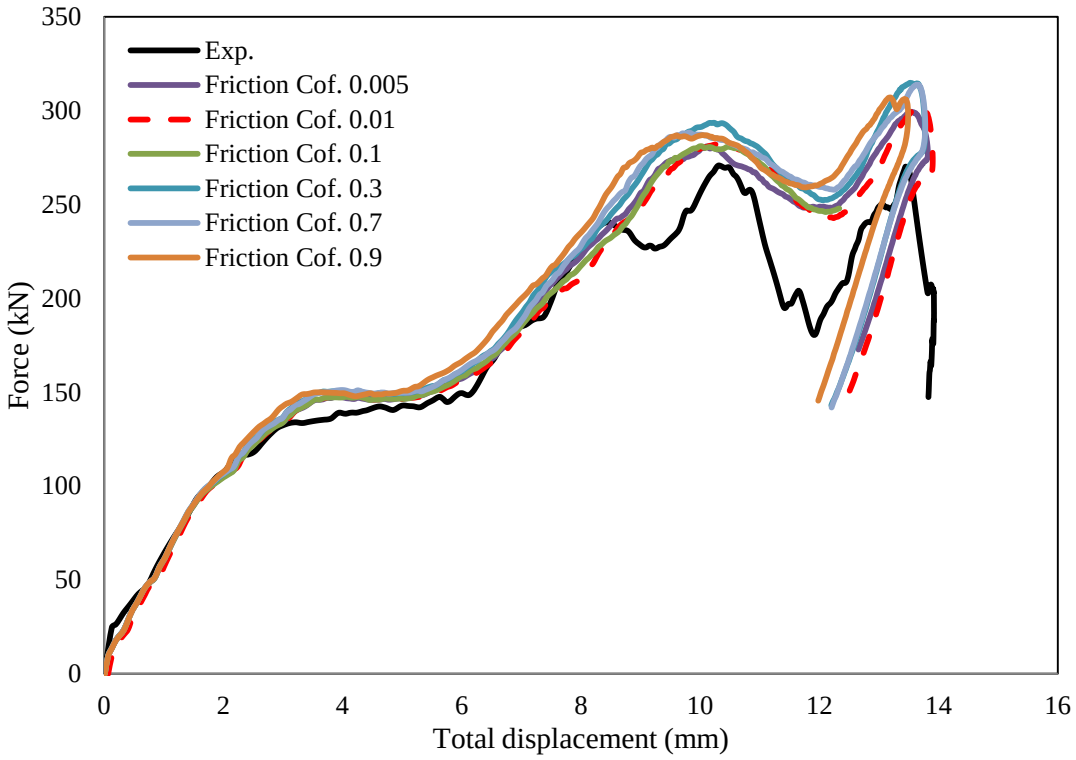

Figure 5.5. The influence of the coefficient of friction between the impactor and the CFRP on the behaviour of the CFST column

The contact pair algorithm is also used to specify the contact between the concrete core and the steel tube. The surfaces on the external face of the impactor and the tube were defined using the element based surface. For the contact pair surfaces, the surface of the stiffer body is set as a master surface and the other one as the slave surface (ABAQUS documentation, 2015). Thus, the concrete surface was selected as the slave one when it is in contact with steel (master surface), while the impactor was selected as a master surface when it is in contact with steel tube (slave surface) as shown in Fig. 5.6. When the contact occurs between a relatively rigid body and a deformable one with improper meshing, the slave surface is likely to over penetrate the slave surface as can be seen from Fig. 5.7. To avoid the penetration of the slave surface by the face of the master surface due to using the pure master-slave contact, a fine mesh was defined between the steel tube and concrete core.

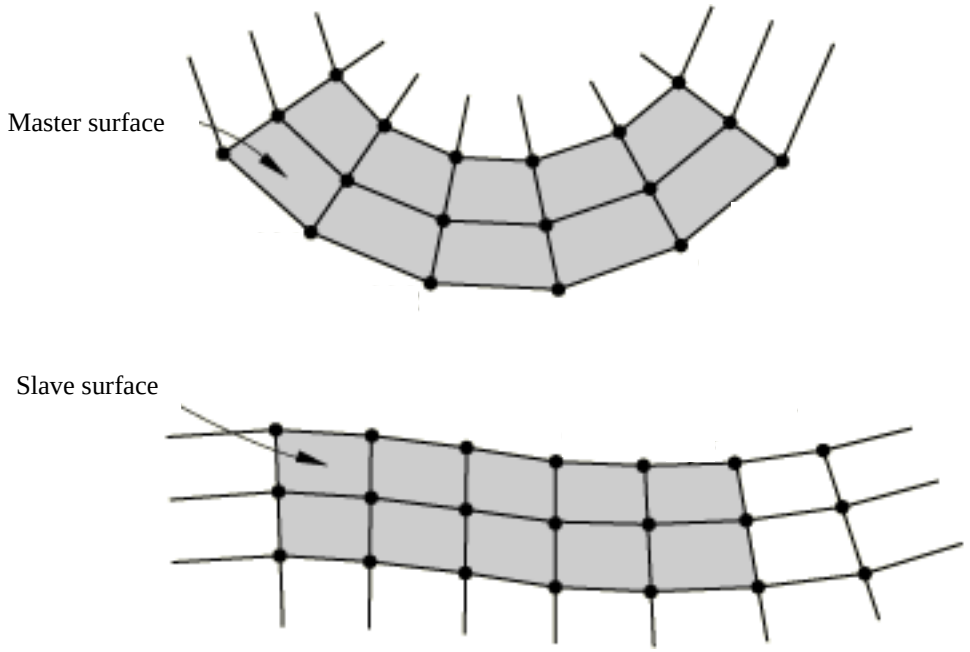

Figure 5.6. A contact pairs master and slave surface (ABAQUS documentation 2015)

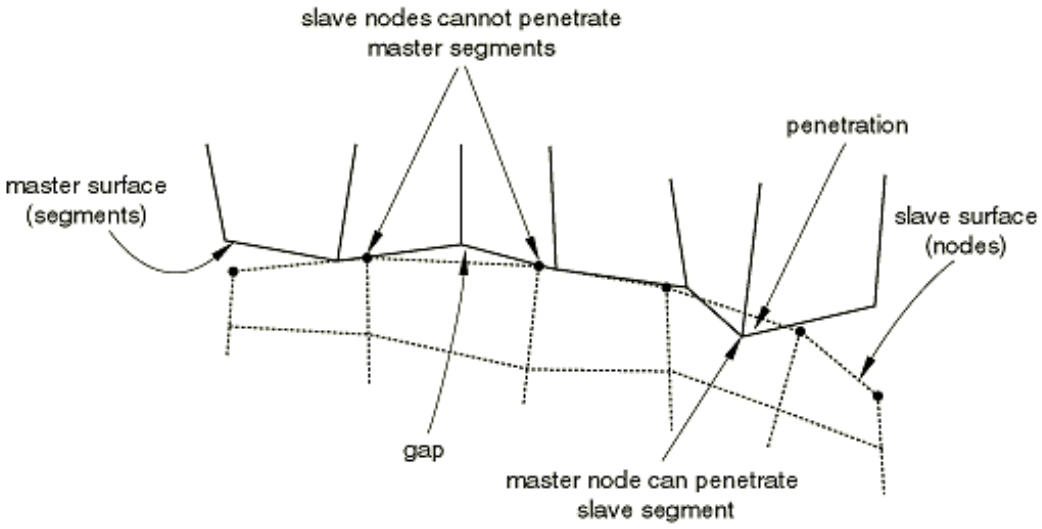

Figure 5.7. The penetration of the slave surface by the master surface due to the use of the coarse mesh with the master-slave contact pair (ABAQUS documentation 2015)

A linear pressure over closure contact in the normal direction and a friction contact with a coefficient of friction of 0.2 in the tangential direction was assumed between the concrete core and the steel tube. The influence of the coefficient of friction between the concrete core and the steel tube was examined. Fig. 5.8 shows that the coefficient of friction has some influence on the impact behaviour of the CFST column, except for the frictionless contact

which showed a significant effect on the total displacement and impact force. Compared with the experimental results, without considering friction the predicted maximum force decreased by 17 %, while the total displacement increased by 22 %. The coffiecint of friction between the steel tube and the concrete is between 0.2 to o.6 (Zhu et al., 2016; Xiang et al., 2016)

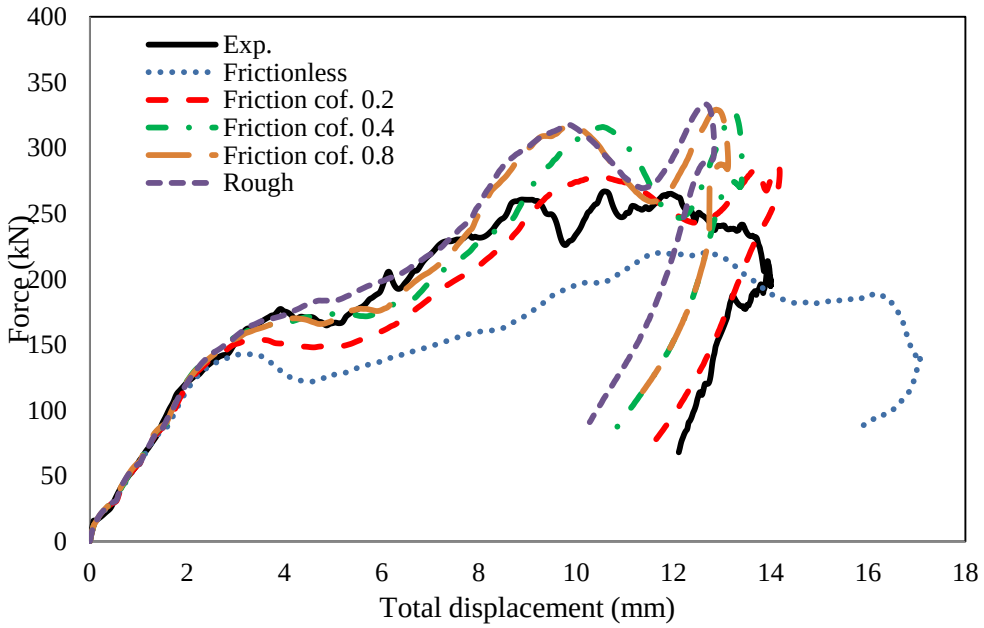

Figure 5.8. The influence of the coefficient of friction on the behaviour of the CFST column

The contact between the CFRP layer and the steel tube was defined with a penalty contact and finite sliding formulation. The tangential behaviour between the CFRP and the steel tube was defined with a coefficient of friction of 0.8 to simulate the bonding condition, while the normal behaviour was assumed to be hard contact with allowable separation after contact. To investigate the influence of the coefficient of the friction between the CFRP and the steel tube, the model was run with different values of friction from frictionless to rough. It was found that that friction has little effect on the behaviour of the strengthened CFST column. However, with frictionless contact properties between the CFRP and the steel tube, the force was less and the total displacement was higher than those captured by the experimental test. The force was slightly higher and the total displacement was slightly

lower than that of the model with coefficient of friction of 0.8. It was found that a reasonable agreement between the experimental results and the numerical ones with using coefficient of friction of 0.8 as shown in Fig. 5.9. Thus, the coefficient of friction of 0.8 between the CFRP and the steel tube was adopted in this study.

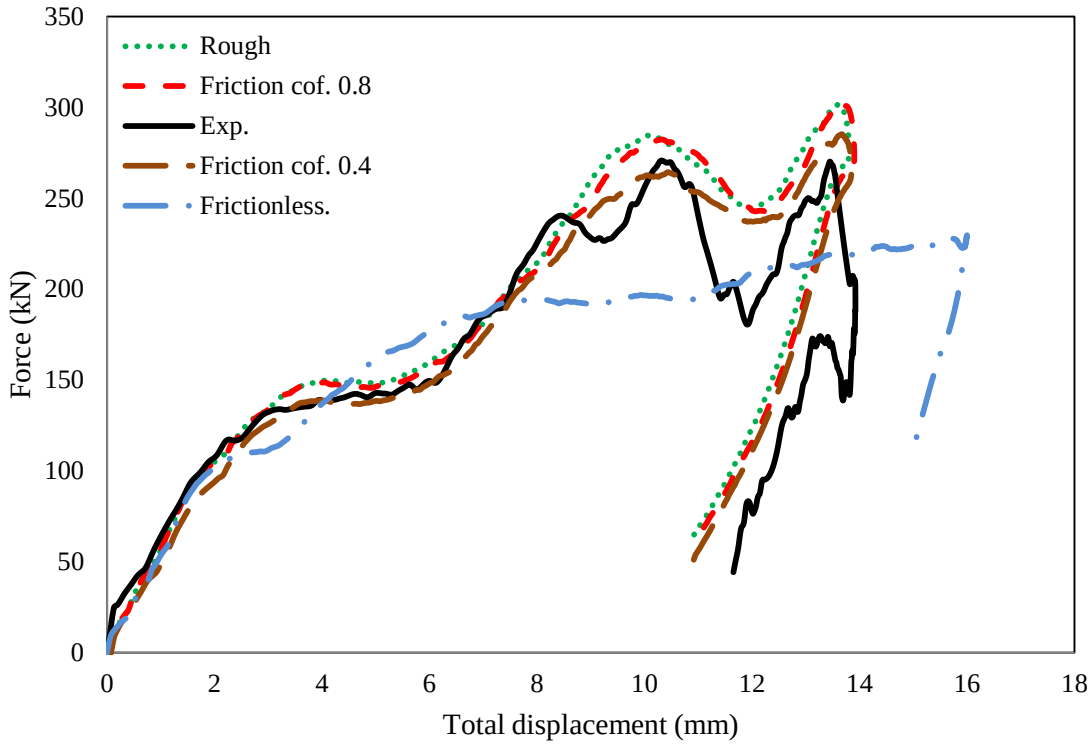

Figure 5.9. The influence of the coefficient of friction between the CFRP and the steel tube on the behaviour of the CFST column

5.2.3.1 Contact force calculations

The development of impact force between the impactor and the CFST column due to impact loading takes a very short time, which depends on the velocity of the impactor at the contact time, the type and the mechanical characteristics of the contact between the impactor and the CFST column and the dynamic and material properties at the time of the impact. Once the two bodies, i.e. impactor and steel tube, separate, the contact force (impact force) disappears. Thus, it is very important to define an accurate simulation for the contact between the bodies contacted to produce realistic true impact forces. The penalty method, which is used in ABAQUS to solve the contacts, can be used to determine the contact force

between the impactor and the CFST column by placing normal interface springs to prevent the penetration between the elements of the master and slave surfaces as can be seen in Fig. 5.10. Once a penetration is detected in a time step, an internal force is given by the spring will be applied to prevent the penetration between the master and the slave surfaces. This force is obtained from the contact stiffness and the penetrated distance and it can be written as (Tavrez, 2001):

$$F = k * x \tag{5.5}$$

where x the penetrated distance and k is the contact stiffness which can be obtained from

$$k = P_f A_e^2 K_B / V_e \tag{5.6}$$

where P_f is the penalty stiffness factor, A_e is the area of the element face in contact, K_B is the bulk modulus and the V_e is the element volume.

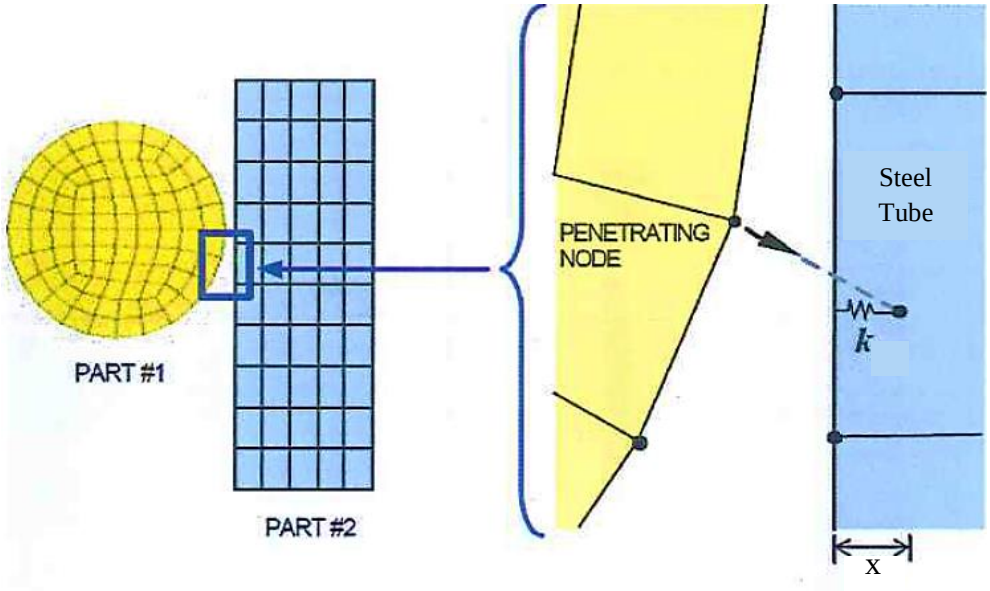

Figure 5.10. The formulation of the contact based on Penalty method (Tavrez, 2001)

5.2.4 Material models

5.2.4.1 Steel

Steel is a widely used material and its properties are well known in tension and compression. The steel tube was modelled as an elasto-plastic martial. The stress-strain curve shown in Fig. 5.11 was adopted in this study to simulate the behaviour of the steel tube. This curve was obtained from the average of three tensile coupon tests in the current study. The "Plastic" option available in ABAQUS is used to simulate the permanent deformation of the steel material. The yield strength, elastic modulus and Poisson's ratio are 450 MPa, 200 GPa and 0.3, respectively. The steel frame was modelled as an elastic perfectly plastic material with yield strength of 500 MPa. The Poisson's ratio and the modulus of elasticity adopted for the steel frame were 0.3 and 200 GPa, respectively.

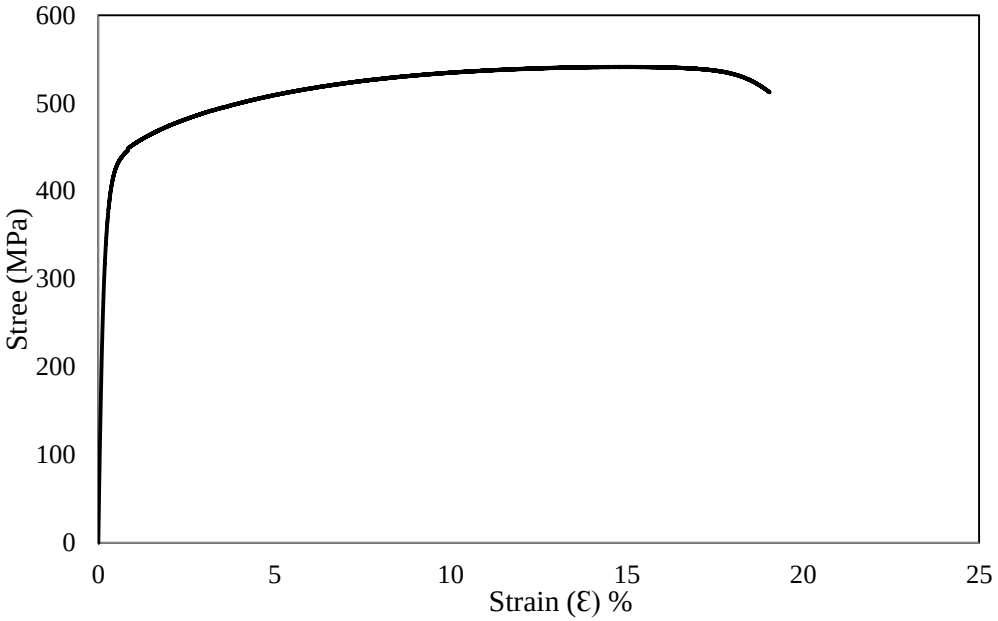

Figure 5.11. Stress-strain curve of the steel tube

5.2.4.2 Concrete core

The concrete damage plasticity (CDP) model available in ABAQUS is utilised in this study to simulate the behaviour of the confined concrete in CFST columns with the tension and compression definitions. Both the elastic and plastic parts are included in the concrete model. The CDP model is based on the assumption that the damage plasticity characterises the failure of concrete in both compressive crushing and tensile cracking, as shown in Fig.

5.12. To represent the plastic behaviour of concrete, the CDP uses the concept of the isotropic damage evolution in combination with isotropic tensile and compressive plasticity. The strain hardening in compression and strain softening in tension as well as the damage initiation in both compression and tension can be defined in this model. Fig. 5.12 (a) shows that under uniaxial tension, the stress-strain is linear up to the failure stress (σ_{t0}). The failure stress starts with the initiation of the micro-cracking in the concrete material and the post failure stress is characterised by a softening stress-strain response. Under uniaxial compression, the stress-strain response follows a linear elastic relationship until the value of the failure stress (σ_{c0}). The strain hardening followed by stress softening represents the concrete response beyond the ultimate stress (σ_{cu}), as shown in Fig 5.12 (b) (ABAQUS documentations. 2015).

The elastic stiffness of the material may be damaged or weakened due to unloading the concrete sample within the stress softening part of the stress-stress relationship. This degradation is represented by two damage variables (d_t and d_c) which are assumed to be functions of the equivalent plastic strains in tension and compression $\left(\varepsilon_t^{pl}, \varepsilon_c^{pl}\right)$, temperature ($\Theta$), and field variables ($f_i$), i.e.

$$d_t = d_t\left(\varepsilon_t^{pl}, \theta, f_i\right) \quad 0 \le d_t \le 1 \tag{5.7}$$

$$d_c = d_c\left(\varepsilon_c^{pl}, \theta, f_i\right) \quad 0 \le d_c \le 1 \tag{5.8}$$

The damage index can take values from zero, which represents the undamaged material, to one, which represents the complete failure. In this study, it is assumed that the tensile and compressive damage d_t and d_c can be calculated respectively by

$$d_t = 1 - \frac{\sigma}{f_t} \tag{5.9}$$

$$d_c = 1 - \frac{\sigma}{f_c'} \tag{5.10}$$

where σ is the corresponding stress to the specific crack opening displacement and inelastic strain in tension stiffening and compression softening range, respectively. f_t and fc' are the

maximum tensile and compressive strengths of concrete, respectively. Under uniaxial tension and compression loading, the relationship between the stress and the strain for the concrete with initial elastic stiffens of E_0, may be expressed as, respectively

$$\sigma_t = (1 - d_t)E_0\left(\varepsilon_t - \varepsilon_t^{pl}\right) \tag{5.11}$$

$$\sigma_c = (1 - d_c)E_0\left(\varepsilon_c - \varepsilon_c^{pl}\right) \tag{5.12}$$

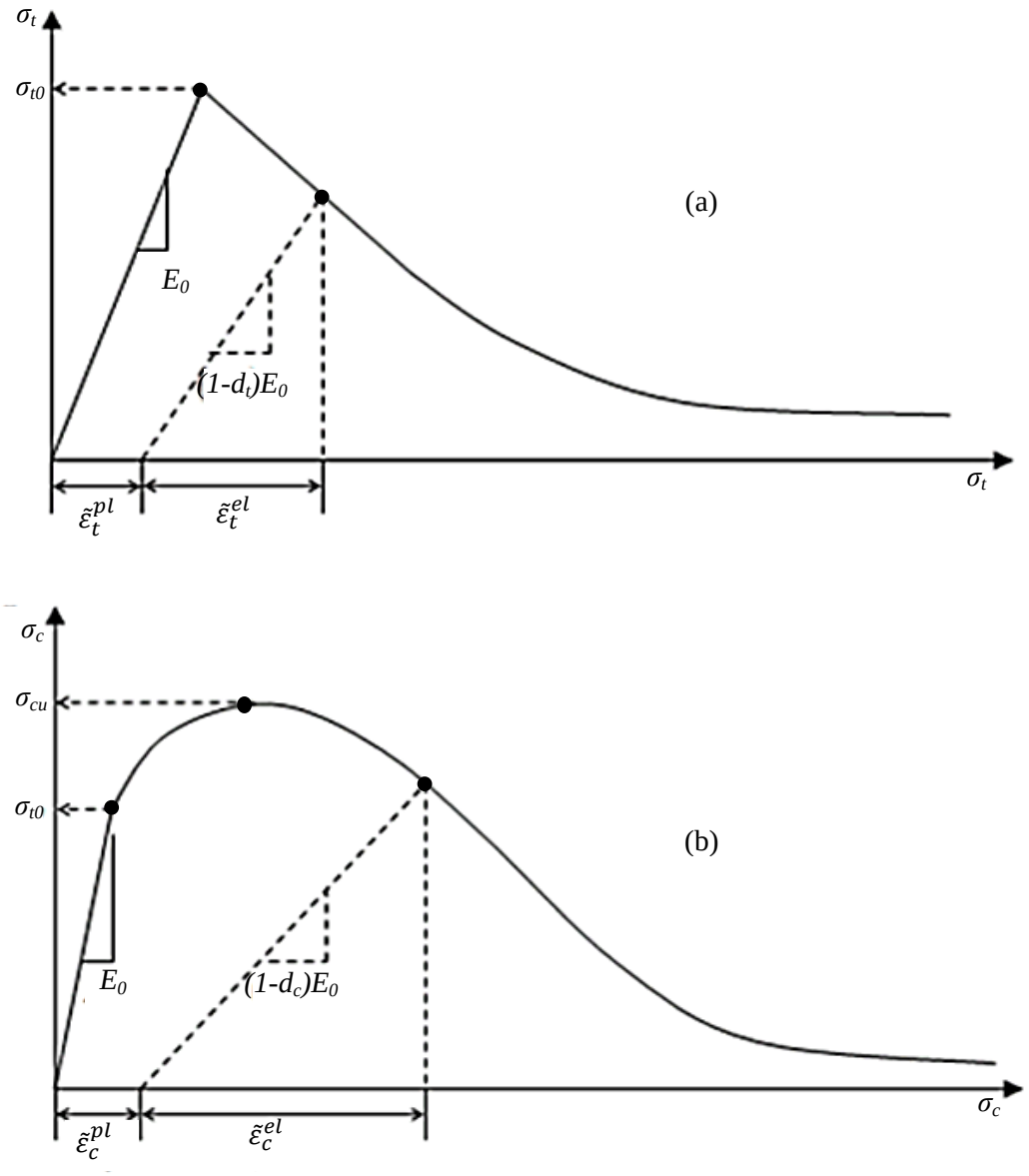

Figure 5.12. Concrete response to uniaxial loading in tension (a) and compression (b) (ABAQUS 6.12 user manual, 2012)

To simulate the confined concrete properties, the confined concrete stress-strain relationship described by Hu et al. (2003) is adopted in this study. Ellobody et al. (2006) and Dai and Lam (2010) adopted this model in their numerical analyses, where the finite element results showed a good agreement with the corresponding experimental data. The difference between the stress-strain relationships of the confined and the unconfined concrete is shown in Fig. 5.13.

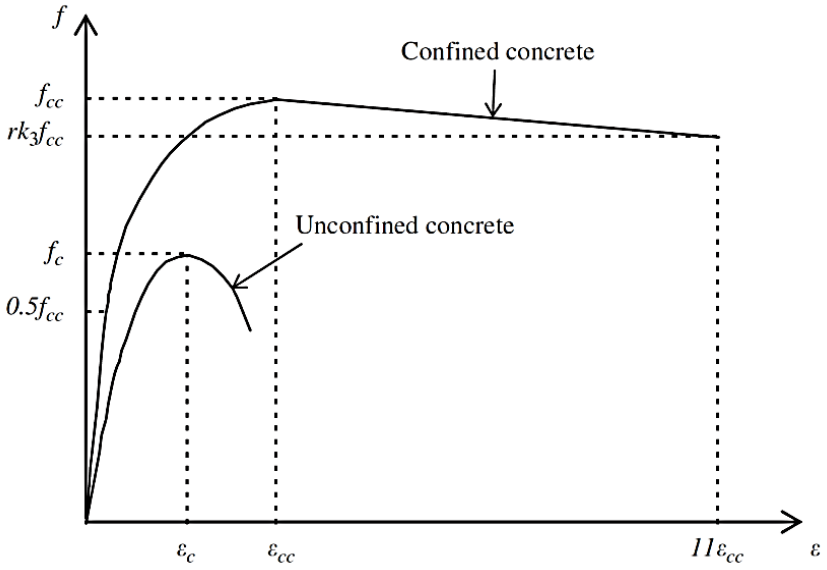

Figure 5.13. Stress-Strain relationship for confined and unconfined concrete (Dai and Lam, 2010)

The f_{ck} is the cylinder compressive strength of the unconfined concrete which is equal to 80 percent of the unconfined cube strength $0.8f_{ck,\ cube}$, while f_{cc} is the cylinder compressive strength of the confined concrete. ε_{ck} and ε_{cc} are the corresponding strain for f_{ck} and f_{cc}, respectively. The axial compressive strength for the confined concrete in the structural hollow section can be predicted by the proposed relationship between f_{cc} and f_{ck} (Mander and Priestley,1988).

$$f_{cc} = f_{ck} + k_1 f_l \tag{5.13}$$

$$\varepsilon_{cc} = \varepsilon_{ck}\left(1 + k_2 \frac{f_l}{f_{ck}}\right) \tag{5.14}$$

Richart et al. (1928) suggested the value of the constants k_1 and k_2 to be 4.1 and 20.5, respectively and the strain of unconfined concrete $\mathcal{E}_{ck}$ can be taken as 0.003. Based on the formulae proposed by Hu et al. (2003), the value of the lateral stress f_l can be predicted as:

$$f_l/f_y = 0.043646 - 0.000832(D/t) \qquad for\ 21.7 \le D/t \le 47 \tag{5.15}$$

$$f_l/f_y = 0.006241 - 0.0000357(D/t) \qquad for\ 47 \le D/t \le 150 \tag{5.16}$$

where D is the external diameter of the tube, t is the wall thickness of the tube and f_y is the yield strength of the steel tube. Hu et al. (2003) and Ellobody et al. (2006) suggested the proportional limit stress for the linear part in the confined concrete stress-strain curve (elastic) to be $0.5f_{cc}$. The modulus of elasticity for the confined concrete E_{cc} can be predicted by the ACI (1999) empirical formula, which is expressed as $E_{cc} = 4700\sqrt{f_{cc}}$ MPa (Dai and Lam 2010). The nonlinear portion of the curve represents the compressive strength f between the elastic limit $0.5f_{cc}$ and the maximum compressive strength f_{cc}. Saenz (1964) suggested the following formula to predict f:

$$f = \frac{E_{cc}\varepsilon}{1+(R+R_E-2)\left(\frac{\varepsilon}{\varepsilon_{cc}}\right)-(2R-1)\left(\frac{\varepsilon}{\varepsilon_{cc}}\right)^2+R\left(\frac{\varepsilon}{\varepsilon_{cc}}\right)^3} \tag{5.17}$$

where

$$R_E = \frac{E_{cc}\varepsilon_{cc}}{f_{cc}}, R = \frac{R_E(R_\sigma-1)}{(R_\varepsilon-1)^2} - \frac{1}{R_\varepsilon}, R_\sigma = R_\varepsilon = 4$$

The start of the third portion of the strain-stress curve is f_{cc}, while its end is $f_u = rk_3f_{cc}$. The correspondence strain for f_u is '$\varepsilon_u = 11\varepsilon_{cc}$' is (Hu et al., 2003; Ellobody and Young, 2006b; Ellobody et al., 2006 and Dai and Lam, 2010). For the circular steel tube section with $21.7 \le (D/t) \le 150$, the value of the parameter k_3 can be obtained from Eq. (5.18) or (5.19) proposed by Hu et al. (2003).

$$k_3 = 1 \qquad for\ 21.7 \le (D/t) \le 40 \tag{5.18}$$

$$k_3 = 0.0000339(D/t)^2 - 0.0100085(D/t) + 1.3491 \quad for\ 40 \le (D/t) \le 150 \tag{5.19}$$

According to Giakoumelis and Lam (2004), Ellobody and Young (2006b), Ellobody et al. (2006) and Dai and Lam (2010), the value of r with a compressive cube strength of 30 MPa

can be taken as 1.0, while with compressive strength of 100 MPa as 0.5. Moreover, a linear interpolation can be used with compressive strengths between 30 MPa and 100 MPa.

There are two options to describe the tensile behaviour in concrete damage plasticity model, i.e. stress-strain curve (strain) or stress-crack width curve (displacement). To avoid the mesh-dependent results, the tensile behaviour for the concrete is defined using the option displacement in this study using the model proposed by Li et al. (2002) which was adopted by Liu (2008). The stress-crack width relationship can be expressed as:

$$\sigma = f_t \left\{ 1 - exp\left[-\left(\frac{0.05}{w_c / w_{ccr}} \right)^{1.3} \right] \right\} \tag{5.20}$$

where *ft* is the tensile strength of concrete and it is obtained from the equation proposed by Li el al. (2002) as

$$f_t = 0.34\sqrt{fc'} \tag{5.21}$$

where *fc'* is the compressive strength of concrete.

The w_c and w_{ccr} are the crack width and the critical crack width, respectively. Here, 1.5 mm is taken for the critical crack width in this study as it was recommended by Begum (2007) and Liu (2008). The stress-crack width curve is shown in Fig. 5.14.

The Poisson's ratio for the concrete under uniaxial tension is slightly lower than that in compression, while the modulus of elasticity is slightly higher than that of the corresponding elastic modulus in compression (Mehta, 1986). In this study, Poisson's ratio of the concrete is taken as 0.2.

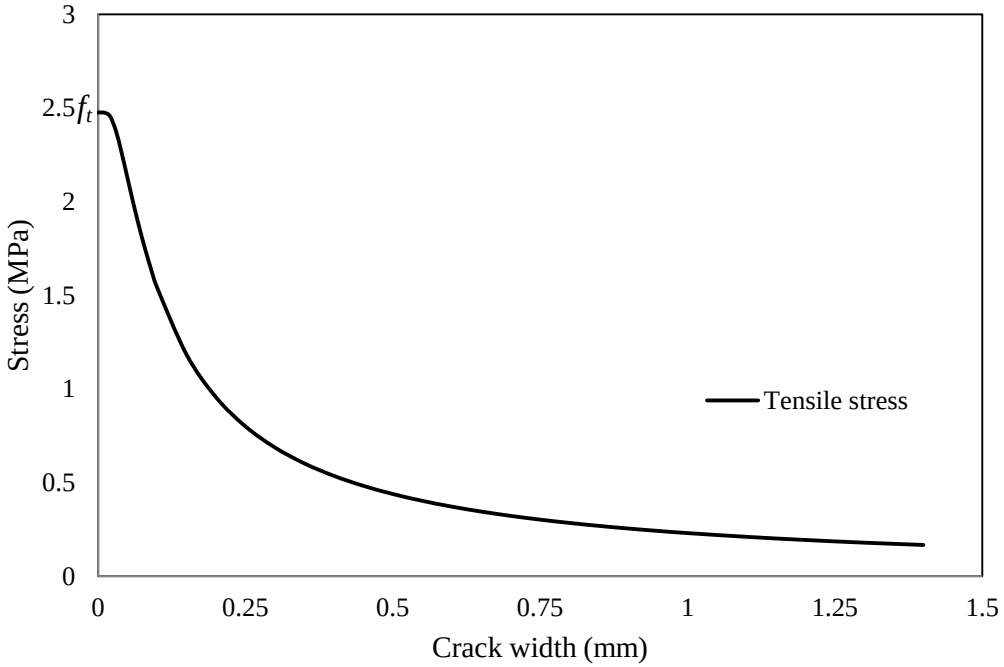

Figure 5.14. Concrete material behaviour model in tension

To complete the CDP model, five other parameters need to be defined which are the dilation angle, the flow potential eccentricity, the ratio of initial equibiaxial compressive yield stress to initial uniaxial compressive yield stress, the ratio of the second stress invariant on the tensile meridian, to that on the compressive meridian and viscosity parameter (K_c). The selected values of these parameters mentioned the above are 20^o, 0.0, 1.16, 0.667 and 0, respectively.

In ABAQUS, the range of the dilation angle is between 0 to 56° and most of the researchers used the one between 20°-30° (Tao et al., 2013). Fig. 5.15 shows the effect of the dilation angle on the impact behaviour of the CFST column. It can be seen that the impact force increased and the total displacement decreased with an increase in the dilation angle. Very good agreement between the numerical and experimental results was obtained with the dilation angle of 20° which is adopted in this study.

Tao et al., (2013) found that the default values for the flow potential eccentricity and for the ratio of initial equibiaxial compressive yield stress to initial uniaxial compressive yield stress which are 0.0 and 1.16, respectively. They can be used with the CDP model because

they have no influence on the concrete response. Thus, the default values of these parameters are adopted in this study.

To study the influence of the parameter K_c on the impact response of the CFST column, a sensitivity study was carried out and the results are shown in Fig. 5.16. It can be seen that with anincrease in the parameter K_c, the impact force decreased and the total displacement increased slightly. Thus, the default value of K_c (0.667) is chosen in this study which showed the most reasonable agreement with experimental data.

The viscosity parameter with the CDP model is ignored in ABAQUS/Explicit and the default value is 0.0. (ABAQUS Documentation, 2015).

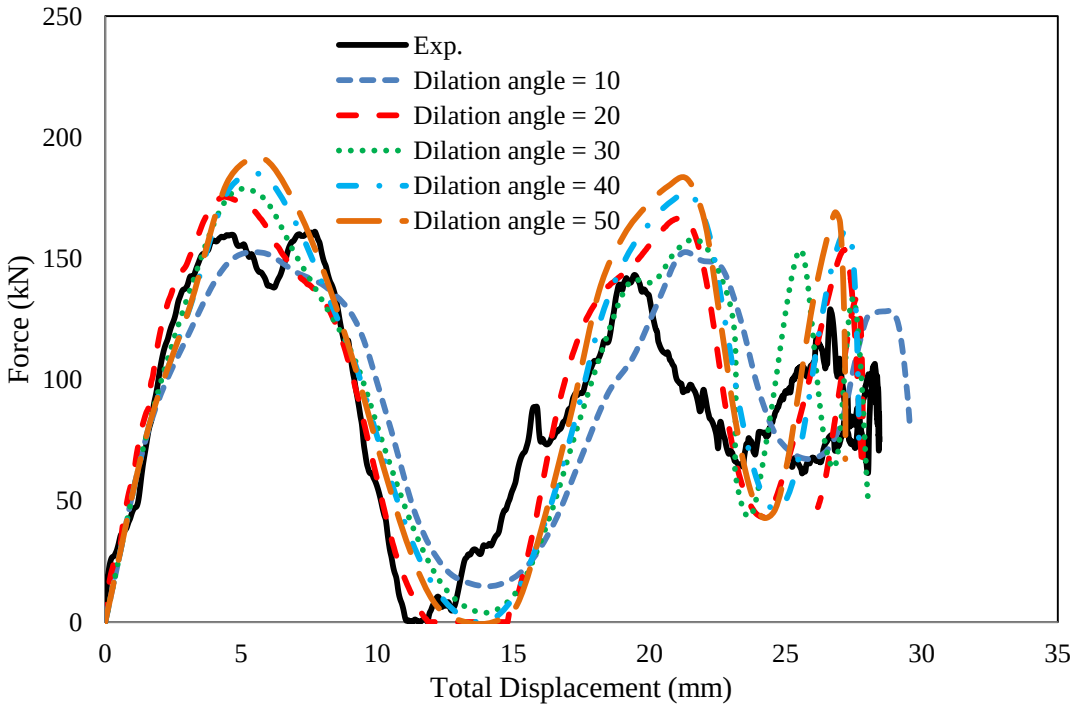

Figure 5.15. The influence of the dilation angle on the impact response of the CFST column

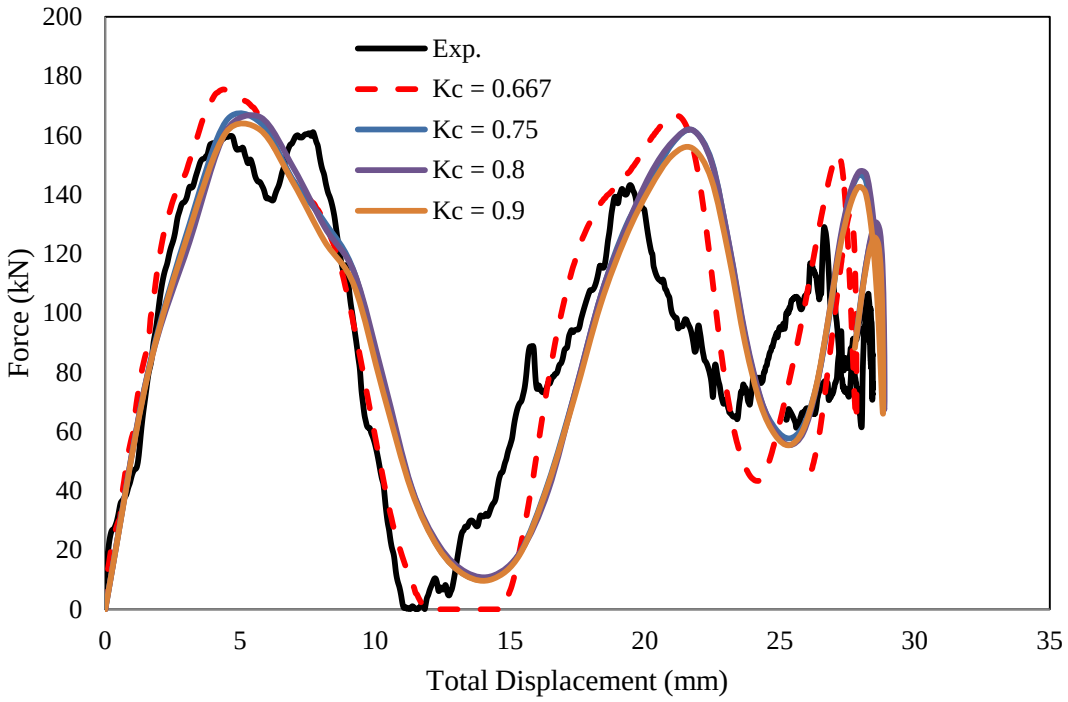

Figure 5.16. The influence of the dilation angle on the impact behaviour of the CFST column

5.2.4.3 Carbon fibre reinforced plastic

The elastic properties and the damage initiation data of the CFRP, which were used in the current finite element analysis, are listed in Table 5.1. Orthotropic elasticity with engineering constants was used to simulate the elastic response of the CFRP layer. The in-plain transverse modulus of elasticity was assumed to be equal to the longitudinal Young's modulus due to the woven nature of the composite. Hence, the in-plane and transverse shear modulus and Poisson's ratio are assumed to be equal. Fig. 5.17 shows the linear elastic response of the CFRP under tensile loading.

Table 5.1. Summary of elasticity properties and the damage initiation data for the CFRP (Rejab, 2013)

E_{11} (GPa)	E_{22} (GPa)	E_{33} (GPa)	ν_{12}	ν_{13}	ν_{23}	G_{12} (GPa)	G_{13} (GPa)	G_{23} (GPa)
48	48	10	0.1	0.1	0.1	5	5	5
X^T (MPa)	X^C (MPa)	Y^T (MPa)	Y^C (MPa)	S^T (MPa)	S^L (MPa)	$G_{ft} = G_{mt}$ (J/m^2)		$G_{fc} = G_{mc}$ (J/m2)
550	150	550	150	120	120	42700*		44970*

* (Zhou, 2015)

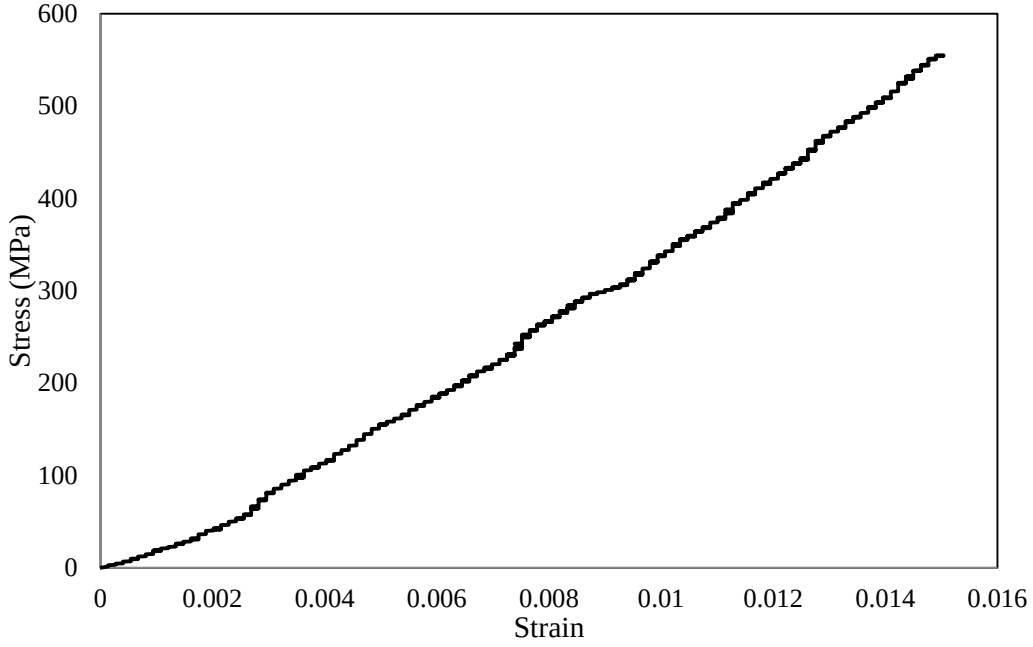

Figure 5.17. Typical tensile stress-strain relationship of the CFRP tested

Hashin's failure criteria was used to model the damage initiation and failure of the CFRP (Hashin, 1973). The stress-strain relationship of the material with the degradable stiffness matrix is given below:

$$\sigma = C_d \varepsilon \tag{5.22}$$

where C_d is the damage elastic matrix, which can be written as:

$$C_d = \frac{1}{D_h}\begin{bmatrix} (1-d_f)/E_1 & (1-d_f)(1-d_m)v_{21}/E_1 & 0 \\ (1-d_f)(1-d_m)v_{12}/E_2 & (1-d_m)/E_2 & 0 \\ 0 & 0 & (1-d_s)GD_h \end{bmatrix} \tag{5.23}$$

where E_1 and E_2 are the two in-plane moduli of elasticity in woven composite, and G is the in-plane shear modulus. The d_f, d_m and d_s are the current state of fibre, matrix and shear damage, respectively. D_h is overall damage variable which can be expressed as:

$$D_h = 1 - (1-d_f)(1-d_m)v_{12}v_{21} \tag{5.24}$$

Based on the Hashin's damage model, four different damage initiation mechanisms were assumed in the analysis, which are:

Fibre tension($\sigma'_{11} \geq 0$):

$$F_f^t = \left(\frac{\sigma'_{11}}{X^T}\right)^2 + \xi\left(\frac{\sigma'_{11}}{S^L}\right)^2 \tag{5.25}$$

Fibre compression($\sigma'_{11} < 0$):

$$F_f^c = \left(\frac{\sigma'_{11}}{X^C}\right)^2 \tag{5.26}$$

Matrix tension($\sigma'_{22} \geq 0$):

$$F_m^t = \left(\frac{\sigma'_{22}}{Y^T}\right)^2 + \left(\frac{\sigma'_{12}}{S^L}\right)^2 \tag{5.27}$$

Matrix compression($\sigma'_{22} < 0$):

$$F_m^c = \left(\frac{\sigma'_{22}}{2S^T}\right)^2 + \left[\frac{Y^C}{2S^T} - 1\right]\frac{\sigma'_{22}}{Y^C} + \left(\frac{\sigma'_{12}}{S^L}\right)^2 \tag{5.28}$$

where X_T, X_C and Y_T, Y_c are the tensile and compressive strength in the longitudinal and transverse directions, respectively. S_L and S_T are the longitudinal and transverse shear strength. ξ is the coefficient which determines the contribution of the shear stress to the fibre tensile failure initiation criterion. Beyond the level in which the damage initiation criterion is satisfied, the increase of the loading will lead to degrade the stiffness coefficient of the material. The damage variable which assumes a range from undamaged to a fully damaged state with values between 0 and 1 will monitor the reduction of the coefficient of the stiffness. This damage variable corresponding to a specific failure mode can be expressed as:

$$d = \frac{\delta_{eq}^f(\delta_{eq} - \delta_{eq}^0)}{\delta_{eq}(\delta_{eq}^f - \delta_{eq}^0)} \tag{5.29}$$

where δ_{eq}^0 is the initial value of the equivalent displacement, which is required to achieve the damage initiation criterion for a specific mode. δ_{eq}^f is the damage displacement.

To introduce a linear damage evolution law, the fracture energies for fibre tension G_{ft}^{F}, fibre compression G_{fc}^{F}, matrix tension G_{mt}^{F} and matrix compression G_{mc}^{F} need to be set before running the numerical analysis to indicate the energy dissipated during the damage process (Table 5.1).

5.2.5 Simulation of the impact loading

ABAQUS/Explicit provides good features which enable the user to simulate and solve the impact problems by using an explicit dynamic finite element formulation. The experimental work conditions of the lateral impact tests were considered in the modelling to provide accurate and realistic results. The initial impact energy was considered by defining the mass of the impactor using the option "inertia" and pre-defining the initial impact velocity which is obtained from the experimental findings. The impact period can be set in the dynamic explicit step. Here, the impact time was set slightly longer than the experimental one to ensure the simulation of the complete failure of the CFST column. By utilizing the contact interaction between the steel tube and the impactor, the impact force can be obtained by using the suitable contact type and contact properties, while the global and total displacements can be determined using the historical output by requesting the displacement in a specific location.

5.2.6 Explicit dynamic algorithm and explicit time integration

Figure 5.18 shows the computational algorithm procedure used in ABAQUS/Explicit. It can be seen that ABAQUS/Explicit uses an explicit dynamic finite element formulation to integrate the dynamic quantities (velocities, accelerations, strains and stresses) by extracting them kinematically from one current time increment to the next one. This procedure reveals that at the end of any time increment, all the values of the nodal dynamic quantities are based on the same quantities as at the beginning of the current time step.

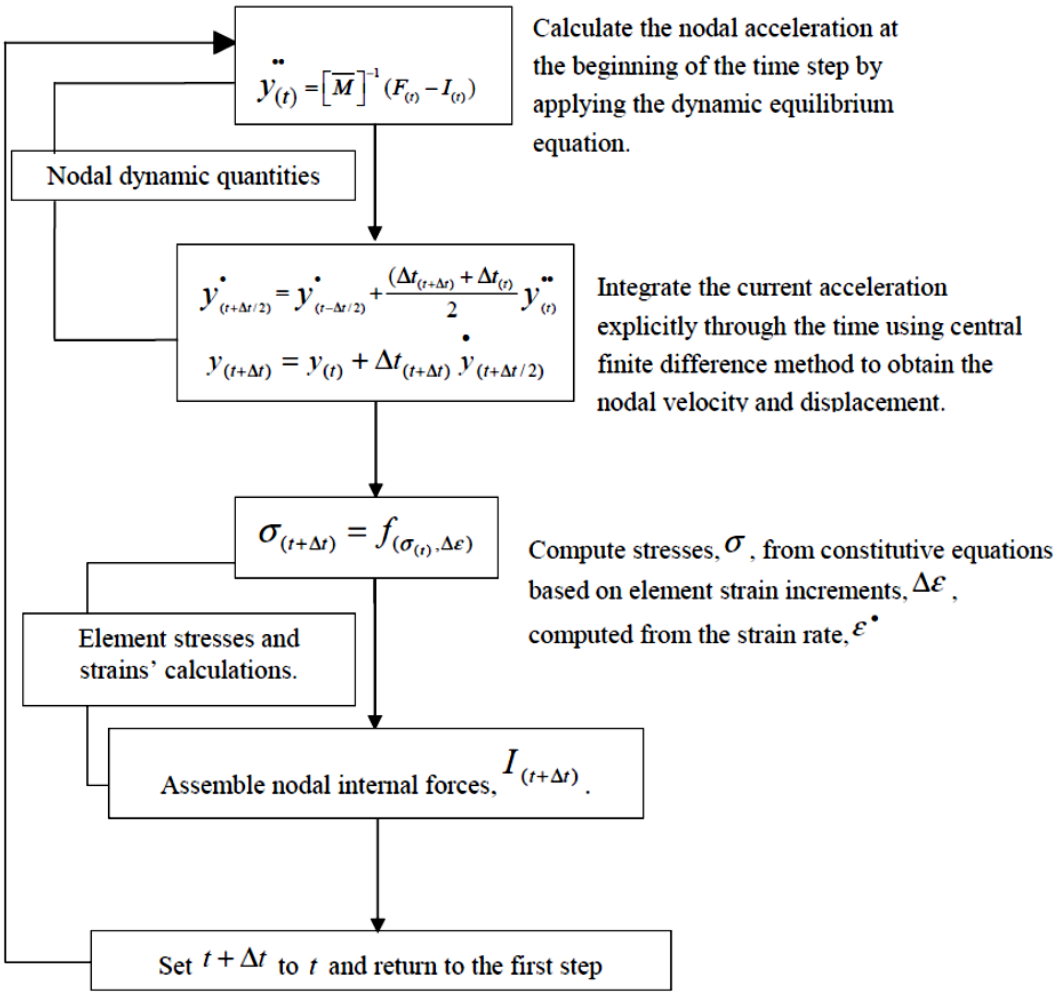

Figure 5.18. The computational algorithm used in ABAQUS/Explicit (Al-Thairy, 2012; ABAQUS documentations, 2016)

in Fig. 5.18,

$\ddot{y}$, $\dot{y}$, y are the nodal acceleration, velocity and deformation respectively;

$[\bar{M}]$ is the total nodal mass matrix of the system;

I is the nodal internal forces of the system;

$F_{(t)}$ is the elements' externally applied forces at the start of the current time step (t);

$\sigma_{(t)}$ is the element stress at the current time step.

for all the numerical modelling in the current study, the time increment is automatically adjusted by using the automatic time increment. The time stability limit is calculated based

on the highest frequency of the individual elements in the system by calculating the maximum time step required for a stable solution

$$\Delta t = \frac{l_e}{c} \tag{5.30}$$

where l_e is the element length taken as the shortest element distance and c is the material wave speed obtained from the equation

$$c = \sqrt{\frac{E}{\rho}} \tag{5.31}$$

where E is the modulus of elasticity of the material, and ρ is the material density.

The l_e for the 8-noded solid element can be defined as

$$l_e = \frac{v_e}{A_{e\,max}} \tag{5.32}$$

where v_e is the element volume and $A_{e\,max}$ is the area of the largest side.

The automatic increment procedure has more control on the progress of the analysis and is more conservative particularly during the initial part of the analysis. No time-step factor was used in this study.

5.2.7 Strain rate effect

As discussed in Section 2.6, due to the low strain rate sensitivity for the associated components of the CFST columns under low velocity impact loading, the strain rate effect has not been considered in this study. Moreover, to prove that the strain rate has a little influence on the impact response of the CFST with no need to consider it in the numerical models of the current study, the CFST column with a L/D ratio of 13.5 was selected to observe the impact behaviour under different strain rates. The equations 2-7, 8, and 9 were used to calculate the dynamic properties of the steel and concrete under compression and tension, respectively. The available option in ABAQUS (* Yield ratio) was used to consider the strain rate with different values in which only the yield ratio with the corresponding

strain rate are required. The strain rate values were 10, 30, 50, 100 s^{-1}. Fig. 5.19 shows the global effect of the strain rate on the material models led to increase the impact load by only 4.3 % and reduce the total displacement by 4.7 % with strain rate of 10 s^{-1}. Increasing the strain rate from 10 to 100 s^{-1} led to increase the impact force by only 3 % and decrease the total displacement by 5.1 %. The local influence of the strain rate is shown in Fig. 5.20. Clearly, the strain rate has more localized effect on the impact response of the CFST column. This is due to the high local deformation under the impactor compared to the global deformation of the CFST column. The impact force increased and the total displacement decreased when the strain rate increased from zero to 100 s^{-1}. These results also reveal that including the strain rate effect in the material models may lead to an overestimate the impact force and an underestimate the total displacement, particularly if the confinement effect is also considered. Therefore, the strain rate was not taken into account in this study and all the presented and discussed results obtained from the numerical models were obtained without considering the strain rate effect.

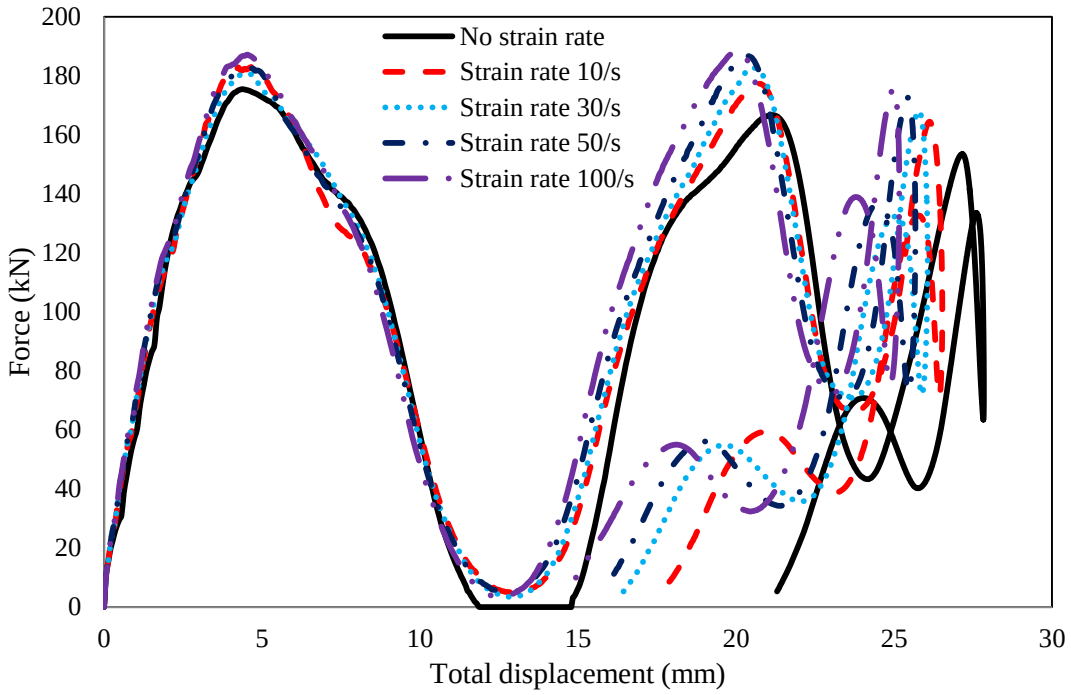

Figure 5.19. The strain rate effect on the global impact response of the CFST columns

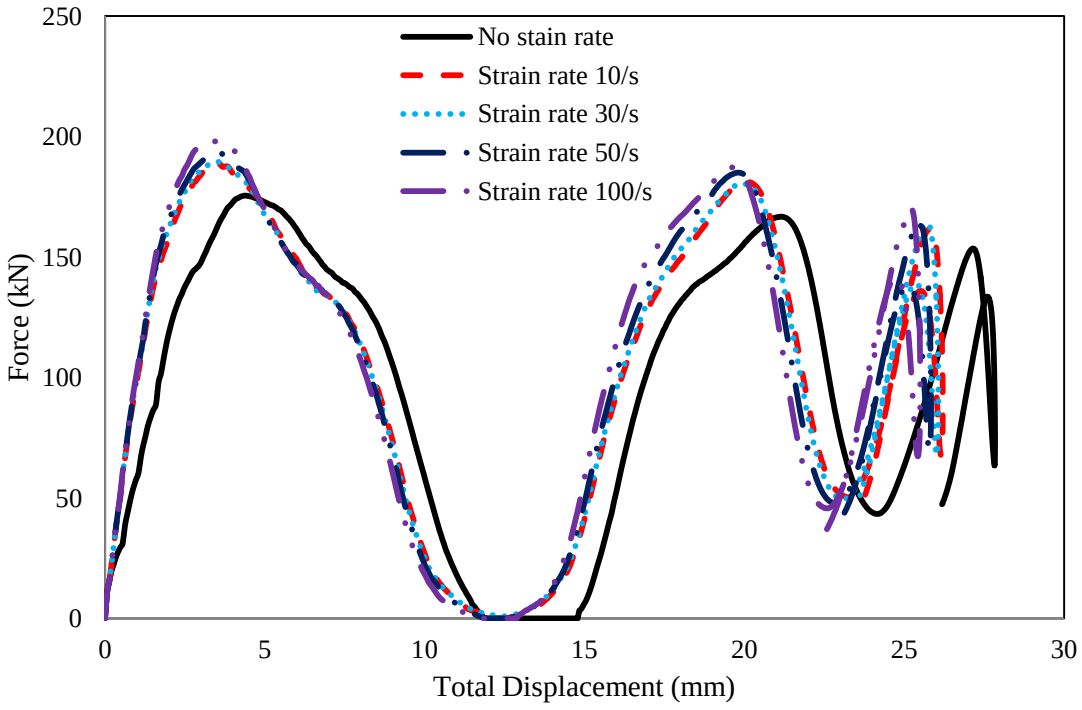

Figure 5.20. The strain rate effect on the local impact response of the CFST columns

5.3 Modelling of CFST columns under compression loading

5.3.1 Element type and mesh size

A full three-dimensional model was used to simulate the behaviour of the CFST columns under concentric and eccentric compression loading, as shown in Figs 5.21 (a) and 5.21 (b), respectively. The C3D8R elements were used to model the concrete core, as shown in Fig 5.22. As explained earlier in Section 5.2.1 on choosing a suitable element type to model the steel tube, the C3D8R elements were also selected to model the steel tube, as can be seen in Fig. 5.22 (c). Two elements were generated through the tube wall thickness. The R3D4 elements were adopted to model the steel end plates. The steel bar was also modelled using the C3D8R elements.

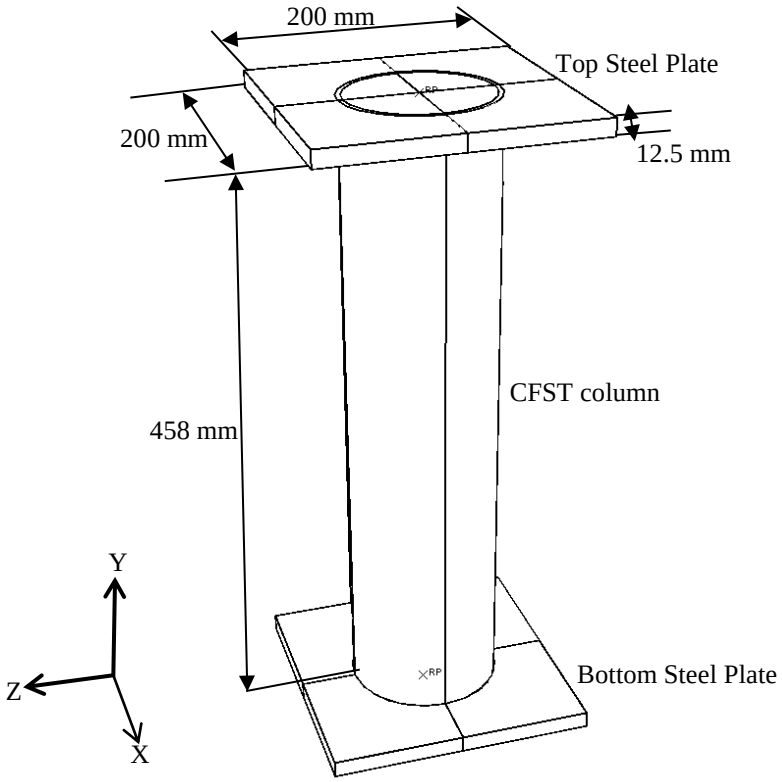

a) geometry of specimen C0

Figure 5.21. Geometric conditions of the CFST columns

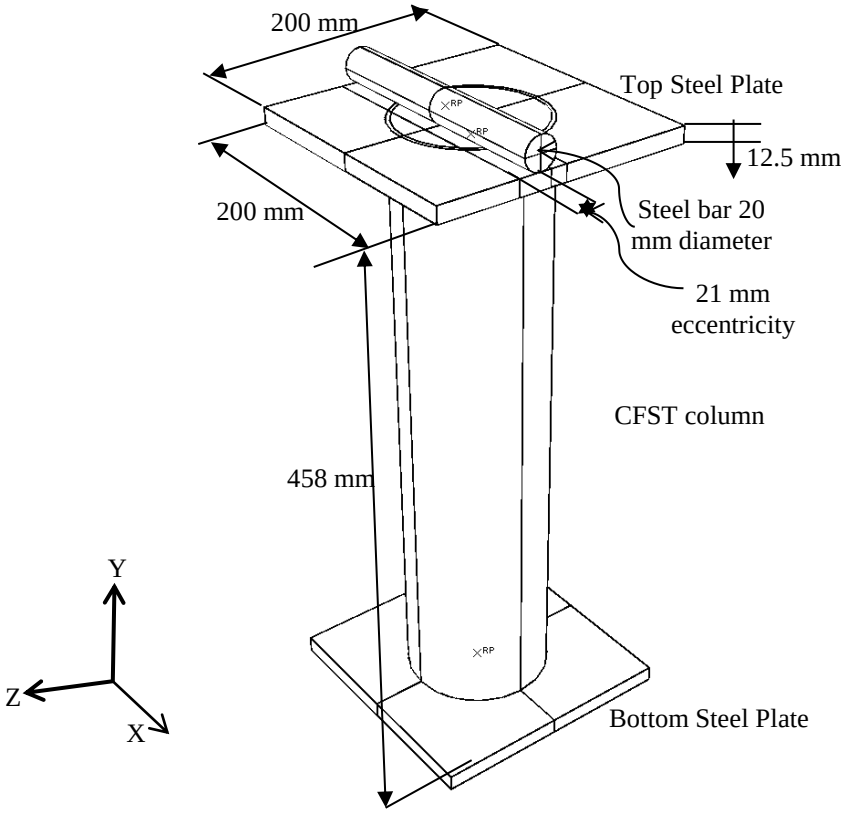

b) geometry of specimen E0

Figure 5.21(continued). Geometric conditions of the CFST columns

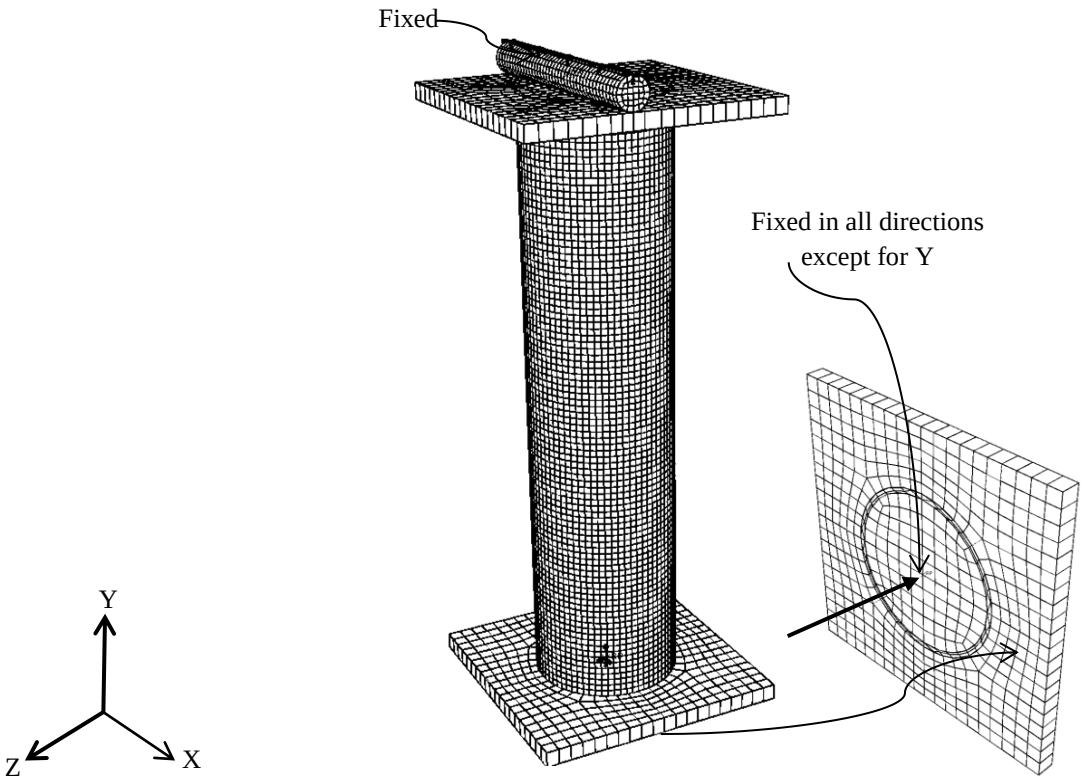

a) mesh, boundary conditions the specimen E0

Figure 5.22. The mesh, boundary and loading conditions of the CFST columns

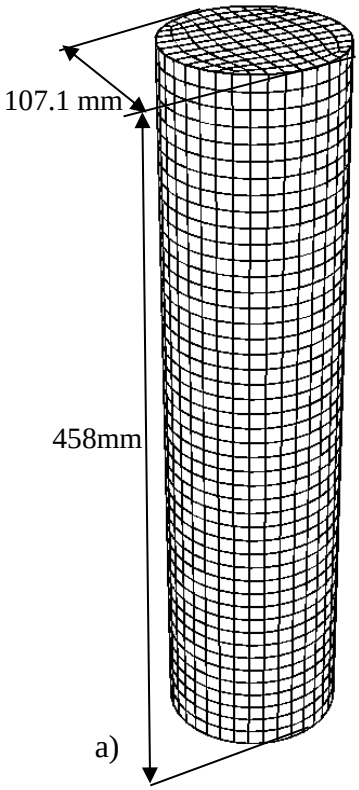

b) mesh of the concrete core

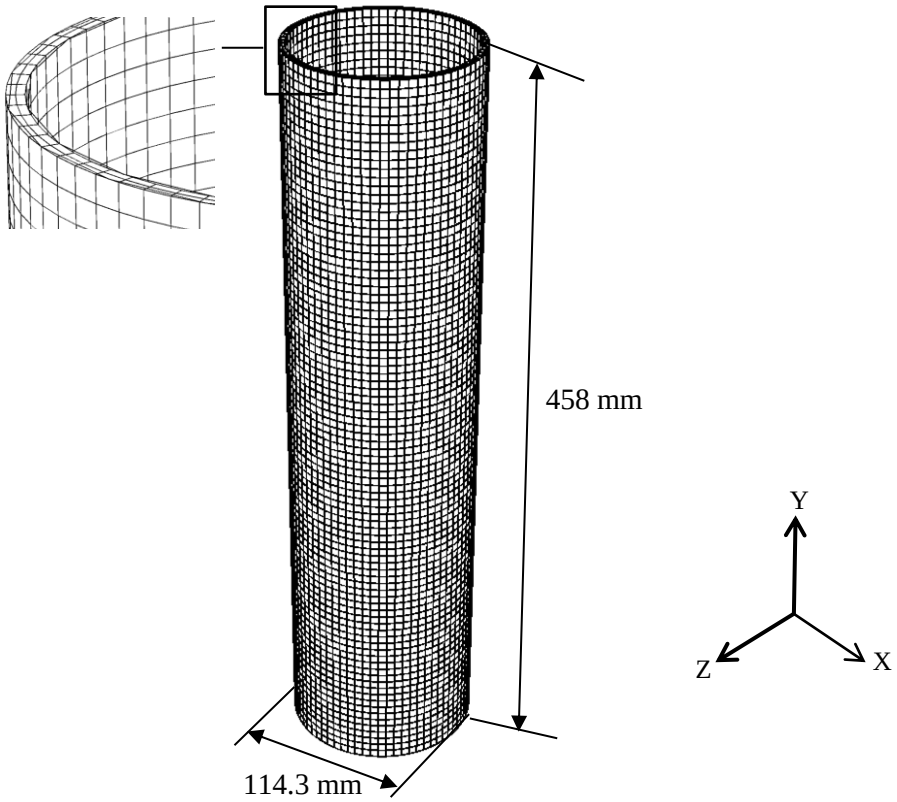

c) mesh of the steel tube

Figure 5.22 (Continued). The mesh, boundary and loading conditions of the CFST columns

A mesh sensitivity study was carried out to determine the efficient and effective element size for the tube and concrete. Fig. 5.23 shows the comparison of the modelling results related to five different meshes. The mesh-0 refers that the element size in the concrete core is 10 mm whilst that in steel tube is 5 mm, with two elements through the tube wall thickness. The mesh-1 means that there are three elements through the wall thickness of the steel tube with element size for both the tube and concrete core as 5 mm, whilst the mesh-2 and the mesh-3 are related to the mesh size of 10 mm and 15 mm, respectively, with the same number of elements through the wall thickness of the steel tube. The mesh-4 refers to the concrete core meshed with 10 mm size and steel tube in 5 mm size with three elements through the wall thickness of the tube. It can be seen that in general the element sizes studied have a slight effect on the force versus deflection curves. However, the local buckling behaviour modelled will be heavily influenced by the mesh density. The study also shows that increasing the element size to 15 mm in mesh-3 led to increase the compression force slightly. In spite of increasing the number of the element layers through the wall thickness and reducing the element size to the mesh-1, the force-deflection curve was very close to that of mesh-0. Further finer meshes do not effectively improve the accuracy of the numerical results. Thus, to reduce the computational time, mesh-0 was adopted in this analysis to simulate the compression behaviour of the CFST columns which gave a reasonably good agreement compared with experimental results.

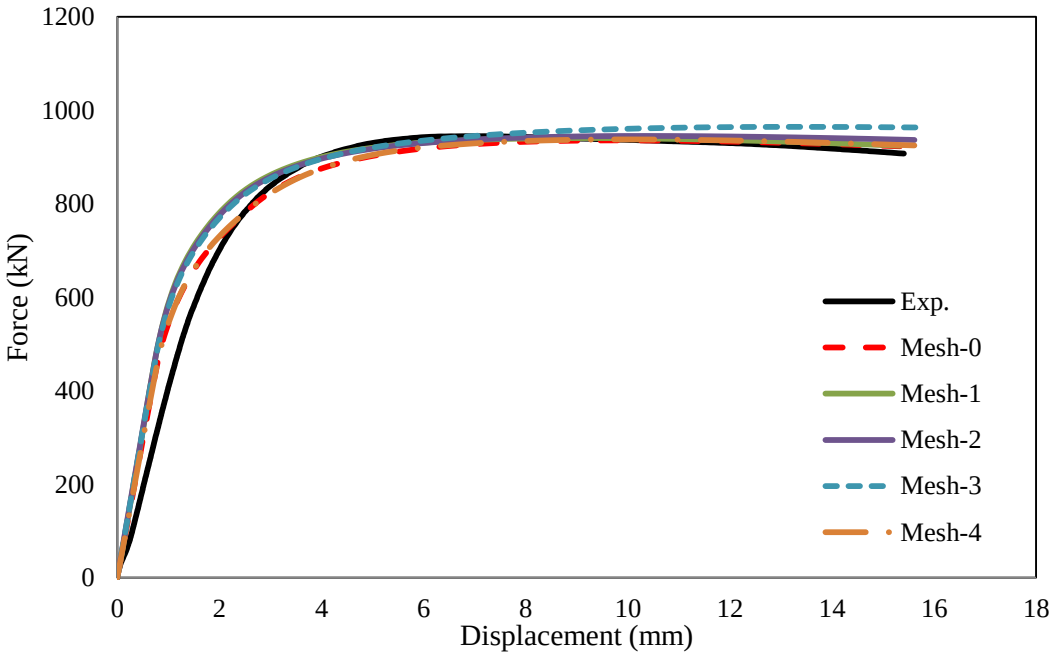

Figure 5.23. The element size effect on the accuracy of the numerical model

5.3.2 Boundary conditions and loading

To model the experimental test conditions, the steel bar on the top for applying the eccentric loading on the column was restricted to mimic the experimental conditions, while the bottom steel endplate was free in the axial direction only to allow the axial deformation, as shown in Fig. 5.22 (a). The same boundary conditions were applied for the columns under concentric loading by restraining the reference point of the top endplate in all directions and release the bottom end plate in Y axis direction i.e. Ux = Uz = URx = URy = URz = 0 and Uy ≠ 0.

5.3.3 Interaction and contact conditions

The concrete surface was selected as slave one when it was in contact with steel (master surface), while the impactor was selected as master surface when it was in contact with steel tube (slave surface). The interaction between the steel tube and the concrete core was defined as surface to surface contact with penalty contact properties. The contact was assumed "hard" with separation possibility after contact was made and the tangential behaviour was adopted. It was found that the compression behaviour of the CFST column is not sensitive to the coefficient of friction between the concrete core and the steel tube (Lam

et al., 2012 and Dai et al., 2014). In this study, the coefficient of friction between the concrete core and the tube is taken as 0.25, adopted by some researchers (Schneider, 1998, Lam et al., 2012 and Ellobody and Young, 2006). The endplates were constrained to the ends of the tube with "Tie" connections. The same contact properties were used for the interaction between the steel endplates and the concrete with a coefficient of friction of 0.2. As can be seen from Fig. 5.24, there is no influence for the coefficient of friction between the end plate and the concrete core. The coefficient of friction between the end plate and the concrete was between 0.15 and 0.3 (Zhu et al., 2016). Thus, the coefficient of friction of 0.2 was adopted in this study. The steel bar which was used to apply the eccentric loading was tied to the top end plate by adopting the steel plate as the master surface and the steel bar as a slave one when they are in contact.

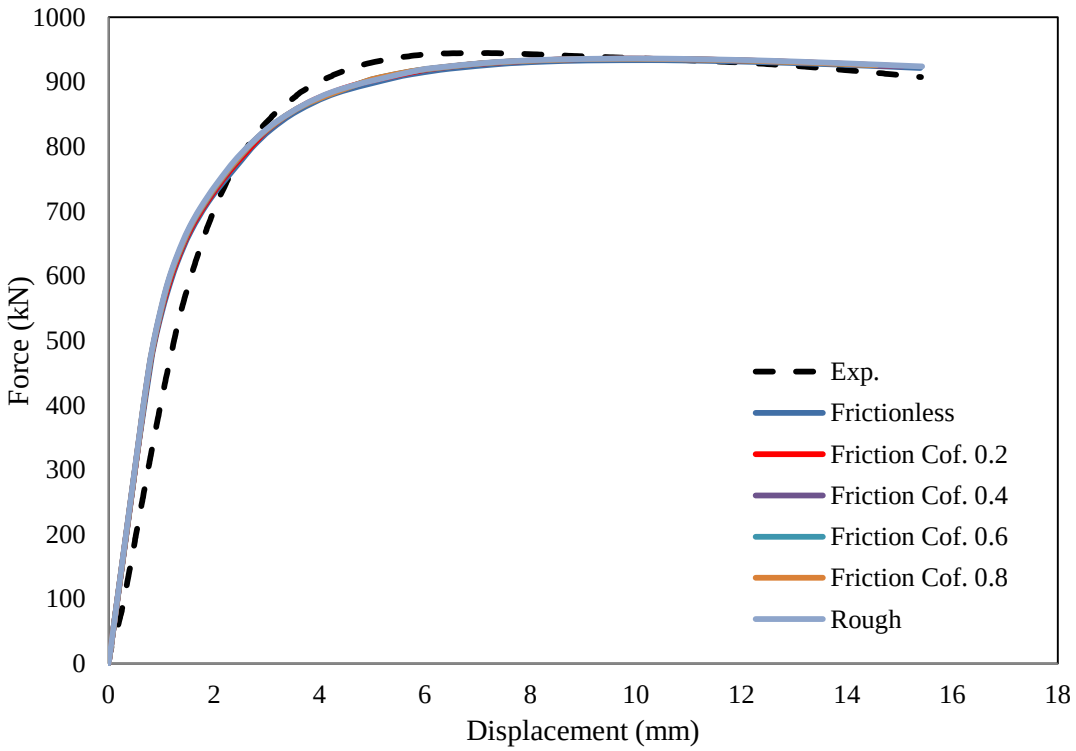

Figure 5.24. The effect of the coefficient of the friction between the end plate and the concrete core on the compression response of the CFST column

5.3.4 Material models

5.3.4.1 Steel

The steel tube under compression was modelled as an elasto-plastic material, following the stress-strain curve shown in Fig. 5.11. The elastic modulus and Poisson's ratio obtained from tests were 200 GPa and 0.3, respectively. The steel bar was modelled as an elastic perfectly plastic material and the yield strength was assumed to be 1500 MPa to minimise the deformation. The Poisson's ratio and the modulus of elasticity adopted for the steel bar were 0.27 and 220 GPa, respectively.

5.3.4.2 Concrete constitutive model

The Drucker Prager (DP) model in ABAQUS is utilised in this study to simulate the behaviour of the confined concrete in CFST columns under eccentric and concentric axial compressive loading. Both of the elastic and plastic parts are included in the concrete model. The DP model uses the modified von Mises yield criterion which is capable of capturing the increase of the shear strength due to the increase of the hydrostatic pressure. This advantage enables the DP model to simulate the concrete core of the CFST column as the concrete is confined by the steel tube and will expand as a result of increasing the hydrostatic pressure (Mollazadeh, 2015).

The linear DP criterion shown in Fig. 5.25 can be expressed as:

$$F = t_{DP} - p\tan\beta - d = 0 \tag{5.33}$$

where

$$t_{DP} = \frac{1}{2}q\left[1 + \frac{1}{k} - \left(1 - \frac{1}{k}\right)\left(\frac{r_{DP}}{q}\right)^3\right] \tag{5.34}$$

P is equivalent pressure stress and it can be obtained from:

$$p = -\frac{1}{3}trace\,(\sigma) = -\frac{1}{3}(\sigma_1 + \sigma_2 + \sigma_3) \tag{5.35}$$

$\sigma_1, \sigma_2, \sigma_3$ are the principal stresses

q is the von Mises equivalent stress which can be written as:

$$q = \sqrt{\frac{3}{2}}(S:S) = \sqrt{\frac{1}{2}[(\sigma_1 - \sigma_2)^2 + (\sigma_2 - \sigma_3)^2 + (\sigma_3 - \sigma_1)^2]} \tag{5.36}$$

$$r_{DP} = \left[\frac{9}{2}(S_1^3 + S_2^3 + S_3^3)\right]^{\frac{1}{3}} \quad (5.37)$$

S is the stress deviator, d is the cohesion of the material, k is the ratio of triaxial tension yield stress to triaxial compression yield stress, and β is the angle of friction of the material.

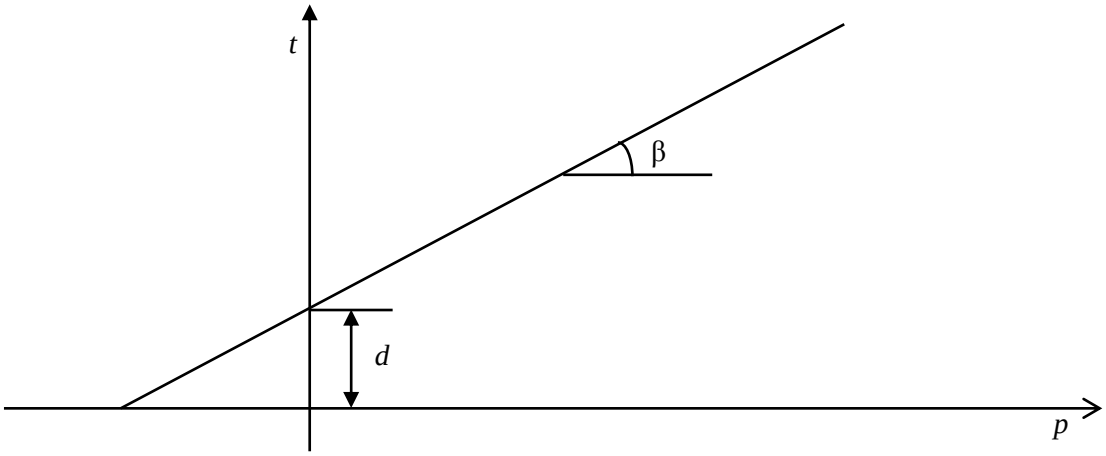

Figure 5.25. Linear Drucker-Prager (ABAQUS, 2015)

The behaviour of NACFST and RACFST columns are characterized as an elastic-perfectly plastic response and as typical softening or stiffness degrading behaviour for the columns under eccentric and concentric loading, respectively. The confined concrete stress-strain relationship described in Section 5.2.4.2 is adopted to simulate the properties of the confined concrete under eccentric loading.

A modified model was utilised to simulate the properties of the confined concrete under concentric loading. This model is based on the four-parts of the stress-strain curve shown in Fig. 5.26. This model was presented by Dai and Lam (2010) to simulate the confined concrete by an elliptical hollow section which showed softening or stiffness degrading behaviour. They included a quick softening by introducing the force "f_e" with corresponding strain "ε_e". The modified model included four stages. The first, second and fourth stages are obtained from the model presented in Section 5.2.4.2. The third stage included the force and strain which can be predicted as (Dai and Lam, 2010).

$$f_e = v_e(f_{cc} - f_u) + f_u \quad (5.38)$$

$$\varepsilon_e = 10\varepsilon_{ck} \tag{5.39}$$

where v_e can be taken as 0.3, f_{cc} is the cylinder compressive strength of the confined concrete and this was determined from Equation (5.13), $f_u = rk_3 f_{cc}$ and ε_{ck} is 0.003.

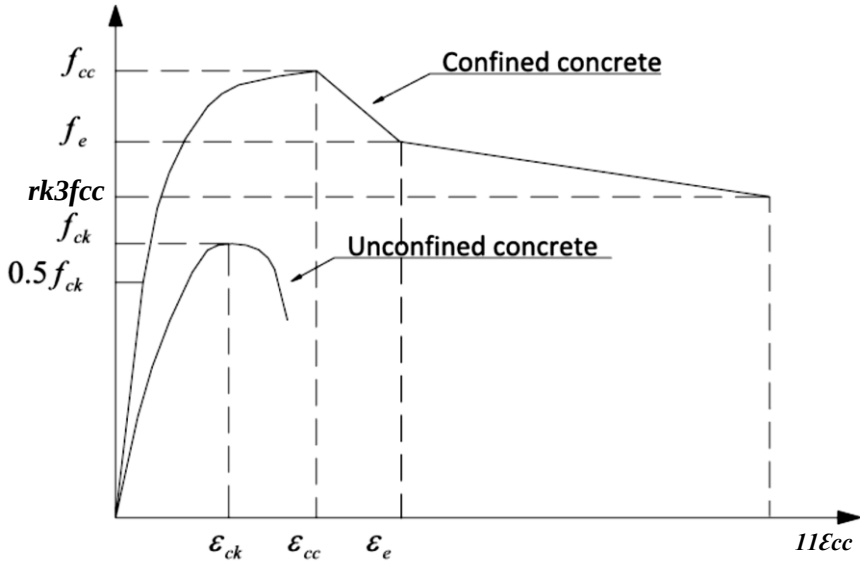

Figure 5.26. Comparison between confined and unconfined concrete for elliptical tubes (Dai and Lam, 2010)

5.3.5 Geometric imperfection

Geometric imperfections were considered due to the possibility of minor defects which were resulted during the manufacturing process of the steel tube. These defects may affect the deformation shape even if they are very small. Here, the elastic Eigen-mode pattern was taken as the global geometric imperfection form. This pattern was obtained from the initial buckling step available in ABAQUS/Standard and then the buckling modes of this step were used in a general static step. The procedures available in ABAQUS documentation to define the imperfection for crushing the steel tube with a 400 mm length were adopted in this study, which include the following steps:

1- Run the model with a Buckle step with the required number of buckling mode (Eigenvalue). A file output (.fil) is requested for the nodal displacement to use the results of the buckling analysis to define the imperfection.
2- The output of the buckling step is linked with the General Static step by editing the input file and use the *IMPERFECTION, FILE=name of the buckle job, STEP=1
3- Define the imperfection as a percentage of the tube wall thickness with each Eigen mode and run the model with different imperfection values and Eigen modes a few times to obtain the right mode of failure as it differs with the changes of the Eigen modes and the value of the imperfection.

These imperfections were defined as a percentage of the wall thickness of the tube by including the imperfection parameters in the Keywords Editor. The maximum imperfection percentage used in this study is 1.8 %. This technique is a user defined procedure and it is just used for comparison purposes between the numerical and experimental results.

5.4 Simulation output of the CFST columns under lateral impact loading

5.4.1 Modelling the structural hollow circular tube under impact loading

Figs. 5.27, 5.28 and 5.29 show the numerical force-total displacement curves, together with experimental ones for the hollow circular tubes subjected to lateral impact loading with lengths of 686 mm, 1029 mm and 1543 mm, respectively. Clearly, the predicted traces of force and total displacement are correlated reasonably well to the corresponding experimental results. For the short tube, the predicted total displacement is slightly lower than the measured one by only 3.8 %, while the experimental and numerical forces are 84 kN and 75 kN, respectively. Fig. 5.28 shows that the numerical model accurately captures the main features of the experimental force-total displacement curve, such as the elastic part followed by the fluctuating force due to the progressive local crushing of the steel tube. However, the final part of the curve was not well predicted, which may be due to the fact that the simulation considers the material properties as the same along the column, whilst in the reality these properties may not be the same due to possible local defects or imperfections. The experimental maximum total displacement for the medium tube was

higher than the predicted one only by 3.2 %, whilst the global displacement was lower by 2.8 %. The test results in Table 5.2 show that the predicted total force and displacement for the long tube are 64.7 kN and 68.7 mm, respectively, whilst the captured ones are 55.3 kN and 75.4 mm, respectively. In spite of these results, agreement between the numerical and measured data for the long tube is good. In general, all the numerical curves show force reduction and displacement increasing with increasing of the length of the steel tube, as expected.

Figs. 5.30, 5.31 and 5.32 indicate that the numerical models are capable of predicting the failure modes of the hollow tubes with different lengths. In the experimental tests, the failure was initiated by the onset of local yielding of the steel tube with local buckling at the mid span of the tube and then the tube bent globally with a certain value of global displacement. This is clearly shown in the simulation with the total displacement of the columns

Table 5.2. The numerical and experimental results for the CFST columns subjected to lateral impact loading

Specimen ID	Force (kN) (Exp.)	Force (kN) (FE)	(%)*	Global dis (mm) (Exp.)	Global dis (mm) (FE)	(%)*	Total disp. (mm) (Exp.)	Total disp. (mm) (FE)	(%)*
SH	84	75	10.71				52.2	50.2	3.83
S0-BI	286.3	290.6	1.50	6.8	7.5	10.29	12.9	13.7	6.20
S50-BI	259.3	275.2	6.13	7.1	7.3	2.82	13.4	13.7	2.24
S0-MI	266	286.3	7.63	6.6	6.8	3.03	14	14.2	1.43
S50-MI	250	286.3	14.52	6.6	6.7	1.52	14.6	14.3	2.05
S0s-MI	274	302.9	10.55	6.6	6.9	4.55	13.6	13.9	2.21
S50s-MI	253	295.8	16.92	6.3	6.8	7.94	13.5	13.8	2.22
S0-SI	220.1	273	24.03	5.8	6.4	10.34	16.4	15.4	6.10
S50-SI	216	271.4	25.65	5.6	6.2	10.71	15.6	15.5	0.64
S0-FI	319	340.7	6.80	8.6	8.2	4.65	11.2	11.2	0.00
S50-FI	317.8	324.1	1.98	8.2	8.1	1.22	11.4	11.5	0.88
MH	74	64.7	12.57				57.1	58.7	2.80
M0	194	187.9	3.14	14.5	14.6	0.69	18.2	19.3	6.04
M50	181.1	188	3.81	14.5	14.5	0.00	19.2	19.4	1.04
M0s	204	180	11.76	13.2	13.5	2.27	17.4	20	14.94
M50s	179.7	182.6	1.61	13.5	13.4	0.74	18.5	20.1	8.65
LH	64.7	55.3	14.53				68.7	75.4	9.75
L0	166	175.5	5.72	24.3	24.8	2.06	28.2	27.8	1.42
L50	164.1	171.6	4.57	25	24.8	0.80	29.8	28.2	5.37
L0s	132.5	141.5	6.79	22.4	23.5	2.8	27	28.5	5.50
L50s	142.1	138.7	2.39	22.4	23.5	6.34	27.8	28.5	2.52

* [(Exp.-FE)/Exp.]*100

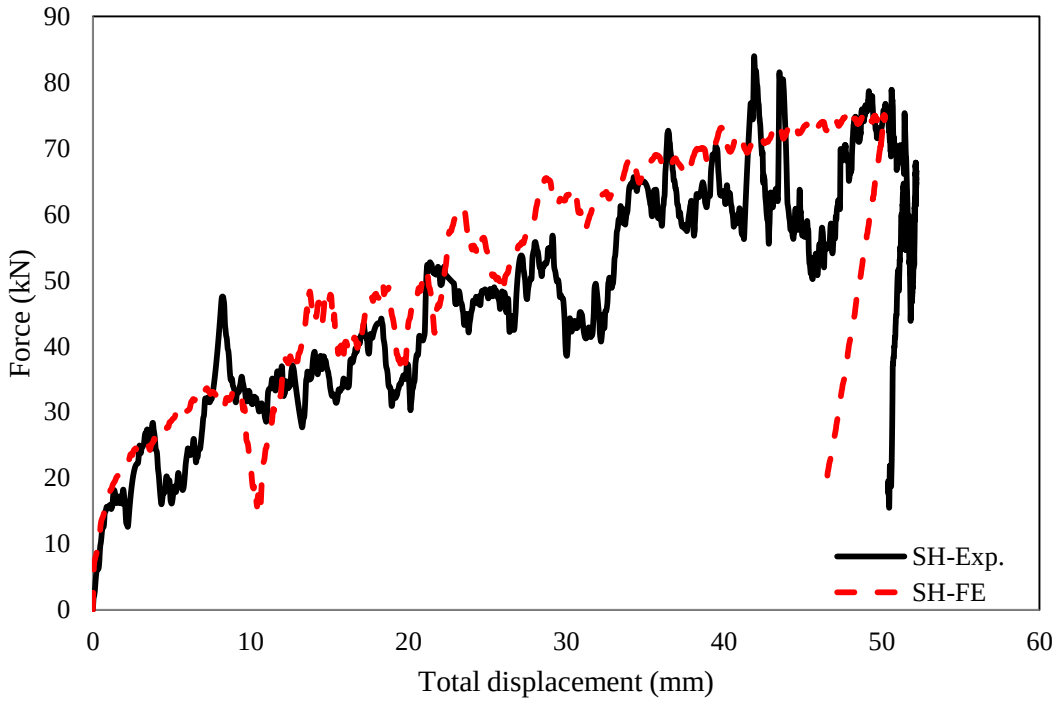

Figure 5.27. The FE and experimental force-total displacement traces for the hollow circular short column under impact loading

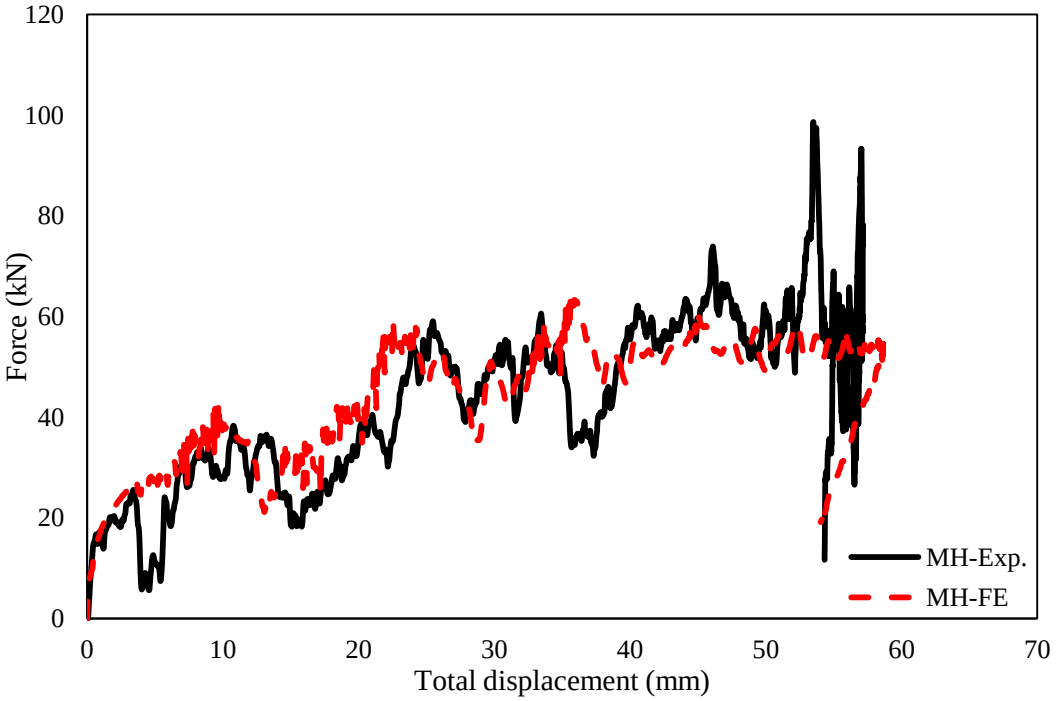

Figure 5.28. The FE and experimental force-total displacement traces for the hollow circular medium column under impact loading

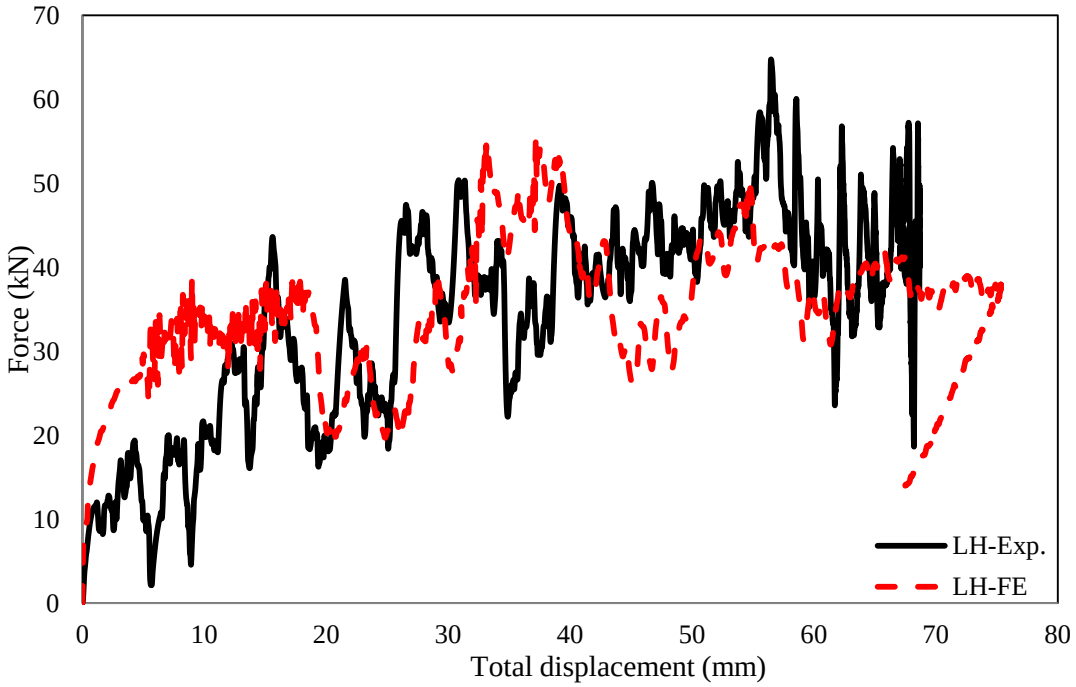

Figure 5.29. The FE and experimental force-total displacement traces for the hollow circular long column under impact loading

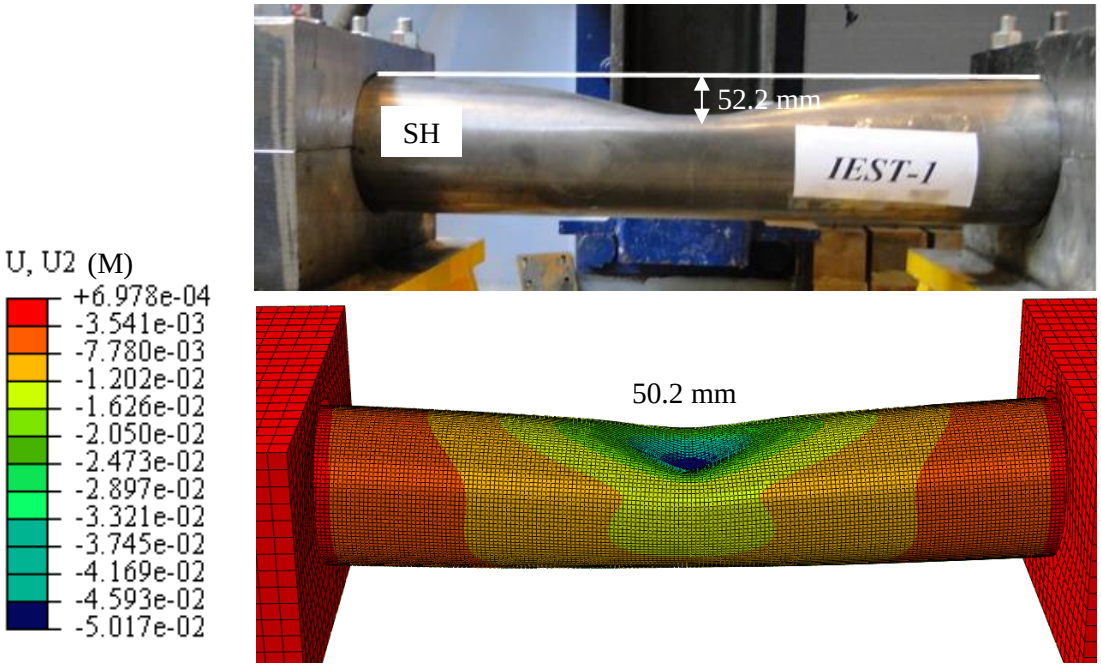

Figure 5.30. The failure pattern for the short hollow tube under lateral impact loading

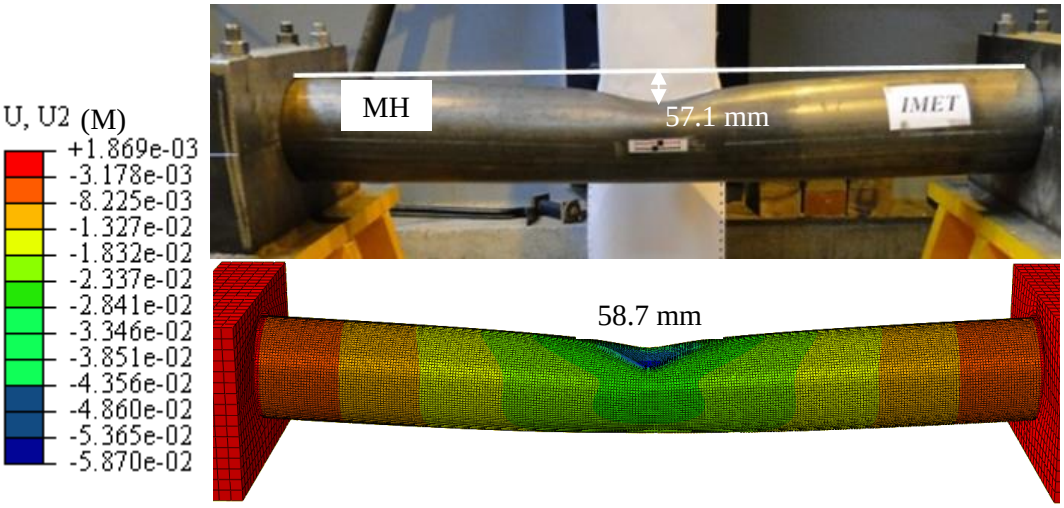

Figure 5.31. The failure pattern for the medium hollow tube under lateral impact loading

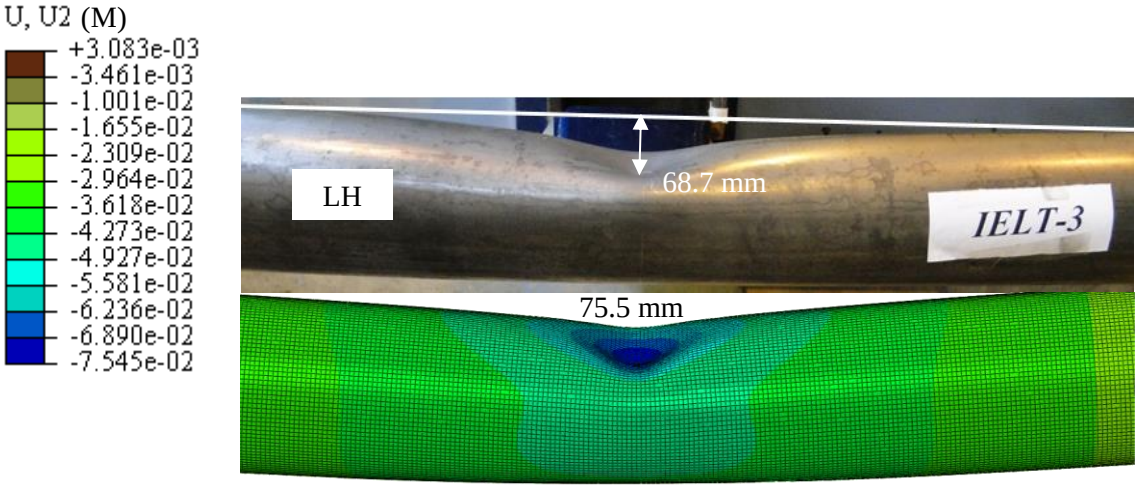

Figure 5.32. The failure pattern for the long hollow tube under lateral impact loading

5.4.2 The influence of the L/D ratio on the impact behaviour of the normal and recycled aggregate CFST columns

Figs. 5.33 and 5.34 present the force-total displacement plots for the normal and recycled aggregate CFST columns with the L/D ratio of 6. In both cases, correlation between the numerical prediction and experimental response is good. The simulated trace for the normal aggregate CFST captures the initial slope, the maximum force and the total and global displacements accurately. The discrepancies between the experimental and numerical force, total displacement and global displacement were only 7.6 , 1.4 and 3.0 %, respectively.

There are slightly over-estimated initial stiffness and maximum force for the recycled aggregate CFST column. However, the agreement between the experimental and simulation data is good and the predicted total and global displacement only differ from the test results by 2.1 % and 1.5 %, respectively.

Figs. 5.35 and 5.36 show a comparison of the predicted and measured force-total displacement traces for normal and recycled aggregate CFST column with the L/D ratio of 9. The predicted traces show a reduction in the impact force after the initial peak force, which may have resulted from the influence of the vibration induced by the relatively low stiffness for the medium columns. Therefore, an attempt was made to investigate the influence of the increase of the stiffness of the column by increasing the coefficient of friction between the steel clamp and the steel tube. The results showed that increasing the coefficient of friction reduced the reduction in the impact force after the initial stage but over-estimated the maximum force and reduced the total displacement, as indicated in Fig. 5.37. In addition to that, the results of the numerical models which are based on the same geometric assumptions and contact and material properties will be highly affected by assuming different values of coefficient of friction, instead of 0.01. Thus, the coefficient of friction of 0.01 was kept constant for all modelling. In spite all of that, the comparison demonstrates that the numerical results for the medium columns are in a good agreement with the experimental data for both traces, i.e. force-total displacement and force-global displacement traces. Table 5.2 reveals that the numerical models have provided the accurate prediction on the force and total displacement for both normal and recycled aggregate CFST column with discrepancies of 3.1 and 6.0 and 3.8 and 1.0 %, respectively. Figs. 5.38 and 5.39 manifest that the FE models are capable of predicting the force-global displacement response for both NACFST and RACFST columns. The global displacement for the experimental NACFST was higher than the predicted one by only 0.7 %, while the very similar global displacement was predicted for the RACFST column.

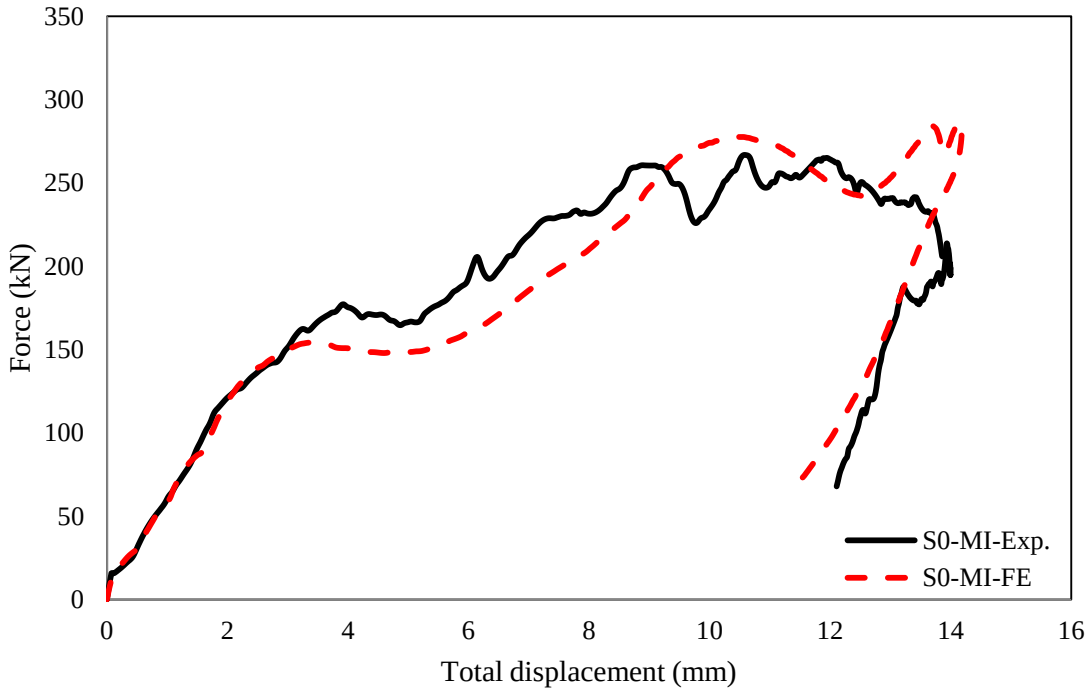

Figure 5.33. The FE and experimental force-total displacement traces for the NACFST column under impact loading with L/D of 6

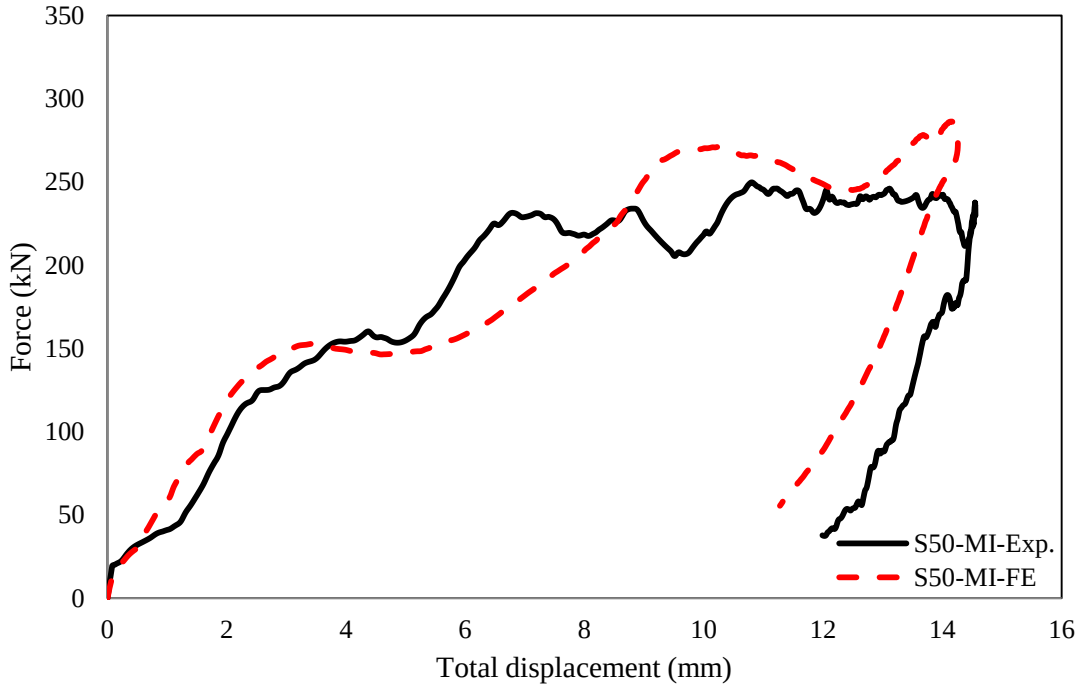

Figure 5.34. The FE and experimental force-total displacement traces for the RACFST column under impact loading with L/D of 6

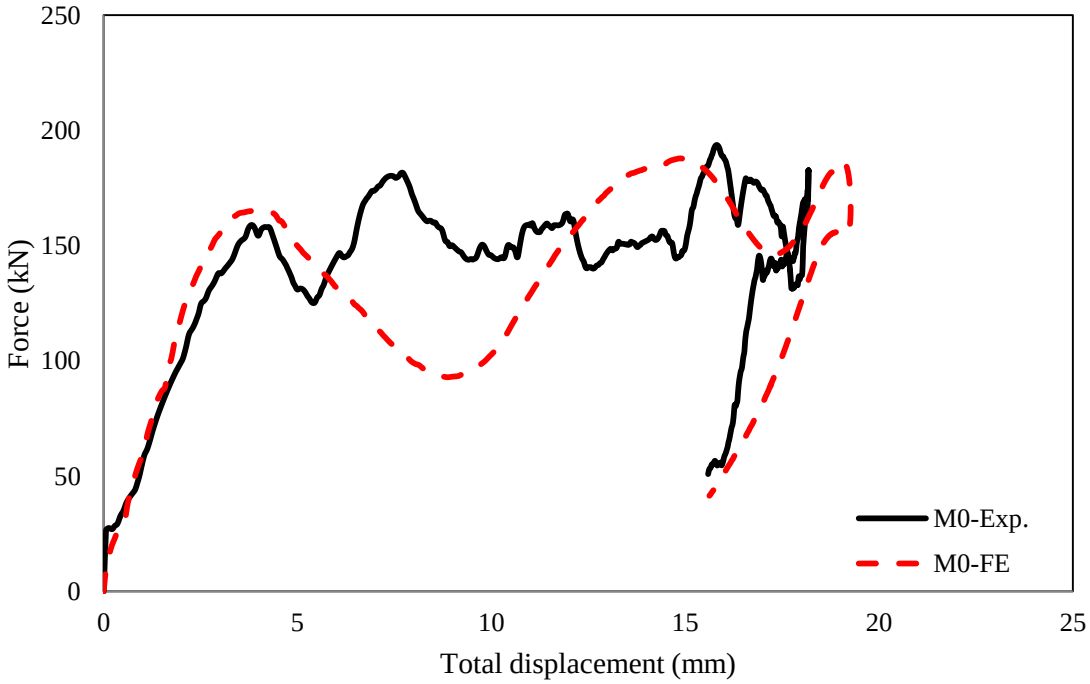

Figure 5.35. The FE and experimental force-total displacement traces for the NACFST column under impact loading with L/D of 9

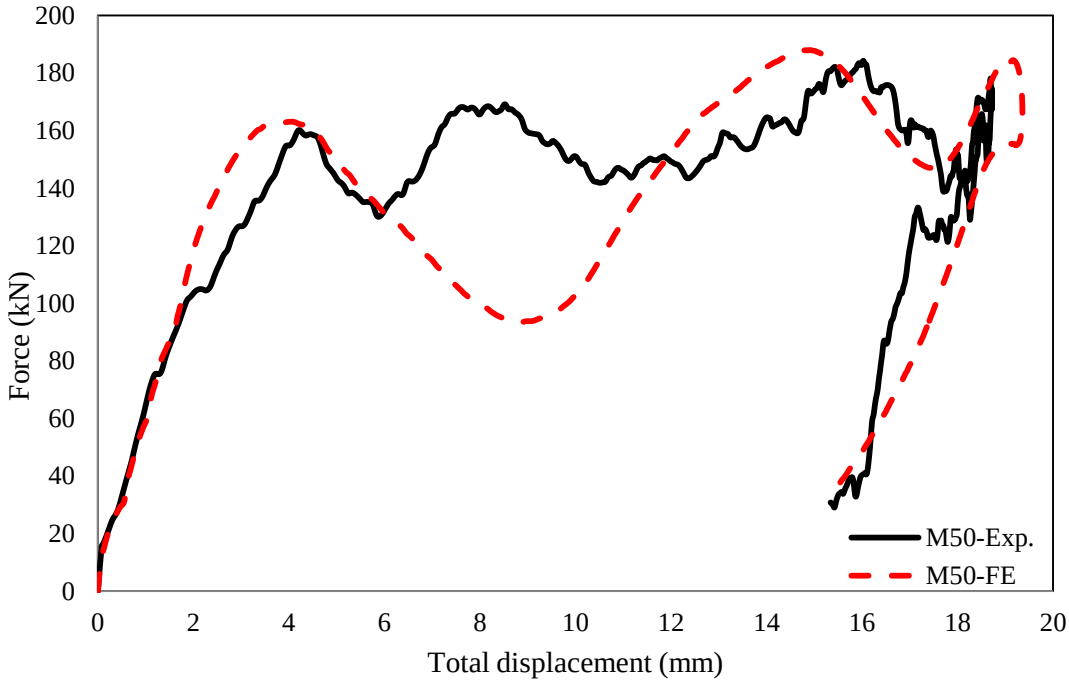

Figure 5.36. The FE and experimental force-total displacement traces for the RACFST column under impact loading with L/D of 9

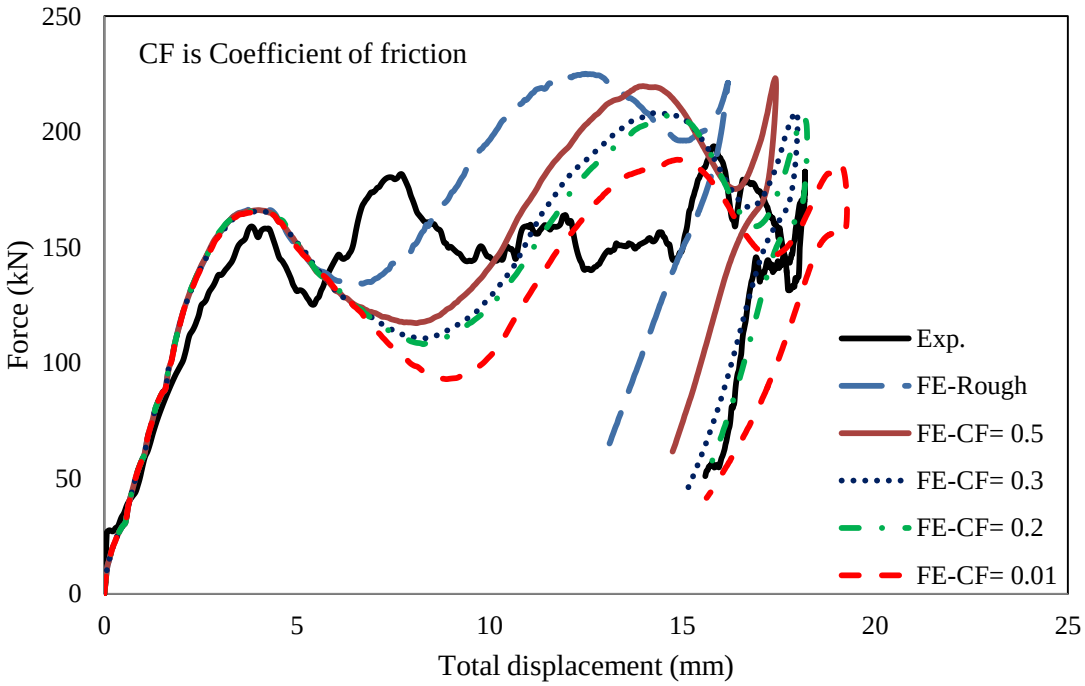

Figure 5.37. The effect of the coefficient of the friction between the steel clamp and steel tube on the impact response of the FE models for the CFST column with L/D of 9 in comparison with the experimental results

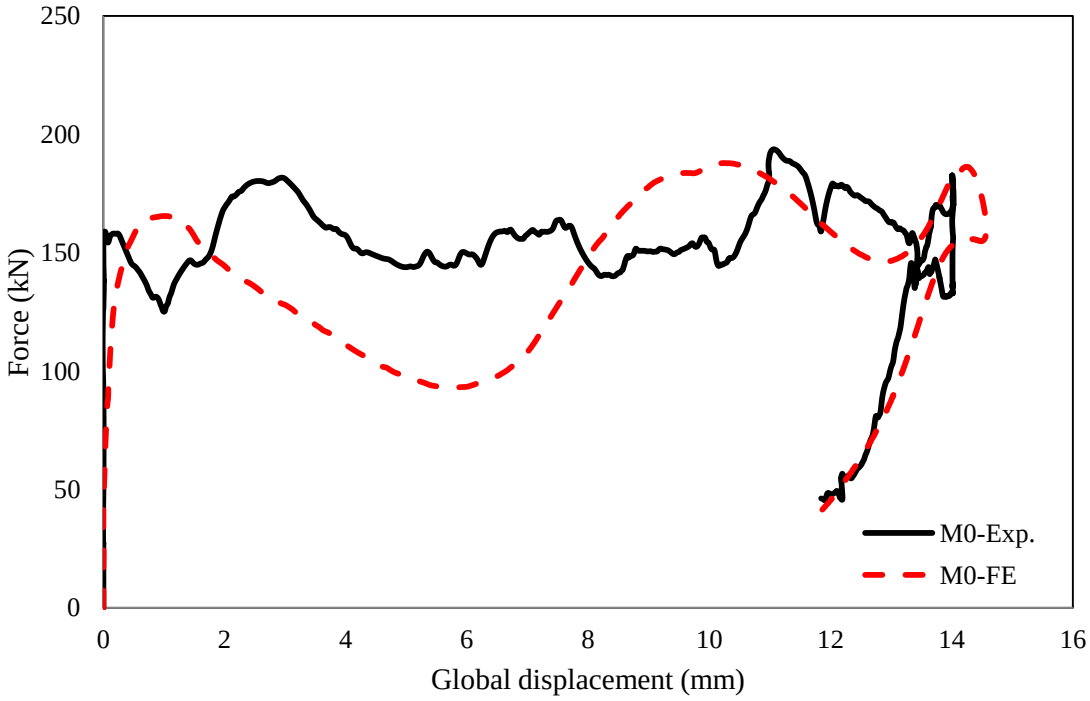

Figure 5.38. The FE and experimental force-global displacement traces for the NACFST column under impact loading with L/D of 9

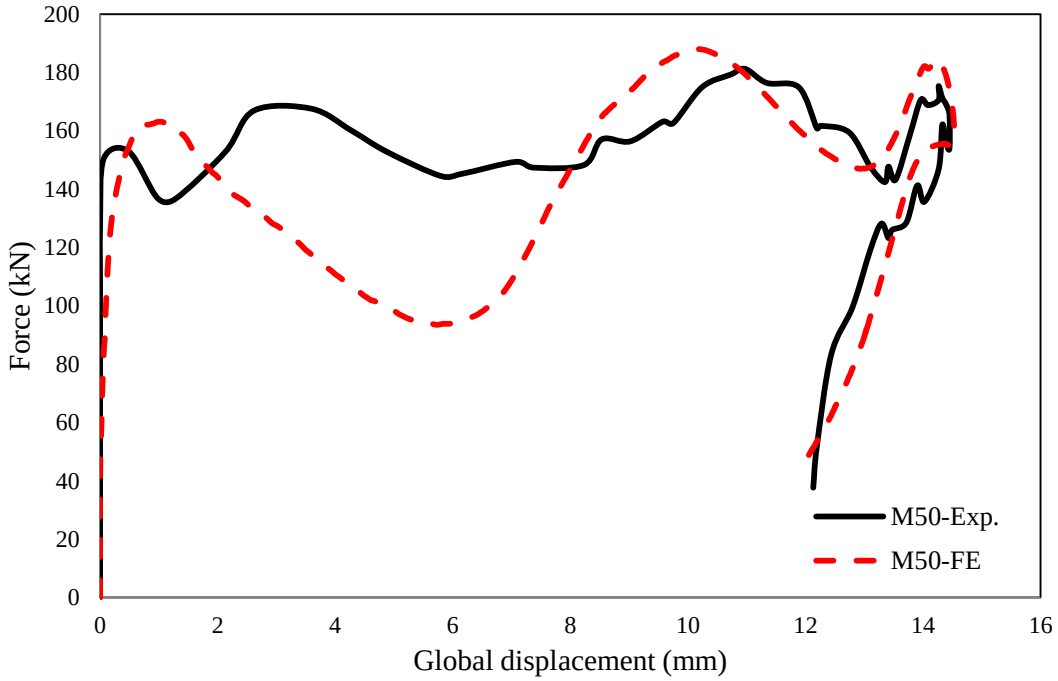

Figure 5.39. The FE and experimental force-global displacement traces for the RACFST column under impact loading with L/D of 9

Figs 5.40 and 5.41 show the force-total displacement traces following the impact behaviour of the NACFST and RACFST columns, respectively. These figures demonstrate that the numerical models have accurately captured the features of the measured force-total displacement curve, which include the elastic stage, the reduction of the force as well as the maximum force and displacements. It can be seen that the predicted trace follows the trend of the experimental one throughout all stages. The predicted force for NACFST and RACFST was slightly lower and the total displacement somewhat higher than those obtained from the tests, as shown in Table 5.2. An examination of the FE global displacement-force relationships shown in Figs 5.42 and 5.43 indicates that compared to the test results, the global displacements are well predicted with small discrepancies of 2.0 % and 0.8 % for the NACFST and RACFST columns, respectively.

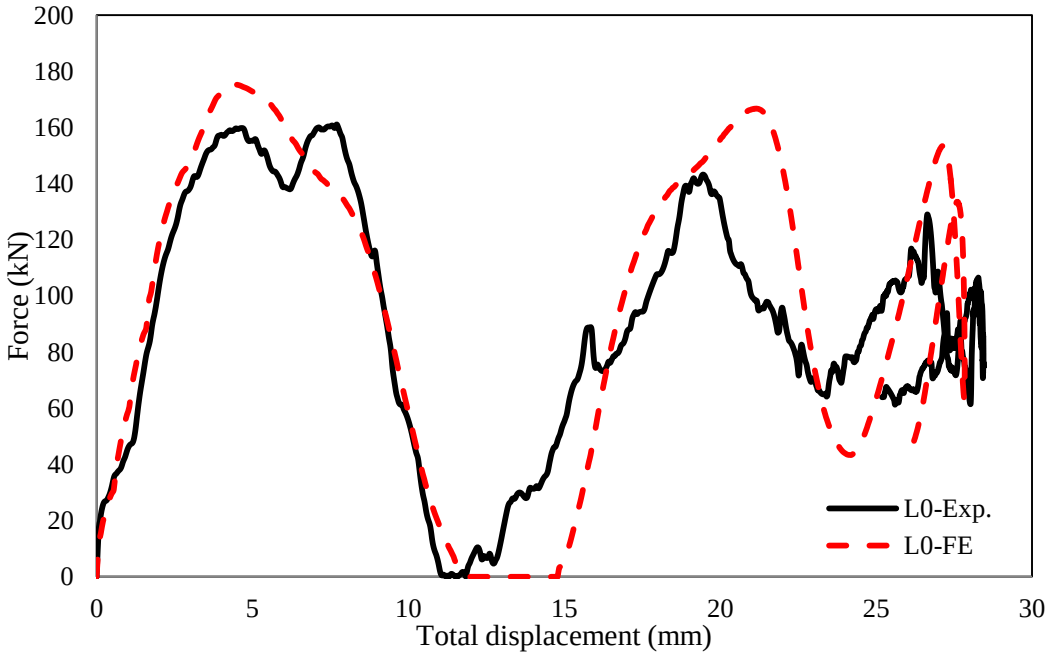

Figure 5.40. The FE and experimental force-total displacement traces for the NACFST column under impact loading with L/D of 13.5

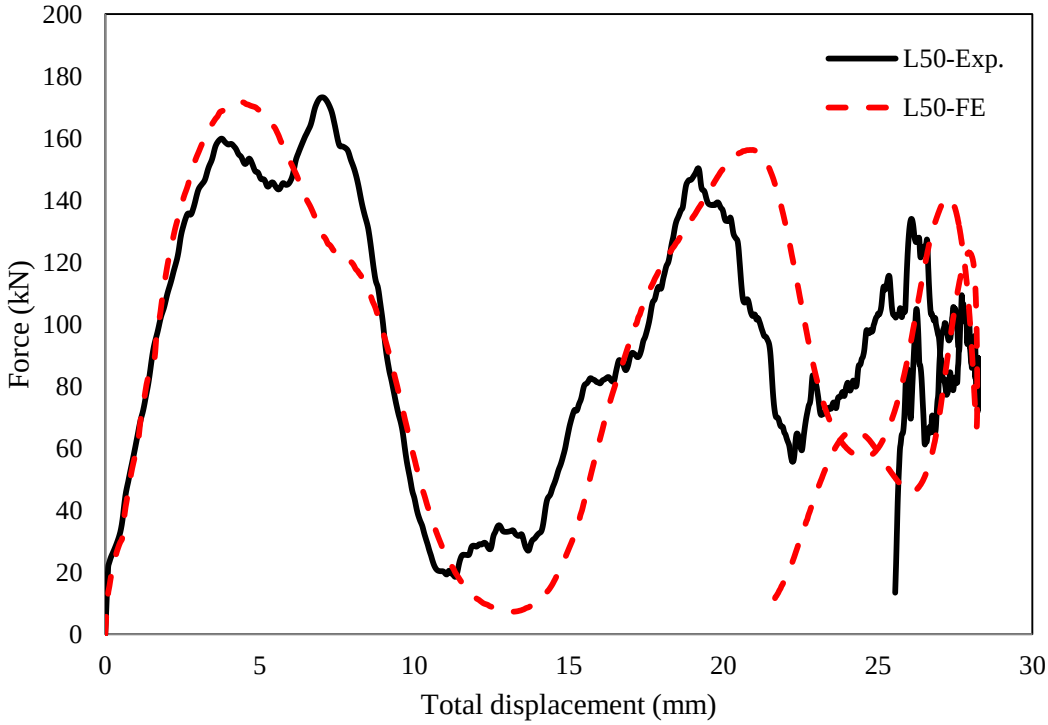

Figure 5.41. The FE and experimental force-total displacement traces for the RACFST column under impact loading with L/D of 13.5

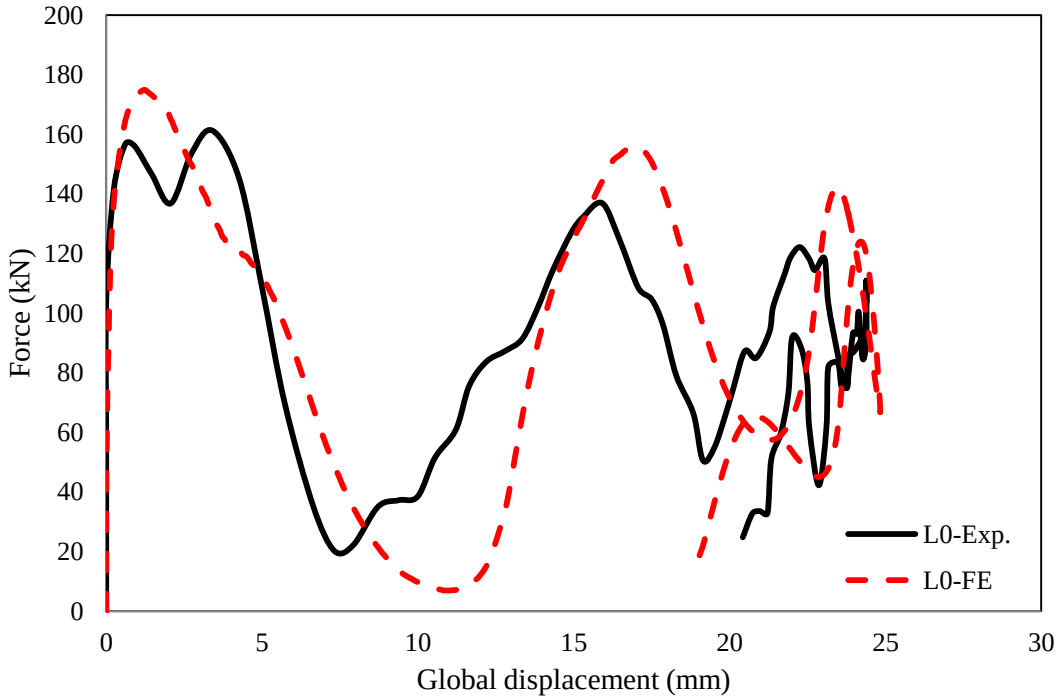

Figure 5.42. The FE and experimental force-global displacement traces for the NACFST column under impact loading with L/D of 13.5

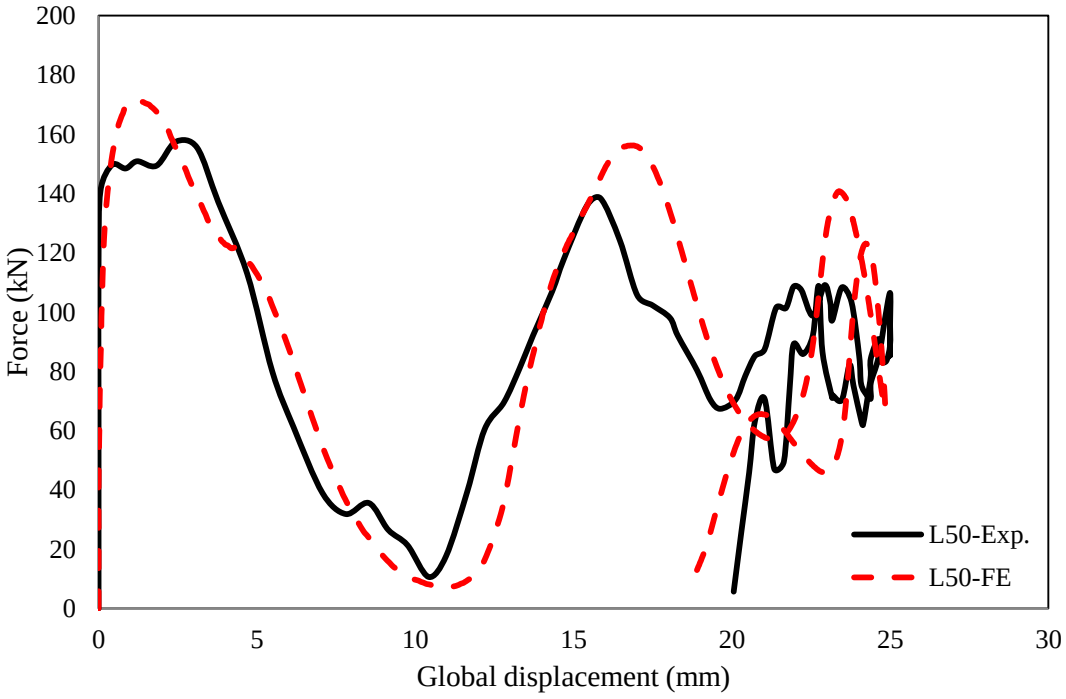

Figure 5.43. The FE and experimental force-global displacement traces for the RACFST column under impact loading with L/D of 13.5

Predictions of the deformation modes of the NACFST and RACFST columns with different L/D ratios are shown in Figs. 5.44 to 5.50. The figures reveal that regardless of the L/D ratios and the type of the concrete, the numerical models developed are capable of simulating the deformation pattern of the CFST column which starts with a large indentation and local deformation once the impactor hits the tube and then the global movement of the whole tube together with impactor up to the rebound stage. Fig 5.46 shows a reasonable good agreement between the numerical and the experimental profiles of the indentation for the CFST columns with different L/D ratios.

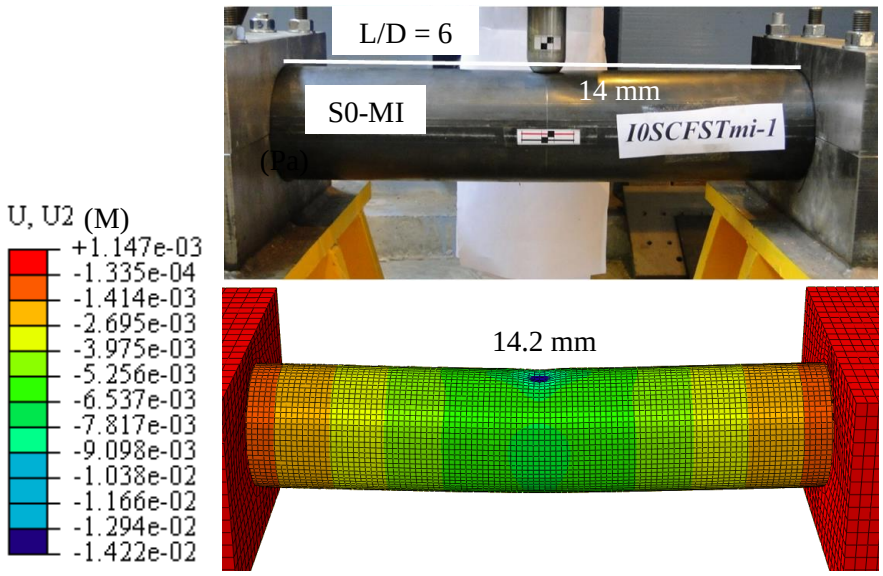

Figure 5.44. The deformation pattern for the NACFST column with a L/D ratio of 6

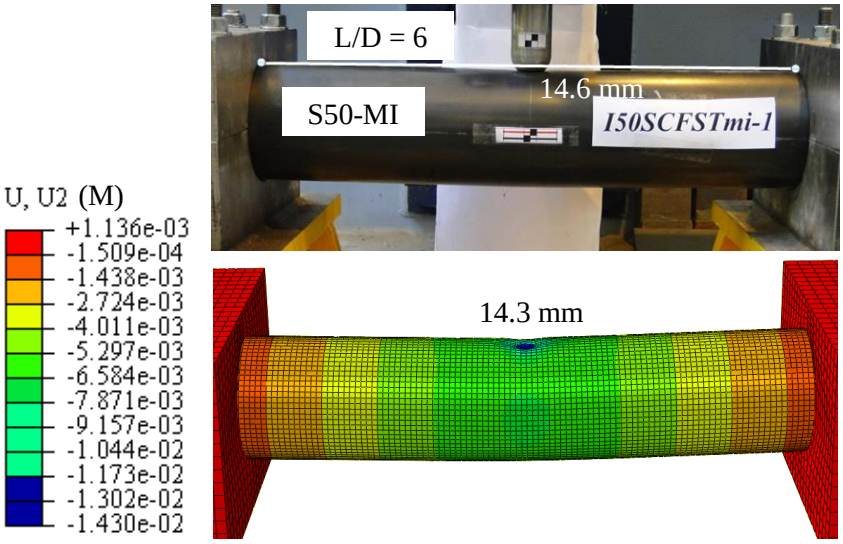

Figure 5.45. The deformation pattern for the RACFST column with L/D ratio of 6

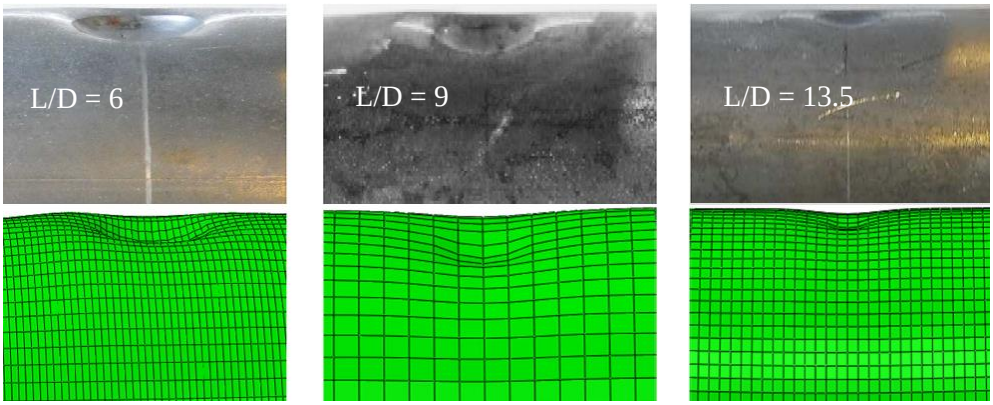

Figure 5.46. The comparison between the experimental and numerical indentation profile for the NACFST column with L/D ratio of 9

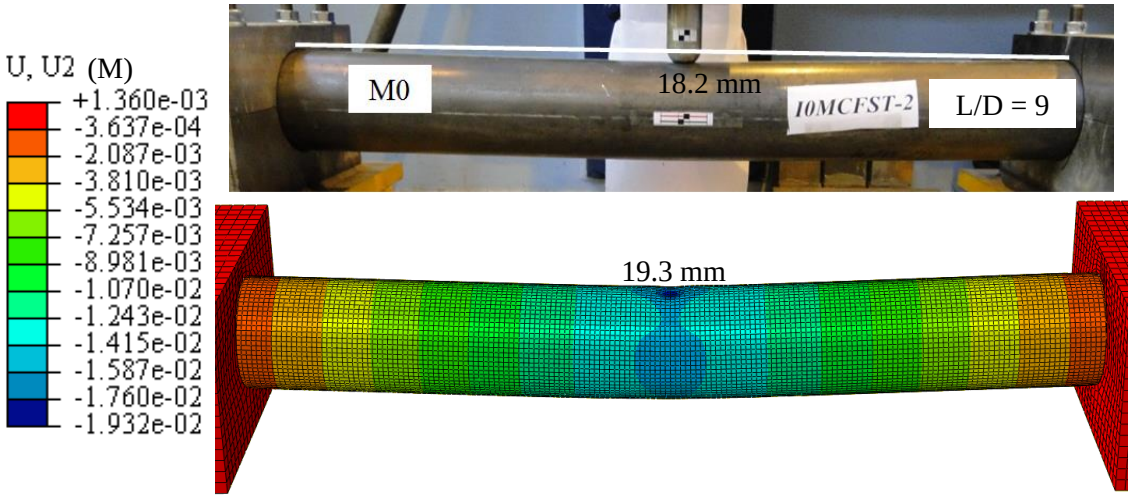

Figure 5.47. The deformation pattern based on the von Mises stress distribution for the NACFST column with L/D ratio of 9

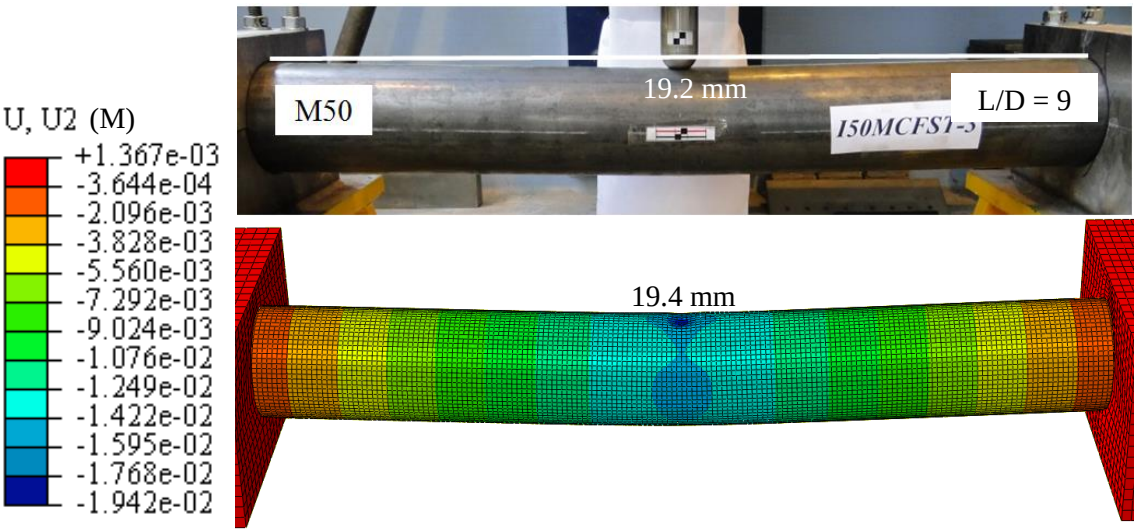

Figure 5.48. The deformation pattern for the RACFST column with L/D ratio of 9

The numerical models also indicate that with increasing the length of the column, the impact force is reduced and the total and global displacements increased, as expected. In addition, the RACFST column shows slightly lower load carrying capacity than the NACFST column. However, both of the NACFST and RACFST columns exhibit the similar deformation mode regardless the L/D ratio. All these predictions agree reasonably well with the experimental findings.

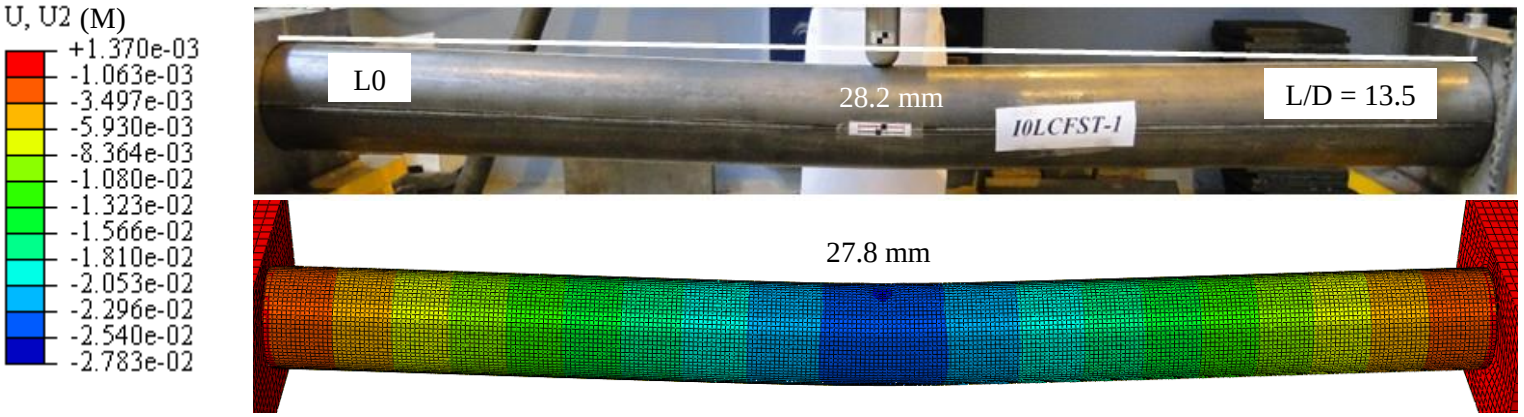

Figure 5.49. The deformation pattern for the NACFST column with L/D ratio of 13.5

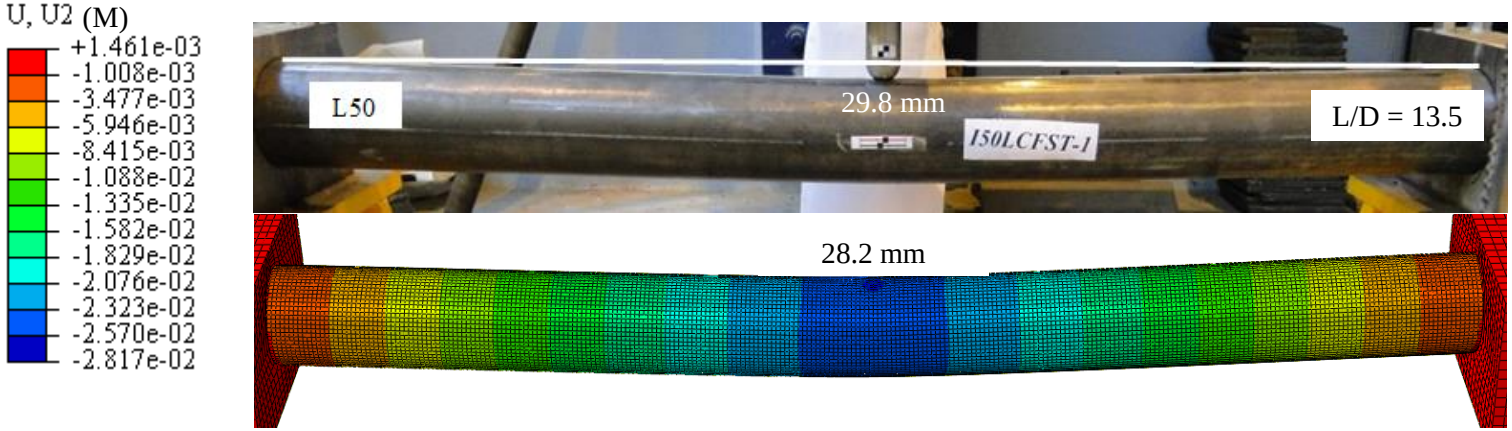

Figure 5.50. The deformation pattern for the RACFST column with L/D ratio of 13.5

5.4.3 The influence of the impactor configurations on the response of the normal and recycled aggregate CFST columns under lateral impact loading

Figs. 5.51 and 5.52 present a comparison between the FE and experimental force-total displacement traces for the NACFST and RACFST short columns hit by a spherical impactor with a diameter of 20 mm. The comparison shows that the predicted trace is following the trend of the measured one throughout the initial and plateau stages. However, the FE models tend to over-estimate the maximum force by 24.0 % and 25.7 % for the NACFST and RACFST columns, respectively. At the same time, the predicted total displacement for the RACFST was 15.5 mm and the measured one was 15.6 mm, whilst the measured and predicted total displacement for the NACFST column were 16.4 mm and 15.4 mm, respectively. In spite of these discrepancies, the numerical and experimental results are overall in a good agreement.

Figs. 5.33 and 5.34 which were described in Section 5.4.2 show that the simulation results for the NACFST and RACFST column impacted by a spherical impactor with diameter of 40 mm are in good agreement with the corresponding tests ones.

Figs. 5.53 and 5.54 manifest that the numerical and experimental results correlate very well for both the NACFST and RACFST columns subjected to lateral impact by a spherical impactor with a diameter of 60 mm. It is clear that the models are able to predict all the basic features from the initial elastic stage to the final point of the test. The simulations of the maximum forces for the NACFST and RACFST columns are higher than those obtained from the test results only by 1.5 % and 6.1 %, respectively, whilst the total displacements are higher by 6.2 % and 2.2 %, respectively.

The NACFST and RACFST columns impacted by a flat square impactor with dimensions of (40 x 40) mm were also modelled. Figs. 5.55 and 5.56 show the comparison between the predicted results and the experimental data. Once again, the maximum force and the total and global displacements are very well predicted. The differences between the experimental

and numerical maximum force, total and global displacements for the NACFST column are less than 7 %, and those for the RACFST column are less than 2 %.

Figs. 5.57 to 5.62 show the predicted and measured deformation patterns for the NACFST and RACFST columns subjected to projectile impact by impactor with different impactor configurations. An examination of these figures between the experimental and numerical results indicates that deformation mode and the failure mechanisms were captured by the numerical models accurately. These include steel tube deformation with the initial contact between the impactor and steel tube and then the local displacement followed by global displacement. The numerical local buckling and global deformation are correlated well with the experimental data.

The force-total displacement traces and the deformation patterns manifest that with increasing the diameter of the spherical impactor, the impact force was increased and the total and global displacement was decreased for both RACFST and NACFST columns.

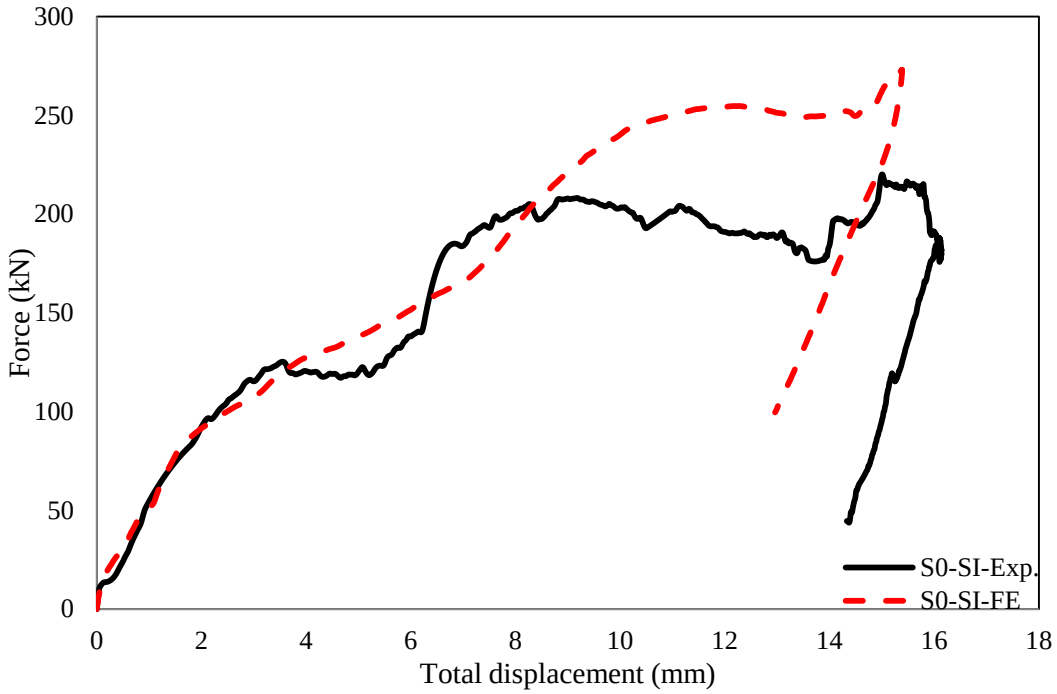

Figure 5.51. The FE and experimental force-total displacement traces for the NACFST column impacted by small spherical impactor with diameter of 20 mm

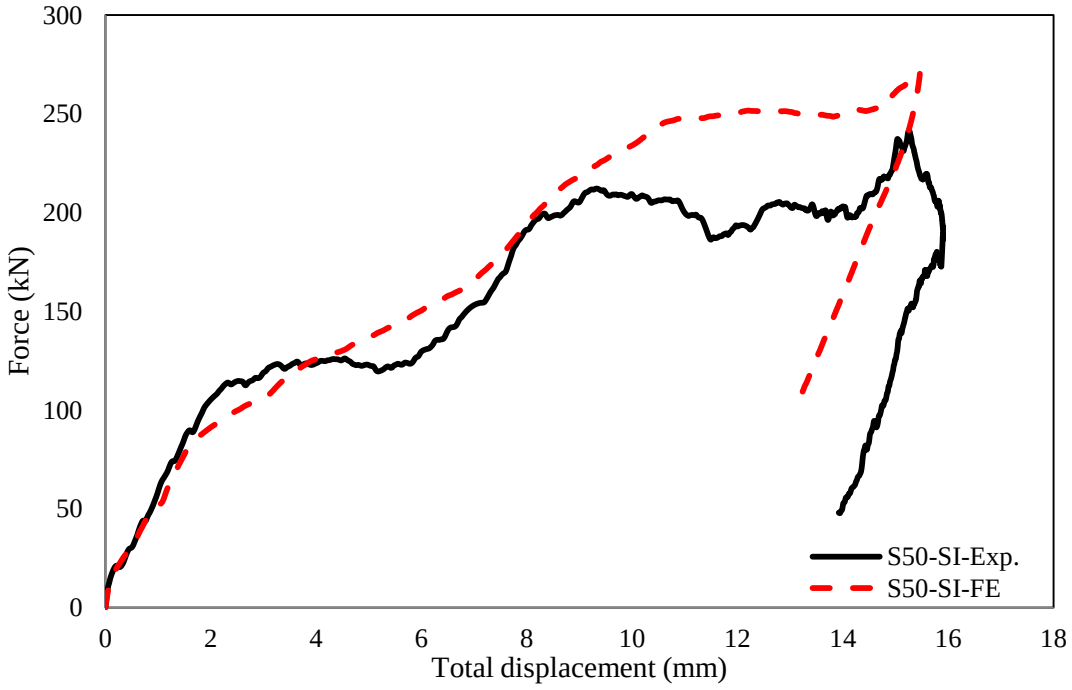

Figure 5.52. The FE and experimental force-total displacement traces for the RACFST column impacted by small spherical impactor with diameter of 20 mm

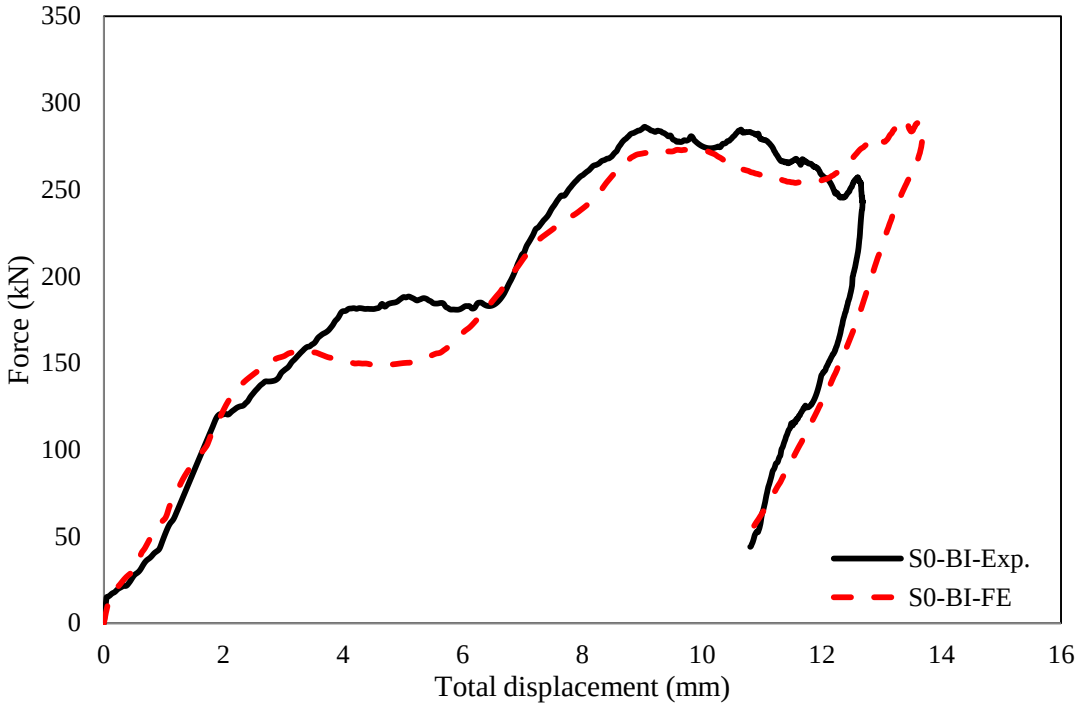

Figure 5.53. The FE and experimental force-total displacement traces for the NACFST column impacted by big spherical impactor with diameter of 60 mm

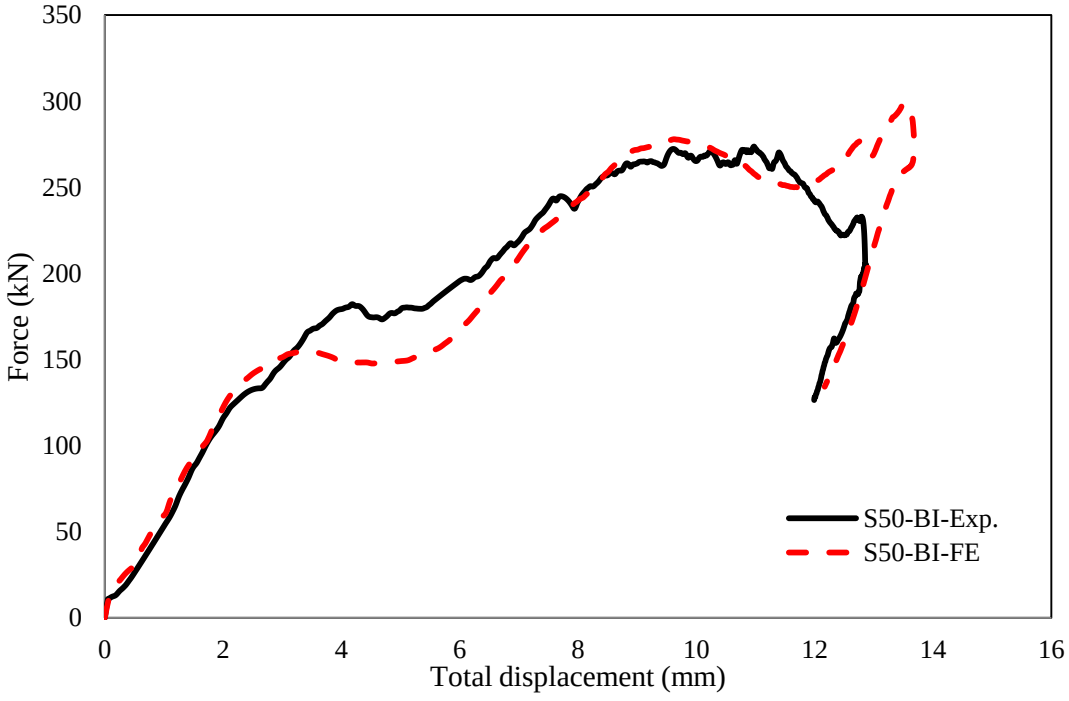

Figure 5.54. The FE and experimental force-total displacement traces for the RACFST column impacted by big spherical impactor with diameter of 60 mm

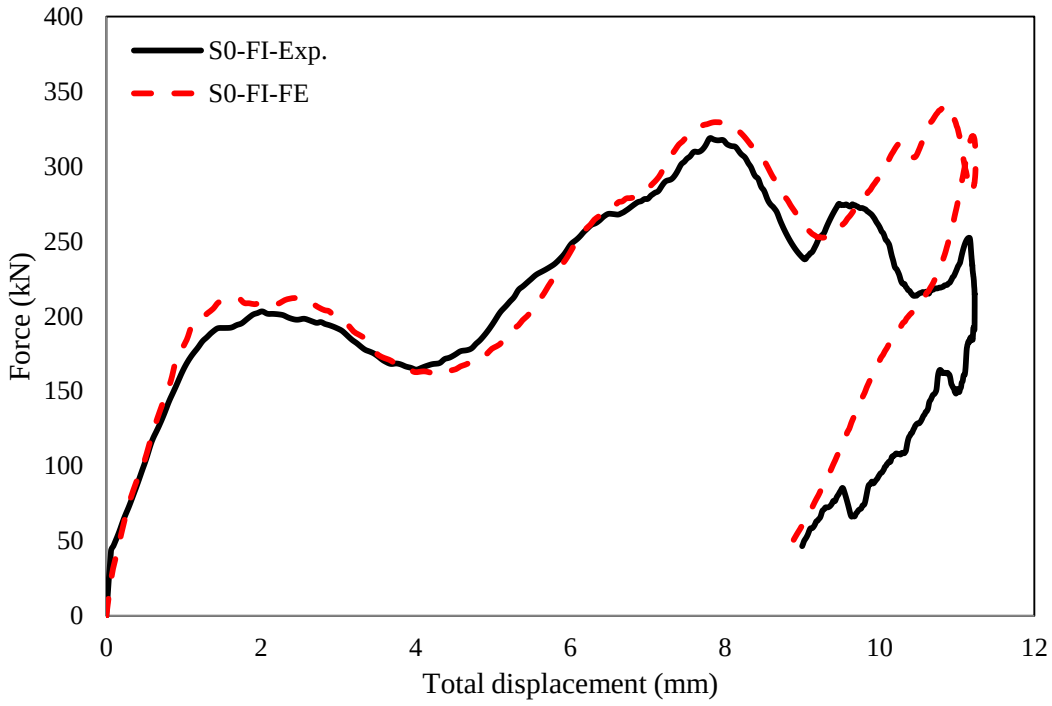

Figure 5.55. The FE and experimental force-total displacement traces for the NACFST column impacted by flat impactor with square section of (40 x 40) mm

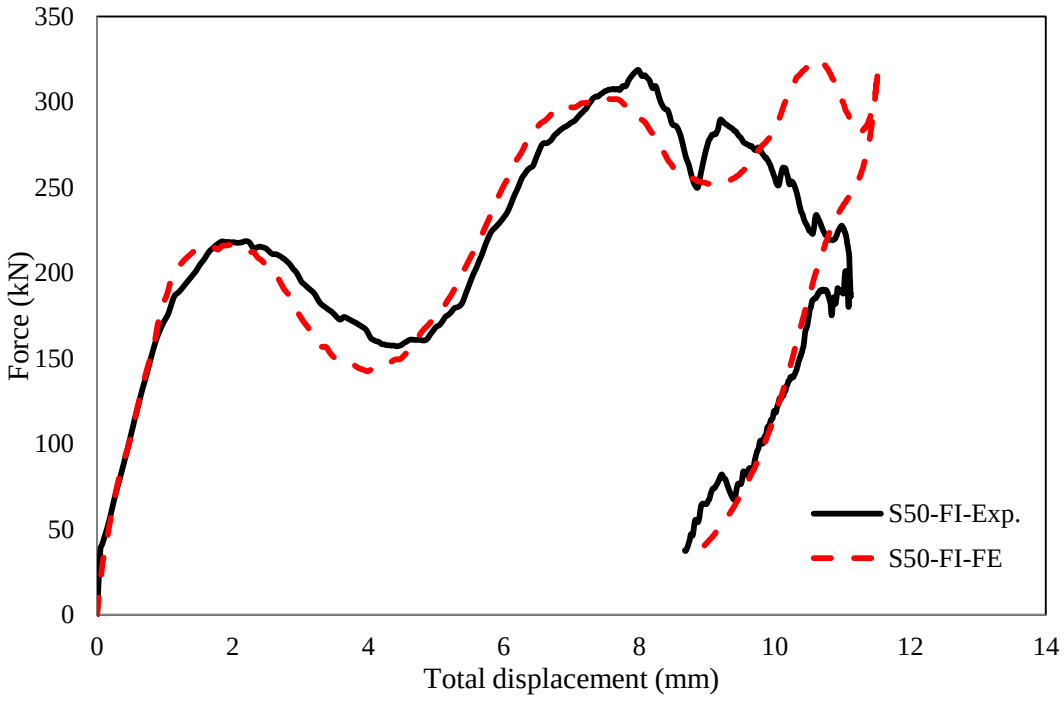

Figure 5.56. The FE and experimental force-total displacement traces for the RACFST column impacted by flat impactor with square section of (40 x 40) mm

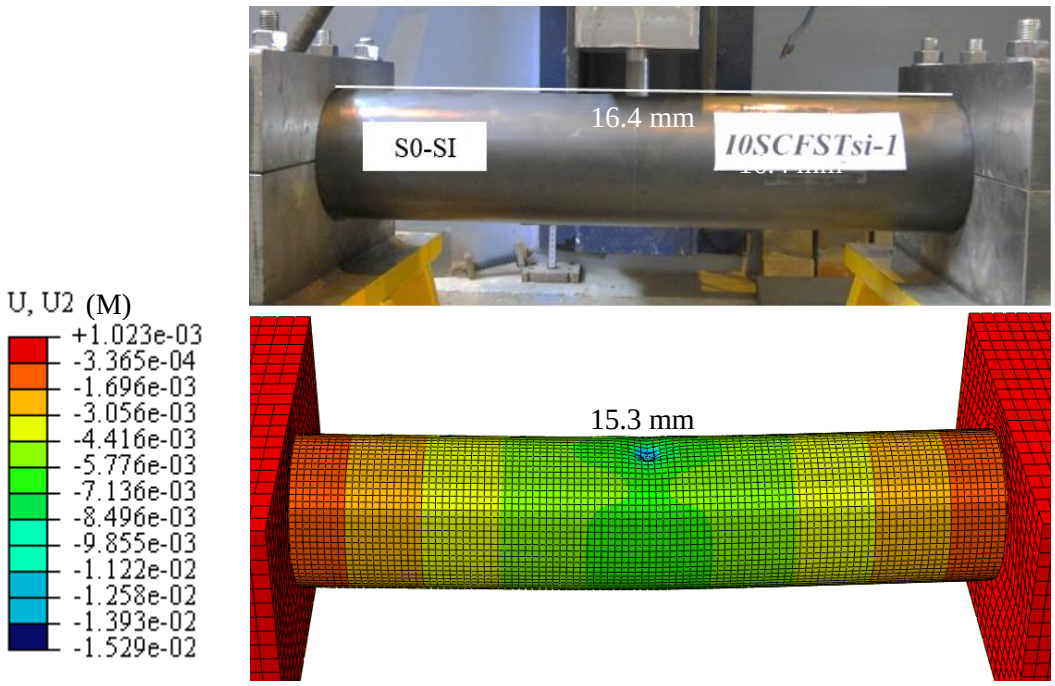

Figure 5.57. The deformation pattern for the NACFST column impacted by small spherical impactor

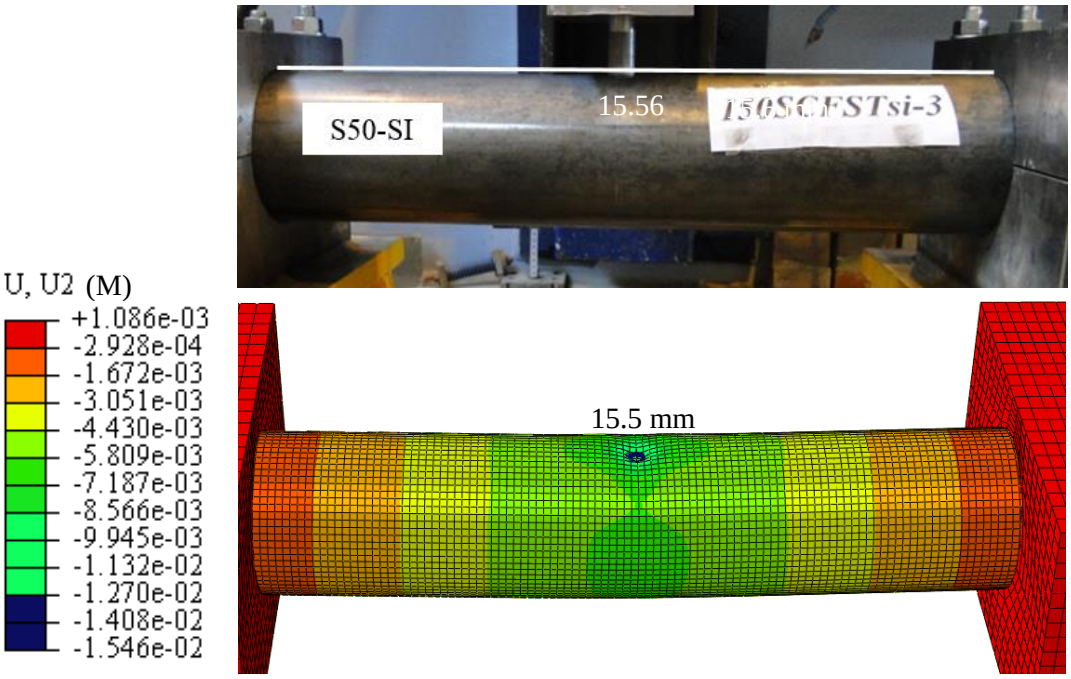

Figure 5.58. The deformation pattern for the RACFST column impacted by small spherical impactor

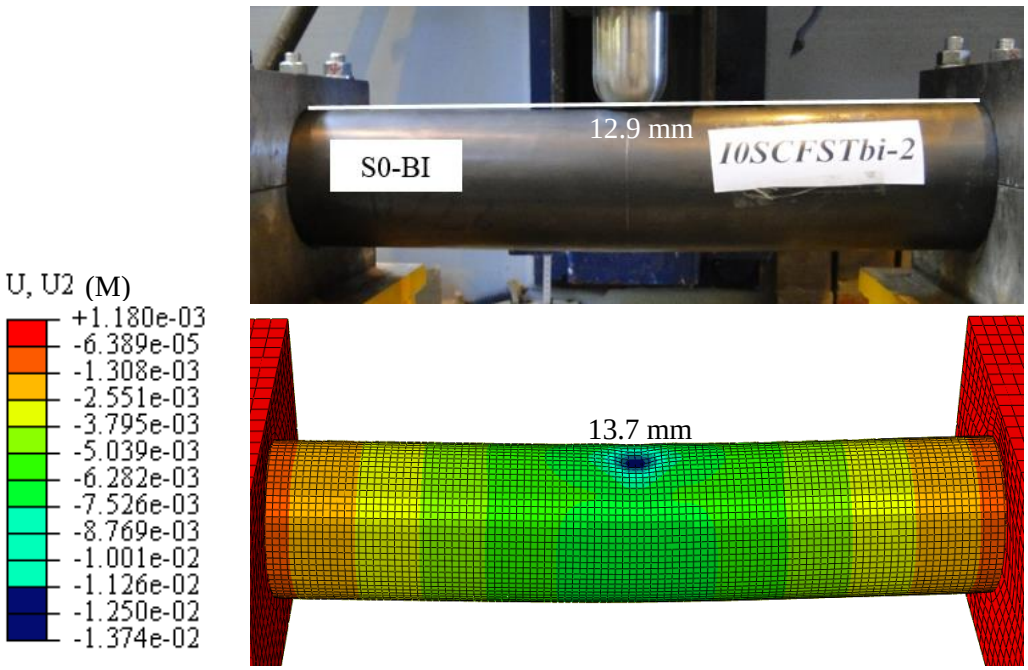

Figure 5.59. The deformation pattern for the NACFST column impacted by big spherical impactor

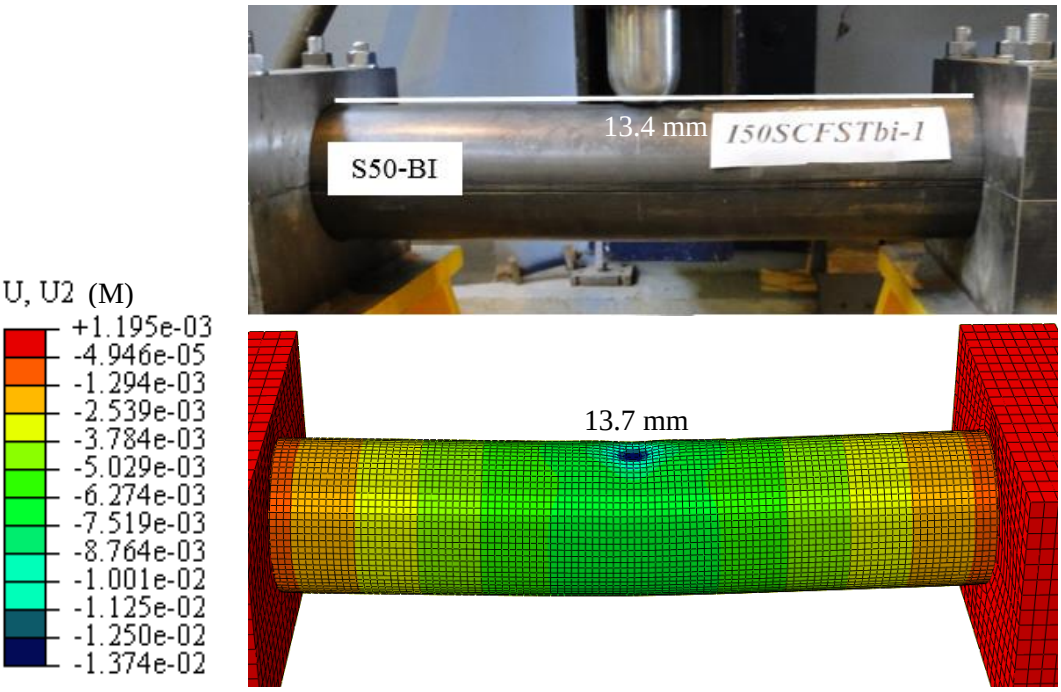

Figure 5.60. The deformation pattern for the RACFST column impacted by big spherical impactor

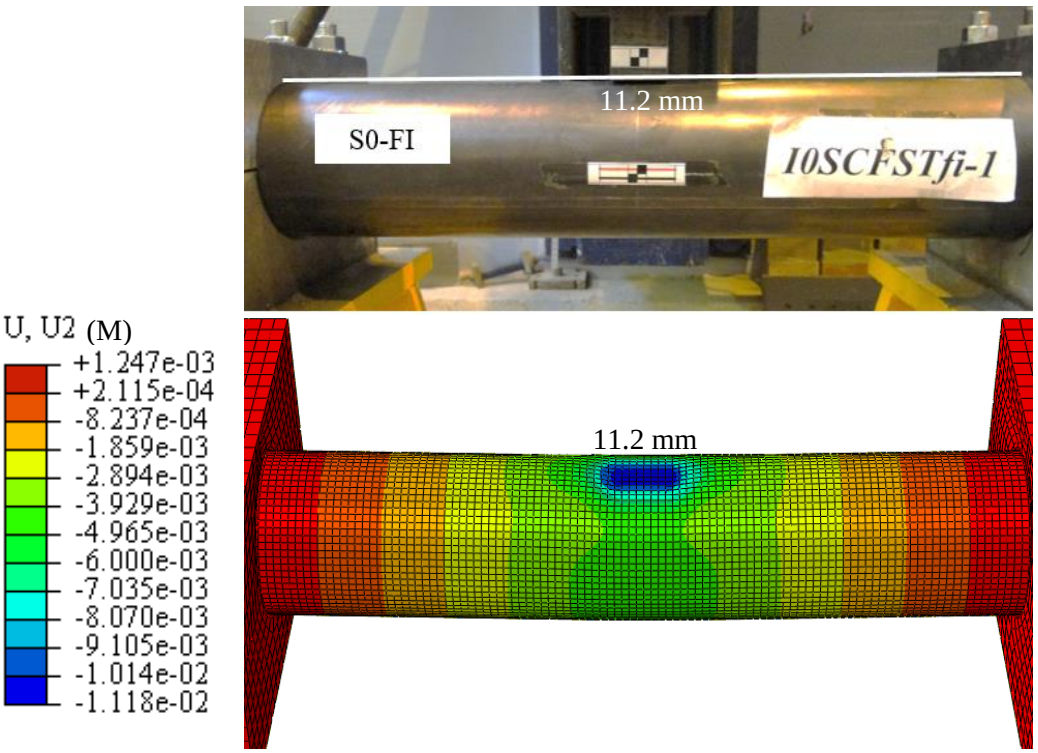

Figure 5.61. The deformation pattern for the NACFST column impacted by flat impactor

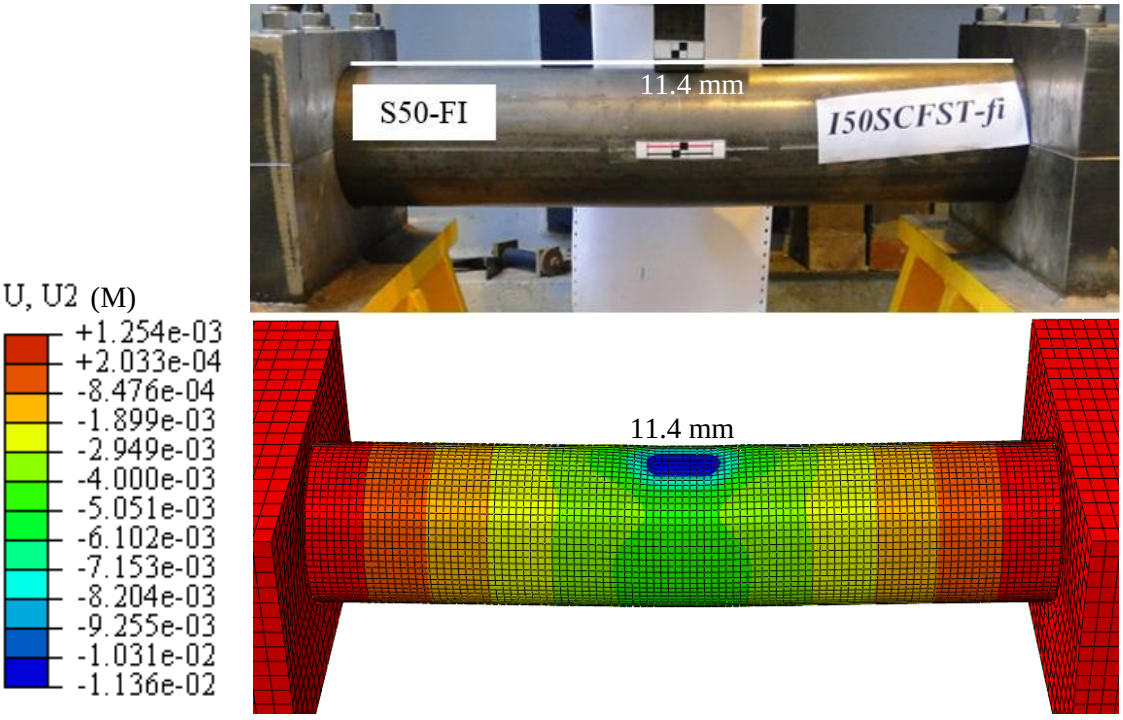

Figure 5.62. The deformation pattern for the RACFST column impacted by flat spherical impactor

5.4.4 Full range analysis

The validated models in the previous section were used to study the behaviour of the CFST columns in term of stress, strain, plasticity, confining pressure between the concrete core and the steel tube and contact stresses at the impacted area underneath the impactor and the support which cannot be obtained from the experimental results. In addition, the models were also used to explain the spikes of the impact force during the impact event, particularly the columns with a L/D ratio of 13.5. Fig. 5.63 shows the time history of the impact force for CFST tubes with L/D ratios of 6,9,13.5 (S0, M0 and L0, respectively).

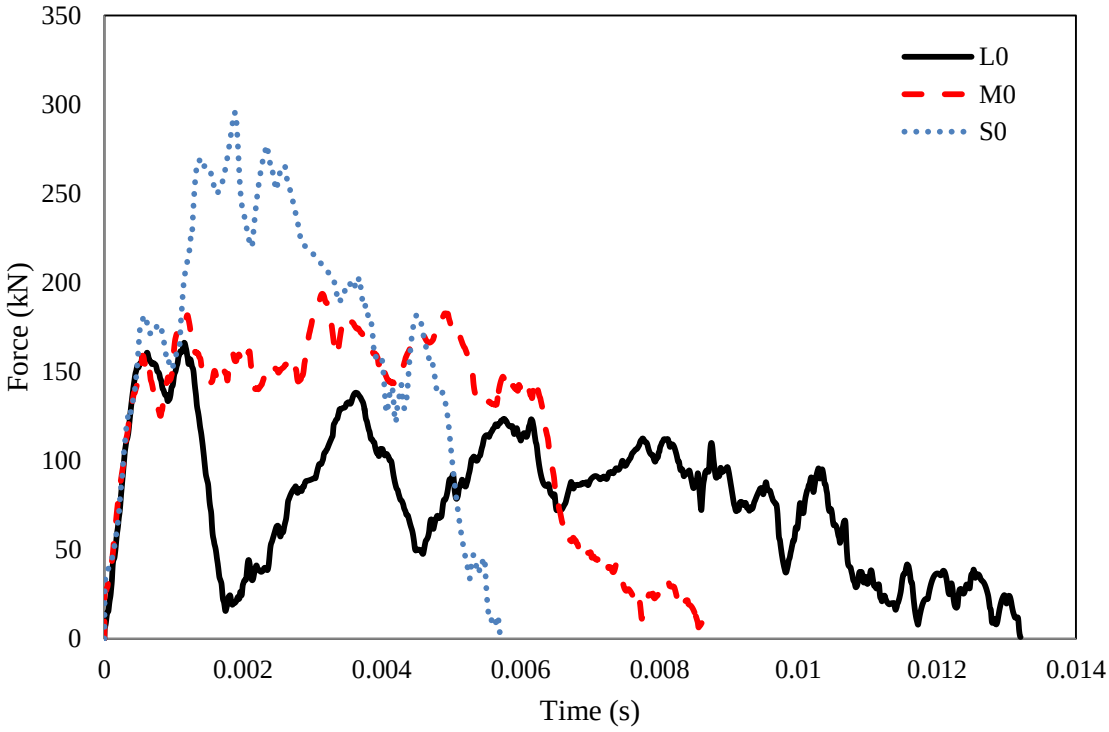

Figure 5.63. The impact force- time history of the CFST columns with different L/D ratio

The impact force for the columns at a time of about 0.0006 s began to decrease slightly. This reduction is due to the decrease of the steel tube stresses at the area underneath the impactor as they exceed its ultimate strength as shown from Fig. 5.64 (a), (b) and (c) for the tube with L/D ratios of 6, 9, and 13.5, respectively. Once the full contact between the tube and concrete occurred, the impact force increased again due to the increase in the contact stiffness. When the impactor hits the CFST column, the velocity of the impactor decreases,

whist the velocity of the CFST increases due the impact action. Then, the velocity for the both impactor and CFST column retreats to zero. Once that happens both of the impactor and CFST column bounce back due to the elastic energy. Fig. 5.65 (a) shows that the velocity of the impactor is slightly lower than the CFST column. The difference between the velocities induces the CFST column to separate from the impactor which led to the fluctuation of the confining pressure, which in turn, causes the fluctuation of the force-total displacement trace of the CFST column with a L/D ratio of 13.5 as shown in Fig. 5.65(b). However, the HSC records did not show any separation between the impactor and CFST column as mentioned in Chapter 4. In addition, the vibration during the impact event leads to the oscillation of the force-displacement trace.

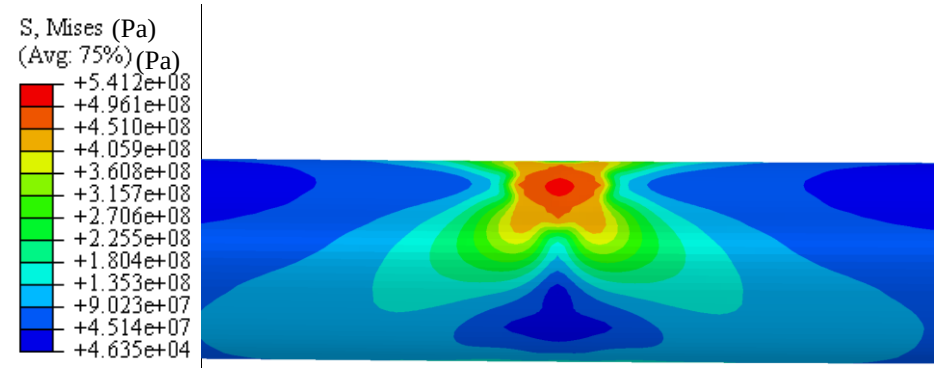

(a) L/D ratio of 13.5

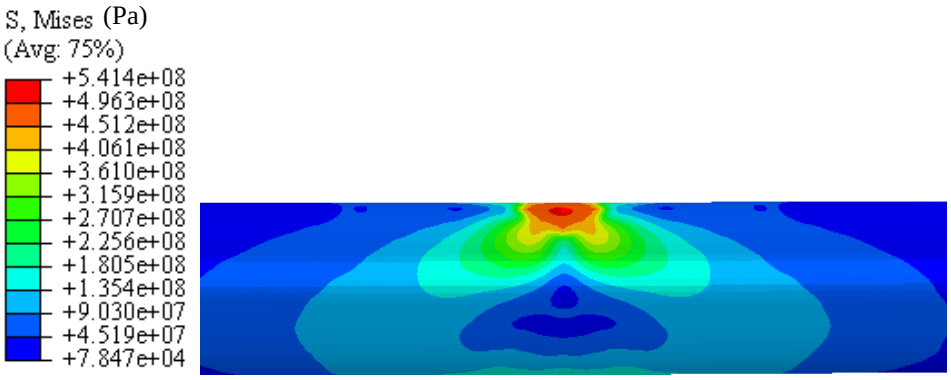

(b) L/D ratio of 9

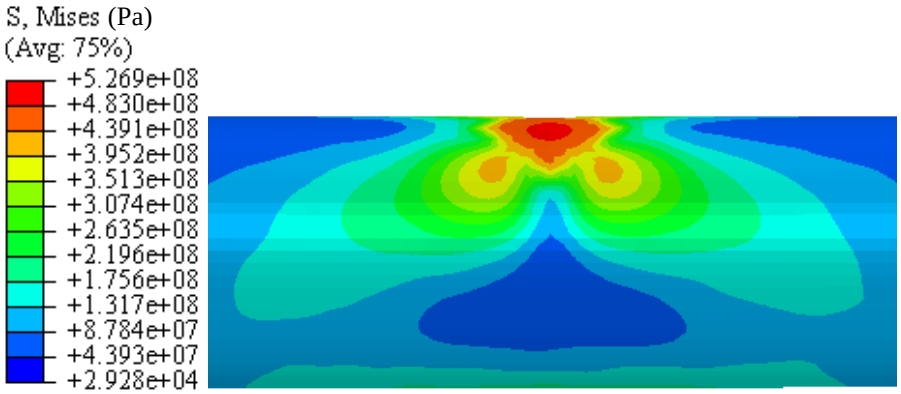

(c) L/D ratio of 6

Figure 5.64. The von Mises stresses for the CFST columns with different L/D ratio at 0.0006 s

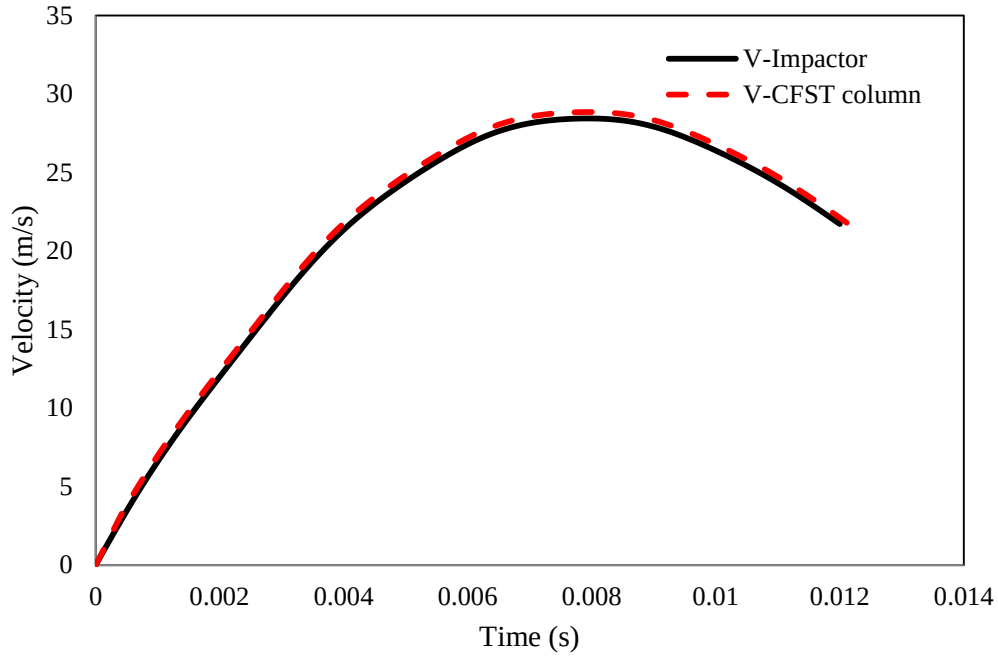

(a) The velocity of the impactor and the CFST column

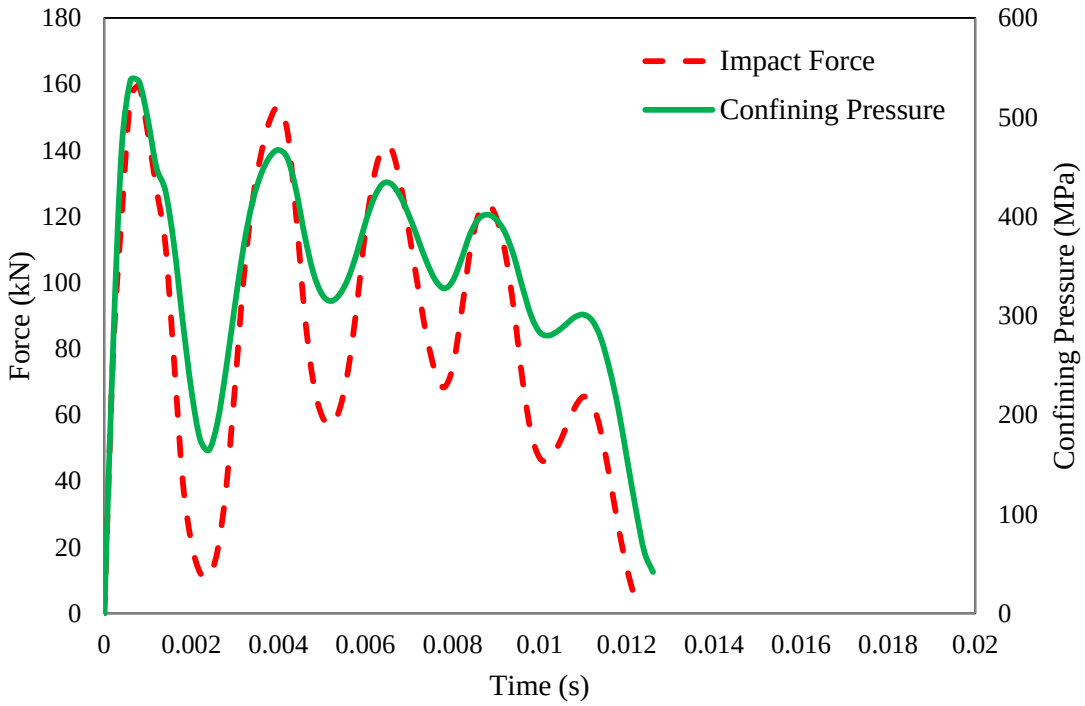

(b) The impact force with confining pressure

Figure 5.65. The fluctuation of the force for the CFST column with L/D ratio of 13.5

Figs 5.66 (a), (b), (c) and (d) show that the cracking of the concrete core and the yielding of the steel tube during the impact event, particularly at mid span of the column. These cracks

and the yielding of steel affect the contact between the concrete core and steel tube which also led to the fluctuation of the confining pressure. Figs. 5.66 (a) and (c) show that the concrete damage increases with increasing the global deformation of the column, leading to the increase of the number and the width of the cracks due to the low tensile strength of the concrete. At the same time, the yielding area of the steel tube is also expanded. Although it does not reach the ultimate strength of steel, this is likely to cause the reduction of the stiffness of the column. Due to the relatively higher stiffness of the CFST column with L/D ratios of 6 and 9 then the one with a L/D ratio of 13.5, the fluctuation of the force-total displacement trace was less. However, the cracks of the concrete core and yielding of the steel tube still led to a few spikes. For examples, the degrading of the impact force at times of 0.002 s and 0.0045 s for the columns with L/D ratios of 6 and 9, respectively, as can be seen in Fig 5.63. Fig. 5.67 shows that the concrete damage and the yielding of the steel tube for these columns. The CFST column with a L/D ratio of 6 is less influenced due to less cracking which results from the relatively high stiffness compared to the other CFST columns. This led to increasing the confining pressure, which in turn led to raise the impact force to the third peak at time of 0.0018 s, as shown in Fig. 5.63. The history of the confining pressure for the CFST columns will be discussed later in this section.

The validated models were used to present the stress and strain distributions of the steel tube and concrete core for the CFST columns with different L/D ratio. Figs. 5.68 (a), 5.68 (b) and 5.68 (c) show the stress distribution of the CFST columns with L/D ratios of 6, 9 and 13.5, respectively. In general, it can be seen that the high stress distributed at the mid span area in particular the area under the impactor. The yielded area expanded with increasing the L/D ratio due to increasing the lateral deflection of the columns, as shown in Fig. 5.68 (a) in which the stresses exceeded the yield strength of the steel. However, the predicted stresses in the indentation area reached the ultimate strength of the steel which is 530 MPa.

Figs 5.69 and 5.70 show the strain and the plastic strain distribution of the steel tube for the CFST columns with different L/D ratios. Only the impacted area exhibited plastic

deformations with relatively small plastic strains, whilst almost no plastic strain appears in the other parts of the tubes. It can be seen that the plastic deformation area and the plastic strain increased with reducing the L/D ratio. This agrees with the experimental results related to increasing the depth and the diameter of the indentation with the reduction of the CFST column span.

The von Mises stress and plastic strain distributions for the concrete core of the CFST columns are shown in Figs 5.71 and 5.72, respectively. These figures reveal that the combined action between the concrete core and the steel tube makes the concrete act in a ductile manner locally. Although the steel tube prevented brittle failure of the concrete, the concrete core exhibited high stresses and strains at the impacted area and the supports which are increased with increasing the span length of the tube.

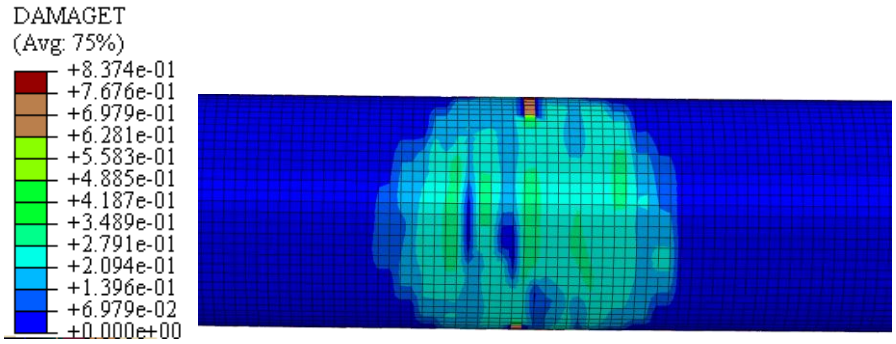

(a) concrete core at 0.001 s

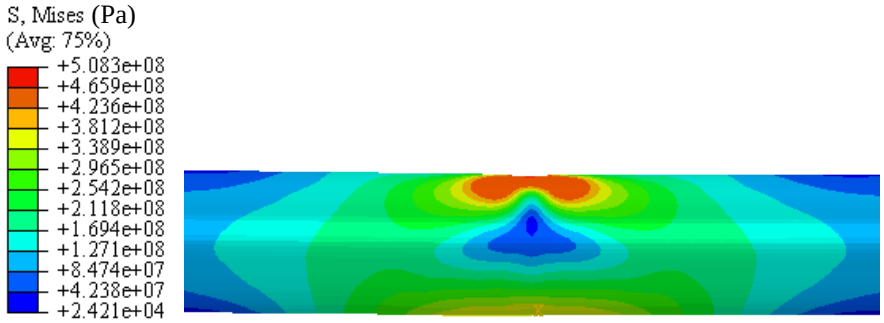

(b) steel tube at 0.001 s

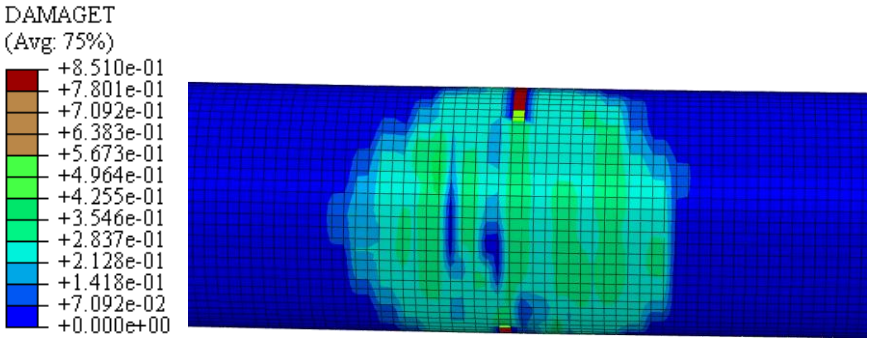

(c) concrete core at 0.002 s

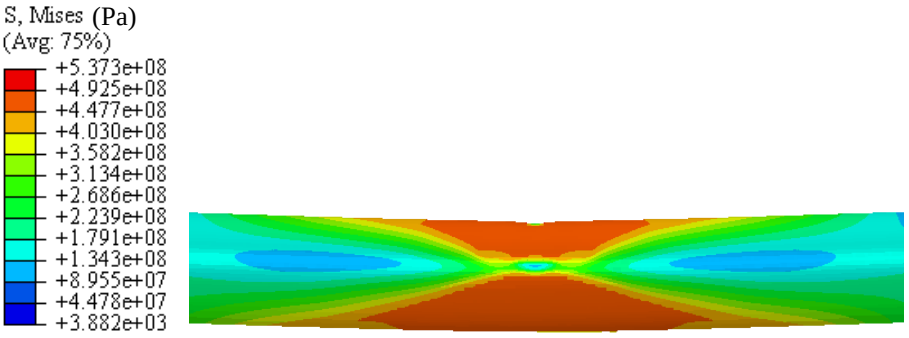

(d) steel tube at 0.002 s

Figure 5.66. The concrete damage and yielding of the steel tube during the impact event for the CFST column with L/D ratio of 13.5

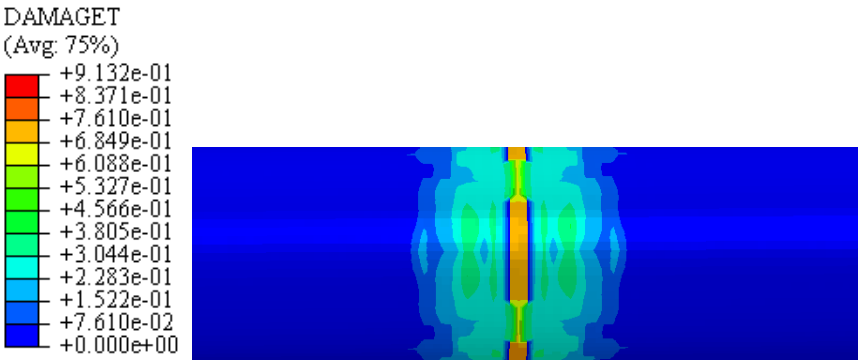

(a) concrete core with L/D ratio of 9 at 0.0045 s

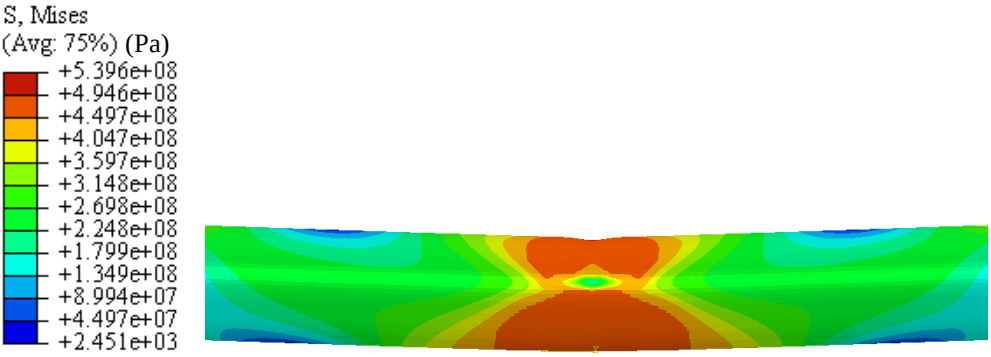

(b) steel tube with L/D ratio of 9 at 0.0045 s

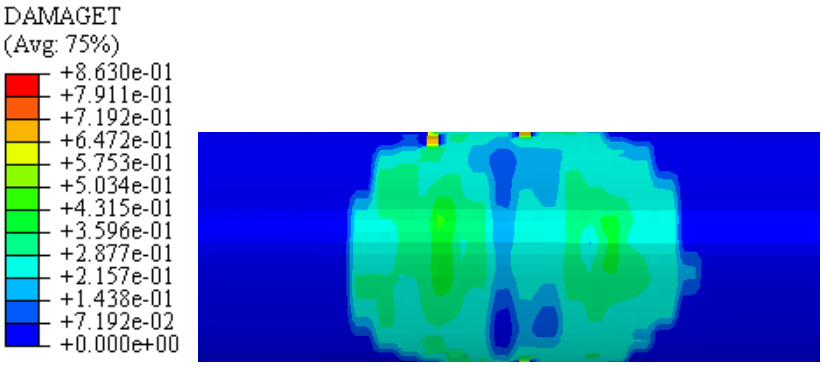

(c) concrete core with L/D ratio of 6 at 0.0021 s

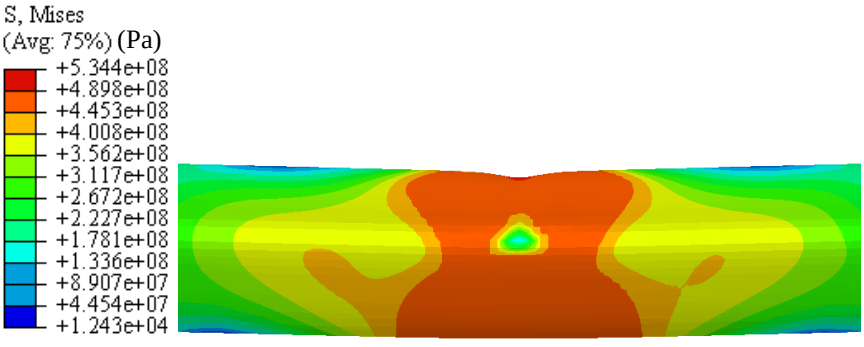

(d) steel tube with L/D ratio of 6 at 0.0021 s

Figure 5.67. The concrete damage and yielding of the steel tube during the impact event for the CFST column with different L/D ratio

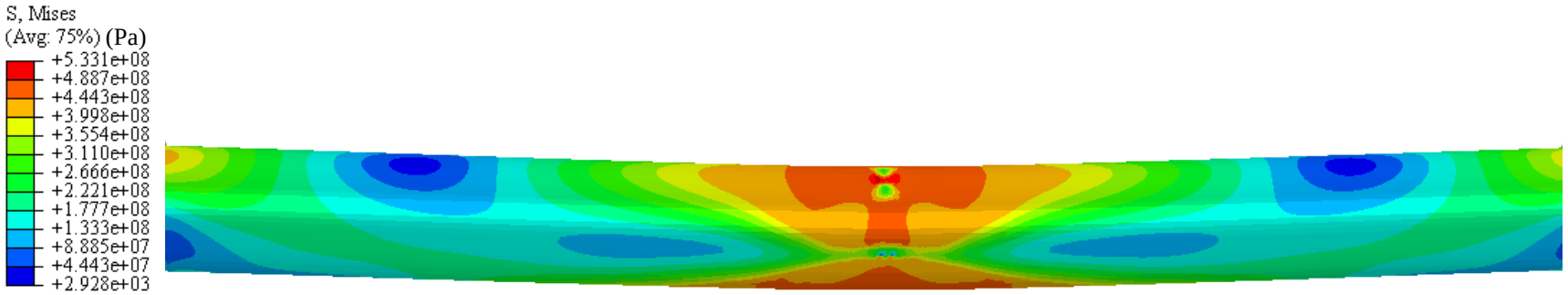

(a) L/D ratio of 13.5

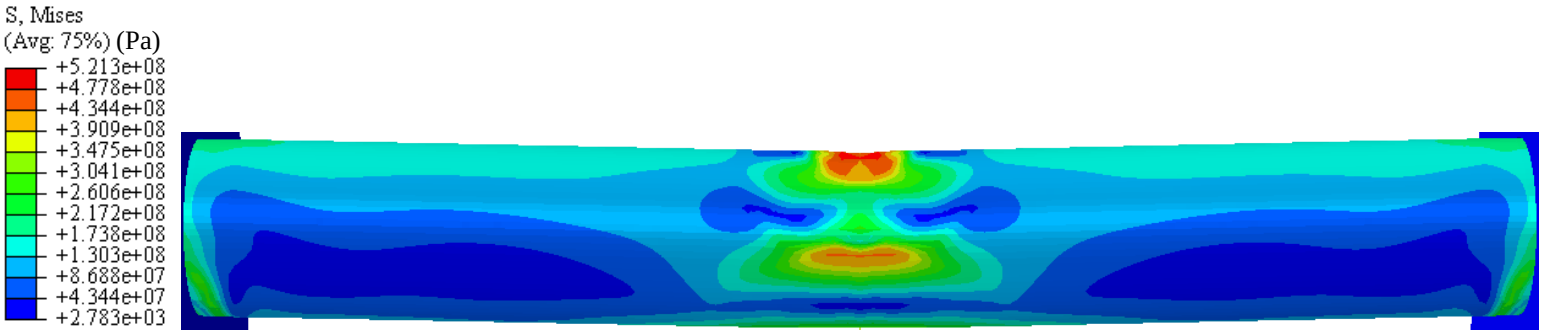

(b) L/D ratio of 9

Figure 5.68. Stress distribution for the steel tube of the CFST columns with different L/ D ratios

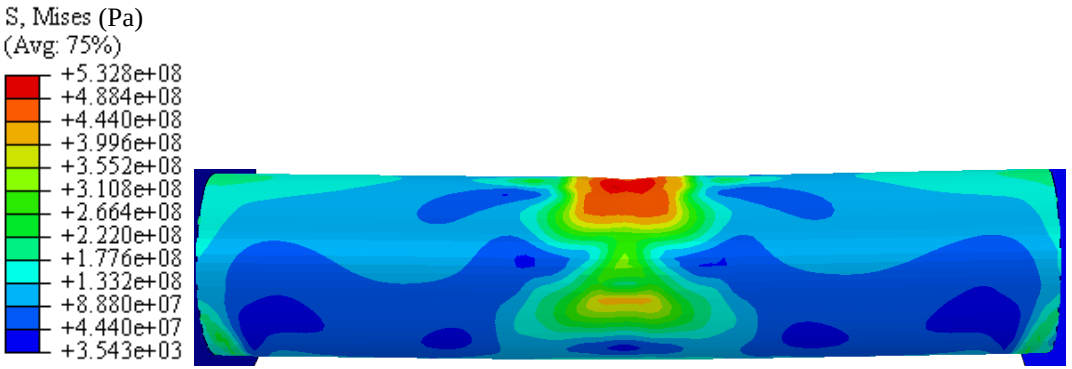

(c) L/D ratio of 6

Figure 5.68 (continued). Stress distribution for the steel tube of the CFST columns with different L/ D ratios

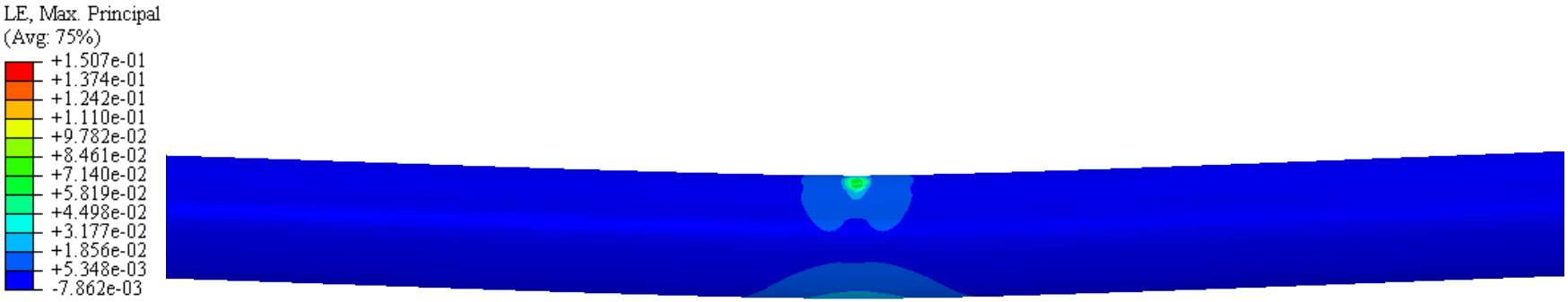

(a) L/D ratio of 13.5

Figure 5.69. Strain distribution for the steel tube of the CFST columns with different L/ D ratios

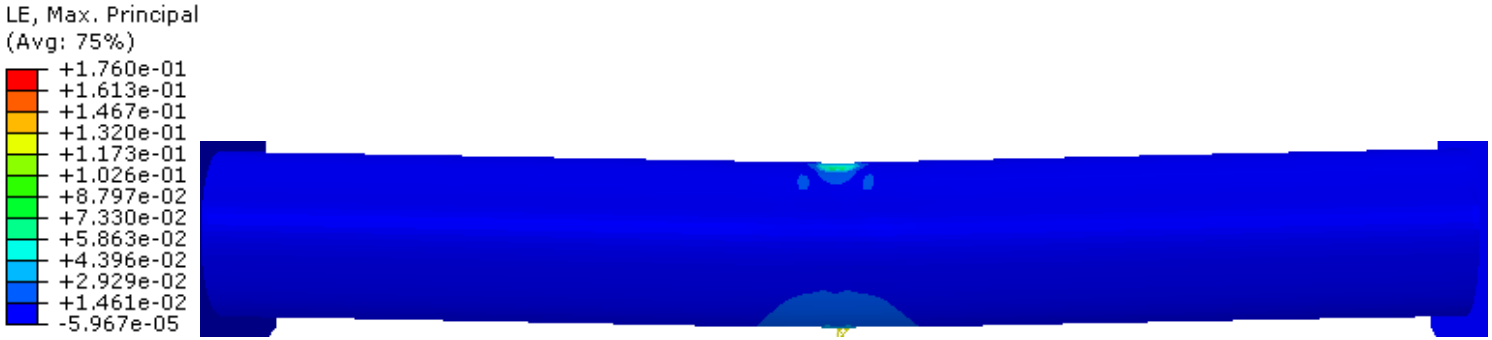

(b) L/D ratio of 9

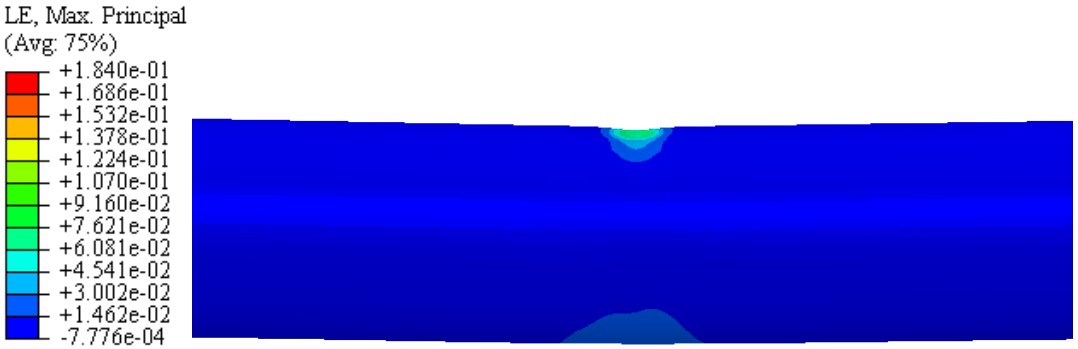

(c) L/D ratio of 6

Figure 5.69. (Continued). Strain distribution for the steel tube for the CFST columns with different L/ D ratios

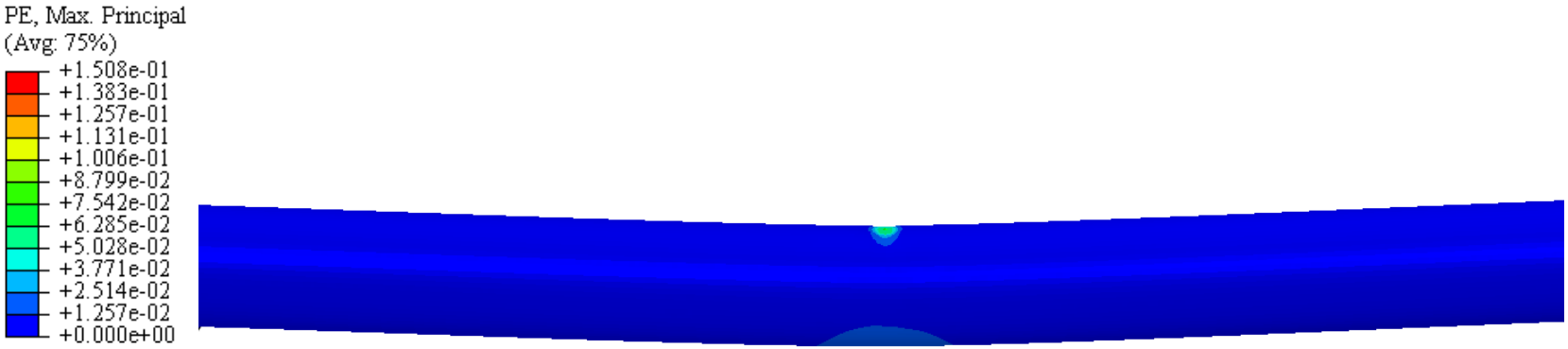

(a) L/D ratio of 13.5

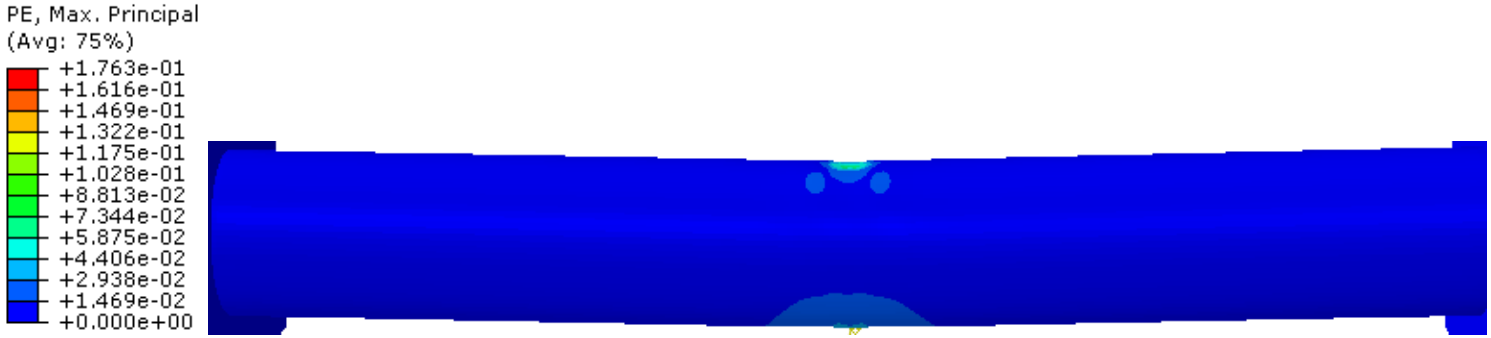

(b) L/D ratio of 9

Figure 5.70. Plastic strain distribution for the steel tube of the CFST columns with different L/ D ratios

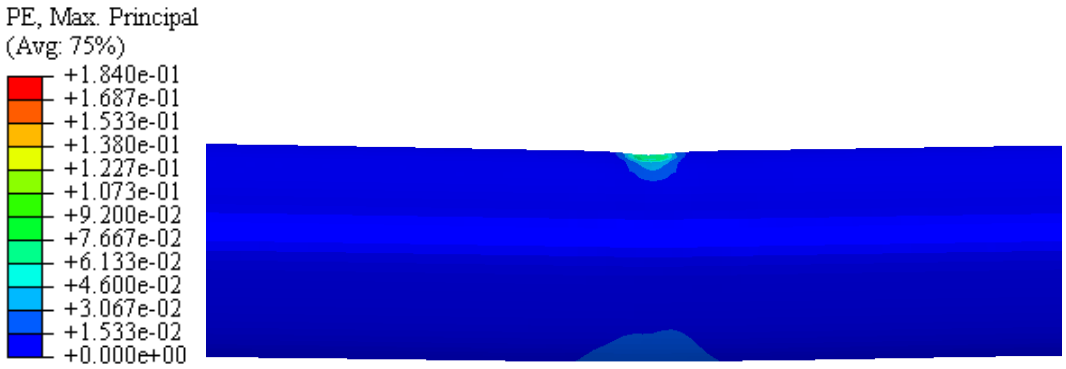

(c) L/D ratio of 6

Figure 5.70. (Continued). Plastic strain distribution for the steel tube of the CFST columns with different L/ D ratios

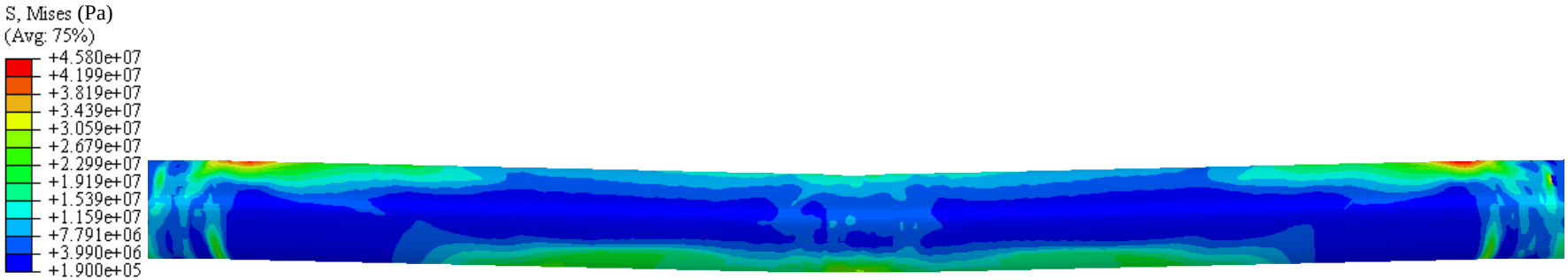

(a) L/D ratio of 13.5

Figure 5.71. Stress distribution for the concrete core of the CFST columns with different L/ D ratios

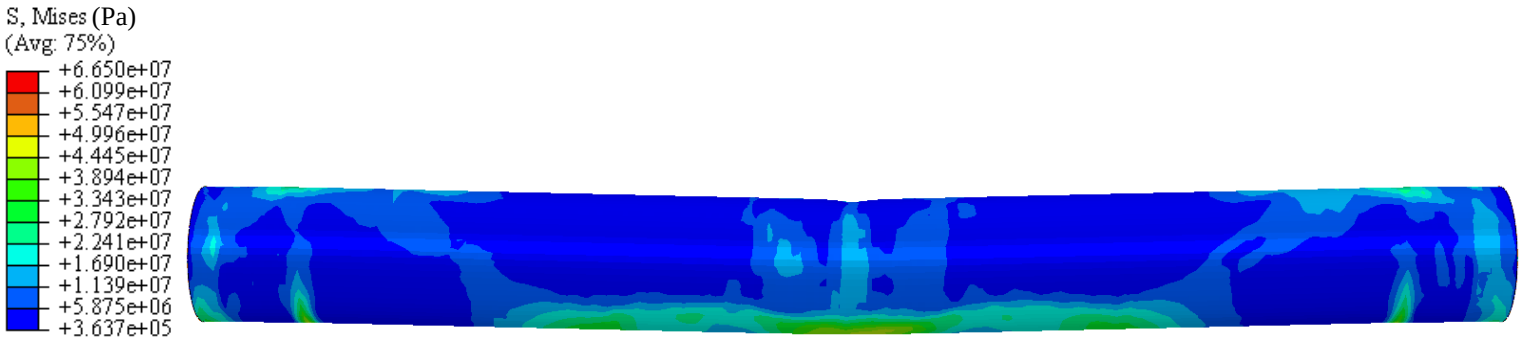

(b) L/D ratio of 9

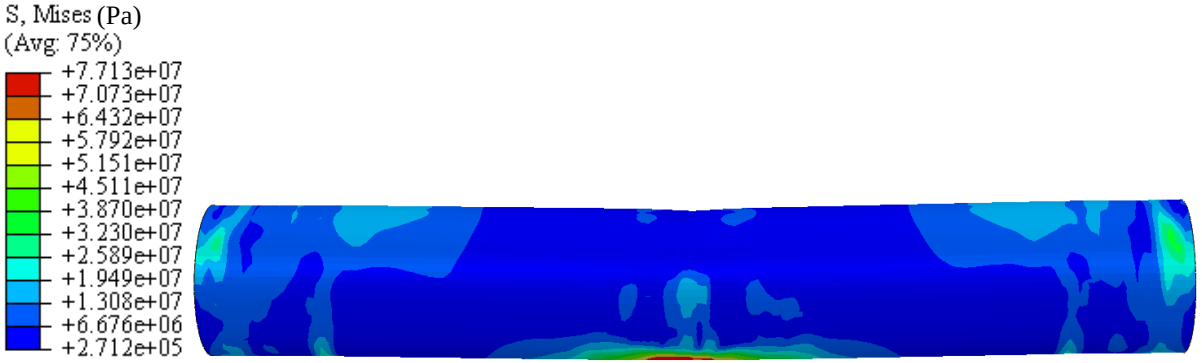

(c) L/D ratio of 6

Figure 5.71. (Continued). Stress distribution for the concrete core of the CFST columns with different L/ D ratios

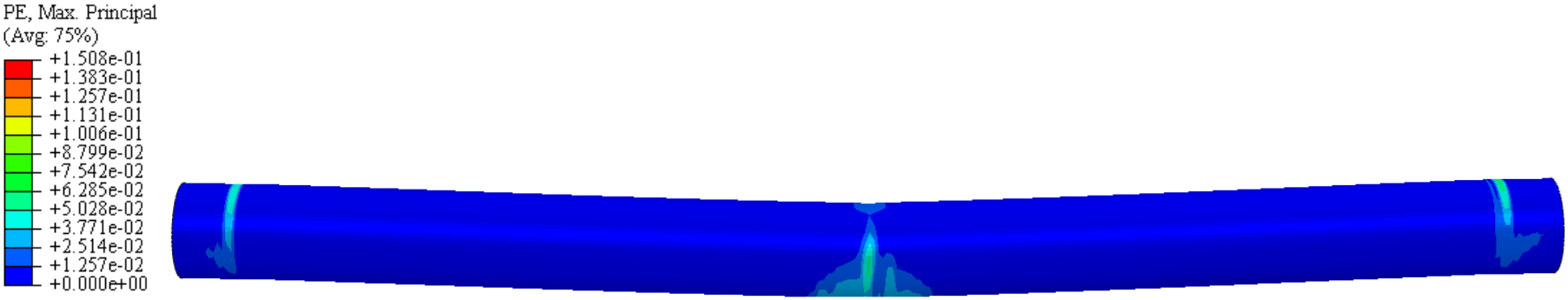

(a) L/D ratio of 13.5

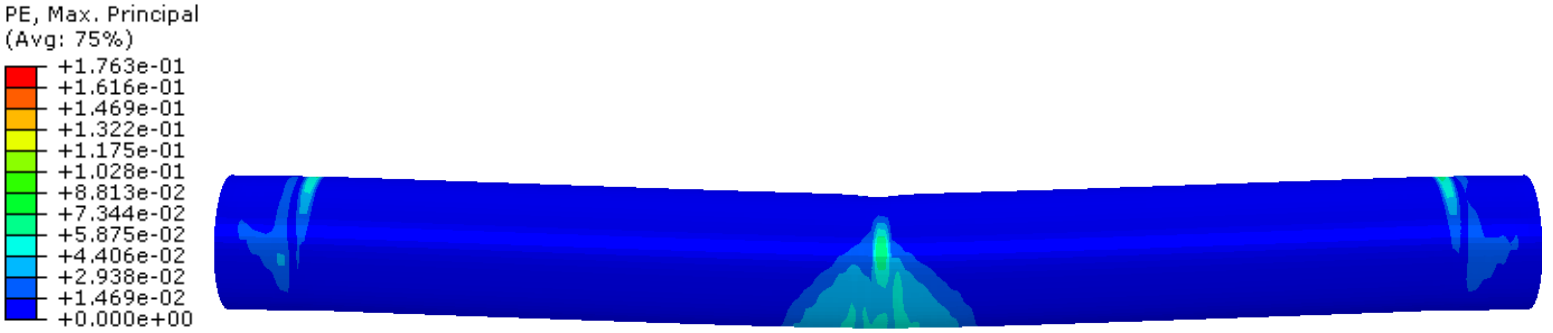

(b) L/D ratio of 9

Figure 5.72. Plastic strain distribution for the concrete core of the CFST columns with different L/ D ratios

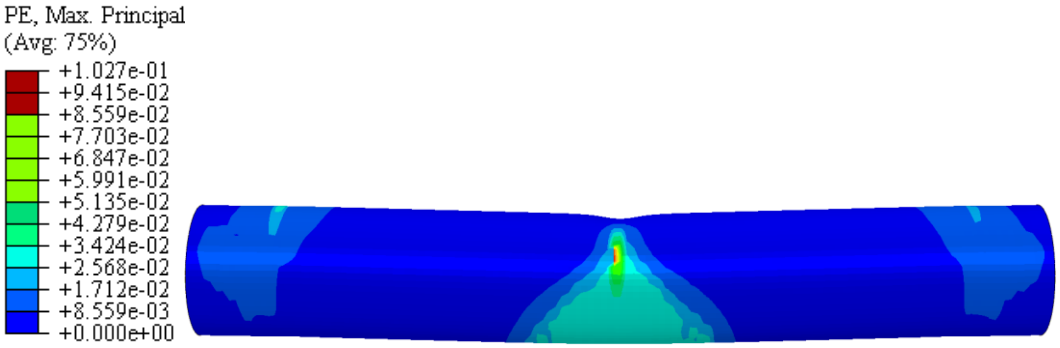

(c) L/D ratio of 6

Figure 5.72 (Continued). Plastic strain distribution for the concrete core of the CFST columns with different L/ D ratios

Fig. 5.73 shows the comparison between the experimental and numerical crack pattern of the concrete cores with different L/D ratios. It can be seen that the models reasonably captured the cracked area similar to that from the experimental results. In addition, the models are capable of showing the crack pattern, especially the model of the CFST column with a L/D ratio of 13.5. Clearly, the models show that the tension damage is increased with increasing the L/D ratio of the CFST columns due to the low stiffness of the columns.

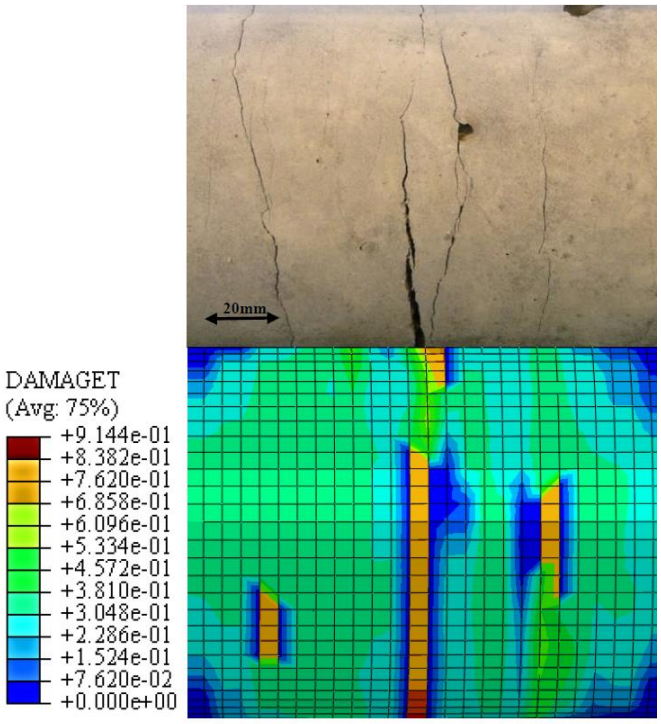

(a) L/D ratio of 13.5

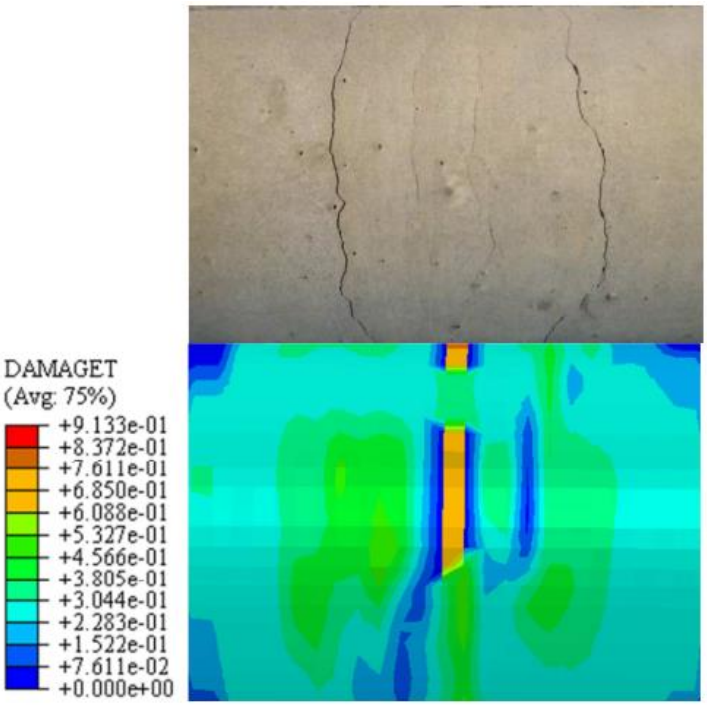

(b) L/D ratio of 6

Figure 5.73. Comparison between the numerical and experimental cracks pattern of the concrete core of the CFST columns with different L/D ratios

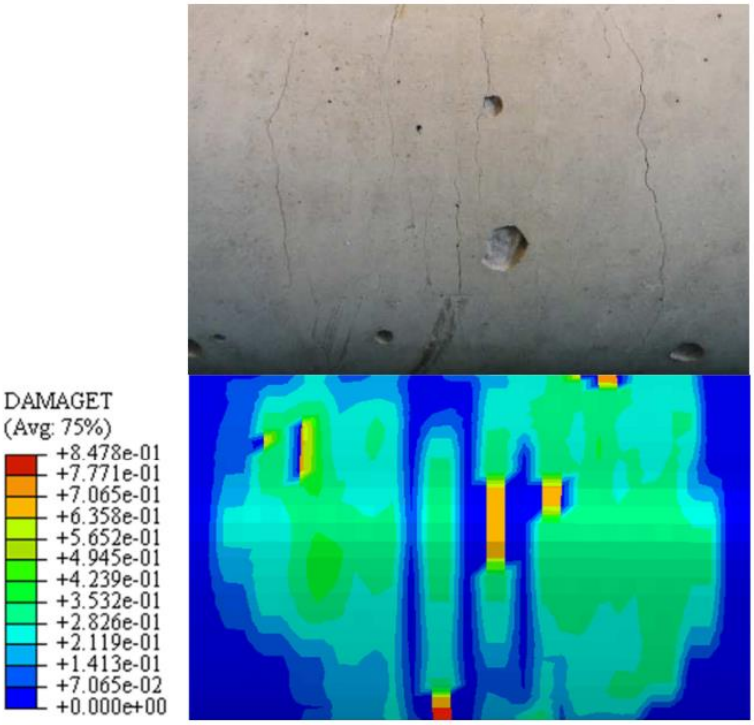

(c) L/D ratio of 6

Figure 5.73 (Continued). Comparison between the numerical and experimental cracks pattern of the concrete core of the CFST columns with different L/D ratios

The confining pressure-time history for the concrete core of the CFST column at selected points is given in Figs. 5.74 (a), 5.74 (b) and 5.75 (c) for the columns with L/D ratios of 13.5, 9 and 6, respectively. The positions of these points are shown in Fig. 5.74 (d). It can be seen that during the impact event the concrete core is under high confining pressure especially near the impacted area. The confining pressure at point 2 is almost zero because of the loss of the contact between the concrete core and the steel tube due to the local buckling at the impacted area, as shown in Fig 5.74 (d). Due to this confining the pressure, the plasticity and the ductility of the concrete are significantly improved. In addition, the local buckling of the steel tube is eliminated due to the existence of the concrete core. It can be seen that the confining pressure varies within the cross section of concrete core for the same column and it decreases with increasing the L/D ratio due to losing the contact between the steel tube and the concrete core which results from the cracks and the deflection of the concrete core as well as the yielding of the steel tube.

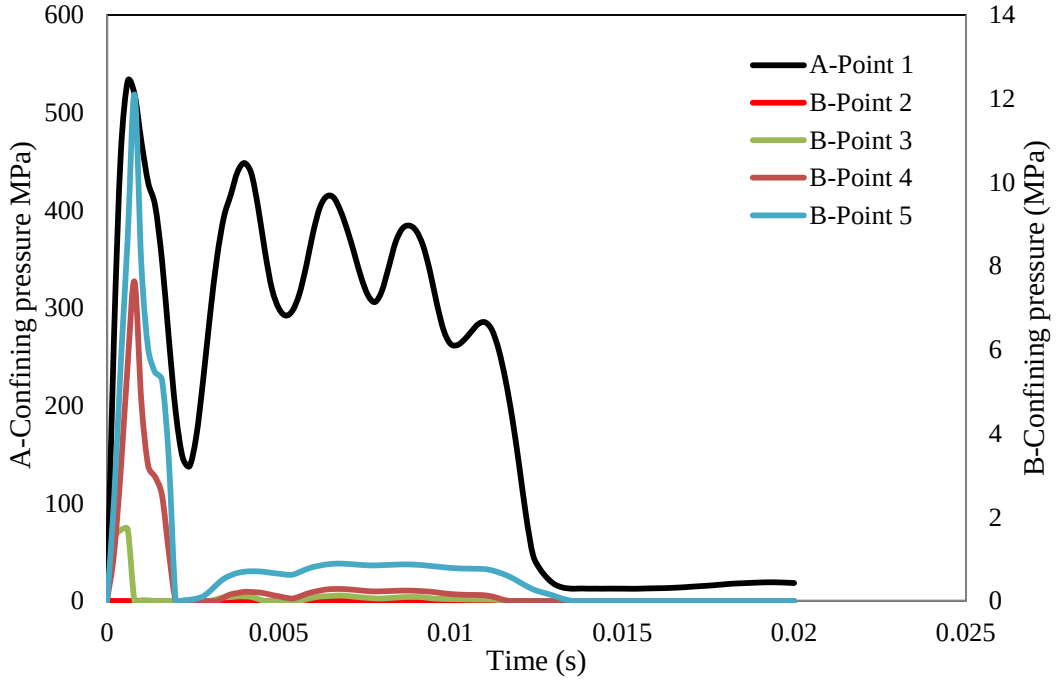

(a) The confining pressure at mid span for the CFST column with L/D ratio of 13.5

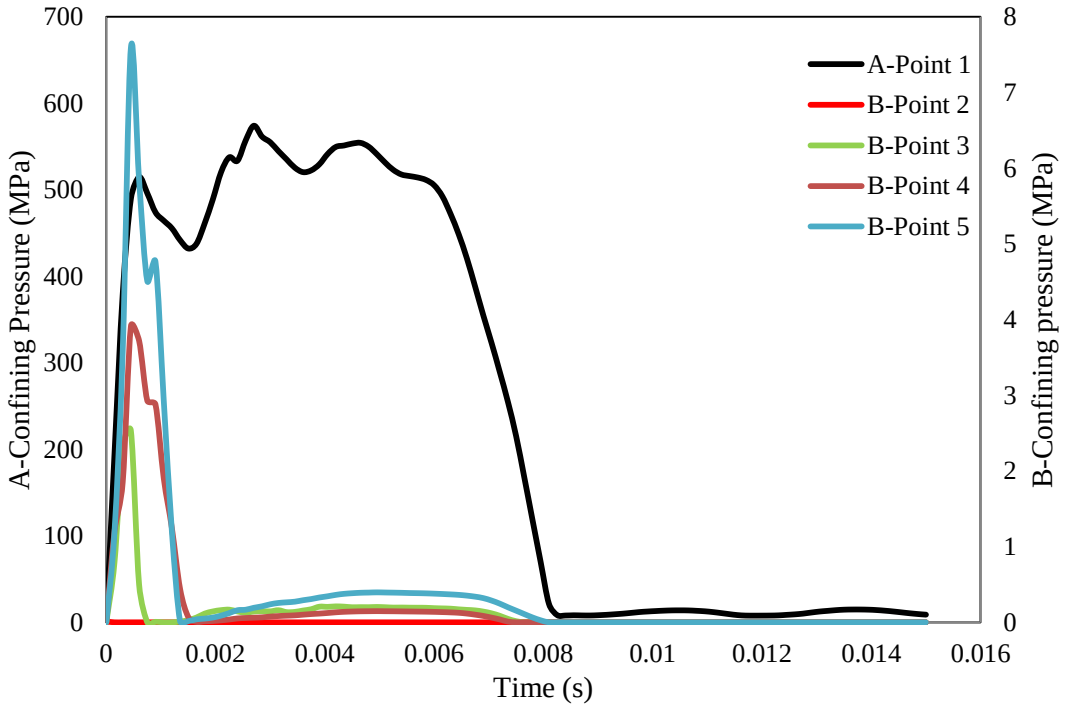

(b) The confining pressure at mid span for the CFST column with L/D ratio of 9

Figure 5.74. The confining pressure history for CFST column with different L/D ratio at mid-span

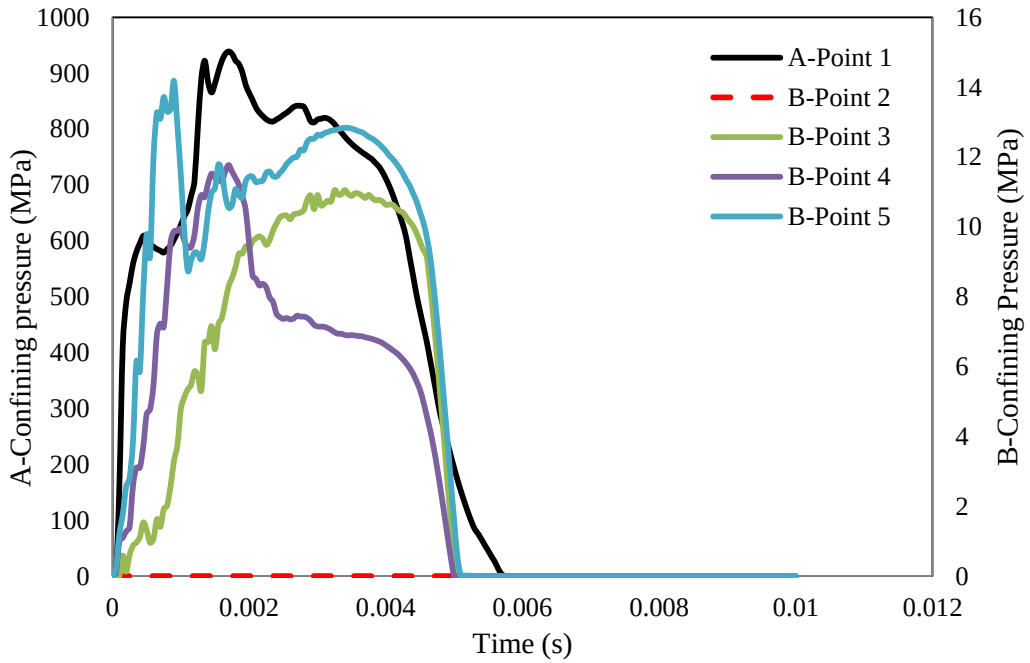

(c) The confining pressure at mid span for the CFST column with L/D ratio of 6

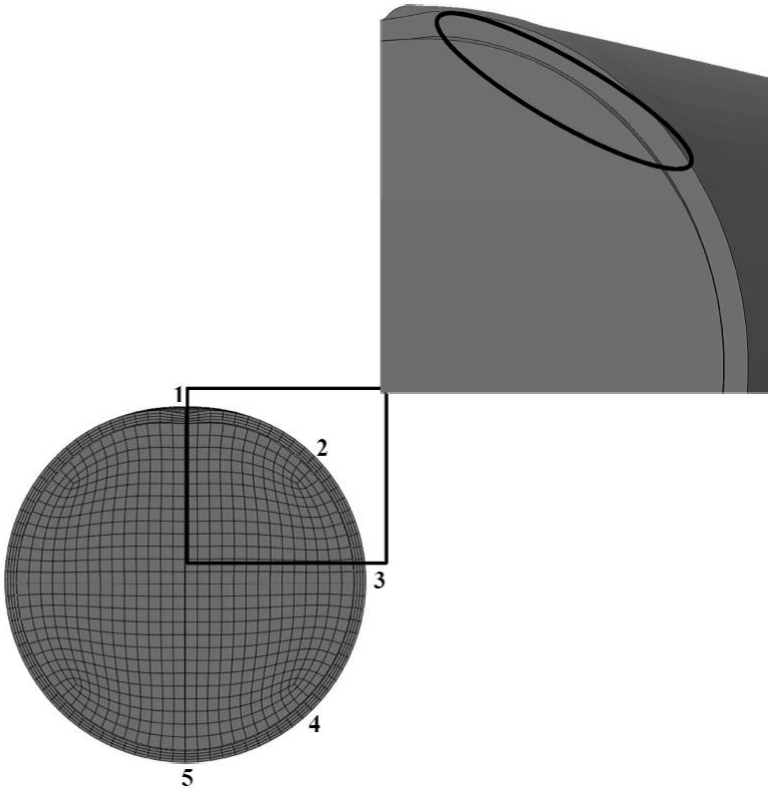

(d) The adopted point where the confining pressure predicted at the mid-span of the CFST columns

Figure 5.74 (continued). The confining pressure history for CFST column with different L/D ratios at mid-span

The contact stresses at the mid span and the supports for the CFST columns with L/D ratios of 13.5, 9 and 6 are shown in Figs 5.75 (a), 5.75 (b) and 5.75 (c), respectively. Again, the contact stresses are decreased with increasing the span length of the columns from 670 to 260 MPa and from 150 to 35 MPa at the mid span and the support, respectively, when the L/D ratio increased from 6 to 13.5. The stresses at the support are significantly less than those at mid span due to the direct impact loading there which induces the column to exhibit much higher responsive stresses.

The friction force for the CFST columns with different L/D ratios is presented in Fig. 5.76. The friction force is also affected by the contact between the concrete core and the steel tube, which in turn, were affected by the stiffness of the column and the material's properties. It can be seen that the friction force decreases (up to certain level) with increasing the L/D ratio due to the concrete core cracks and yielding of the steel tube which led to some of the contact loss between the concrete core and the steel tube.

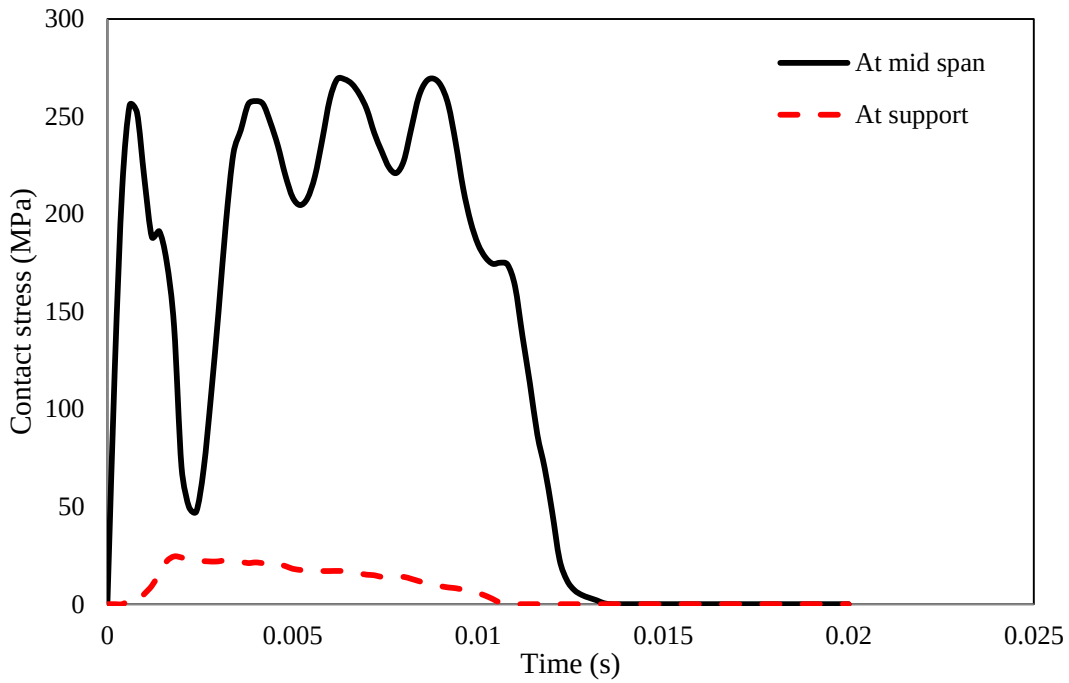

(a) The contact stresses for the CFST column with L/D ratio of 13.5

Figure 5.75. The contact stresses history for CFST column with different L/D ratio

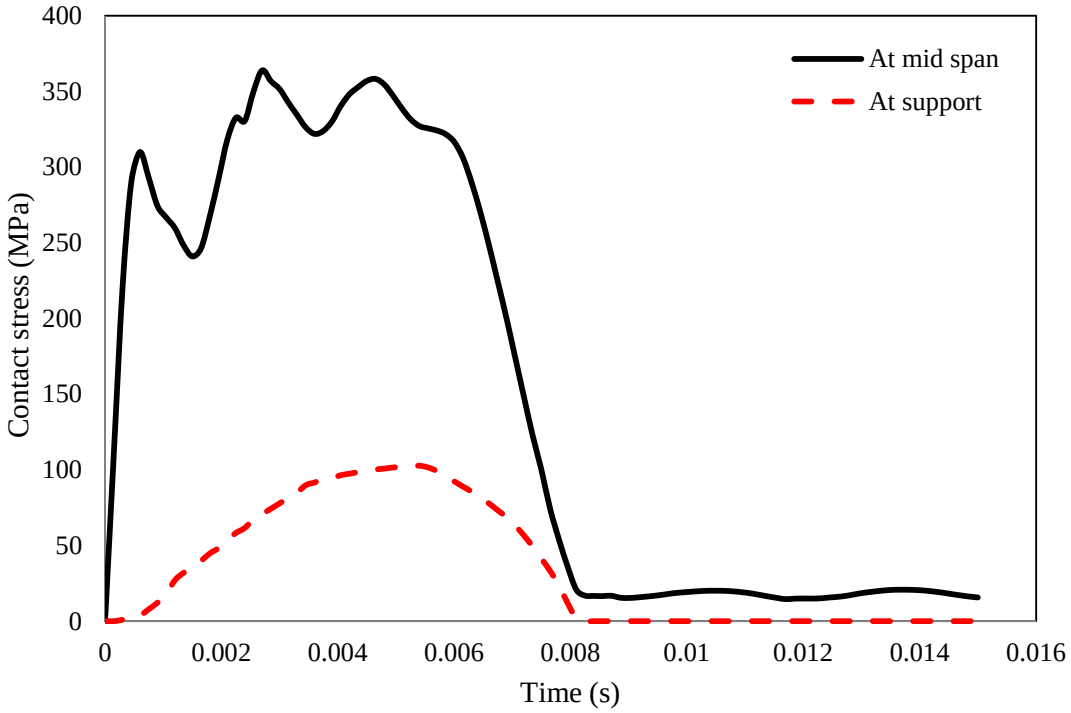

(b) The contact stresses for the CFST column with L/D ratio of 9

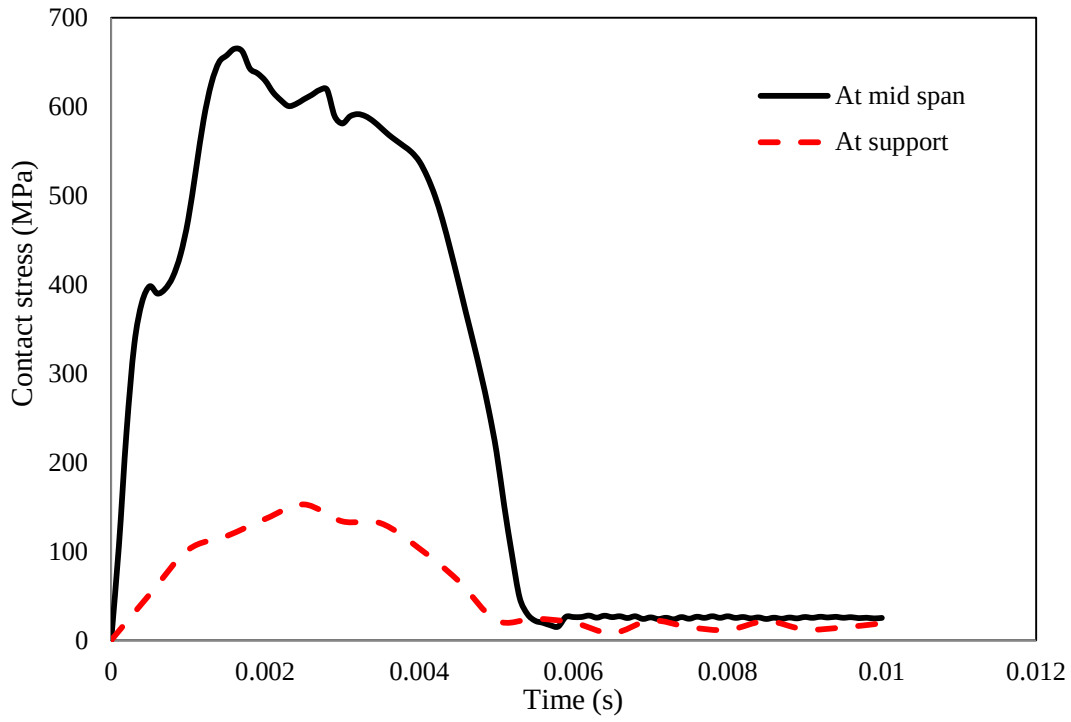

(c) The contact stresses history for CFST column with L/D ratio of 6

Figure 5.75 (continued). The contact stresses history for CFST column with different L/D ratio

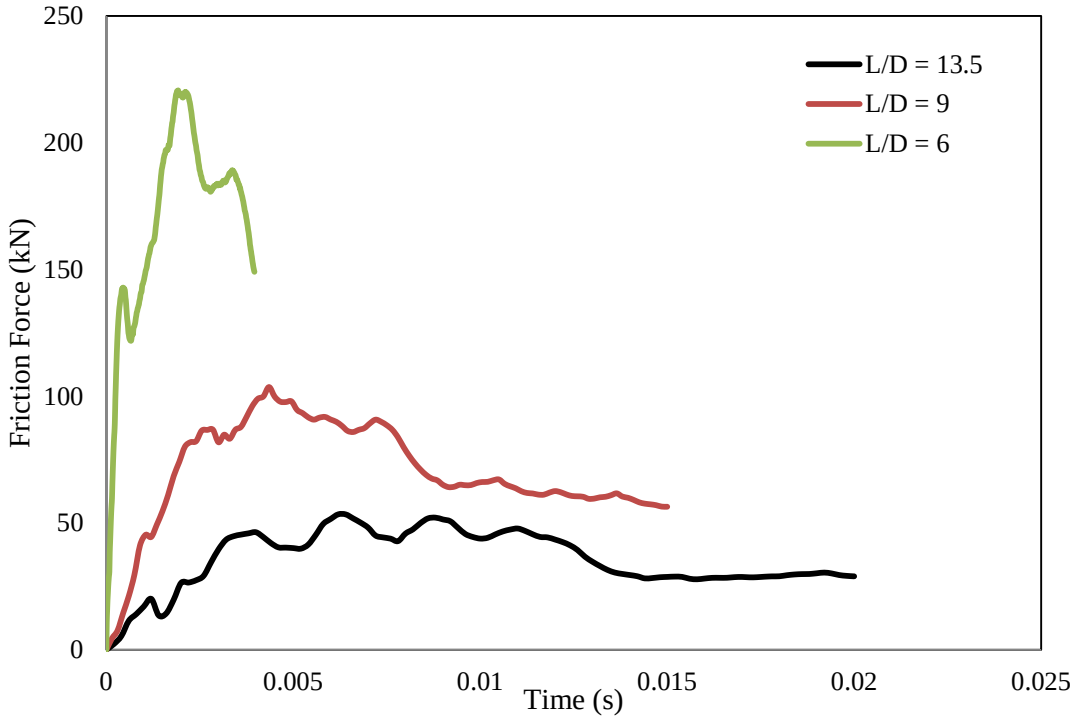

Figure 5.76. The friction force for the CFST column with different L/D ratio

5.4.5 The impact behaviour of the NACFST and RACFST columns strengthened with CFRP

The comparisons between the numerical and experimental force-total displacement traces for the strengthened NACFST and RACFST with a L/D ratio of 6 are shown in Figs 5.77 and 5.78, respectively, with a very good agreement. Clearly, the model captured the main features of the force-total displacement trace. The maximum force and the total displacement predicted for the NACFST column are 302.9 kN and 13.9 mm, respectively, while the corresponding experimental ones are 274 kN and 13.6 mm, respectively. The global displacement was also captured by the numerical model and the results show that the predicted displacement is higher than the experimental one by 4.6 % and 7.9 % for the NACFST and RACFST columns, respectively.

Figs, 5.79 and 5.80 show the force-total displacement traces for the strengthened NACFST and RACFST column with the L/D ratio of 9. The numerical and experimental results are overall in a good agreement, except for the second peak force. The force reduction occurs again here, which is the same as the case explained earlier in Section 5.4.2. There is a small

difference between the experimental and the simulated global displacements, which is 2.3 % for the NACFST column and 0.7 % for the RACFST column.

The validation of the numerical models for the NACFST and RACFST columns with the L/D ratio of 13.5 is shown in Figs. 5.81 and 5.82. The results show very good correlation between the numerical predictions and experimental results in terms of the maximum force, global and total displacements. It can be seen that the numerical models provides good predictions of the initial, plateau and failure or unloading stages. The model gives a slightly lower estimate of the initial stiffness of the columns but, does not affect the overall good correlation. There are only 2.4 % and 6.8 % differences between the predicted and experimental maximum force for the RACFST and NACFST columns, respectively. In addition, the global and total displacements of the numerical results were in a reasonable good agreement with the experimental ones as well.

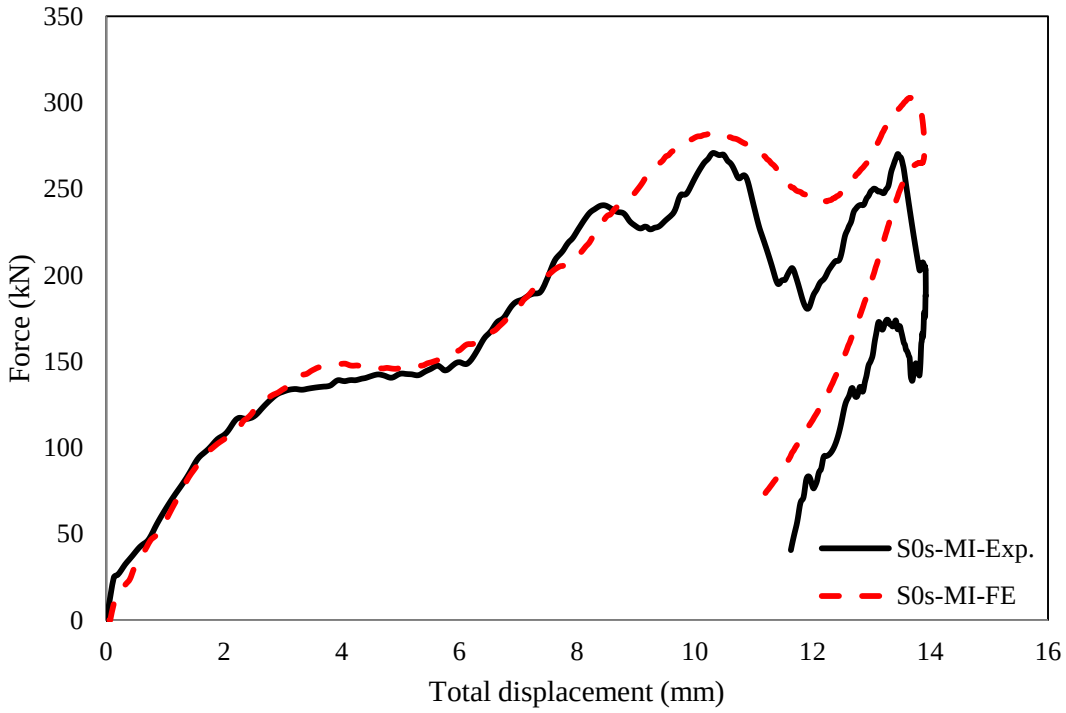

Figure 5.77. The FE and experimental force-total displacement traces for the NACFST column strengthened by CFRP with L/D of 6

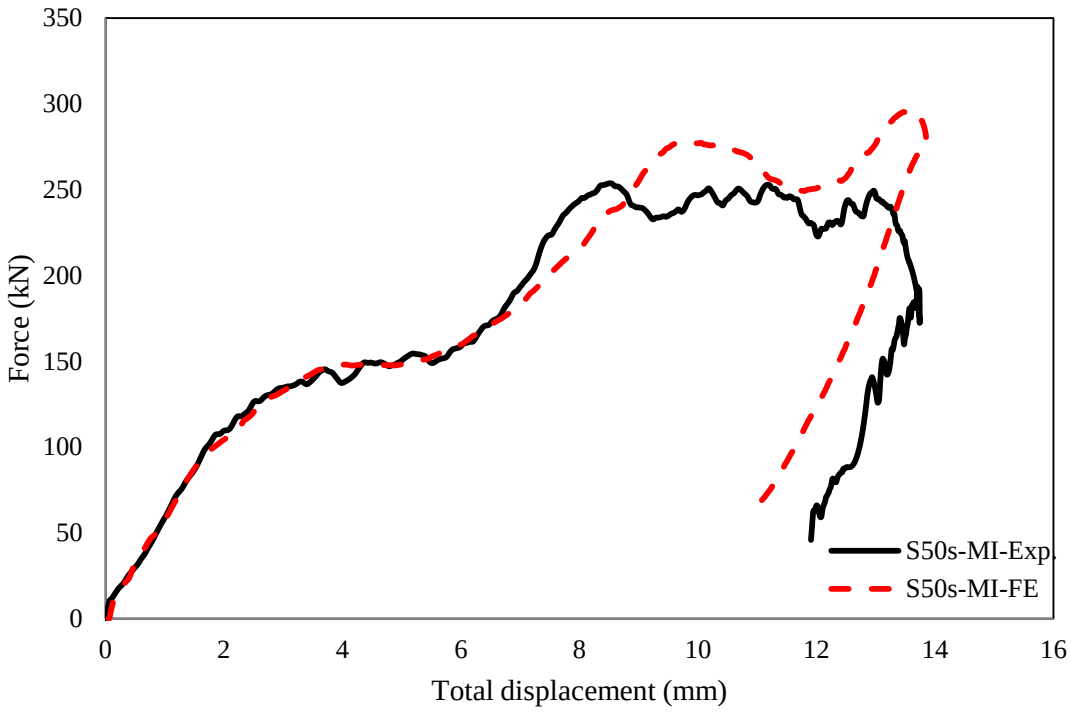

Figure 5.78. The FE and experimental force-total displacement traces for the RACFST column strengthened by CFRP with L/D of 6

Figure 5.79. The FE and experimental force-total displacement traces for the NACFST column strengthened by CFRP with L/D of 9

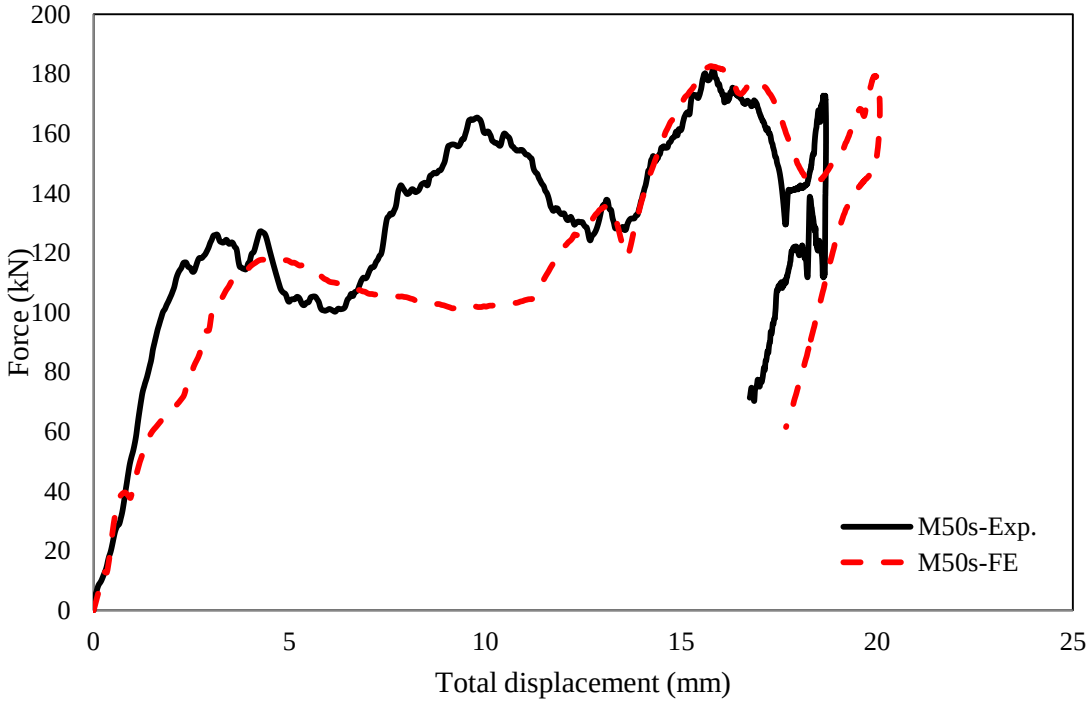

Figure 5.80. The FE and experimental force-total displacement traces for the RACFST column strengthened by CFRP with L/D of 9

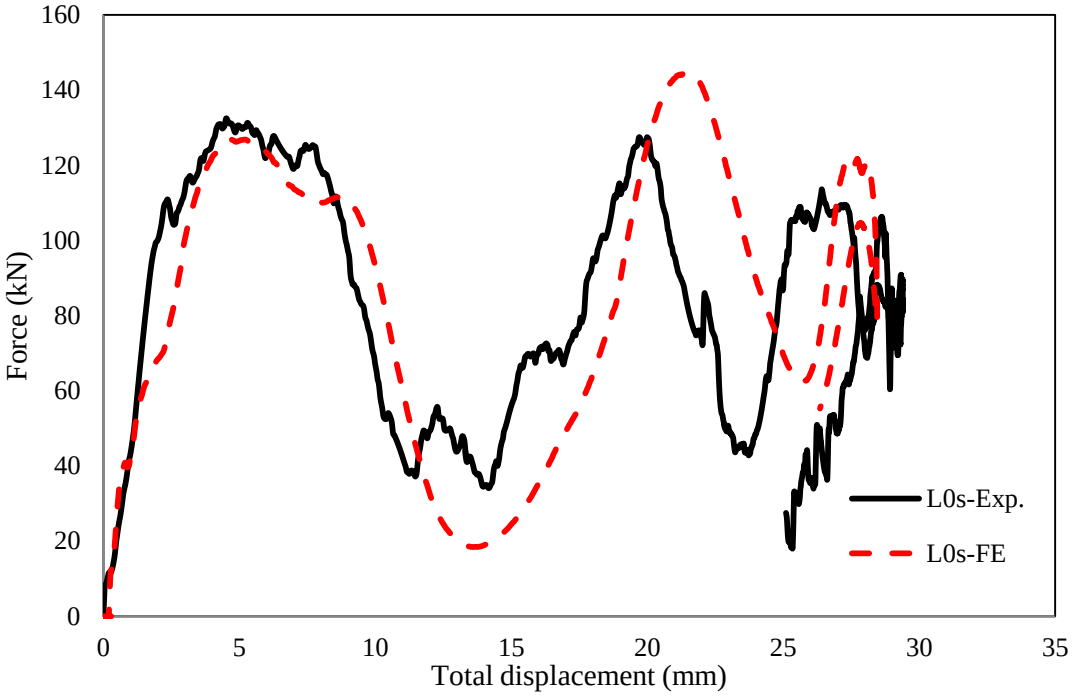

Figure 5.81. The FE and experimental force-total displacement traces for the NACFST column strengthened by CFRP with L/D of 13.5

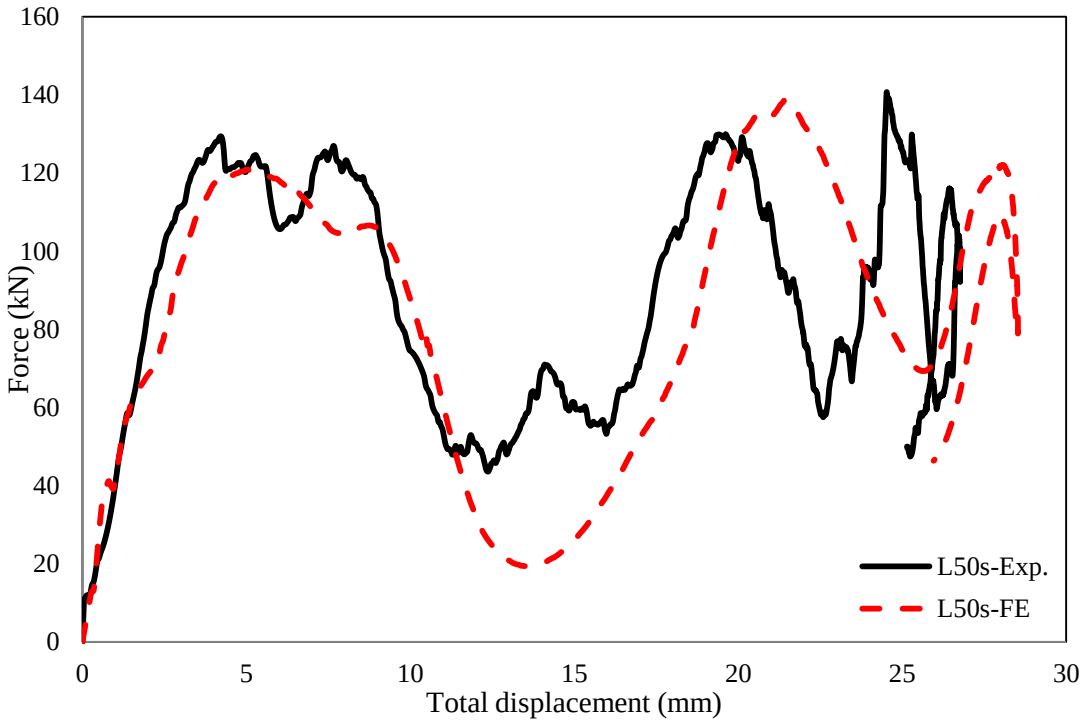

Figure 5.82. The FE and experimental force-total displacement traces for the RACFST column strengthened by CFRP with L/D of 13.5

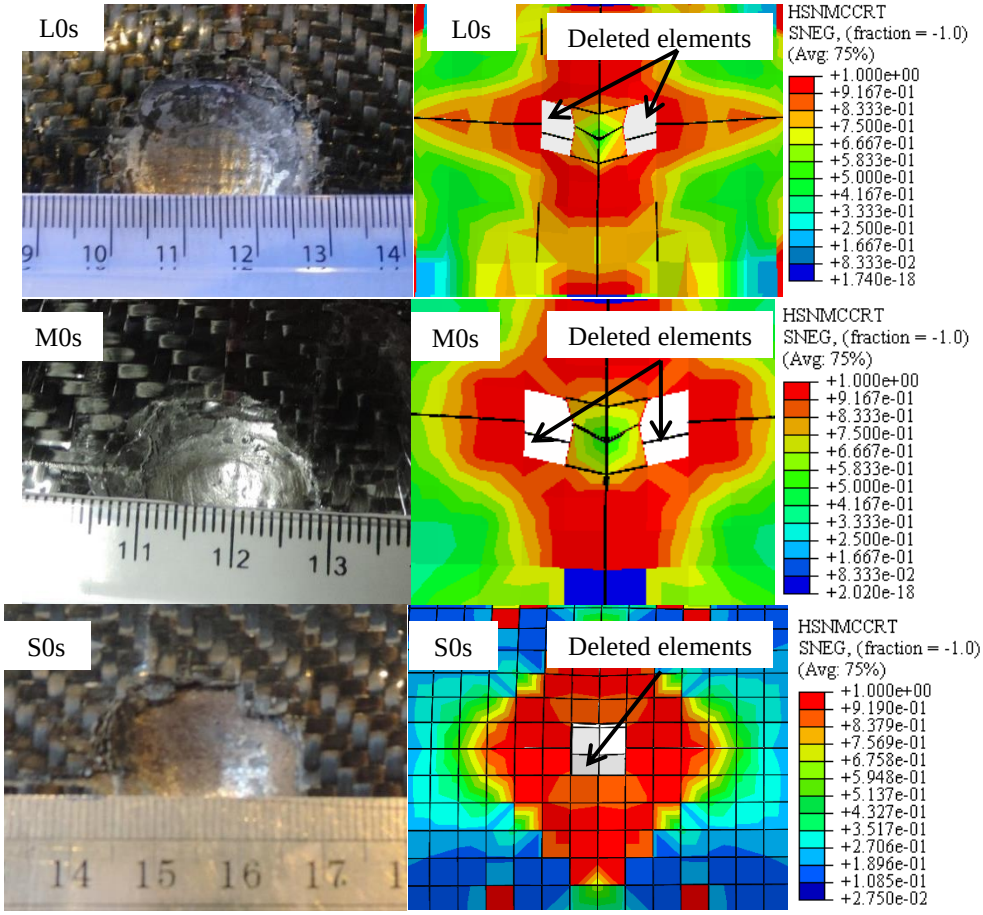

Figure 5.83. The experimental and predicted (HSNMCCRT) modes of failure of the NACFST columns strengthened with FRP with different L/D ratios

(HSNMCCRT) Hashin's matrix compression damage initiation criterion

Fig. 5.83 shows the comparison between the predicted and experimental deformation mode for the CFST columns with different L/D ratios. The predicted failed areas where the failure status index reaches a unit are similar to the experimental ones, although not all the damaged elements were deleted. The force-displacement presented previously and deformation pattern shown here reveal that the numerical models are capable of capturing the load-displacement trace and deformation mode for the strengthened NACFST and RACFST columns with a variety of L/D ratios.

5.4.6 Prediction the total and absorbed energies

The area beneath the total displacement-force trace was calculated to obtain the total and absorbed energies. The results are tabulated in Table 5.3. Clearly, the numerical models generally give a good prediction of the total and absorbed energies with a high degree of accuracy, with the largest error being approximately 13 %. Although the FE model slightly overestimated the impact force for the NACFST hit by the small impactor with the L/D ratio of 6, the difference between the numerical and experimental total and absorbed energies was only 7.6 % and 5.3 %, respectively, whilst for the RACFST columns was 8.3 % and 4.2 %. The comparison between the experimental and numerical total energy for the NACFST columns with the L/D ratio of 9 shows very good correlation and the numerical energy is higher than the experimental one by only 1.1 %, while the experimental absorbed energy is slightly lower than the predicted one by only 1.9 %. Figs 5.84 (a), 5.84 (b) and 5.84 (c) show the absorbed energy by the components of the CFST column, i.e. the concrete core and the steel tube. It can be seen that the energies absorbed by the concrete core and the steel tube account for 36%, 23.5% and 22% and 64.4%, 76.5% and 78% for the CFST columns with L/D ratios of 6, 9 and 13.5, respectively. In general, the steel tube absorbed much higher energy than the concrete core due to high tensile strength and high ductility.

Table 5.3. The numerical and experimental total and absorbed energies the CFST columns subjected to lateral impact loading

Specimen ID	Total energy (J) (Exp.)	Total energy (J) (FE)	(%)*	Absorbed energy (J) (Exp.)	Absorbed energy (J) (FE)	(%)*
SH	2442.0	2607.1	6.8	2268.0	2413.9	6.4
S0-BI	2478.0	2652.5	7.0	2152.0	2164.9	0.6
S50-BI	2481.0	2651.2	6.9	2217.0	2173.1	2.0
S0-MI	2687.0	2681.4	0.2	2340.0	2178.4	6.9
S50-MI	2659.0	2678.8	0.7	2314.0	2185.9	5.5
S0s-MI	2522.0	2591.2	2.7	2247.0	2074.2	7.7
S50s-MI	2486.0	2590.3	4.2	2199.0	2062.8	6.2
S0-SI	2546.0	2738.4	7.6	2308.0	2186.4	5.3
S50-SI	2527.0	2736.6	8.3	2277.0	2180.7	4.2
S0-FI	2455.0	2608.8	6.3	2191.0	2182.9	0.4
S50-FI	2509.0	2608.0	3.9	2214.0	2187.8	1.2
MH	2460.0	2612.9	6.2	2336.0	2407.1	3.0
M0	2616.0	2645.8	1.1	2182.0	2223.5	1.9
M50	2653.0	2646.3	0.3	2229.0	2224.3	0.2
M0s	2470.0	2416.3	2.2	2060.0	2054.0	0.3
M50s	2445.0	2393.3	2.1	2013.0	2037.7	1.2
LH	2351.0	2654.4	12.9	2253.0	2418.7	7.4
L0	2643.0	2673.0	1.1	2257.0	2256.0	0.0
L50	2729.0	2674.0	2.0	2449.0	2281.0	6.9
L0s	2464.0	2546.0	3.3	2095.0	2153.0	2.8
L50s	2449.0	2367.7	3.3	2084.0	1990.9	4.5

* [(Exp.-FE)/Exp.]*100

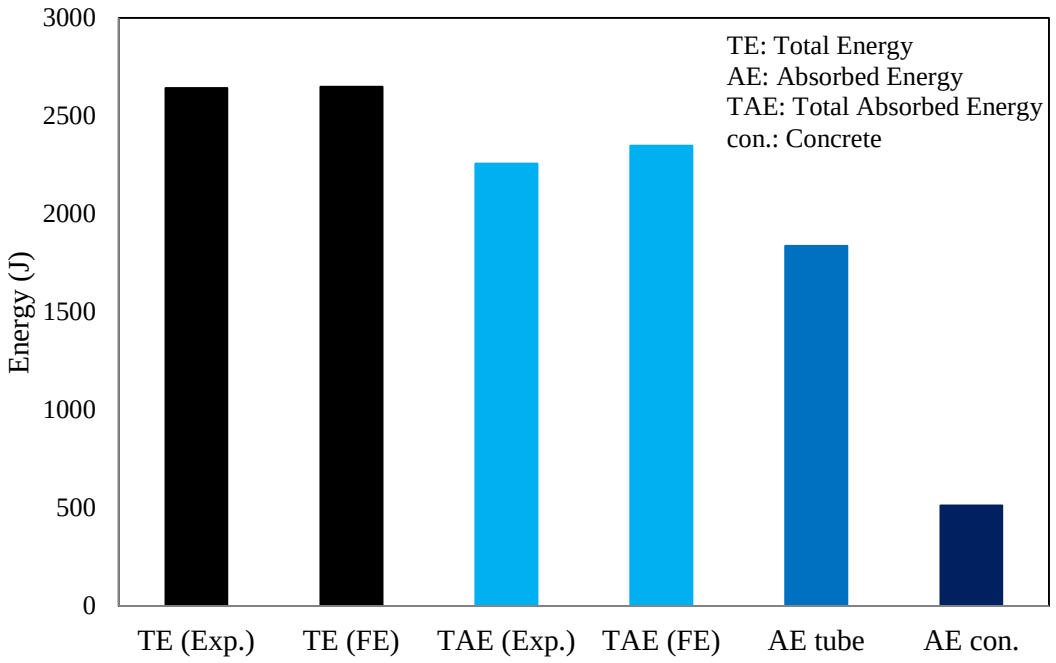

(a) L/D ratio of 13.5

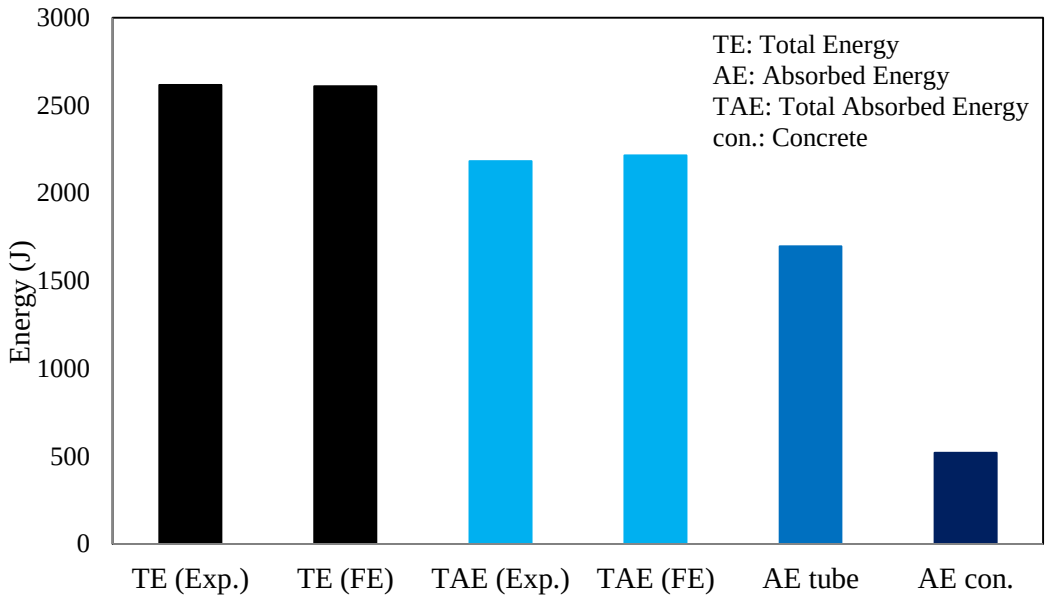

(b) L/D ratio of 9

Figure 5.84. The absorbed energy of the CFST columns components with different L/D ratios

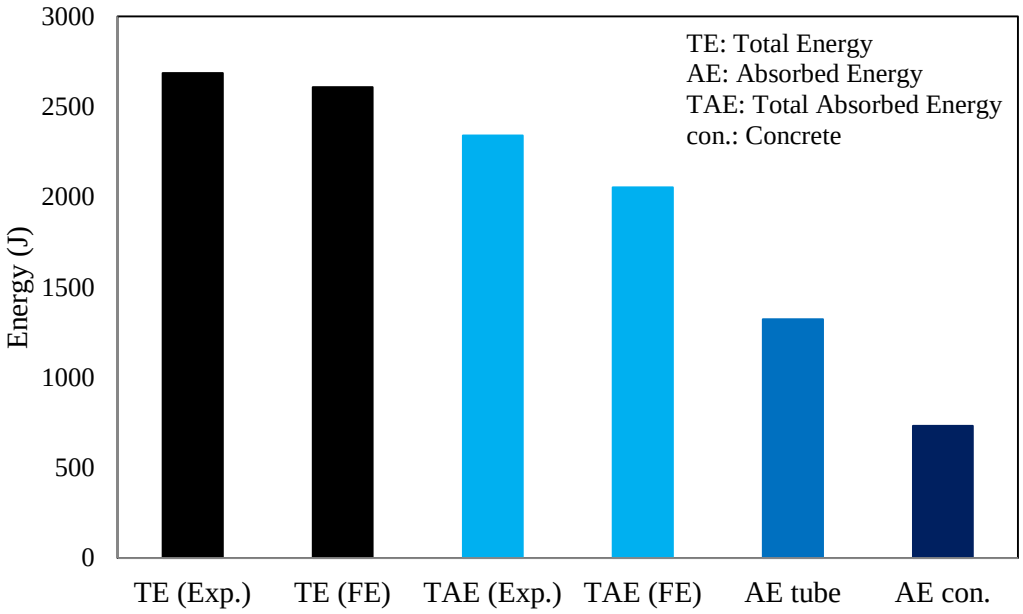

(c) L/D ratio of 6

Figure 5.84 (continued). The absorbed energy of the CFST columns components with different L/D ratios

5.5 Modelling the CFST column under compression loading

The CFST columns under compression loading were modelled with three different variables, i.e. the type of concrete (normal and recycled aggregate), the loading conditions (eccentric and concentric) and the wall thickness of the tube. The comparison between the numerical and experimental results includes the load-displacement relationship and the mode of failure.

Fig. 5.85 shows the predicted and experimental load-displacement traces for the NACFST column with a wall thickness of 3.6 mm subjected to concentric compression loading. The figure indicates that the numerical model captures the basic features of the force-displacement trace, which are the elastic, the yielding and post yielding stages. There is only 5 % difference between the numerical and experimental maximum compression loads. Fig. 5.86 shows that the force-displacement trace for the RACFST columns is well predicted using the same numerical model. However, the model underestimates the softening or the stiffness degradation for the final part of the trace due to the confinement effect which seems to be higher in the numerical model. Despite that, the predicted maximum force of 1150 kN correlates well to the experimental one of 1148 kN.

Figs. 5.87 and 5.88 show the good correlation between the predicted and measured load-displacement trace for the NACFST and RACFST columns with a wall thickness of 3 mm, respectively. The numerical trace exhibits slightly higher stiffness throughout the elastic stage, with the softening behaviour of the curve being underestimated. In spite of all these discrepancies, the agreement between the simulation and the test results is generally good. The maximum force predicted for the NACFST and RACFST columns are 1086 kN and 1054 kN, respectively, while the corresponding experimental ones are 1089 kN and 1074 kN.

The comparisons between the numerical simulation and experimental data for the NACFST and RACFST columns under eccentric compression loading are shown in Figs. 5.89 and 5.90, respectively. The comparison of the results manifest that the force-displacement trace is very well predicted, although there are slightly over-estimated initial stiffnesses of the NACFST and RACFST columns.

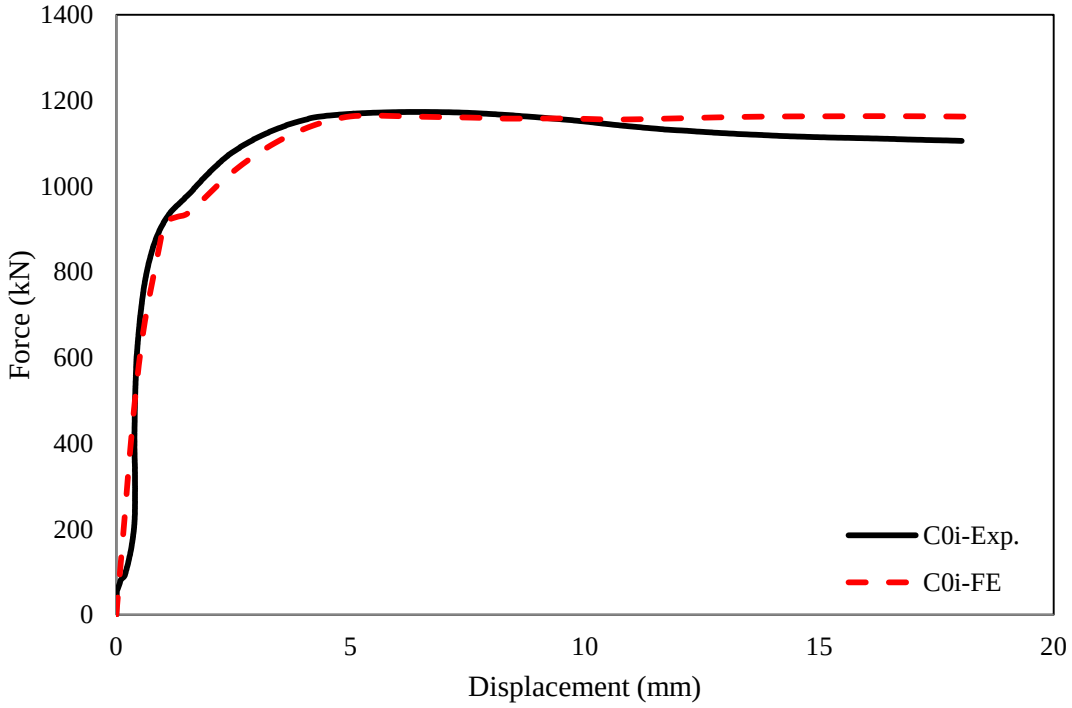

Figure 5.85. The force-displacement curve for the NACFST column under concentric compression loading with wall thickness of 3.6 mm

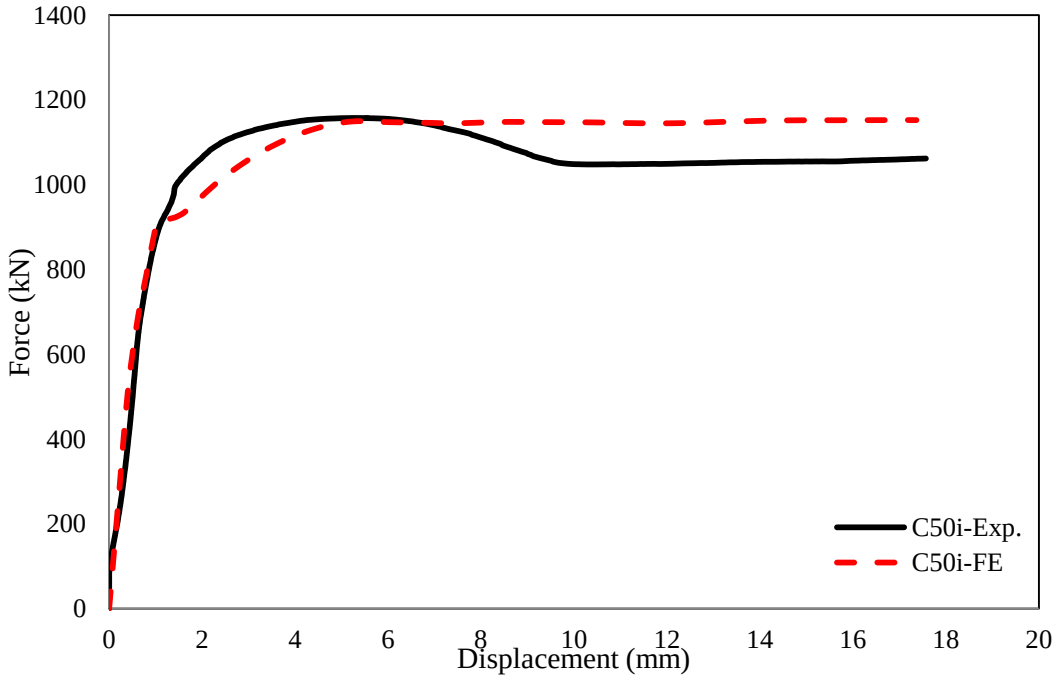

Figure 5.86. The force-displacement curve for the RACFST column under concentric compression loading with wall thickness of 3.6 mm

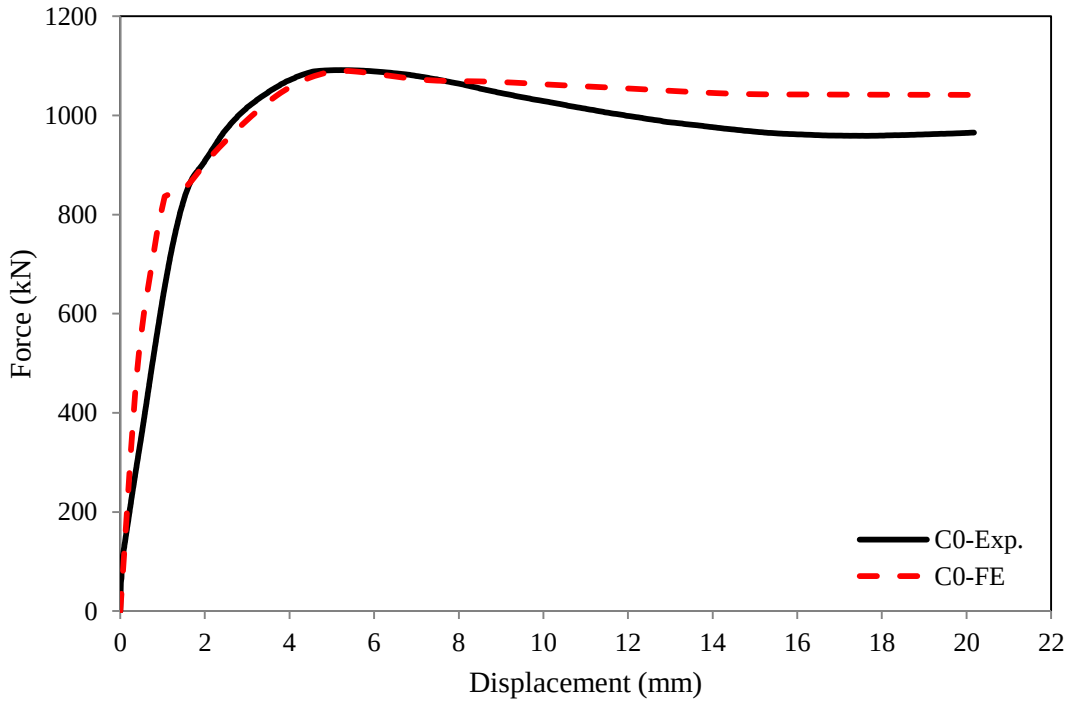

Figure 5.87. The force-displacement curve for the NACFST column under concentric compression loading with wall thickness of 3 mm

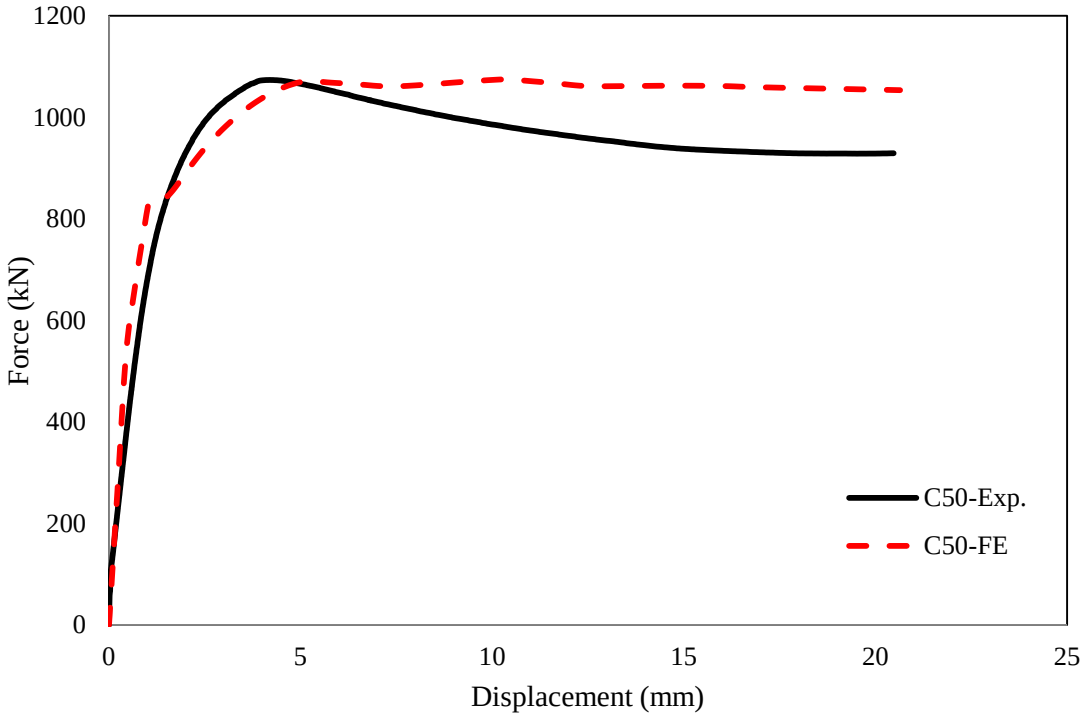

Figure 5.88. The force-displacement curve for the RACFST column under concentric compression loading with wall thickness of 3 mm

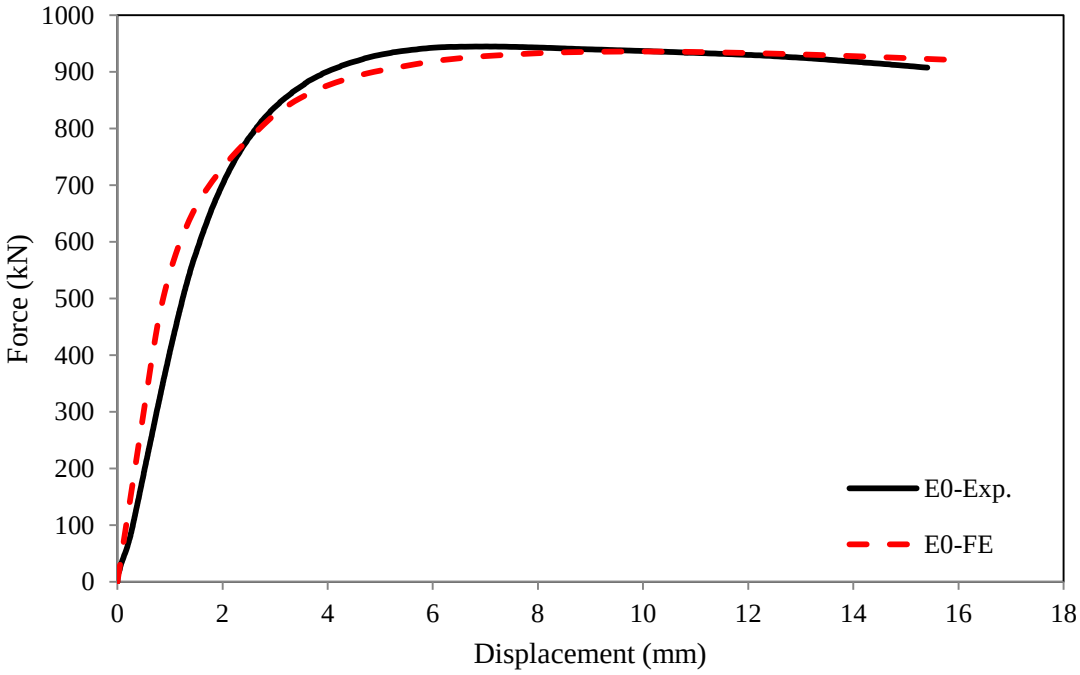

Figure 5.89. The force-displacement curve for the NACFST column under eccentric compression loading with wall thickness of 3 mm

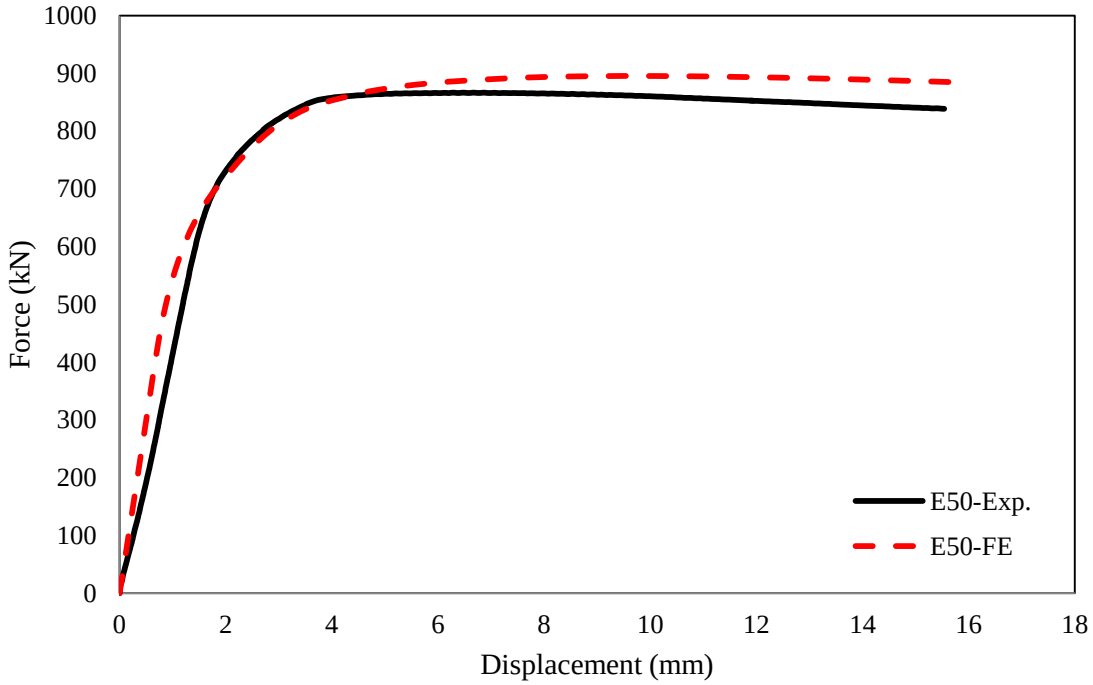

Figure 5.90. The force-displacement curve for the RACFST column under eccentric compression loading with wall thickness of 3 mm

The results show that the numerical models are capable of predicting the effect of the loading eccentricity, which reduces the load carrying capacity of the columns. In addition, the numerical results show that RACFST columns have slightly lower load carrying capacities than their counterpart tubes filled with normal aggregate.

Fig. 5.91 shows the comparison between the numerical and experimental modes of failure for NACFST column subjected to eccentric loading. It is clear that the correlation between those modes is very good. The numerical models predicted the global buckling as well as the local outward buckling which are the main characteristics of the failure mode of the column.

Two different failure patterns were shown during the experimental tests for the NACFST and RACSFTS columns under concentric compression load. The numerical mode captured these two modes very well, as shown in Figs. 5.92(a) and 5.92(b). The first model includes two outward crumples, the first one near the top and the second one close to the mid height of the column, while the other only includes one outward buckle near the mid height of the

tube. Both of these modes were very well predicted by the numerical models. This indicates that the numerical models developed are able to capture the features of both the force-displacement trace and failure mode.

Finally, the failure pattern for the columns with a wall thickness of 3.6 mm is similar to that of the CFST column wall thickness of 3 mm. In addition to the crumples at the top and at the mid height of the columns, the numerical model predicts one additional outward buckle at the bottom of the column which is similar to the top one, as can be seen from Fig. 5.93. However, this mode of failure is also expected, which was shown in the previous research (Giakoumelis and Lam, 2004, Yu et al., 2007).

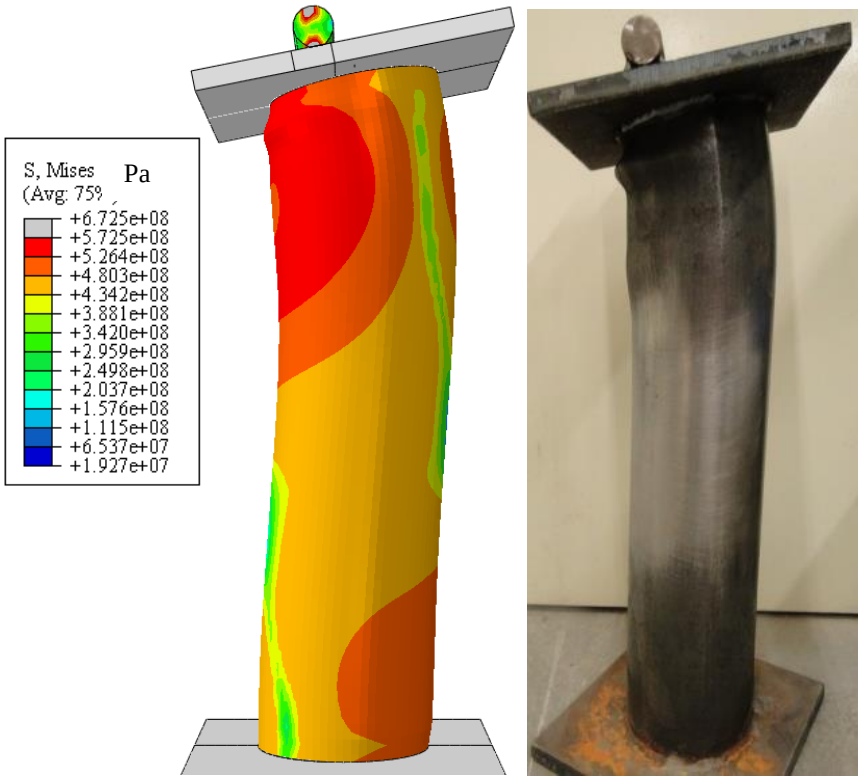

Figure 5.91. The comparison between the numerical and experimental failure mode of the CFST columns subjected to eccentric loading with tube wall thickness of 3 mm

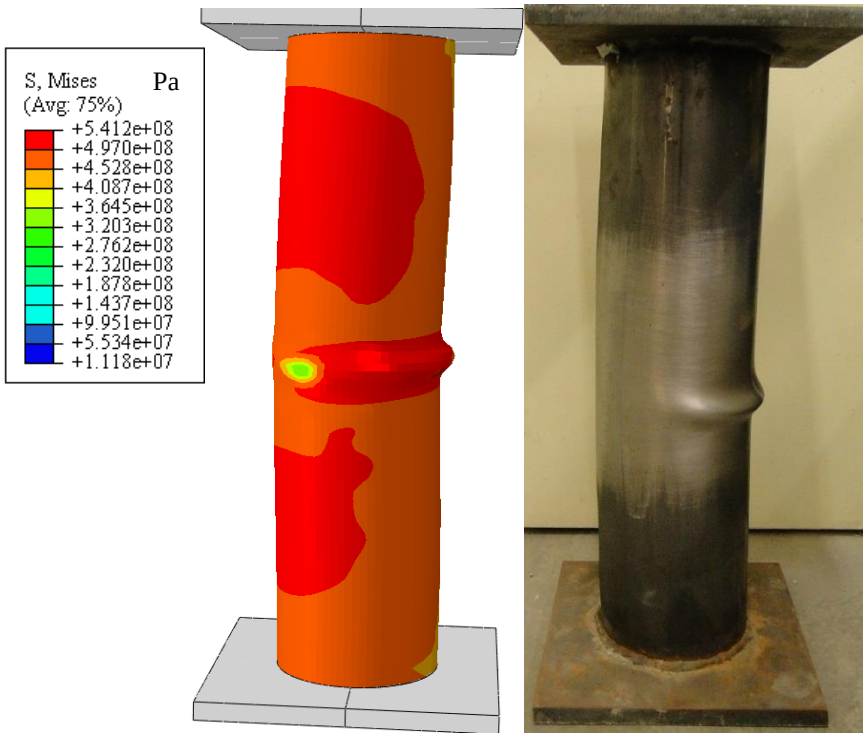

a) One outward buckle at the mid height of the column

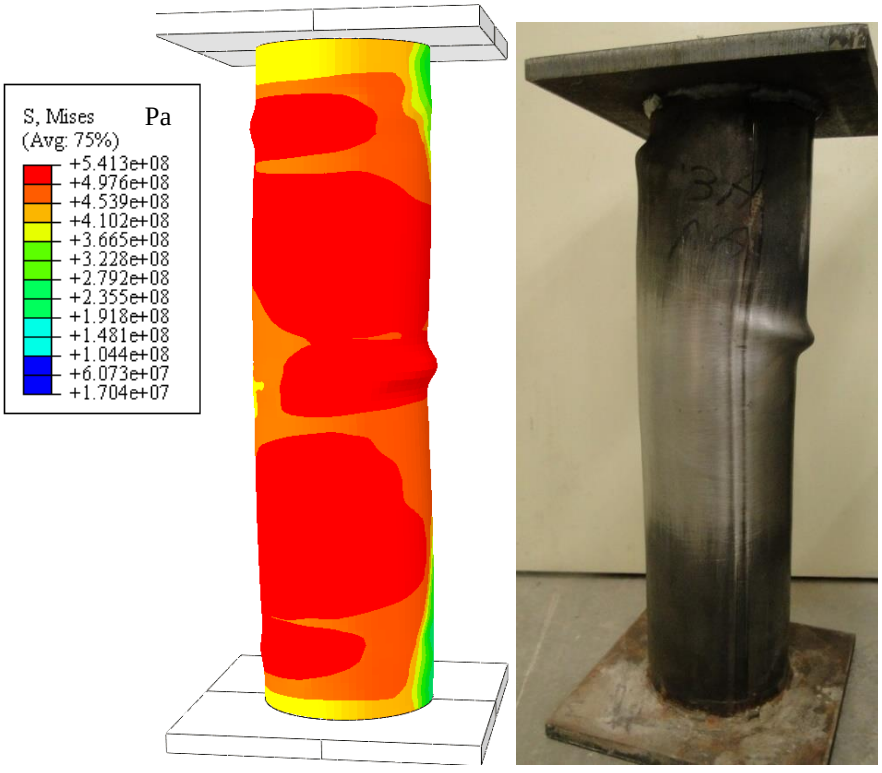

b) Most of the columns failed with two crumples

Figure 5.92. The comparison between the numerical and experimental failure modes of the CFST columns subjected to concentric loading with tube wall thickness of 3 mm

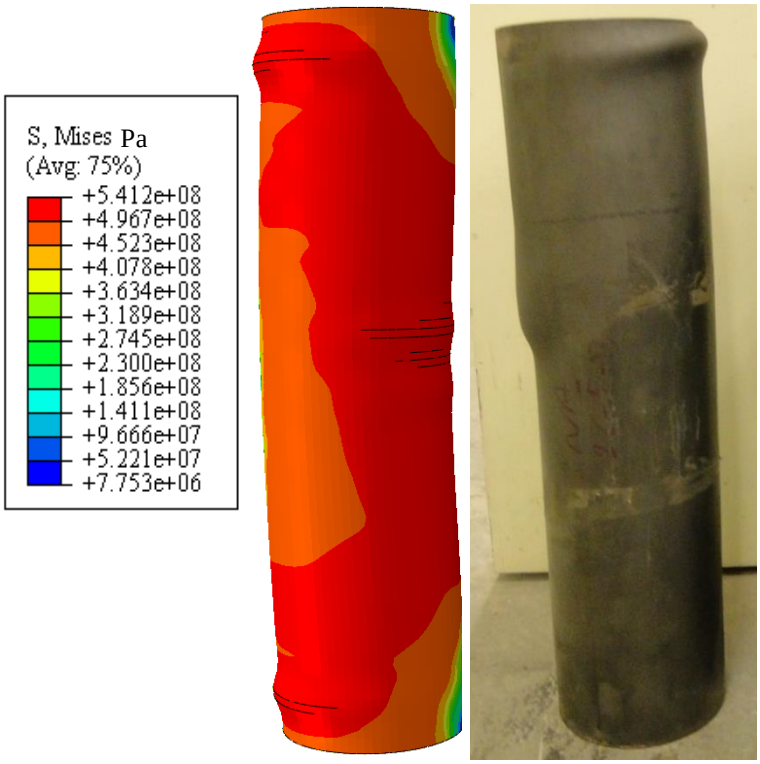

Figure 5.93. The comparison between the numerical and experimental failure mode of the CFST columns subjected to concentric loading with tube wall thickness of 3.6 mm

Figs. 5.94 and 5.95 show the numerical and experimental load-displacement curves for the CFRP strengthened NACFST and RACFST columns, respectively, with a wall thickness of 3 mm subjected to concentric compression loading. Very good agreement between the numerical and experimental results can be seen from Fig. 5.94. There is only 1.2% difference between the numerical and experimental maximum compression loads. Fig. 5.95 shows that the force-displacement trace for the RACFST columns strengthened with CFRP is well predicted using the same numerical model. However, the model underestimates the softening or the stiffness degradation for the final part of the curve due to the confinement effect which seems to be lower in the numerical model after the CFRP layer rupture. Despite that, the predicted maximum force of 1108.7 kN correlates well with the experimental one of 1130.5 kN.

Fig. 5.96 shows that the numerical and experimental load-displacement curve for the NACFST column strengthened with CFRP under eccentric loading. It can be seen that the curve is very well predicted by the numerical model. The predicted and experimental maximum compression loads were 934.5 and 939 KN, respectively.

The comparisons between the numerical simulation and experimental data for the CFRP strengthened RACFST under eccentric compression loading are shown in Figs. 5.97. The comparison of the results indicates that the force-displacement trace is very well captured, although there is slightly over-estimated initial stiffness of the NACFST and RACFST columns.

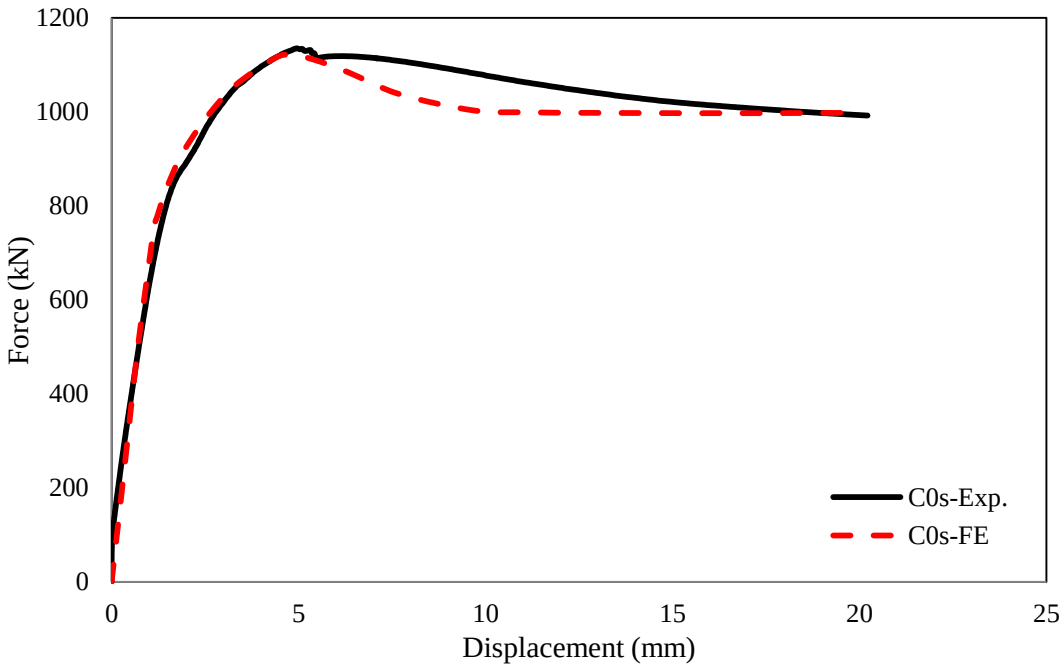

Figure 5.94. The force-displacement curve for the CFRP strengthened NACFST column under concentric compression loading

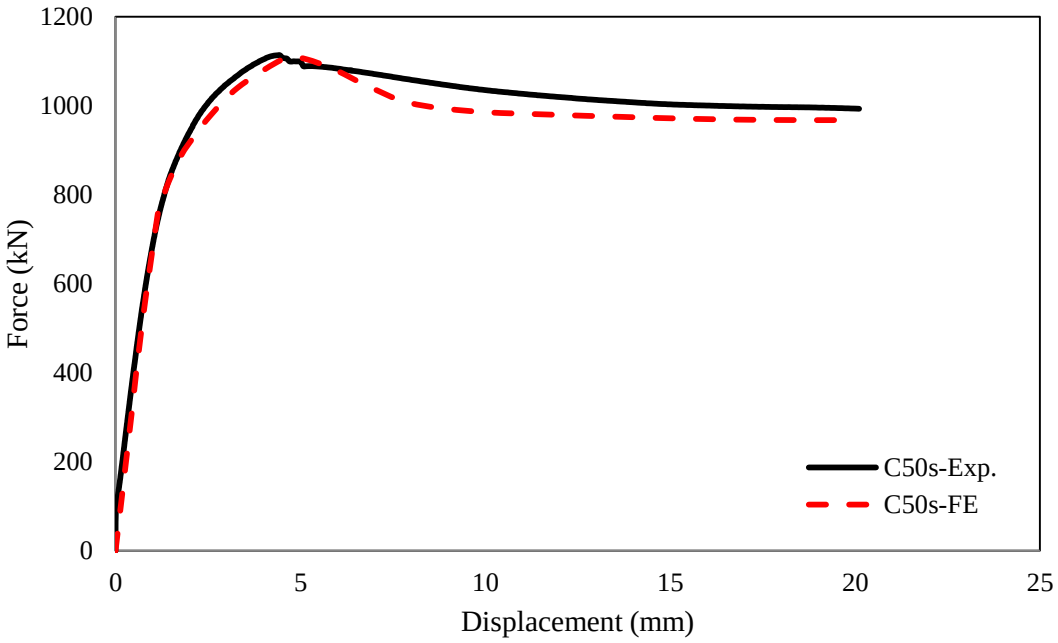

Figure 5.95. The force-displacement curve for the CFRP strengthened RACFST column under concentric compression loading

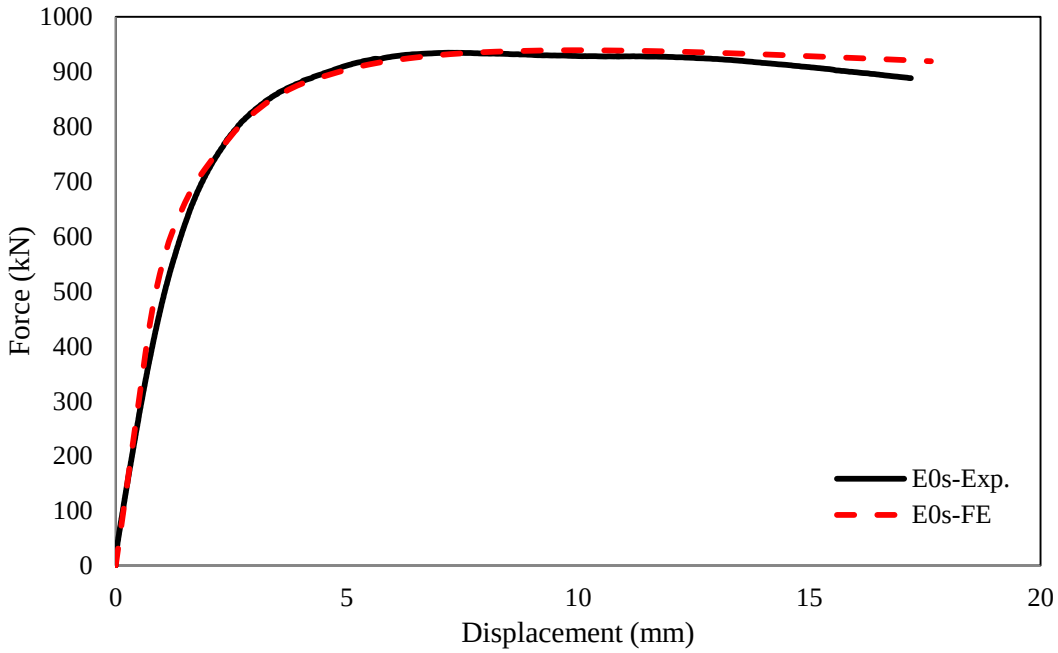

Figure 5.96. The force-displacement curve for the CFRP strengthened NACFST column under eccentric compression loading

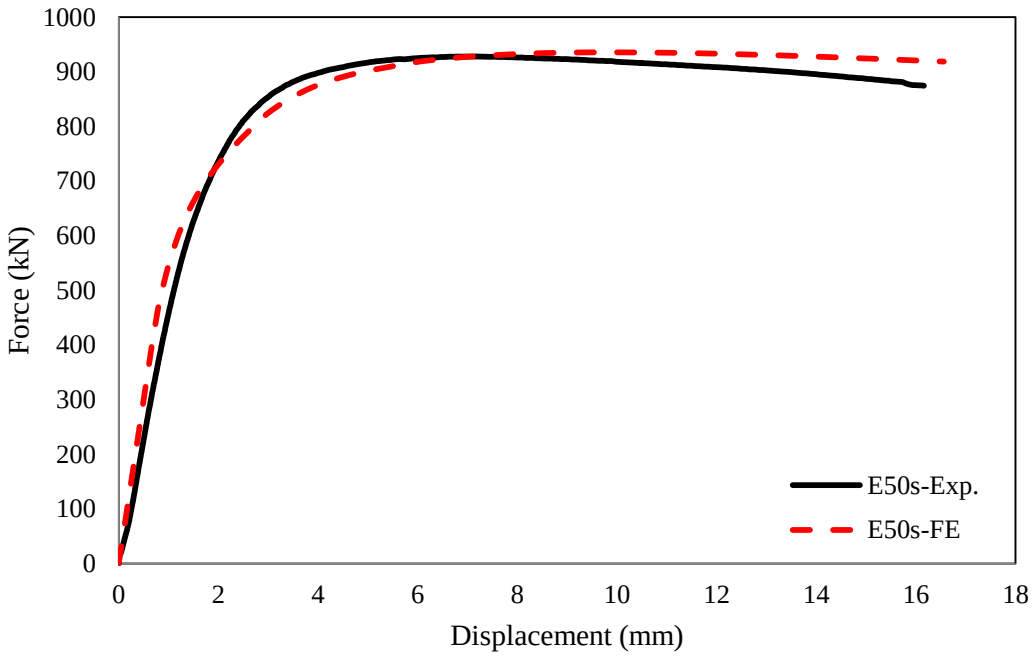

Figure 5.97. The force-displacement curve for the CFRP strengthened RACFST column under eccentric compression loading

5.6 Paramedic study based on the FE models

The validated numerical models presented in Section 5.4 were used to carry out parametric studies in order to investigate the influence of other parameters on the impact behaviour of the CFST columns under lateral impact loading, which were not covered. The parametric studies are divided into two parts. The first part presents the results of parametric studies which were conducted to investigate the effects of the material properties (f_y, f_c'), the impact energy (IE), the tube geometry (D/t ratio), the boundary conditions (BC), and impact location (IL) on the response of the CFST columns. Then, the results of the studies are presented to examine the influence of the parameters IE, D/t ratio and the length of the CFRP bond on the behaviour of the strengthened CFRP columns.

It is mentioned earlier in Chapter 3 that the L/D ratios of 6, 9 and 13.5 covered the most popular range of L/D ratios in the real construction and experimental research and they are within the limitations of the design codes. Comparing the results of the parametric studies with experimental and validated numerical results will lead to more reliable and robust results. Thus, the L/D ratios of 6, 9 and 13.5 were kept constant to investigate the effects of

various parameters on the impact response of the CFST columns. The influences of the D/t ratio and the IL were studied with three different L/D ratios (6, 9, and 13.5), while the effect of the BC was examined with two L/D ratios (9, 13.5). The impact energy and the material property effects were investigated with L/D ratio of 13.5 only. For the strengthened CFST columns, the effects of the bond length of the CFRP were investigated with three L/D ratios (6, 9, and 13.5). The columns with a L/D ratio of 13.5 were used to study the effect of the D/t ratio, while the column with L/D ratio of 9 was used to examine the influence of the impact energy on the behaviour of the CFRP strengthened CFST columns. Table 5.4 and Table 5.5 show the details of the parametric study variables for the unstrengthened and strengthened CFST columns, respectively.

Table 5.4. Summary of the parametric variation for the unstrengthened CFST column

No.	L/D	BC	IL (mm) distance from the support	D/t	f_y (Mpa)	$f_{c'}$(Mpa)	IE (kJ)
1	6	Fix-Fix	32	32	450	C50	2.61
2	9	Fix-Fix	32	32	450	C50	2.61
3	13.5	Fix-Fix	32	32	450	C50	2.61
4	6	Fix-Fix	215	32	450	C50	2.61
5	9	Fix-Fix	215	32	450	C50	2.61
6	13.5	Fix-Fix	215	32	450	C50	2.61
7	6	Fix-Fix	260	23	450	C50	2.61
8	9	Fix-Fix	430	23	450	C50	2.61
9	13.5	Fix-Fix	680	23	450	C50	2.61
10	6	Fix-Fix	260	38	450	C50	2.61
11	9	Fix-Fix	430	38	450	C50	2.61
12	13.5	Fix-Fix	680	38	450	C50	2.61
13	6	Fix-Fix	260	67	450	C50	2.61
14	9	Fix-Fix	430	67	450	C50	2.61
15	13.5	Fix-Fix	680	67	450	C50	2.61
16	9	Fix-Fix	430	32	450	C50	2.61
17	13.5	Fix-Fix	680	32	450	C50	2.61
18	9	Fix-Pin	430	32	450	C50	2.61
19	13.5	Fix-Pin	680	32	450	C50	2.61
20	9	Pin-Pin	430	32	450	C50	2.61
21	13.5	Pin-Pin	680	32	450	C50	2.61
22	13.5	Fix-Fix	680	32	450	C30	2.61
23	13.5	Fix-Fix	680	32	450	C60	2.61
24	13.5	Fix-Fix	680	32	450	C70	2.61
25	13.5	Fix-Fix	680	32	450	C80	2.61
26	13.5	Fix-Fix	680	32	250	C50	2.61
27	13.5	Fix-Fix	680	32	350	C50	2.61
28	13.5	Fix-Fix	680	32	550	C50	2.61
29	13.5	Fix-Fix	680	32	650	C50	2.61
30	13.5	Fix-Fix	680	32	750	C50	2.61
31	13.5	Fix-Fix	680	32	450	C50	0.85
32	13.5	Fix-Fix	680	32	450	C50	2.61
32	13.5	Fix-Fix	680	32	450	C50	3.43
33	13.5	Fix-Fix	680	32	450	C50	3.85

Table 5.5. Summary of the parametric variation for the strengthened CFST column

No.	L/D	BC	Length of the CFRP bond (mm)	D/t	KE (kJ)
1	6	Fix-Fix	347	32	2.61
2	9	Fix-Fix	574	32	2.61
3	13.5	Fix-Fix	907	32	2.61
4	6	Fix-Fix	520	32	2.61
5	9	Fix-Fix	860	32	2.61
6	13.5	Fix-Fix	1360	32	2.61
7	13.5	Fix-Fix	454	23	2.61
8	13.5	Fix-Fix	454	38	2.61
9	9	Fix-Fix	287	32	0.48
10	9	Fix-Fix	287	32	1.31
11	9	Fix-Fix	287	32	1.33
12	9	Fix-Fix	287	32	3.57
13	9	Fix-Fix	287	32	3.85

5.6.1 The parameters affecting the unstrengthened CFST columns

5.6.1.1 The influence of the impact location

To examine the effect of the impact location on the impact response of the CFST columns, two locations were adopted as a distance from the support to the centre of the impactor, i.e. 32 mm and 215 mm. Figure 5.98 shows the comparison between the force-total displacement traces for the CFST with a L/D ratio of 6. Clearly, the impact location has a limited influence on the impact response of the short tube, with the force being increased by only 4.9 % and the displacement being decreased by 6.4 % when the impactor hit the tube at a distance of 32 mm from the support. The short distance between the mid span and the support induces the column to exhibit the similar initial stiffness, regardless the location of the impact. However, the influence of the impact location on deformation pattern is different, i.e. when moving the location towards the support there is softening between the first and the second peak loads. On the contrary, the columns with L/D ratios of 9 and 13.5 showed that the impact location has a significant influence on the behaviour of the CFST columns. The initial stiffness and the follow-up hardening increase when the distance between the support and the impactor decreases. This is clearly noted from Figs. 5.99 and

5.100 for the CFST with L/D ratios of 9 and decreased from 18.2 mm to 13 mm when the distance between the support and the centre of the impactor decreased from 430 to 33 mm for the columns with a L/D ratio of 9. For the column with a L/D ratio of 13.5, the force increased by 61.2 % and the total displacement decreased by 45.2 % when the impactor hit the column at a distance of 32 mm from the support.

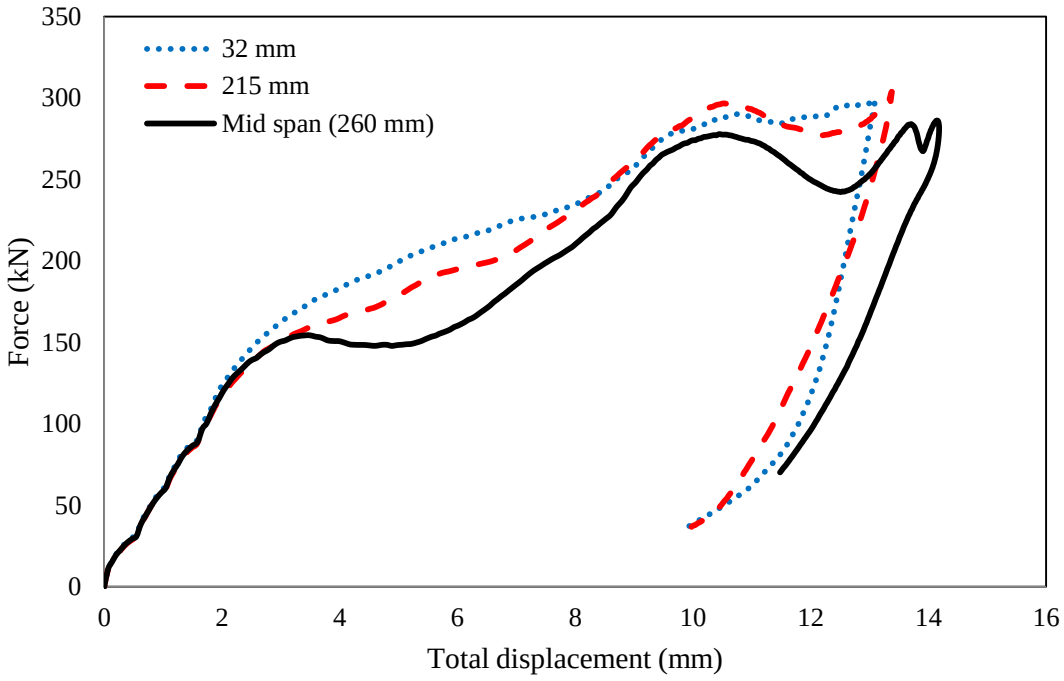

Figure 5.98. The effect of the impact location on the response of the CFST columns with L/D ratio of 6

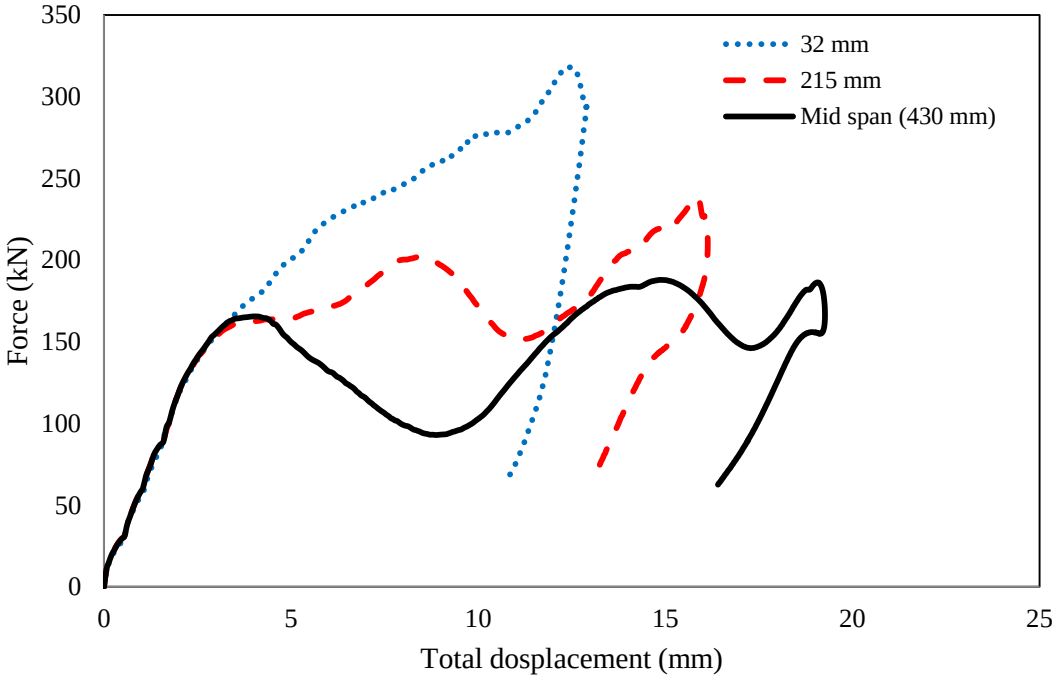

Figure 5.99. The effect of the impact location on the response of the CFST columns with L/D ratio of 9

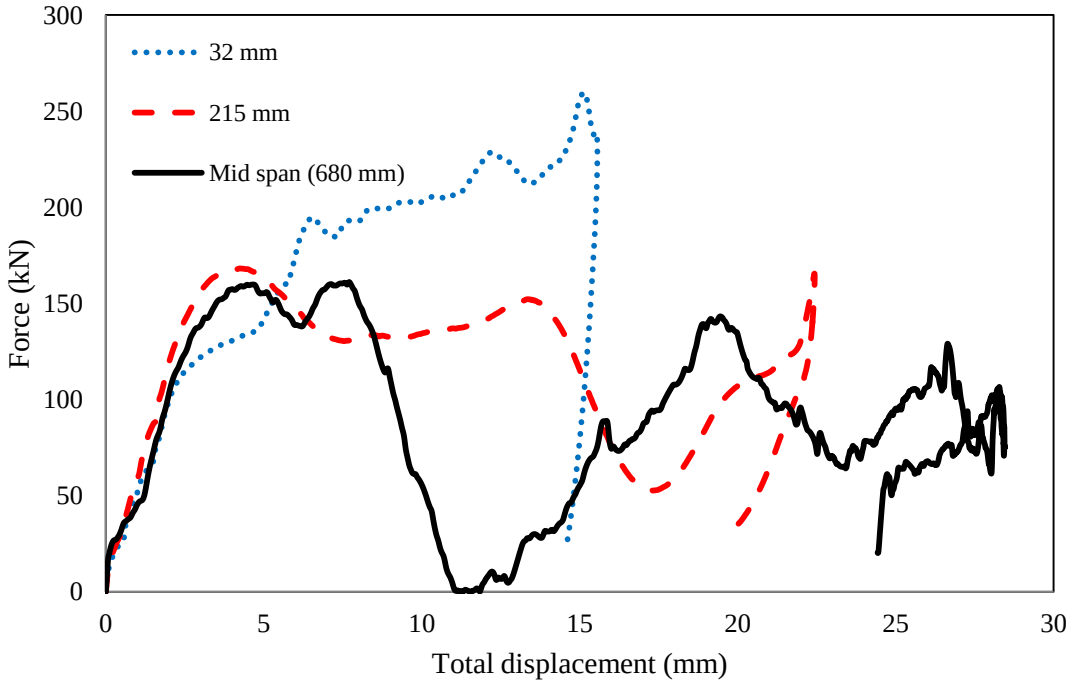

Figure 5.100. The effect of the impact location on the response of the CFST columns with L/D ratio of 13.5

5.6.1.2 The effect of the D/t ratio

Three different values of the tube wall thickness were considered to study the influence of the D/t ratio on the impact behaviour of the CFST columns. The values selected were 1.7, 3 and 5 mm which give D/t ratios of 67, 38 and 23, respectively. Fig. 5.101 shows that the D/t ratio has a considerable effect on the impact response. For the column with L/D ratio of 6, the force decreased from 327 kN to 193 kN when the D/t increased from 23 to 67, while the displacement increased from 13 mm to 18 mm. With the same D/t ratio, the force reduced by 36 % and the displacement increased by 62 % for the columns with a L/D ratio of 9, while the force reduction was only 15.7 % and the displacement increase was 37.6 % with L/D of 13.5. It can be seen that the effect of D/t ratio reduces with increasing the L/D ratio which reduces the stiffness of the column. On other hand, the D/t ratio increases the stiffness and the deformation resistance of CFST column with the same L/D ratio.

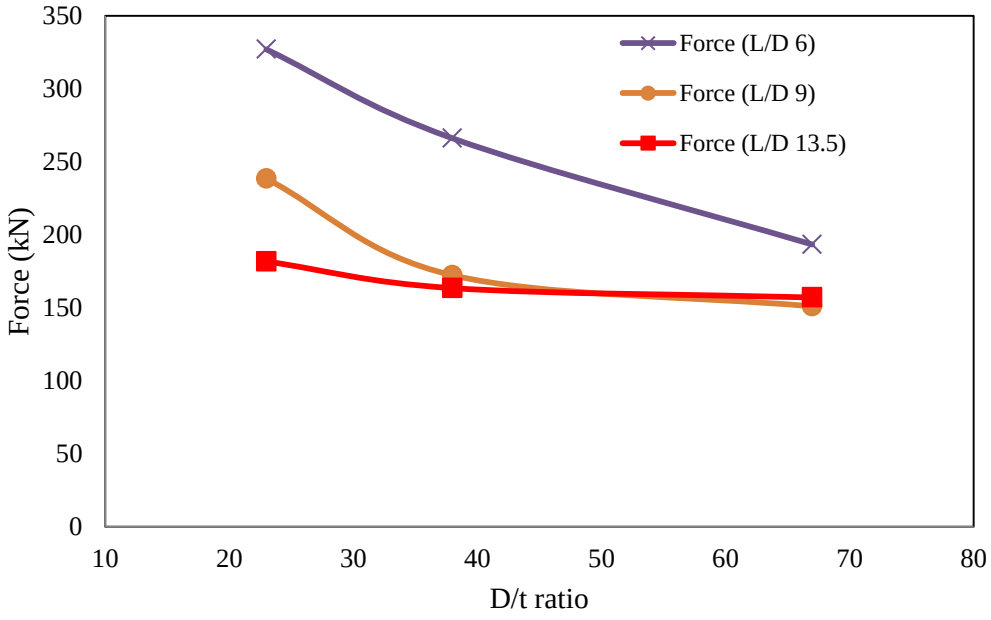

Figure 5.101. The influence of the D/t on the behaviour of the CFST column

5.6.1.3 The effect of the boundary condition

The effect of the boundary condition on the response of the CFST columns was studied by taking three different types of support, i.e. fix-fix, fix-pin and pin-pin with two values of L/D ratio. The impact velocity and mass were set to 7 m/s and 106.5 kg. The comparison

between the force-total displacement curves related to the different support types for the columns with L/D ratios of 9 and 13.5 is shown in Fig. 5.102 and Fig. 5.103, respectively. The figures indicate that the BCs influence the displacement more than the impact force. It can be seen that the force slightly reduced when the BC changed from the Fix-Fix to Pin-Pin, particularly for the one with a L/D ratio of 9. At the same time, the total displacement decreased from 25 mm to 23 mm and from 17 mm to 15.7 mm for the columns with L/D ratio of 13.5 and 9, respectively. However, in general the columns with both ends fixed behave better than other support types, as expected. It can be seen that during the first stage of the force-total displacement trace, there is hardly any effect on the response due to changing the BCs. However, the change in the force and displacement occurs after the first peak for both columns with both the L/D ratios.

5.6.1.4 The influence of the yield strength of the steel tube

To study the effect of the yield strength of the steel tube on the impact force and the lateral displacement of the CFST columns under impact loading, different values of yield strengths were selected, which were 250, 350, 550, 650 and 750 MPa. Such the effect on the total displacement and impact force can be seen from Fig. 5.104.

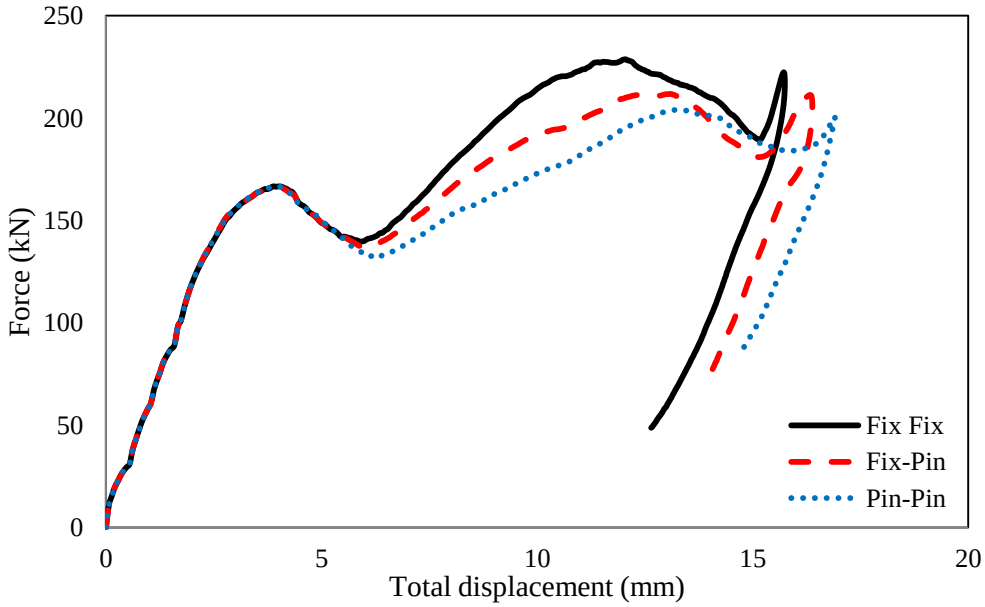

Figure 5.102. The force-total displacement traces for the CFST with different boundary conditions and L/D of 9

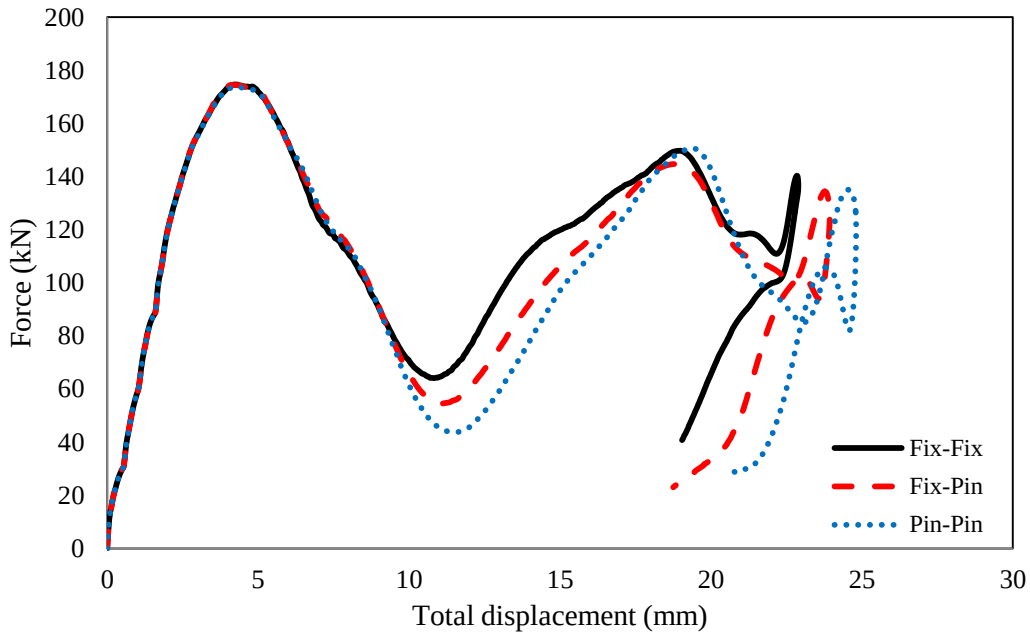

Figure 5.103. The force-total displacement traces for the CFST with different boundary conditions and L/D of 13.5

The figure reveals that for higher values of (f_y), the maximum force and the total displacement are substantially affected. The impact force increased by 34 % when the (f_y) increased from 250 MPa to 750 MPa, whilst the total displacement decreased by 45 %. Table 5.6 presents a summary of the predicted impact forces and the total and global displacements with different values of (f_y). Increasing the strength of the tube will increase the deformation resistance of the tube which leads to reduce the indentation and the lateral displacement. At the same time, increasing the yield strength will increase the column capacity due to the enhancement of the confinement effect of the steel tube. However, the variation of the total displacement is nonlinear with varying the tube yield strength.

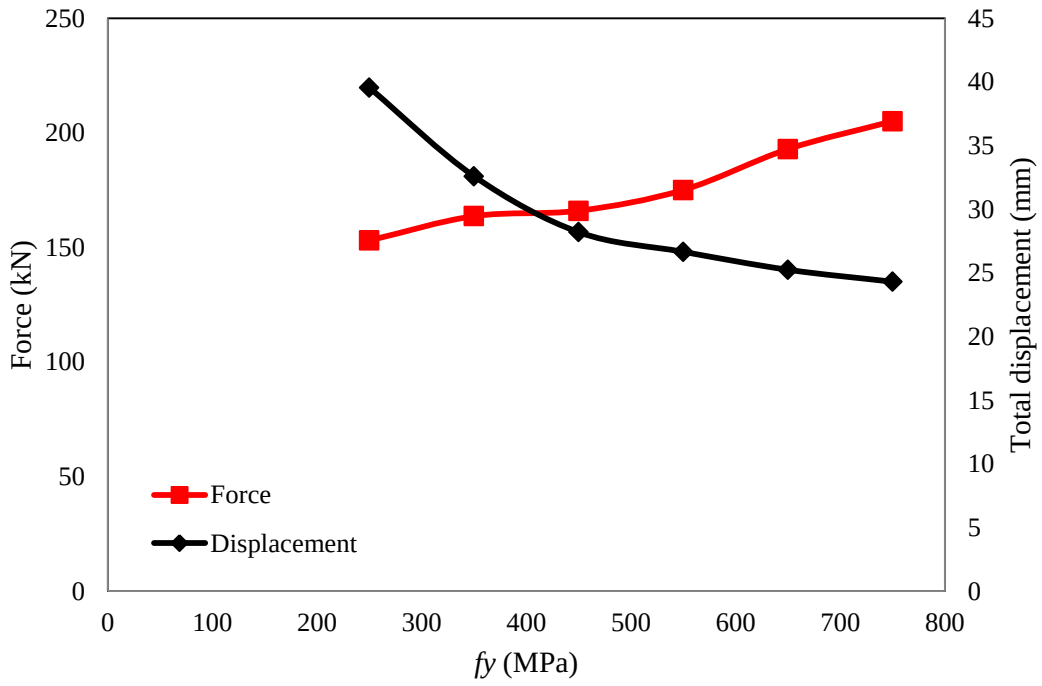

Figure 5.104. The influence of the yield strength of the steel tube on the impact response of the CFST column

Table 5.6. The predicted maximum force and deflection for the CFST column with different values of yield strength for the steel tube.

fy (Mpa)	Force (kN)	Total dis. (mm)	Global dis. (mm)
250	153.1	39.5	36.5
350	163.6	32.6	29.1
450	166.0	28.2	24.3
550	175.1	26.7	22.9
650	192.9	25.2	21.2
750	205.1	24.3	20.0

5.6.1.5 The influence of the compressive strength of the concrete core

The effect of the concrete compressive strength ($f_{c'}$) on the impact behaviour of the CFST column was studied, with the results being shown in Fig. 5.105. The values of $f_{c'}$ investigated are C30, C60, C70 and C80. It can be observed from the results that increasing the compressive strength of concrete has a small effect on the impact response of the CFST columns. This is due the fact that increasing the concrete strength leads to decreasing the

confining effect which results in the reduction of the amount of the micro cracking and the dilatatory behaviour (Johnston, 1976). Increasing the concrete strength from C30 to C80 led to increase the impact force by only 4.2 % and reduce the total displacement by only 0.8 %. This is due to the confinement provided by the steel tube, in which the concrete core only plays a secondary role in the system. Therefore, a low strength concrete can be used in the concrete filled steel tube columns without risking the performance under low velocity impact loading.

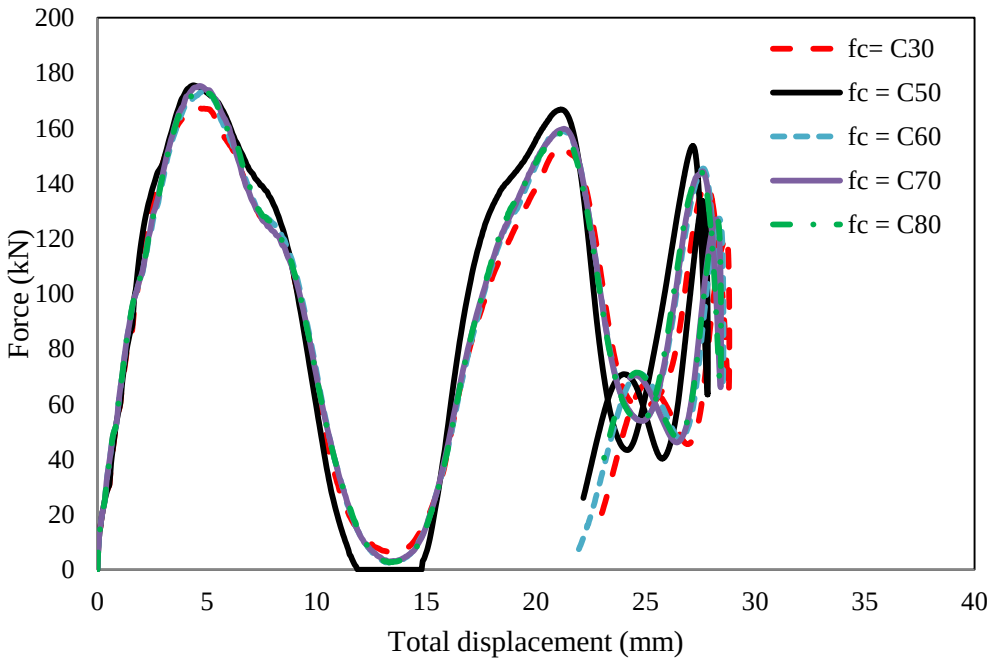

Figure 5.105. The influence of the concrete compressive strength on the impact behaviour of the CFST column with L/D ratio of 13.5

5.6.1.6 The effect of the impact energy

Examination of the influence of the impact energy (IE) on impact response was carried out by using a range of impact velocity and mass. The impact velocity range was from 3 m/s to 8.5 m/s, while the mass range was from 20 kg to 140 kg. Fig. 5.106 shows that the impact energy affects the impact force and the total displacement significantly. When the *IE* increases, both the total displacement and the impact force increase. The impact force increases from 124.2 kN to 194.2 kN and the displacement increases from 13.2 mm to 37

mm by increasing the IE from 0.85 kJ to 3.85 kJ. An increase of the initial impact energy up to a certain level makes the column dissipate more energy due to increasing the impact force and the corresponding displacement induced by the loading with high strain-rates.

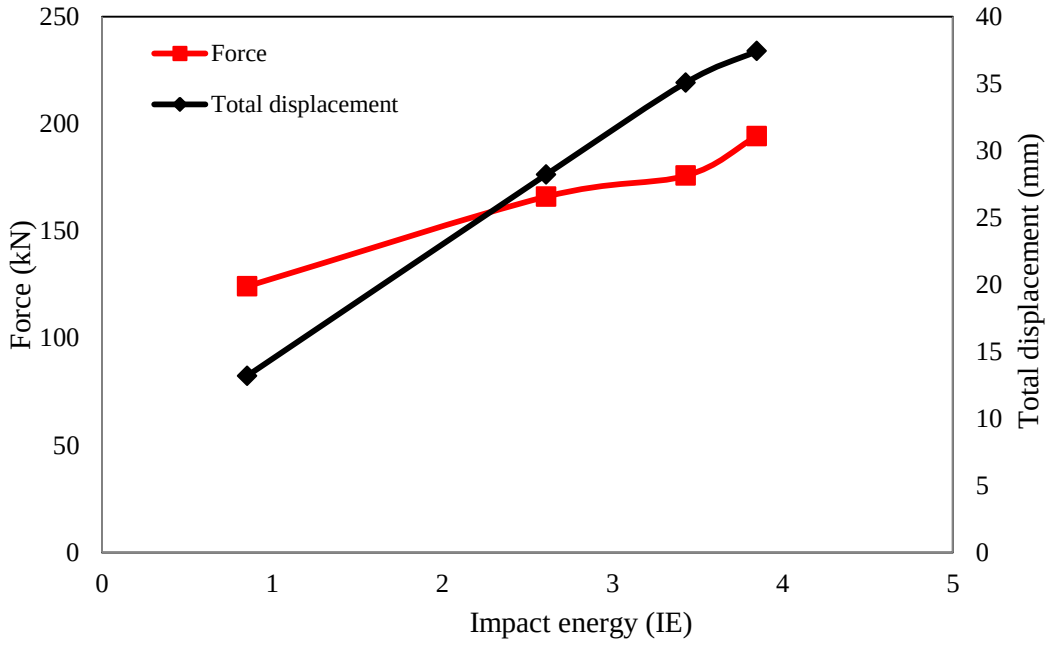

Figure 5.106. The impact energy influence of the impact force and the displacement of the CFST columns

5.6.2 The parameters affecting the strengthened CFST columns

5.6.2.1 Effect of the bonding length of the CFRP

As CFRP is an expensive material, to reduce its quantity but keep the strengthened member with a reasonably high stiffness will lead to economic and strong structural members. Hence, the length of one layer of CFRP wrapping was increased from 1/3 to 2/3 and full length of the clear span of the column to examine the influence of the bonding length of the CFRP layer on the impact response of the CFRP strengthened CFST columns. As shown in Table 5.5, three L/D ratios were again adopted in this study, i.e. 6.0, 9.0 and 13.5. Thus, the length of the CFRP layer was varied from 453 mm to 1360 mm for the column with a L/D ratio of 13.5, from 287 mm to 860 mm and from 174 to 520 mm for the columns with L/D ratios of 9 and 6, respectively. The other variables such as f_y, $f_c^{'}$, impact velocity and mass of

the impactor were kept constant during this study to investigate the impact behaviour of the strengthened CFST columns subjected to the prescribed change of the parameters.

Increasing the CFRP bonding length to more than 1/3 of the clear span of the strengthened CFST column with a L/D ratio of 6 does not have much effect on the impact force and the total displacement of the CFST columns, as shown in Fig. 5.107. This is due to the short length of the tube which exhibited higher stiffness and impact resistance than the other columns even without CFRP strengthening.

Increasing the length of the CFRP layer from 1/3 to 2/3 of the clear span of the CFST column with L/D ratios of 9 and 13.5 has a reasonably significant influence on the column stiffness and the total displacement of the columns. The corresponding total displacement reduced by 7% and 3.6% for the CFST columns with L/D ratios of 9 and 13.5, as can be seen in Fig. 5.108 and Fig. 5.109, respectively. The full CFRP wrapping for the CFST columns with L/D ratios of 9 and 13.5 has the almost the same effect as increasing the CFRP bond length from 1/3 to 2/3 of the clear span of the columns. Modest improvement in terms of the columns stiffness and little enhancement on the column deformation resistance were shown, when the CFRP reinforcement length increased from 574 to 907 mm and from 907 to 1360 mm for the medium and long tube, respectively. Alam et al., (2016) found that the lateral displacement was reduced with increasing the bonding length up to approximately 2/3 of the column span and increasing the bond length more than the 2/3 of columns span has small effect on the impact response of the CFST columns.

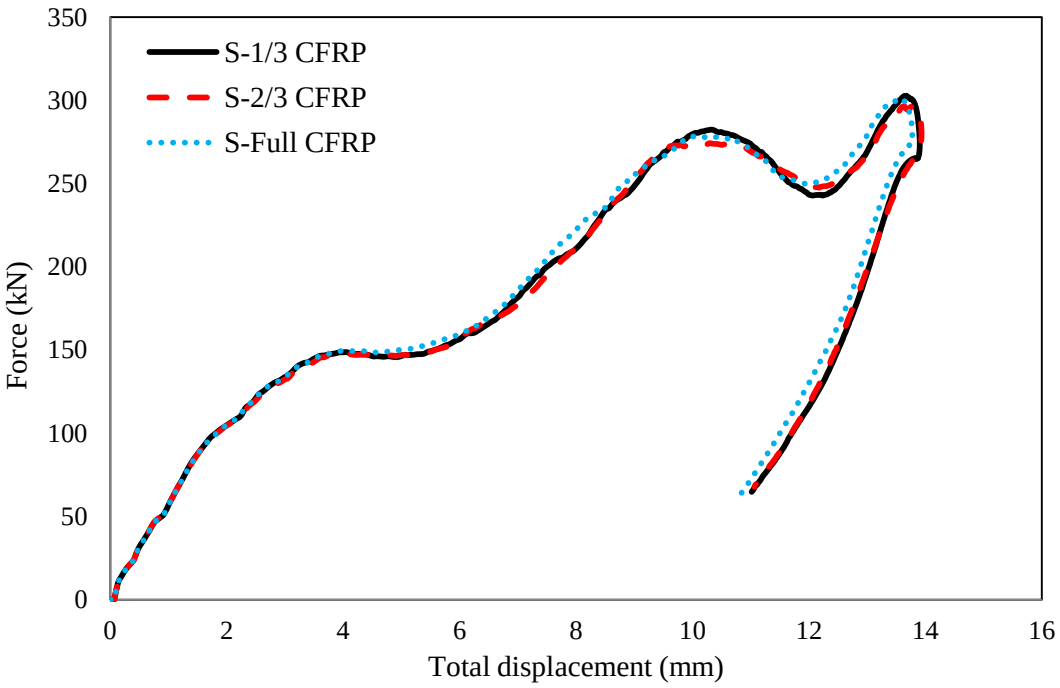

Figure 5.107. The effect of the bond length of the CFRP layer on the impact response of the CFST columns with L/D ratio of 6

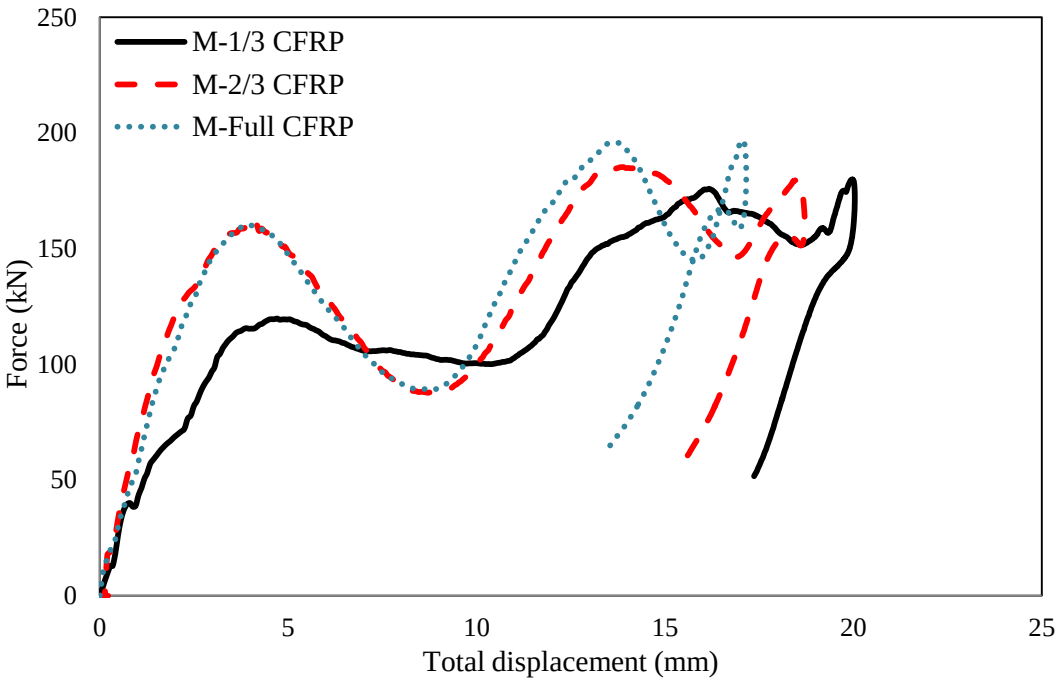

Figure 5.108. The effect of the bond length of the CFRP layer on the impact response of the CFST columns with L/D ratio of 9

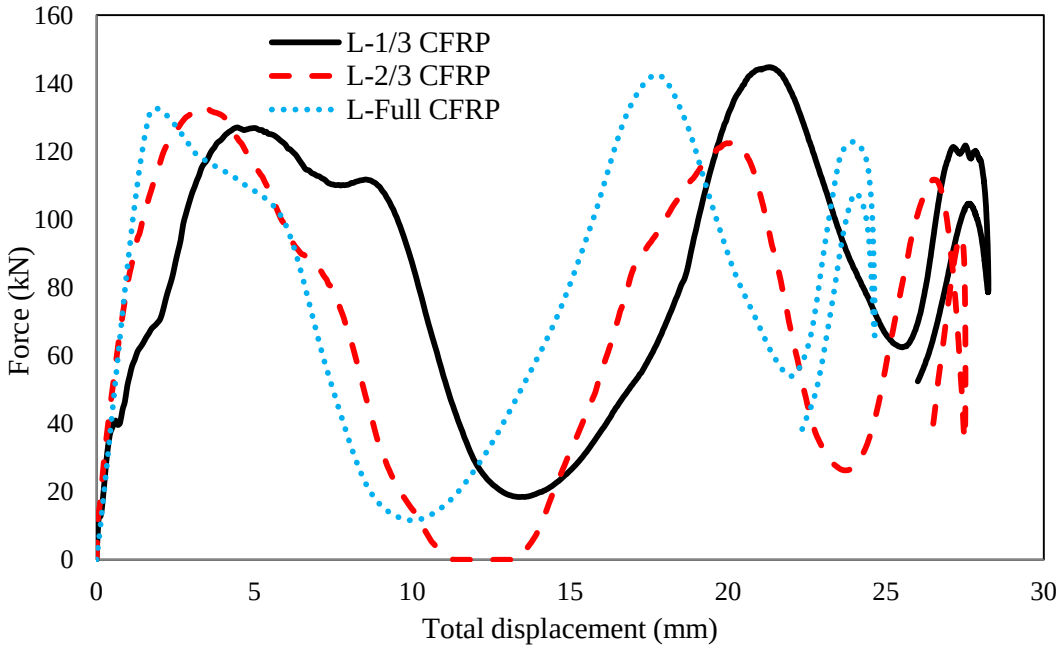

Figure 5.109. The effect of the bond length of the CFRP layer on the impact response of the CFST columns with L/D ratio of 13.5

5.6.2.2 The influence of the D/t ratio

Two values of D/t ratios were selected to study the effect of the wall thickness of the tube on the impact behaviour of the strengthened CFST column. The chosen values are 23 and 38 in addition to the experimental one which is 32. The results shown in Fig 5.110 reveal that the D/t ratio has a reasonable effect on the impact load and total displacement of the columns. The force decreased from 183.7 kN to 151.8 kN and the displacement increased from 23.4 mm to 29.8 mm when the D/t increased from 23 to 38. The reason is that increasing D/t ratio leads to a decrease the tube thickness, the load carrying capacity and increasing the total displacement due to the weakening confinement.

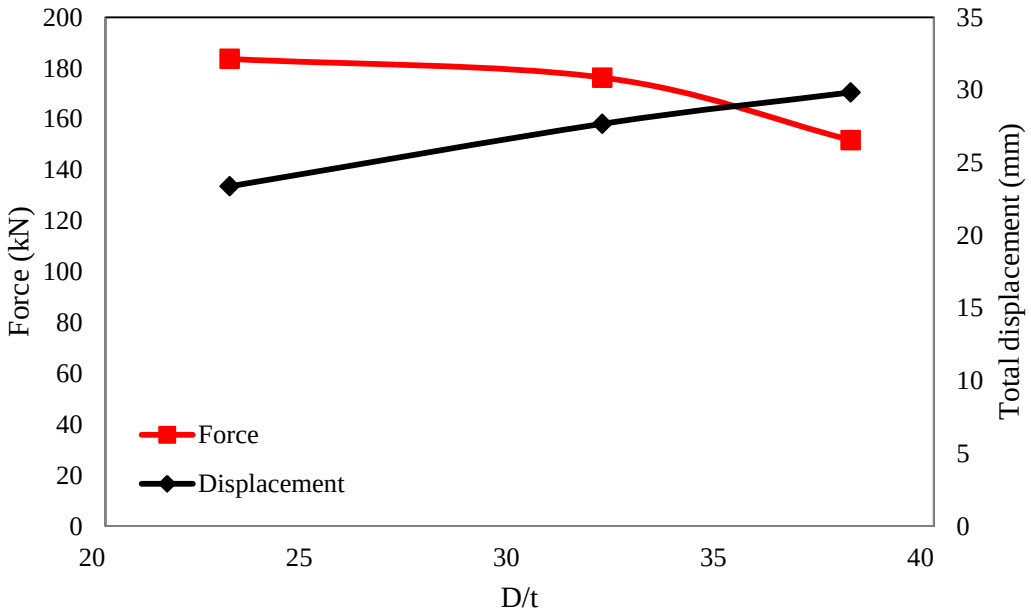

Figure 5.110. The effect of the D/t ratio on the impact response of the CFST columns with L/D ratio of 13.5

5.6.2.3 The effect of changing the impact energy

The impact energy was varied by changing the impact velocity and the impact mass. The adopted velocity values were 3, 5 and 8.5 m/s, while the values of the mass were 55 kg and 150 kg. As expected, the impact force and the total displacement increased with increasing the impact energy, as shown in Fig. 5.111. The force increased by 60 % and the displacement increased by 265 % when the impact energy increased from 0.48 kJ to 3.85 kJ.

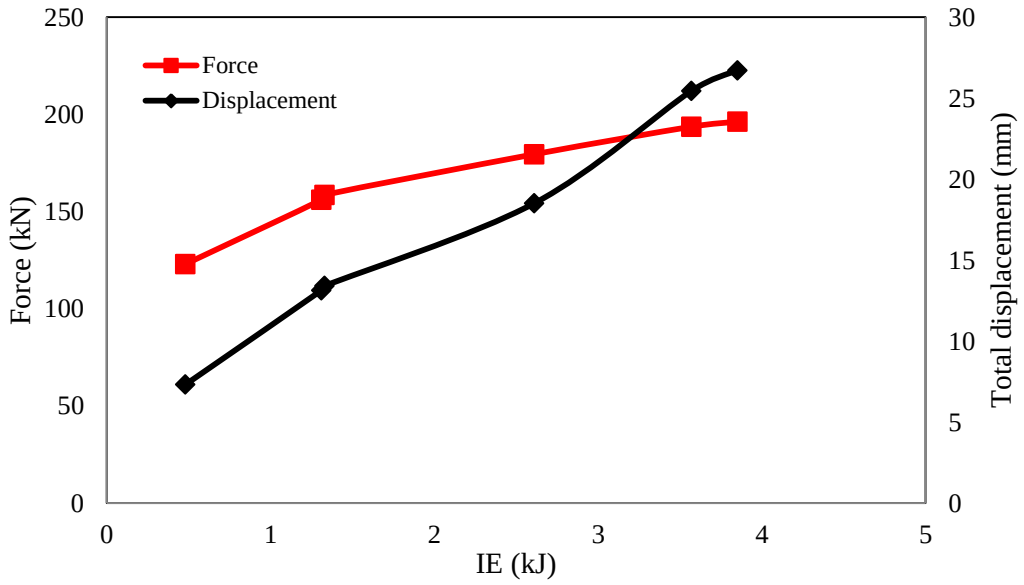

Figure 5.111. The effect of the IE on the impact response of the CFST columns with L/D ratio of 9

5.7 Summary

This chapter has presented the numerical simulation procedures and theories used to predict the response of the CFST columns under lateral impact and quasi-static axial compressive loadings. The commercial code ABAQUS was used for developing the FE models. The geometry, material properties, contact properties, BC and loading conditions for the different models were presented and discussed. Based on the mesh sensitivity studies, the suitable element size for both concrete and steel tube for the impact and compression models were selected. The steel for the endplate was modelled as an elastic-perfectly plastic material, while the concrete was modelled with considering the confinement effect by using the stress-strain curve of the confined concrete. Hashin's failure criteria was used to model the behavior of CFRP. Concrete Damage Plasticity and Drucker Prager models were used to simulate the concrete core under the impact and compression models, respectively. The numerical models were validated against the corresponding experimental results. Both the force-displacement trace and deformation were presented and discussed. The comparisons between the numerical and experimental results were made for the impact and compression.

Reasonable good agreements between the experimental data and FE results were shown. The deformation patterns and the total and absorbed energies are also very well predicted.

In addition, the numerical parametric studies based on the validated FE models were carried out to examine the influences of several parameters on the impact response of the unstrengthened and strengthened CFST columns, which are presented in this chapter. The effect of the impact location, D/t ratio, the impact energy, boundary conditions and the material properties on the impact force and total displacement were studied and discussed. The results showed that the impact location has a considerable influence, while the concrete compressive strength has insignificant effect on the CFST behaviour. Increasing the D/t ratio from 23 to 67 led to an increase of the total displacement and reduction of the impact force. The total displacement decreased by 45% and the impact force increased by 34% when the yield strength of the steel tube increased from 250 MPa to 750 MPa. Based on the predicted results, increasing the impact energy up to a certain point caused an increase for both the impact force and total displacement. Several parameters were also studied to investigate their effects on the response of the CFRP strengthened CFST columns. Increasing the length of the CFRP layer from 1/3 to 2/3 of the clear span for the CFST columns has a considerable influence on the column stiffness and the total displacement of the columns. However, the influence of the full length CFRP wrapping is almost the same of the effect 2/3 length CFRP wrapping for all columns regardless the L/D ratio.

CHAPTER 6

CONCLUSIONS AND RECOMMENDATIONS FOR FUTURE WORK

6.1 Introduction

This study was conducted with the aim to gain a better understanding of the behaviour of the CFST columns under both quasi-static and dynamic loadings. The research work includes series of experimental work, numerical modelling using ABAQUS/Standard and ABAQUS/Explicit and parametric studies of the CFST columns under quasi-static compressive and impact loading, respectively.

The experimental work covers material and structural tests, with the latter including dynamic and quasi-static tests. The CFST columns were subjected to lateral impact loading to study the effects of several parameters, such as the type of concrete (recycled and normal aggregate concrete), the length of the tube, impactor configuration (flat and spherical) and the strengthening with CFRP. In addition, the response of the CFST columns with certain L/D ratio under eccentric or concentric loadings was investigated to examine the influence of the CFRP strengthening, the type of the concrete and the D/t ratio.

Numerical models were developed and validated against the corresponding experimental results. Based on these models, parametric studies were further carried out to investigate the influence of the parameters with more variation. Furthermore, the simplified models were proposed to predict the maximum impact force and the total displacement.

This chapter summarises the main findings of the study and provides recommendations for future work.

6.2 Experimental study

6.2.1 The impact test

In general, the findings show that the RACFST and NACFST specimens have similar deformation modes in relation to a number of parameters, i.e. the tube length, the type of concrete, the impactor configuration and the CFRP reinforcement. The maximum force and the total displacement of the RACFST tubes are comparable to those of the NACFST counterparts due to the comparable compressive strengths of both types of concrete. The

strengthened RACFST specimens exhibit similar behaviour to those with normal aggregate. The RACFST tube can therefore be recommended as a structural composite member for construction due to the comparable load carrying capacity to the NACFST tube and conservation of the natural resources, as long as the recycled aggregate used has appropriate mechanical properties. However, the proportions of constituent materials of the RA should be determined in accordance with Standard [EN 933-11 & AC] and should be characterised in the relevant categories [EN 12620 + A1]. Based on the experimental and numerical results of the CFST columns under low velocity lateral impact loading within the current study conditions, the following conclusions can be drawn.

- In general, The results of the LDV and the HSC showed that the impact response for the NACFST and RACFST columns is almost the same with a small reduction in the load carrying capacity and deformation resistance on the later. The impact event can be divided into three stages, i.e. initial, plateau and final stage. Stage one showed a rapid increase in the impact force with a small corresponding lateral displacement, whilst in the plateau stage, the lateral displacement increased steadly with little increase with the associated impact force. The impact force decreased to zero and the permanent displacement was captured in the third stage. In addition, for all columns regardless of the L/D ratio, no rebound was captured during the impact period studied and the oscillations within the force-displacement traces are due to the vabiration and the change of the material's properties which in turn affected the confining pressure between the concrete core and the steel tube. Due to the column stiffness reduction, the impact event period increased with an increase of the L/D ratio.
- The concrete filling contributes to increasing the maximum force by 217, 182 and 157 % respectively for the short, medium and long tubes, which causes a significant reduction in the total and global displacements. For the short tube, the global and total displacements are reduced by 31 % and 75 %, respectively. The total

displacement is decreased by 68% for the tube with a L/D ratio of 9, while it is decreased by 75% for the one with a L/D ratio of 13.5. Furthermore, the concrete core plays a vital role in changing the deformation mode of the specimens, with reducing the total and global displacements as well as avoiding the local buckling. The concrete filling sustains a substantial deformation resistance which reduces the local indentation significantly regardless the L/D ratio.

- The results also indicate that the load carrying capacity is reduced by 27 % and 38 % when the tube length is increased from 686mm to 1029 mm and 1543mm, respectively.
- The impactor configuration has a great effect on the impact force and the displacement for the tubes filled either the normal or the recycled aggregate concrete. Enlarging the spherical diameter from 20 mm to 60 mm increases the impact force from 220 kN to 286 kN and reduced the total displacement from 16.3 mm to 13 mm. The indentation depth is also reduced from 10.2 mm to 4.9 mm, while the global displacement is increased by 17.2 %. The influence of the flat impactor is greater than the spherical one on the impact force, total and global displacements.
- The CFRP plays a significant role in enhancing the resistance to global displacement. It reduces the contact force due to the low contact stiffness of the CFRP layer particularly for the long CFST columns. The contact force for the strengthened long NACFST column is 146.3 kN, while it is 166.2 kN for the unstrengthened counterpart. The strengthened columns show slightly higher initial stiffness than the unstrengthened ones, irrespective the type of concrete filling. The local indentation depth for the strengthened columns is higher than those without a CFRP jacket with the same spherical impactor diameter due to the reduction of the global deformation which in turn induces the column to deform locally and increases the local energy absorption. The indentation depth for the strengthened

long NACFST column is increased by 36 %, whilst it increases by 14.3 % and 11 % for the strengthened medium and short NACFST columns, respectively. One layer of the CFRP reinforcement has reduced the global displacement by about 8.3 % and 6.2 % for the long and medium tubes, respectively.

- The D/t ratio has a reasonable effect on the impact behaviour of the NACFST and RACFST columns. Using the same spherical impactor and with a D/t ratio of 38, both of the NACFST and RACFST columns exhibit lower stiffness than those with a D/t ratio of 32. This is due to less confinement between the concrete core and steel tube. The total displacement is increased by 20.2 % and 27.3 % for the NACFST and RACFST columns when the D/t ratio is increased from 32 to 38, respectively.

6.2.2 The compression test

- The NACFST and RACFST columns exhibit almost the same behaviour under compression loading. The maximum force for the NACFST column is only 2 % and 7 % higher than the corresponding RACFST column under concentric and eccentric loading, respectively. Furthermore, no obvious difference was recorded between the mode of failure of the NACFST and RACFST columns.
- The eccentric loading significantly influences the bearing capacity of all the specimens. The maximum force is reduced by 14.5 % and 19.4 %, while the axial shortening reduction is 23.3 % and 24.4 % for the NACFST and RACFST columns, respectively.
- With the CFRP jacketing, the specimens show a higher stiffness during the elastic stage. Under concentric loading, the adopted arrangement of the small CFRP reinforcement increases the maximum force only by 5 % and 4 %; however, the axial displacement reduces by 20 % and 14 % for the NACFST and RACFST columns, respectively. The effectiveness of the CFRP reinforcement can be examined by calculating the column stiffness using the maximum force and the associated axial displacement. The CFRP arrangement adopted in this study

enhances the stiffness of the NACFST and RACFST columns by 53 % and 87 %, respectively. Under eccentric loading, the additional confinement provided by the CFRP increases the ultimate capacity for the NACFST column by 3.4 %, whilst the maximum force is increased from 866 kN to 928 kN for the RACFST column.

- It was found that reducing the D/t ratio from 38 to 32 causes increases of the maximum force from 1092 kN to 1167 kN and from 1074 kN to 1158 kN for the NACFST and RACFST specimens, respectively. In addition, the axial displacement is decreased by 17.3 % for the NACFST column and by 15 % for the RACFST column.

6.3 Numerical modelling

- The results presented in this study provide strong evidence that the 3D non-linear finite element models developed are capable of predicting the impact force, the total and global displacements and the deformation shape for the CFST columns subjected to lateral impact loading. This proves that the associated geometrical, material and contact properties used are appropriate and performed effectively. The numerical results show that the CFST columns under low velocity impact loading have an insignificant strain rate effect.
- The comparison between the numerical and experimental force-total displacement curves for the hollow circular tubes subjected to lateral impact loading with different L/D ratios show that the predicted force and total displacement are correlated reasonably well to the corresponding experimental results. In addition, the deformation modes predicted are similar to those captured experimentally.
- In terms of the impact force and the global and total displacements, the agreement between the predicted results and the corresponding experimental data is reasonably good with different L/D ratios and concrete types. With a L/D ratio of 6, the discrepancies between the experimental and numerical force, total displacement and global displacement were only 7.6, 1.4 and 3.0 %, respectively. The numerical

models also indicate that with increasing the length of the column, the impact force is reduced but the total and global displacements are increased. In addition, the RACFST column shows a slightly lower load carrying capacity than the NACFST column. However, both of the NACFST and RACFST columns exhibit similar deformation modes regardless of the L/D ratio. All these predictions agree reasonably well with the experimental findings.

- The numerical and experimental results correlate very well for both the NACFST and RACFST columns subjected to lateral impact by flat and spherical impactors with different diameters. It is clear that the models are able to predict all features of the traces from the initial elastic stage to the final point of the test. However, the FE models tend to over-estimate the maximum force for the CFST columns hit by the small impactor by 24.0 % and 25.7 % for the NACFST and RACFST columns, respectively. Meanwhile, the predicted total displacement for the RACFST is 15.5 mm in comparison to the measured one of 15.6 mm, whilst the measured and predicted total displacement for the NACFST column are 16.4 mm and 15.4 mm, respectively. In addition, the numerical results of the stress, strain and plastic strain distribution for the steel tube and concrete core as well as the confining pressure history and deformation pattern of the concrete core demonstrate the robustness of the numerical models.
- The numerical models have well captured the force-total displacement traces and the deformation shapes of the CFRP strengthened CFST columns and provided good predictions of the initial, plateau and failure or unloading stages. There are only 2.4 % and 6.8 % differences between the predicted and experimental maximum force respectively for the RACFST and NACFST columns, with a L/D ratio of 13.5.
- In general, the numerical models give predictions of the total and absorbed energies with a high degree of accuracy, with the greatest error being approximately 13 %. Also, the numerical results were able to predict the absorbed energy by the CFST

column components, i.e. steel tube and concrete core. The results reveals that the concrete core absorbed less energy than the steel tube and the contribution of the steel tube to absorb the applied impact energy increases with increasing the span length of the column. The absorbed energy by the concrete core and the steel tube account for 36 % and 23.5 %, 22 % and 64.4 %, 76.5 % and 78 % for the CFST columns with L/D ratios of 6, 9 and 13.5, respectively.

- The predicted and experimental load-displacement traces for the NACFST and RACFST column subjected to concentric or eccentric compression loadings also show a reasonably good agreement with the experimental ones. These models have captured the basic features of the force-displacement trace, i.e. the elastic stage, the yielding stage and post yielding stage. The various failure patterns are also well predicted.
- Using the validated models, parametric studies have been carried out on parameters covering the D/t, impact location, materials properties, impact energy, boundary conditions and the bonding length of the CFRP. The numerical predictions show that reducing the D/t ratio increases the load carrying capacity and decreases the displacement. The higher concrete strength and steel tube strength contribute to the increase of the impact force and the decrease of the displacement due to the higher stiffness of the tube. Increasing the length of the CFRP layer from 1/3 to 2/3 of the clear span for the CFST columns has a considerable influence on the column stiffness and the total displacement of the columns. However, the influence of the full length CFRP wrapping is almost the same as the effect of 2/3 length CFRP wrapping for all columns, regardless the L/D ratio.

6.4 Recommendations for future work

Based on the investigation work and output above, a number of further research studies can be carried out to improve the knowledge and understanding of the CFST columns in some areas which could not be covered in this study:

- The present study focuses on the behaviour of the CFST columns under lateral impact loading. The impact response of other section shapes, such as rectangular, square or even unconventional sections shapes, may be investigated experimentally and numerically. Also, full scale columns in accordance to the practical CFST columns in real structures such as bridges and buildings with taking into account the limitations of the design codes for the L/D and D/t ratios would be valuable to be studied under high velocity impact up to 120 km/h (33.3 m/s), This is an averaged maximum speed limit in the UK and USA (National speed limits, 2017, National motorists association, 2017).
- The current study has focused on the impact perpendicular to the target. Therefore, further studies could be undertaken experimentally and numerically to investigate the influence of the oblique impact at different locations on the column.
- Further studies could be carried out experimentally and numerically to investigate the effect of the axially loaded CFST columns subjected to lateral impact with different section shapes.
- Since the effect of the strain rate is not considered in the current study due the low impact velocity, further study can be conducted to investigate the influence of the strain rate on the impact behaviour of the CFST columns subjected to high velocity impact. In addition, it would be very valuable to study the strain rate effect on the constituents of the CFST column separately, i.e. concrete core and steel tube.

Reference

AASHTO 2007. LRFD Bridge design specifications. American Association of State Highway and Transportation Officials. Washington, D.C, USA.

ABAQUS, online documentation. Version 6.12., 2015.

ABAQUS, Theory Manual. Version 6.12. Pawtucket: Hibbitt, Karlsson & Sorensen, Inc., 2015.

ABAQUS/CAE User's Manual. Version 6.12. Pawtucket: Hibbitt, Karlsson & Sorensen, Inc., 2015.

Abed, F., AlHamaydeh, M. and Abdalla, S., 2013. Experimental and numerical investigations of the compressive behavior of concrete filled steel tubes (CFSTs). Journal of Constructional Steel Research, 80, pp.429-439.

Abramowicz, W. and Jones, N., 1984. Dynamic axial crushing of square tubes. International Journal of Impact Engineering, 2(2), pp.179-208.

ACI 1992. Analysis and design of reinforced and prestressed-concrete guide way structures. Reported by ACI Committee 358.

ACI Committee 318-05, 2005. Building code requirements for structural concrete, American concrete institute, Detroit, Michigan.

ACI Committee 318-95, 1995. Building code requirements for structural concrete. Detroit, Michigan.

ACI Committee 318-99, 1999. Building code requirements for structural concrete, American concrete institute, Detroit, Michigan.

Adachi, T., Tanaka, T., Sastranegara, A., Yamaji, A., Kim, S., and Yang, I., 2004. Effect of transverse impact on buckling behaviour of a column under static axial compressive force. International Journal of Impact Engineering, 30, 465-475.

Aghdamy, S., Thambiratnam, D.P., Dhanasekar, M. and Saiedi, S., 2015. Computer analysis of impact behavior of concrete filled steel tube columns. Advances in Engineering Software, 89, pp.52-63.

AINSI/AISC 360-05, 2005. Specification for Structural Steel Buildings. American Institute of Steel Construction, Inc., Chicago, Illinois.

AISC 303, 2005. Code of Standard Practice for Steel Buildings and Bridges. American Institute of Steel Construction, Inc., Chicago, Illinois.

AISC-LRFD, 1993. Manual of steel construction, load and resistance factor design, (including commentary). American Institute of Steel Construction. Chicago. USA

AISC-LRFD. Load and resistance factor design specification for structural steel buildings. 2nd ed. Chicago (USA): American Institute of Steel Construction (AISC); 1999.

Akçaoğlu, T., Tokyay, M. and Çelik, T., 2002. Effect of coarse aggregate size on interfacial cracking under uniaxial compression. Materials letters, 57(4), pp.828-833.

Alam, M.I. and Fawzia, S., 2015. Numerical studies on CFRP strengthened steel columns under transverse impact. Composite Structures, 120, pp.428-441.

Alam, M.I., Fawzia, S. and Liu, X., 2015. Effect of bond length on the behaviour of CFRP strengthened concrete-filled steel tubes under transverse impact. Composite Structures, 132, pp.898-914.

Alam, M.I., Fawzia, S. and Zhao, X.L., 2016. Numerical investigation of CFRP strengthened full scale CFST columns subjected to vehicular impact. Engineering Structures, 126, pp.292-310.

Al-Mosawe, A., Al-Mahaidi, R. and Zhao, X.L., 2016. Experimental and Numerical Study on Strengthening of Steel Members Subjected to Impact Loading Using Ultrahigh Modulus CFRP. Journal of Composites for Construction, 20(6), pp.04016044.

Al-Thairy, H., 2012. Behaviour and Design of Steel Column Subjected to Vehicle Impact. PhD thesis, University of Manchester, UK.

American Concrete Institute. Building code requirements for reinforced concrete (ACI, 318-89), and Commentary. 1989.

ANSI/AISC 360-05, 2005. Specification for Structural Steel Buildings. American Institute of Steel Construction. Chicago, Illinois.

Architectural Institute of Japan (AIJ), 2001. Standards for structural calculation of steel reinforced concrete structures, 5th Ed. Tokyo, Japan.

Australia Standards AS3600 Reinforced concrete structures. Sydney: Standards Australia; 1994.

Australia Standards AS4100 Steel structures. Sydney: Standards Australia; 1998.

Bambach, M.R., 2011. Design of hollow and concrete filled steel and stainless steel tubular columns for transverse impact loads. Thin-Walled Structures, 49(10), pp.1251-1260.

Bambach, M.R., Jama, H., Zhao, X.L. and Grzebieta, R.H., 2008. Hollow and concrete filled steel hollow sections under transverse impact loads. Engineering structures, 30(10), pp.2859-2870.

Begum, M., Driver, R.G. and Elwi, A.E., 2007. Finite-element modeling of partially encased composite columns using the dynamic explicit method. Journal of structural engineering, 133(3), pp.326-334.

Begum, M., Driver, R.G. and Elwi, A.E., 2007. Numerical simulations of the behaviour of partially encased composite columns (Vol. 68, No. 07).

Bergmann R., Matsui C., Meinsama C., Dutta D., 1995. Design guide for concrete filled hollow section columns under static and seismic loading (CIDECT). Eds.) Germany.

Birch, R.S. and Jones, N., 1990. Measurement of impact loads using a laser Doppler velocimeter. Proceedings of the Institution of Mechanical Engineers, Part C: Journal of Mechanical Engineering Science, 204(1), pp.1-8.

Bischoff, P.H. and Perry, S.H., 1991. Compressive behaviour of concrete at high strain rates. Materials and structures, 24(6), pp.425-450.

British Standard Institute. BS5400, Part 5. Concrete and composite bridges. London (UK); 1979.

British Standards Institution, Cement Composition, specifications and conformity criteria for common cements, BS EN 197-1, 2011.

British Standards Institution, Concrete. Guide to specifying concrete, 5328-1, 1997.

British Standards Institution, Concrete. Methods for specifying concrete mixes, 5328-2, 1997.

British Standards Institution, Concrete. Plastics. Determination of tensile properties. Test conditions for isotropic and orthotropic fibre-reinforced plastic composites, 527-4, 1997.

British Standards Institution, Specification for aggregates from natural sources for concrete, BS 882, 1992.

British Standards Institution, Tensile testing of metallic materials. Method of test at ambient temperature, BS 10002-1, 2001.

British Standards Institution, Testing concrete. Methods for mixing and sampling fresh concrete in the laboratory, BS 1881-125, 2013.

British Standards Institution, Testing hardened concrete. Compressive strength of test specimens, BS EN 12390-3, 2009.

British Standards Institution, Tests for mechanical and physical properties of aggregates. Determination of particle density and water absorption, BS EN 1097-6, 2013.

Broadhouse, B. J., 1986. A computer code for dynamic analysis of stress transients in reinforced concrete. Safety and Engineering Science Division, AEE, Winfrith, AEEW-R2124.

Bruneau, M. and Marson, J., 2004. Seismic design of concrete-filled circular steel bridge piers. Journal of bridge engineering, 9(1), pp.24-34.

Buth, C. E., Williams, W. F., Brackin, M. S., Lord, D., Geedipally, S. R., & Abu-Odeh, A. Y., 2010. Analysis of large truck collisions with bridge piers: phase 1. Report of guidelines for designing bridge piers and abutments for vehicle collisions (No. FHWA/TX-10/9-4973-1).

Chakradhara M, Bhattacharyya SK & Barai SV., 2011. Behaviour of recycled aggregate concrete under drop weight impact load. Construction and Building Materials, 25, pp. 69-80.

Chan, A.K.C., 1986. Impact behaviour of model prestressed concrete beams (Doctoral dissertation), University of Sheffield.

Chen, C., Zhao, Y. and Li, J., 2014. Experimental Investigation on the Impact Performance of Concrete-Filled FRP Steel Tubes. Journal of Engineering Mechanics, 141(2), p.04014112.

Chen, J. and Jin, W.L., 2010. Experimental investigation of thin-walled complex section concrete-filled steel stub columns. Thin-Walled Structures, 48(9), pp.718-724.

Chen, Z., Xu, J., Xue, J. and Su, Y., 2014. Performance and calculations of recycled aggregate concrete-filled steel tubular (RACFST) short columns under axial compression. International Journal of Steel Structures, 14(1), pp.31-42.

Comite Euro-International du Beton. CEB-FIP Model Code 1990. Trowbridge, Wiltshire, UK: Redwood Books; 1993.

Crawdford, J.E., Magallanes, J.M., Lan, S., and Wu, Y., 2011. User's manual and documentation for release III of the K&C concrete model in LS-DYNA. TR-11-36-1, Technical report, Karagozian & Case. Burbank, CA.

Dai, X. and Lam, D., 2010. Axial compressive behaviour of stub concrete-filled columns with elliptical stainless steel hollow sections. Steel and Composite Structures, 10(6), pp.517-539.

Dai, X. and Lam, D., 2010. Numerical modelling of the axial compressive behaviour of short concrete-filled elliptical steel columns. Journal of Constructional Steel Research, 66(7), pp.931-942.

Dai, X.H., Lam, D., Jamaluddin, N. and Ye, J., 2014. Numerical analysis of slender elliptical concrete filled columns under axial compression. Thin-Walled Structures, 77, pp.26-35.

DBJ 13-51-2003. Technical specification for concrete-filled steel tubular structures. Fuzhou; 2003

De Oliveira, W.L.A., De Nardin, S., de Cresce El, A.L.H. and El Debs, M.K., 2009. Influence of concrete strength and length/diameter on the axial capacity of CFT columns. Journal of Constructional Steel Research, 65(12), pp.2103-2110.

Deng, Y. and Tuan, C.Y., 2013. Design of concrete-filled circular steel tubes under lateral impact. ACI Structural Journal, 110(4) pp. 691-701

Deng, Y., Tuan, C.Y. and Xiao, Y., 2011. Flexural behaviour of concrete-filled circular steel tubes under high-strain rate impact loading. Journal of Structural Engineering, 138(3), pp.449-456.

Dietenberger, M., Buyuk, M. and Kan, C.D., 2005. Development of a high strain-rate dependent vehicle model. National crash analysis center Virginia, Bamberg.

Ding, F.X., Liu, J., Liu, X.M., Yu, Z.W. and Li, D.W., 2015. Mechanical behaviour of circular and square concrete filled steel tube stub columns under local compression. Thin-Walled Structures, 94, pp.155-166.

Dong, J.F., Wang, Q.Y. and Guan, Z.W., 2013. Structural behaviour of recycled aggregate concrete filled steel tube columns strengthened by CFRP. Engineering Structures, 48, pp.532-542.

Dundu, M., 2012. Compressive strength of circular concrete filled steel tube columns. Thin-Walled Structures, 56, pp.62-70.

Elchalakani, M., Zhao, X.L. and Grzebieta, R.H., 2001. Concrete-filled circular steel tubes subjected to pure bending. Journal of Constructional Steel Research, 57(11), pp.1141-1168.

Ellobody, E. and Young, A., 2006. Design and behaviour of concrete-filled cold-formed stainless steel tube columns. Engineering structures, 28(5), pp.716-728.

Ellobody, E. and Young, B., 2006. Nonlinear analysis of concrete-filled steel SHS and RHS columns. Thin-walled structures, 44(8), pp.919-930.

Ellobody, E., Young, B. and Lam, D., 2006. Behaviour of normal and high strength concrete-filled compact steel tube circular stub columns. Journal of Constructional Steel Research, 62(7), pp.706-715.

ENV 1994-1-1:1994. British. Standards Institution, London W1A2BS, 1994.

Etxeberria, M., Vázquez, E., Marí, A. and Barra, M., 2007. Influence of amount of recycled coarse aggregates and production process on properties of recycled aggregate concrete. Cement and concrete research, 37(5), pp.735-742.

Eurocode 1: EC1 1-1, 2001: Actions on structures – Part 1-1: General actions – Densities, self-weight, imposed loads for buildings. Final Draft prEN 1991-1-1,Technical committee CEN/TC 250, European Committee for Standardization.

Eurocode 1: EC1 1-7, 2003. Actions on structures – Part 1-7: General actions – Accidental actions. Final Project Team Draft [Stage 34], Draft prEN 1991-1-7, Technical committee CEN/TC 250 European Committee for Standardization.

Eurocode 1: EC1 2-7, 1998. Actions on structures – Part 2-7: Accidental actions due to impact and explosions. ENV 1991-2-7, Technical committee CEN/TC 250 European Committee for Standardization

Eurocode 4. Design of composite steel and concrete structures, Part1.1: General rules and rules for buildings (together with United Kingdom National Application Document).

Eurocode 4. Design of composite steel and concrete structures, Part 1.1, General rules and rules for buildings. ENV 1994 1-1, 1992.

Eurocode1 2002. BS EN 1991-1-1-:2002, Eurocode 1: Actions on structures - Part 1-1: General actions — Densities, self-weight, imposed loads for buildings- (ANNEX B), Incorporating corrigenda December 2004 and March 2009.

Eurocode1 2003. BS EN 1991-2:2003, Eurocode 1: Actions on structures - Part 2: Traffic loads on bridges, Incorporating Corrigenda, December 2004 and February 2010.

Eurocode1 2006. BS EN 1991-1-7:2006, Eurocode 1- Actions on structures - Part 1-7: General actions — Accidental actions, Incorporating corrigendum, February 2010.

Eurocode3 2005. BS EN 1993-1-1:2005, Eurocode 3 — Design of steel structures - Part 1-1: General rules and rules for buildings, Incorporating Corrigenda February 2006 and April 2009.

Eurocode3, 2005. BS EN 1993-1-1:2005. Design of steel structures-Part 1-1: General rules and rules for buildings, Incorporating Corrigenda February 2006 and April 2009.

Eurocode3, 2014. Design of steel structures-Part 1-1: General rules and rules for buildings, Incorporating Corrigenda.

Fitzwilliam, J. and Bisby, L.A., 2010. Slenderness effects on circular CFRP confined reinforced concrete columns. Journal of Composites for Construction, 14(3), pp.280-288.

GangaRao, H.V., Taly, N. and Vijay, P.V., 2006. Reinforced concrete design with FRP composites. CRC press.

Gho, W.M. and Liu, D., 2004. Flexural behaviour of high-strength rectangular concrete-filled steel hollow sections. Journal of Constructional Steel Research, 60(11), pp.1681-1696.

Giakoumelis, G. and Lam, D., 2004. Axial capacity of circular concrete-filled tube columns. Journal of Constructional Steel Research, 60(7), pp.1049-1068.

Grote, D.L., Park, S.W. and Zhou, M., 2001. Dynamic behavior of concrete at high strain rates and pressures: I. experimental characterization. International Journal of Impact Engineering, 25(9), pp.869-886.

Gupta, P.K. and Singh, H., 2014. Numerical study of confinement in short concrete filled steel tube columns. Latin American Journal of Solids and Structures, 11(8), pp.1445-1462.

Halliwell, S., 2002. Polymers in building and construction (Vol. 154). iSmithers Rapra Publishing.

Han, L.H., 2000. The influence of concrete compaction on the strength of concrete filled steel tubes. Advances in Structural Engineering, 3(2), pp.131-137.

Han, L.H., Hou, C.C., Zhao, X.L. and Rasmussen, K.J., 2014. Behaviour of high-strength concrete filled steel tubes under transverse impact loading. Journal of Constructional Steel Research, 92, pp.25-39.

Han, L.H., Hou, C.C., Zhao, X.L. and Rasmussen, K.J., 2014. Behaviour of high-strength concrete filled steel tubes under transverse impact loading. Journal of Constructional Steel Research, 92, pp.25-39.

Han, L.H., Li, W. and Bjorhovde, R., 2014. Developments and advanced applications of concrete-filled steel tubular (CFST) structures: Members. Journal of Constructional Steel Research, 100, pp.211-228.

Han, L.H., Tao, Z. and Yao, G.H., 2008. Behaviour of concrete-filled steel tubular members subjected to shear and constant axial compression. Thin-Walled Structures, 46(7), pp.765-780.

Harries, K.A. and Kharel, G., 2003. Experimental investigation of the behavior of variably confined concrete. Cement and Concrete research, 33(6), pp.873-880.

Hashin, Z. and Rotem, A., 1973. A fatigue failure criterion for fiber reinforced materials. Journal of composite materials, 7(4), pp.448-464.

He, D., Dong, J., Wang, Q. and Chen, X., 2011, July. Mechanical behaviour of recycled concrete filled steel tube conlumns strengthened by CFRP. In Multimedia Technology (ICMT), 2011 International Conference on (pp. 1110-1113). IEEE

Hu, H.T., Huang, C.S. and Chen, Z.L., 2005. Finite element analysis of CFT columns subjected to an axial compressive force and bending moment in combination. Journal of Constructional Steel Research, 61(12), pp.1692-1712.

Hu, H.T., Huang, C.S., Wu, M.H. and Wu, Y.M., 2003. Nonlinear analysis of axially loaded concrete-filled tube columns with confinement effect. Journal of Structural Engineering, 129(10), pp.1322-1329.

Huang, C.S., Yeh, Y.K., Liu, G.Y., Hu, H.T., Tsai, K.C., Weng, Y.T., Wang, S.H. and Wu, M.H., 2002. Axial load behavior of stiffened concrete-filled steel columns. Journal of Structural Engineering, 128(9), pp.1222-1230.

Huo, J., Zheng, Q., Chen, B. and Xiao, Y., 2009. Tests on impact behaviour of micro-concrete-filled steel tubes at elevated temperatures up to 400 C. Materials and structures, 42(10), pp.1325-1334.

ImPREESSion 6, 2002. Necolet Tecnonlgies. Weisang GmbH & Co. KG. Germany.

Institute; 1999.

Jiang, S.F., Wu, Z.Q. and Niu, D.S., 2010. Experimental study on fire-exposed rectangular concrete-filled steel tubular (CFST) columns subjected to bi-axial force and bending. Advances in Structural Engineering, 13(4), pp.551-560.

Johansson, M., 2002. Composite action and confinement effects in tubular steel-concrete columns. Chalmers University of Technology.

Johnston, B. G., 1976. Guide to Stability Design Criteria for Metal Structures. Column research council of engineering foundation. NY, USA.

Jones, N., 2012. Structural impact. Cambridge university press.

Kang, J. Y., Choi, E. S., Chin, W. J. and Lee, J. W., 2007. Flexural behavior of concrete filled steel tube members and its application. International Journal of Steel Structures, 7, 319-324.

Knowles, R.B. and Park, R., 1969. Strength of concrete filled steel tubular columns. Journal of the structural division, 95(12), pp.2565-2588.

Konno, K., Sato, Y., Kakuta, Y. and Ohira, M., 1998. The property of recycled concrete column encased by steel tube subjected to axial compression. Transactions of the Japan Concrete Institute, 19, pp.231-238.

Konno, K., Sato, Y., Ueda, T. and Onaga, M., 1999. Mechanical property of recycled concrete under lateral confinement. Transactions of the Japan Concrete Institute, 20, pp.287-292.

Kono, S., Watanabe, F. and Kajitani, A., 2001. Stress-Strain Relation of Confined Concrete under Dynamic Loading. In Fourth International Conference on Fracture Mechanics of Concrete and Concrete Structures, pp. 585-592.

Kovac, B., 2010. Structural response of circular concrete filled tube piers in integral bridges, MSc, Universitat Politècnica de Catalunya.

Lam, D. and Testo, N., 2008. Structural design of concrete filled steel elliptical hollow sections. Composite Construction VI, pp.20-24.

Lam, D. and Wong, K., 2005. Axial capacity of concrete filled stainless steel columns. ASCE Journal of Structures, pp.1107-1120

Li, Q., Duan, Y. and Wang, G., 2002. Behaviour of large concrete specimens in uniaxial tension. Magazine of concrete research, 54(5), pp.385-391.

Li, Q.M. and Meng, H., 2003. About the dynamic strength enhancement of concrete-like materials in a split Hopkinson pressure bar test. International Journal of solids and structures, 40(2), pp.343-360.

Liew, J.R., Sohel, K.M.A. and Koh, C.G., 2009. Impact tests on steel–concrete–steel sandwich beams with lightweight concrete core. Engineering Structures, 31(9), pp.2045-2059.

Liu, J., 2008. Rehabilitation and repair of reinforced concrete short columns with external steel collars (Doctoral thesis, University of Alberta)

LRFD. 1995. Manual of steel Construction: Load and Resistance Factor Design. American Institute of steel Construction, Chicago, Illinois.

Makarem, F.S. and Abed, F., 2013. Nonlinear finite element modelling of dynamic localizations in high strength steel columns under impact. International Journal of Impact Engineering, 52, pp.47-61.

Malvar, L.J. and Crawford, J.E., 1998. Dynamic increase factors for concrete. Naval Facilities Engineering Service Center Port hueneme CA.

Malvar, L.J. and Ross, C.A., 1998. Review of strain rate effects for concrete in tension. ACI Materials Journal, 95(6).

Malvar, L.J. and Ross, C.A., 1998. Review of strain rate effects for concrete in tension. Materials Journal, 95(6), pp.735-739.

Malvar, L.J., Crawford, J.E., Wesevich, J.W. and Simons, D., 1997. A plasticity concrete material model for DYNA3D. International Journal of Impact Engineering, 19(9-10), pp.847-873.

Mander, J.B., Priestley, M.J. and Park, R., 1988. Theoretical stress-strain model for confined concrete. Journal of structural engineering, 114(8), pp.1804-1826.

Mirmiran, A., Shahawy, M., Samaan, M., Echary, H.E., Mastrapa, J.C. and Pico, O., 1998. Effect of column parameters on FRP-confined concrete. Journal of Composites for Construction, 2(4), pp.175-185.

Mirmiran, A., Zagers, K. and Yuan, W., 2000. Nonlinear finite element modeling of concrete confined by fiber composites. Finite Elements in Analysis and Design, 35(1), pp.79-96.

Mohamed, H.M., Abdel-Baky, H.M. and Masmoudi, R., 2010. Nonlinear stability analysis of concrete-filled fiber-reinforced polymer-tube columns: experimental and theoretical investigation. ACI Structural Journal, 107(6).

Mollazadeh M. H., 2015. Load Introduction into Concrete Filled Steel Tubular Coulmns (Doctoral thesis, The University of Manchester).

Morino, S. and Tsuda, K., 2002. Design and construction of concrete-filled steel tube column system in Japan. Earthquake Engineering and Engineering Seismology, 4(1), pp.51-73.

Morino, S., Uchikoshi, M. and Yamaguchi, I., 2001. Concrete-filled steel tube column system-its advantages. International Journal of Steel Structures, 1(1), pp.33-44

Nishida, M. and Tanaka, K., 2006. Experimental study of perforation and cracking of water-filled aluminum tubes impacted by steel spheres. International Journal of Impact Engineering, 32(12), pp.2000-2016.

Ottosen, N.S., 1977. A failure criterion for concrete. American Society of Civil Engineers. Engineering Mechanics Division. Journal

Padmini, A.K., Ramamurthy, K. and Mathews, M.S., 2009. Influence of parent concrete on the properties of recycled aggregate concrete. Construction and Building Materials, 23(2), pp.829-836.

Perea, T., 2010. Analytical and experimental study on slender concrete-filled steel tube columns and beam-columns.

Portolés, J.M., Romero, M.L., Bonet, J.L. and Filippou, F.C., 2011. Experimental study of high strength concrete-filled circular tubular columns under eccentric loading. Journal of constructional steel research, 67(4), pp.623-633.

Prichard, S.J. and Perry, S.H., 2000. The impact behaviour of sleeved concrete cylinders. Structural Engineer, 78(17), pp.23-7.

Qu, H., Li, G., Chen, S., Sun, J. and Sozen, M., 2011. Analysis of circular concrete-filled steel tube specimen under lateral impact. Advances in Structural Engineering, 14(5), pp.941-952.

Rao, M.C., Bhattacharyya, S.K. and Barai, S.V., 2011. Behaviour of recycled aggregate concrete under drop weight impact load. Construction and Building Materials, 25(1), pp.69-80.

Reid, S.R., Reddy, T.Y. and Gray, M.D., 1986. Static and dynamic axial crushing of foam-filled sheet metal tubes. International Journal of Mechanical Sciences, 28(5), pp.295-322.

Rejab, M.R., 2013. The Mechanical Properties of Novel Lightweight Structures Based on Corrugated-Cores, (Doctoral thesis, University of Liverpool).

Remennikov, A.M., Kong, S.Y. and Uy, B., 2010. Response of foam-and concrete-filled square steel tubes under low-velocity impact loading. Journal of Performance of Constructed Facilities, 25(5), pp.373-381.

Richardson, M.O.W. and Wisheart, M.J., 1996. Review of low-velocity impact properties of composite materials. Composites Part A: Applied Science and Manufacturing, 27(12), pp.1123-1131.

Rossi, P. and Toutlemonde, F., 1996. Effect of loading rate on the tensile behaviour of concrete: description of the physical mechanisms. Materials and structures, 29(2), pp.116-118.

Sangi, A., 2011. Reinforced Concrete Structures Under Impact Loadings. PhD thesis, Heriot-Watt University.

Schneider, S.P., 1998. Axially loaded concrete-filled steel tubes. Journal of Structural Engineering, 124(10), pp.1125-1138.

Schwer, L., 2010. An introduction to the Winfrith concrete model. Schwer Engineering & Consulting Services, pp.1-28.

Schwer, L.E. and Malvar, L.J., 2005. Simplified concrete modelling with *MAT_CONCRETE_DAMAGE_REL3. JRI LS-Dyna User Week, pp.49-60.

Shams, M. and Saadeghvaziri, M.A., 1997. State of the art of concrete-filled steel tubular columns. ACI Structural Journal, 94(5), pp 558-569.

Shams, M., 1997. Non-linear evaluation of concrete-filled steel tubular columns. PHD. , New Jersey Institute of Technology.

Shan, Chen, Zhang, Xiao, Yi and Lu, 2007. Behavior of concrete filled tubes and confined concrete filled tubes under high speed impact. Advances in Structural Engineering, 10(2), pp.209-218.

Shanmugam, N.E. and Lakshmi, B., 2001. State of the art report on steel–concrete composite columns. Journal of constructional steel research, 57(10), pp.1041-1080.

Standards Association of Australia. SAA steel structures code, AS4100. Sydney, Australia: Standards Association of Australia, 1998.

Starossek, U., Falah, N. and Lohning, T., 2010. Numerical analyses of the force transfer in concrete-filled steel tube columns. Structural Engineering and Mechanics, 35(2), pp.241-256.

Sundarraja, M.C. and Prabhu, G.G., 2011. Investigation on strengthening of CFST members under compression using CFRP composites. Journal of Reinforced Plastics and Composites, 72, pp. 75-83.

Susantha, K.A.S., Ge, H. and Usami, T., 2001. Uniaxial stress–strain relationship of concrete confined by various shaped steel tubes. Engineering Structures, 23(10), pp.1331-1347.

Tao, Z., Han, L.H. and Wang, L.L., 2007. Compressive and flexural behaviour of CFRP-repaired concrete-filled steel tubes after exposure to fire. Journal of Constructional Steel Research, 63(8), pp.1116-1126.

Tao, Z., Han, L.H. and Zhuang, J.P., 2007. Axial loading behavior of CFRP strengthened concrete-filled steel tubular stub columns. Advances in Structural Engineering, 10(1), pp.37-46.

Tao, Z., Wang, Z.B. and Yu, Q., 2013. Finite element modelling of concrete-filled steel stub columns under axial compression. Journal of Constructional Steel Research, 89, pp.121-131.

Taverz, F. A., 2001. Simulation of Behaviour of Composite Grid Reinforced Concrete Beams Using Explicit Finite Element Methods. Master of Science. University of Wisconsin-Madison, USA.

Teng, J.G. and Lam, L., 2004. Behavior and modeling of fiber reinforced polymer-confined concrete. Journal of structural engineering, 130(11), pp.1713-1723.

tubular structures. Tokyo (Japan): Architectural Institute of Japan; 1997.

Veritas, D.N., 2010. Design against accidental loads. Recommended Practice DNV-RP-C204.

Wang, R., Han, L.H. and Hou, C.C., 2013. Behavior of concrete filled steel tubular (CFST) members under lateral impact: Experiment and FEA model. Journal of Constructional Steel Research, 80, pp.188-201.

Wang, Y., Chen, J. and Geng, Y., 2015. Testing and analysis of axially loaded normal-strength recycled aggregate concrete filled steel tubular stub columns. Engineering Structures, 86, pp.192-212.

Wang, Y., Qian, X., Liew, J.R. and Zhang, M.H., 2014. Experimental behavior of cement filled pipe-in-pipe composite structures under transverse impact. International Journal of Impact Engineering, 72, pp.1-16.

Wang, Z.B., Yu, Q. and Tao, Z., 2015. Behaviour of CFRP externally-reinforced circular CFST members under combined tension and bending. Journal of Constructional Steel Research, 106, pp.122-137.

Wu, Y. and Crawford, J.E., 2015. Numerical modeling of concrete using a partially associative plasticity model. Journal of Engineering Mechanics, 141(12), pp.04015051-1-04015051-24.

Xiao, 2004. Applications of FRP composites in concrete columns. Advances in Structural Engineering, 7(4), pp.335-343.

Xiao, J., Huang, Y., Yang, J. and Zhang, C., 2012. Mechanical properties of confined recycled aggregate concrete under axial compression. Construction and Building Materials, 26(1), pp.591-603.

Xiao, Y., He, W. and Choi, K.K., 2005. Confined concrete-filled tubular columns. Journal of Structural Engineering, 131(3), pp.488-497.

Xiao, Y., Shan, J., Zheng, Q., Chen, B. and Shen, Y., 2009. Experimental studies on concrete filled steel tubes under high strain rate loading. Journal of Materials in Civil Engineering, 21(10), pp.569-577.

Xiaoqing, M. and Stronge, W.J., 1985. Spherical missile impact and perforation of filled steel tubes. International Journal of Impact Engineering, 3(1), pp.1-16.

Yang, Y.F. and Han, L.H., 2006. Experimental behaviour of recycled aggregate concrete filled steel tubular columns. Journal of Constructional Steel Research, 62(12), pp.1310-1324.

Yang, Y.F. and Han, L.H., 2011. Behaviour of concrete filled steel tubular (CFST) stub columns under eccentric partial compression. Thin-Walled Structures, 49(2), pp.379-395.

Yang, Y.F. and Ma, G.L., 2013. Experimental behaviour of recycled aggregate concrete filled stainless steel tube stub columns and beams. Thin-Walled Structures, 66, pp.62-75.

Yang, Y.F., Han, L.H. and Wu, X., 2008. Concrete shrinkage and creep in recycled aggregate concrete-filled steel tubes. Advances in Structural Engineering, 11(4), pp.383-396.

Yang, Y.F., Han, L.H. and Zhu, L.T., 2009. Experimental performance of recycled aggregate concrete-filled circular steel tubular columns subjected to cyclic flexural loadings. Advances in Structural Engineering, 12(2), pp.183-194.

Yang, Y.F., Zhang, Z.C. and Fu, F., 2015. Experimental and numerical study on square RACFST members under lateral impact loading. Journal of Constructional Steel Research, 111, pp.43-56.

Young, B. and Ellobody, E., 2006. Experimental investigation of concrete-filled cold-formed high strength stainless steel tube columns. Journal of Constructional Steel Research, 62(5), pp.484-492.

Yousuf, M., Uy, B., Tao, Z., Remennikov, A. and Liew, J.R., 2013. Transverse impact resistance of hollow and concrete filled stainless steel columns. Journal of Constructional Steel Research, 82, pp.177-189.

Yousuf, M., Uy, B., Tao, Z., Remennikov, A. and Liew, J.R., 2014. Impact behaviour of pre-compressed hollow and concrete filled mild and stainless steel columns. Journal of Constructional Steel Research, 96, pp.54-68.

Yousuf, M., Uy, B., Tao, Z., Remennikov, A. and Liew, R., 2012. Impact Behaviour and Resistance of Hollow and Concrete Filled Mild Steel Columns. Australian Journal of Structural Engineering, (13), pp.65-80.

Yu, T., Teng, J.G., Wong, Y.L. and Dong, S.L., 2010. Finite element modeling of confined concrete-I: Drucker–Prager type plasticity model. Engineering Structures, 32(3), pp.665-679.

Yu, Z.W., Ding, F.X. and Cai, C.S., 2007. Experimental behaviour of circular concrete-filled steel tube stub columns. Journal of Constructional Steel Research, 63(2), pp.165-174.

Zaini, S.S., 2015. Impact resistance of pre-damaged ultra-high performance fibre reinforced concrete (UHPFRC) slabs (Doctoral thesis, University of Liverpool).

Zeghiche, J. and Chaoui, K., 2005. An experimental behaviour of concrete-filled steel tubular columns. Journal of Constructional Steel Research, 61(1), pp.53-66.

Zeinoddini, M., Harding, J.E. and Parke, G.A.R., 1999. Dynamic behaviour of axially pre-loaded tubular steel members of offshore structures subjected to impact damage. Ocean Engineering, 26(10), pp.963-978.

Zeinoddini, M., Harding, J.E. and Parke, G.A.R., 2002. Axially pre-loaded steel tubes subjected to lateral impacts: an experimental study. International Journal of Impact Engineering, 27, pp. 669-690.

Zeinoddini, M., Harding, J.E. and Parke, G.A.R., 2008a. Axially pre-loaded steel tubes subjected to lateral impacts (a numerical simulation) c. International Journal of Impact Engineering, 35, pp.1267-1279.

Zeinoddini, M., Harding, J.E. and Parke, G.A.R., Interface Forces in Laterally Impacted Steel Tubes. Experimental Mechanics, 48, pp.265–280

Zhang, J., Liu, Q.Q. and Wang, L.S., 2005. Effect of coarse aggregate size on relationship between stress and crack opening in normal and high strength concretes. Journal of Materials Science and Technology, 21(5), p.691-700.

Zheng, D. and Li, Q., 2004. An explanation for rate effect of concrete strength based on fracture toughness including free water viscosity. Engineering Fracture Mechanics, 71(16), pp.2319-2327.

Zhou C, Jiang W, Oan T. Guide for design and construction of concrete filled steel tubular structures, No. 12. Chinese Architecture and Industry Press, 1991.

Zhou C, Jiang W, Oan T., 1991. Guide for design and construction of concrete filled steel tubular structures, No. 12. Chinese Architecture and Industry Press.

Zhou, J., 2015. The Energy-Absorbing Behaviour of Novel Aerospace Composite Structures, (Doctoral thesis, University of Liverpool).

Web: www.funonthenet.in

Web: www.highestbridges.com

Web: www.sptimes.com

Web: www.nbcbayarea.com

Web: www.gov.uk/speed-limits

Web:www.motorists.org/

http://www.easycomposites.co.uk

Appendix A

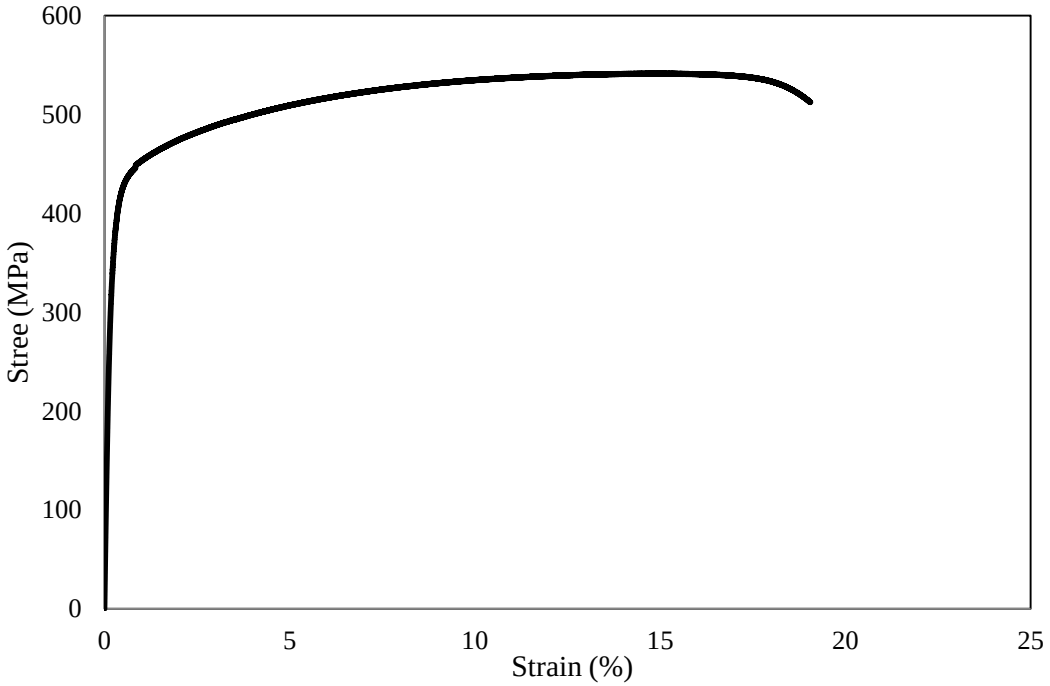

Figure A.1. The experimental stress-strain curve for the steel sample of the tube

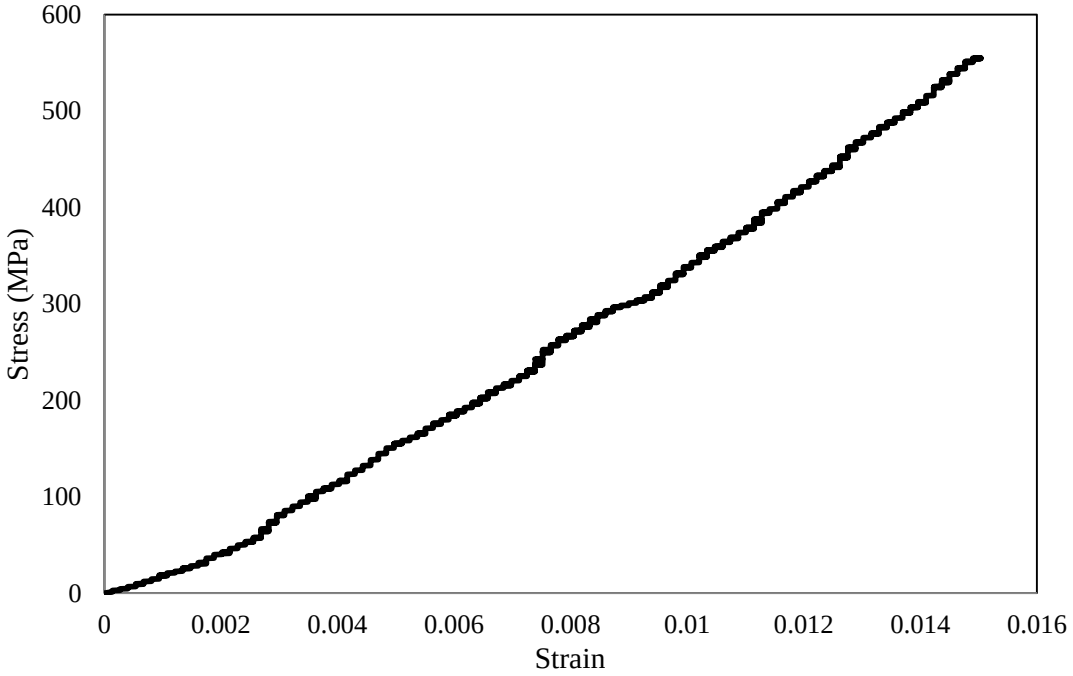

Figure A.2. The experimental stress-strain curve for the CFRP sample

Table A.1. The cube compressive strength for the impact test specimens

Specimen ID	cube1	cube2	cube3	Compressive strength (MPa)
S0	57.1	55.4	57.6	56.7
S50	53.6	54.2	54.9	54.3
S0s	57.1	55.4	57.6	56.7
S50s	53.6	54.2	54.9	54.3
S0-BI	57.1	55.4	57.6	56.7
S50-BI	53.2	52.1	53.7	53
S0-MI	57.1	55.4	57.6	56.7
S50-MI	53.2	52.1	53.7	53
S0s-MI	57.1	55.4	57.6	56.7
S50s-MI	53.2	52.1	53.7	53
S0-SI	57.1	55.4	57.6	56.7
S50-SI	53.2	52.1	53.7	53
S0-FI	57.1	55.4	57.6	56.7
S50-FI	53.2	52.1	53.7	53
M0	55	56.1	56.8	55.97
M50	51.1	52.8	52.7	52.2
M0s	55	56.1	56.8	55.97
M50s	51.1	52.8	52.7	52.2
L0	54.6	54.1	53.9	54.2
L50	50.1	51	50.6	50.57
L0s	54.6	54.1	53.9	54.2
L50s	50.1	51	50.6	50.57

Table A.1. The cube compressive strength for the compression test specimens

Specimen ID	cube1	cube2	cube3	Compressive strength (MPa)
C0i	56	56.2	57.9	56.7
C50i	55	53.6	54.3	54.3
C0	56	56.2	57.9	56.7
C50	55	53.6	54.3	54.3
C0s	56	56.2	57.9	56.7
C50s	55	53.6	54.3	54.3
E0	56	56.2	57.9	56.7
E50	55	53.6	54.3	54.3
E0s	56	56.2	57.9	56.7
E50s	55	53.6	54.3	54.3

Table A.1. The compression test experimental results

Specimen ID	Max. force (kN)	Max. dis. (mm)
C0i-1	1169	17.0
C0i-2	1173	16.5
C0i-3	1167	16.7
C50i-1	1158	17.5
C50i-2	1149	17.8
C50i-3	1161	17.4
C0-1	1092	20.2
C0-2	1100	20.6
C0-3	1091	20.2
C50-1	1074	20.5
C50-2	1081	20.8
C50-3	1086	20.6
C0s-1	1143	16.7
C0s-2	1140	16.4
C0s-3	1147	16.5
C50s-1	1100	17.8
C50s-2	1114	18.0
C50s-3	1117	17.6
E0-1	935	14.8
E0-2	934	15.5
E0-3	945	15.5
E50-1	880	16.1
E50-2	870	15.7
E50-3	866	15.5
E0s-1	975	15.4
E0s-2	970	15.1
E0s-3	966	15.4
E50s-1	925	14.9
E50s-2	932	15.2
E50s-3	928	15.0

The properties and the specifications of the epoxy laminating resin EL2

(www.easycomposites.co.uk).

easycomposites
share the knowledge

EPOXY LAMINATING RESIN

EL2

Key Features

- Easy to use
- Medium Viscosity Resin
- Outstanding Wetting Abilities
- Good Mechanical Properties
- Choice of Hardener Speed

Product Description

EL2 is a high performance general purpose epoxy laminating resin for use in wet-lay or vacuum bagging carbon fibre, aramid or glass lamination.

This medium viscosity epoxy exhibits excellent wetting characteristics especially when used with carbon fibre and aramid fibre (such as Kevlar®) reinforcement making airbubbles in the laminate less likely than with some alternative epoxy systems.

The resin also exhibits excellent cured mechanical properties far in excess of many more traditional epoxy resin brands (as can be seen from the technical data sheets). Improved mechanical properties mean stronger, lighter, higher performance parts.

Recommended Uses

Use as a general purpose laminating epoxy, wet-laying or vacuum bagging composites such as glass fibre, carbon fibre and aramid fibre (Kevlar).

When cured the epoxy exhibits good flexural strength making it will suited to the lamination of structural parts. The resin also exhibits very good clarity making it also suitable for use when laminating unpainted carbon fibre composites.

Properties

The table below shows the typical uncured properties:

Property	Units	Resin	Hardener	Combined
Material	-	Epoxy Resin	Formulated Amine	Epoxy
Appearance	-	Clear Liquid	Amber Liquid	Clear Liquid
Viscosity @20 °C	mPa.s.	1200 – 1800	5 - 80	1000 – 1400
Density @20 °C	g/cm³	1.13 – 1.17	0.90 – 1.06	1.05 – 1.15

How to Use

EL2 is a chemical product for professional use. It is essential to read and understand the safety and technical information before use.

Follow the guidelines for safe use outlined in the SDS which include the use of appropriate hand and eye protection during mixing and use.

Mix Ratio

Mix Ratio 100:30 by Weight

EL2 Epoxy Laminating Resin should be mixed with AT30 FAST or AT30 SLOW Hardener at a ratio of 100 parts of resin to 30 part sof hardener, by weight. FAST and SLOW hardeners can be blended to achieve pot-life and demould times anywhere between those stated. However, you must still maintain the correct overall ratio of resin to hardener to ensure a proper cure.

When working with any epoxy resin, it is essential to mix the resin and hardener exactly at the correct mix ratio. Failure to do so will result in a poor or only partial cure of the resin, greatly reduced mechanical properties and possibly other adverse effects. Under no circumstances add 'extra hardener' in an attempt to speed up the cure time; epoxies do not work in this way.

Mixing Instructions

EL2 is a highly reactive (fast curing) resin system. Only weigh out and mix as much resin as you can use within the pot life.

Weigh or measure the exact correct ratio of resin and hardener into a straight sided container. Using a suitable mixing stick begin to mix the resin and hardener together to combine them completely.

Spend at least one minute mixing the resin and hardener together, paying particular attention to the sides and base of the container. Remember: Any resin that has not been thoroughly combined with hardener will not cure.

Once you have finished mixing in one container, it is good practice to transfer the mixed resin into a second container and undertake further mixing of the resin using a new mixing stick. Doing so will eliminate the risk of accidentally using unmixed resin from the bottom or sides of the container.

Pot-Life / Working Time / Cure Time

EL2 is a highly reactive resin system and once the resin has been mixed with the hardener, the reaction will start to give off heat (exotherm) which will further accelerate the cure of the resin, especially when the resin is in the mixing pot.

Transfer the resin from the mixing pot onto the part as soon as possible to extend the working time and avoid the risk of uncontrollable rapid cure in the mixing pot.

As with all epoxies, the pot-life/working time will vary significantly depending on the ambient temperature, the starting temperature of the resin and hardener and the amount of resin mixed.

EL2 can be used in ambient temperatures between 15°C (59°F) and 30°C (86°F). For best results, an ambient temperature of at least 20°C (68°F) is recommended. Ensure that both resin and hardener containers are within this temperature range before use.

The table below gives an indication of pot-life and cure properties:

	Pot-Life @ 25 °C	Gelation @ 25 °C	Demould Time @ 25 °C
AT30 SLOW*	95 - 115mins	8.5 - 10.5hrs	20 - 30hrs
AT30 FAST*	12 - 17mins	2 - 3hrs	4 - 6hrs

*Fast and slow hardeners can be blended to achieve pot-life and demould timesanywhere between those stated above.

Full Cure / Post-Cure

As with most epoxy systems, where parts cure in normal ambient temperatures, full cure is not reached for several days. Although parts will be handleable after the listed demould time (at 25°C), full mechanical properties will take at least 14 days to develop in (at 25°C). Where possible, avoid exposing the cured resin to full service rigours for at least this time.

As with many post-cure cycles for resins, the post-cure cycle for our EL2 Epoxy Resin is not too sensitive and a range of different post-cure cycles will produce good results, specifically improved mechanical performance and elevated HDT/operating temperature. Post-curing parts that will be used at or exposed to elevated operating temperatures (such as vehicle bonnets/hoods in direct sunlight, engine-bay parts, car interior parts etc.) is strongly recommended to prevent distortion of the parts when they are put into service and experience these higher temperatures.

Where possible, parts should be post-cured still inside the mould to reduce distortion and improve surface finish (i.e. reduce 'print-through'). When post-curing parts in the mould, it is important to post-cure them without demoulding at all (i.e. don't demould and then put them back into the mould) otherwise you can get some strange patterns on the surface where some areas are post cured in direct contact with the mould surface and others are not.

A simple and very effective post-cure cycle with the EL2 Epoxy Laminating Resin is as follows:

CYCLE #1 SUITABLE FOR MOST SITUATIONS

- 24hrs at room temperature
- 6hrs at 60°C

If you're encountering any surface finish issues (faint print-through) then you can experiment with a slower 'ramp rate' which sometimes improves things:

CYCLE #2 SUGGESTED FOR SUBTLE IMPROVEMENTS TO SURFACE FINISH

- 24hrs at room temperature
- 2hrs at 40°C
- 2hrs at 50°C
- 5hrs at 60°C

If you need to push the HDT of the finished part higher then you could increase post-cure up to a maximum of 80°C as follows:

CYCLE #3 SUGGESTED FOR HIGHEST POSSIBLE HDT/OPERATING TEMPERATURE

- 24hrs at room temperature
- 2hrs at 40°C
- 2hrs at 50°C
- 2hrs at 60°C
- 2hrs at 70°C
- 4hrs at 80°C

These are all just suggestions. Most situations just call for option #1; 6hrs at 60°C. Many customers also find that they can dispense with the 24hrs cure at ambient and simply load newly infused parts into the oven to begin the cure however this is something that you would need to experiment with yourself. A cure at ambient temperature before post-cure is generally favoured with most resin systems.

Mechanical Properties

Cured Resin Properties

	Units	AT30 SLOW	AT30 FAST
Hardness	Shore D	84 - 88	85 - 89
Linear Shrinkage	%	0.5	0.5
Tensile Strength	MPa	70.0 - 80.0	67.0 - 75.0
Elongation at Break	%	6.0 - 10.0	6.0 - 8.0
Flexural Strength	MPa	103 - 117	120 - 130
Flexural Modulus	MPa	2600 - 3200	3600 - 4000
H.D.T	°C	82 - 88	70 - 76

Transport and Storage

Resin and hardener should be kept in tightly seal containers during transport and storage. Both the resin and hardener should be stored in ambient conditions of between 10°C (50°F) and 25°C (77°F).

When stored correctly, the resin and hardener will have a shelf-life of 12 months. Although it may be possible to use the resin after a longer period, a deterioration in the performance of the resin will occur, especially in relation to clarity and cure profile.

Pay particular attention to ensuring that containers are kept tightly sealed. Epoxy hardeners especially will deteriorate quickly when exposed to air.

Disclaimer

This data is not to be used for specifications. Values listed are for typical properties and should not be considered minimum or maximum.

Our technical advice, whether verbal or in writing, is given in good faith but Easy Composites Ltd gives no warranty, express or implied, and all products are sold upon condition that purchasers will make their own tests to determine the quality and suitability of the product for their particular application and circumstances.

Easy Composites Ltd shall be in no way responsible for the proper use and service of the product, nor for the safeguarding of personnel or property, all of which is the duty of the user. Any information or suggestions are without warranty of any kind and purchasers are solely responsible for any loss arising from the use of such information or suggestions. No information or suggestions given by us shall be deemed to be a recommendation to use any product in conflict with any existing patent rights. Before using any of our products, users should familiarise themselves with the relevant technical and safety datasheets provided by Easy Composites Ltd.

easycomposites™
share the knowledge

Easy Composites Ltd
Unit 39, Park Hall Business Village, Longton, Stoke on Trent, Staffordshire, ST3 5XA, United Kingdom.
Tel. +44 (0)1782 454499, Fax. +44 (0)1782 596868, Email sales@easycomposites.co.uk, Web www.easycomposites.co.uk